UNIVERSITÀ
DEGLI STUDI
FIRENZE

DOTTORATO DI RICERCA IN

SCIENZE DELLA TERRA

CICLO XXXV

Ferrate removal of metal contaminants in the environmental remediation field: synchrotron radiation studies applied to the Hg contaminated waters from Abbadia San Salvatore, Amiata area

Settore Scientifico Disciplinare

GEO/09

GEO/06

Dottorando
Dott. Baroni Tommaso

Supervisore
Prof. Di Benedetto Francesco

Coordinatore
Prof. Moretti Sandro

- Abstract -

In the past decades, high-valent iron compounds, commonly called ferrates (containing Fe(IV-V-VI)), have drawn lot of interests as sustainable chemical treatments for drinking water/wastewaters/industrial effluents remediation. Due to their properties such as high oxidizing power over the entire pH, selective reactivity and non-toxic decomposition by-products with high coagulant performances, ferrate(VI) have been proposed as multi-purpose water treatment chemicals/coagulants/disinfectants. While a large literature has been produced about the elements-bearing acid mining drainage elements and the Hg release currently represents an ongoing environmental challenge, almost no studies have been published regarding the mercury removal from water using ferrate(VI), except for two inconsistent papers examining the removal of a wide range of metal ions from lab prepared solutions (Bartzatt et al., 1992; Murmann & Robinson, 1974). This study investigates the Hg-removal from water by ferrate(VI) in comparison with more traditional (e.g. $FeCl_3$, "Fe(III)") and modern methods (e.g. nanoscale iron based reductants, nZVIs and bimetallic Fe(0)+Ag(0) NPs), while starting to elucidate its removal mechanism using synchrotron radiation techniques (X-ray Absorption Spectroscopy). Particularly, for the first time, natural contaminated waters were tested, using samples collected from the Abbadia San Salvatore former Hg-mining area (ASSM) with starting Hg content of ~ 167 and 202 ppb. Together with two solid reagents containing Fe(VI) (Mixfer and solid ferrate "SFe(VI)"), a liquid ferrate synthesized with an original procedure was also tested ("LFe(VI"). The synthesis was developed at the Department of Earth Science of the University of Florence and achieved yields comparable to the best liquid ferrate syntheses ever published. From tests using 500 ppb and 1 ppm Hg(II) laboratory-prepared solutions, LFe(VI) presented ~ 91 % Hg removal, in agreement with the preliminary studies published and comparable with the Fe(III) results. Because of the much more complex nature of ASSM contaminated water, such efficiencies have not been replicated in terms of absolute values, due to the presence inside of the natural-water precipitate and in the suspected suspended particulate of β-HgS particles, as highlighted by SEM and XAS observations. Due to Fe(VI) oxidative power, HgS was dissolved by the application of the ferrates(VI) products, increasing the Hg(II) content in the water but efficiently removing and collecting mercury from sources normally difficult to reach, as well as impacting on the factors favorable to methyl-mercury formation (e.g. reducing conditions). The nZVIs tested did not show results comparable with the Hg removal from literature, probably due to a strong passivation layer affecting their surfaces. Moreover, due to their reductive properties (Hg(II) adsorbed and reduced to Hg(0)), mitigating the risk posed by formation of volatile Hg(0) has to be considered prior to their application. The bimetallic Fe+Ag NPs showed the highest efficiencies under the ASSM natural conditions and the formation of an Hg-Ag amalgam (adsorption Hg(II) -> reduction to Hg(0) -> amalgamation). Hg amalgam formation provides benefits in respect to mechanical strength and stability, likely reducing the tendency of Hg(0) to volatilize. While being far from perfect and presenting high degrees of improvements, this study succeeded in creating a solid platform for testing environmental remediation procedures with natural matrices. Possible future developments regarding this project involve repeating the removal tests varying more the boundary conditions, the combination of different reagents, e.g. KClO + nZVIs and KClO + Fe+Ag NPs, in order to evaluate the possible synergistic effects, and the use of instruments not available to the Department of Earth Sciences, such as an XPS microscope or a HR-TEM.

- Contents –

- Abbreviations -

ABTS: 2,2-azino-bis(3-ethylbenzothiazoline-6-sulfonate)

AC: Activated Carbon

Ag NP: Ag(0) NanoParticle

AOM: Algal Organic Matter

AOX: Adsorbable Organic Haloids

ASS: Abbadia San Salvatore

ASSM: Abbadia San Salvatore Mining area

BDD: Boron Doped Diamond

BSE: Back-Scattered Electrons

BTC: Basal Trachydacitic Complex

CIF: Cristallographic Information File

COD: Chemical Oxygen Demand

COF: Covalent Organic Framework

CV: Cyclic Voltammetry

CWA: Chemical Warfare Agent

DL: Detection Limit

DOC: Dissolved Organic Carbon

DW: Deionized Water

EDX: Energy Dispersive X-ray

EH1, EH2: Experimental Hutch 1, Experimental Hutch 2

EPA: Environmental Protection Agency

ESRF: European Synchrotron Radiation Facility

EXAFS: Extended X-ray Absorption Fine Structure

FC: Field Cooled

Fe+Ag NPs: Fe(0) and Ag(0) NanoParticles

FS: Ferrate Solutions®

FTIR: Fourier Transform Infrared spectroscopy

FTT: Ferrate Treatment Technologies

FWHM: Full Width at Half Maximum

GCWW: Greater Cincinnati Water Works

GEM: Gaseous Elemental Mercury

GF/A, GF/C, P-0: filter pore indexes

GITA: Galleria ITAlia

HgSS: Hg Standard Solution

ICP-MS: Inductively Coupled Plasma Mass-Spectrometry

LCF: Linear Combination Fit

LFe(VI): Liquid Ferrate(VI)

LISA: Linea Italiana per la Spettroscopia di Assorbimento di raggi X

LM: Line Method

MAMD: Mount Amiata Mining District

MB: Mass Balance

MEMA: Centro di Servizi di Microscopia Elettronica e Microanalisi

MSA: MercaptoSuccinic Acid

NOM: Natural Organic Matter

nZVI: Zero Valent Iron nanoparticle

ppb: part per billion

ppm: part per million

RCPTM: Regional Centre of Advanced Technologies and Materials

RET: Recovered Earth Technologies

S63: Hg contaminated soil from Petrineri mine

S6N: ASSM piezometer

SAED: Selected Area Electron Diffraction

SE: Secondary Electrons

SEM: Scanning Electron Microscope

SFe(VI): Solid Ferrate(VI)

SHE: Standard Hydrogen Electrode

STP: Sewage Treatment Plant

TEM: Transmission Electronic Microscopy

TMP: Tuscany Magmatic Province

TQ: Tal Quale (meaning "as it is")

UV: UltraViolet

UV-Vis: UltraViolet-Visible

VESTA: Visualization for Electronic and STructural Analysis

WHO: World Health Organization

XANES: X-ray Absorption Near the Edge Structure

XAS: X-ray Absorption Spectroscopy

XPS: X-ray Photoelectron Spectroscopy

XRD, XRPD: X-Ray Powder Diffraction

ZFC: Zero Field Cooled

ZVI: Zero Valent Iron

α-HgS: cinnabar

β-HgS: metacinnabar

ε: molar absorptivity

- Introduction -

In the past decades, high-valent iron compounds, commonly called ferrates (containing Fe(IV-V-VI)), have drawn lot of interests as sustainable chemical treatments for drinking water/wastewaters/industrial effluents remediation. Due to their properties such as high oxidizing power over the entire pH, selective reactivity and non-toxic decomposition by-products whit high coagulant performances, ferrates have been proposed as multi-purpose water treatment chemicals/coagulants/disinfectants. While a large literature has been produced about the elements-bearing acid mining drainage elements and the Hg release currently represents an ongoing environmental challenge, almost no studies have been published regarding the mercury removal from water using ferrates, except for two inconsistent papers examining the removal of a wide range of metal ions from lab prepared solutions (Bartzatt et al., 1992; Murmann & Robinson, 1974). This study investigates the Hg-removal from water by ferrates in comparison with more traditional ($FeCl_3$) and modern (nanoscale iron based reductants) methods, while starting to elucidate Fe(VI) removal mechanism using synchrotron radiation techniques (X-ray Absorption Spectroscopy). Particularly, for the first time, natural contaminated waters were tested, using samples collected from the Abbadia San Salvatore former Hg-mining area (Tuscany, Italy).

1.1. Ferrates: review and state-of-the-art

In the wide range of iron valence states, chemicals with higher oxidation states have been synthesized in laboratory, ranging from Fe(IV) to Fe(VIII) (Schmidbaur, 2018). In particular, ferrate(VI) (Fe(VI)) has received particular attention for its role in the development of “super iron” batteries, in the green chemistry synthesis and oxidation of modern pollutants for environmental remediation (DeLuca et al., 1983; Filip et al., 2011; Jain et al., 2009; J.-Q. Jiang et al., 2018; J.-Q. Jiang & Lloyd, 2002; J. Jiang et al., 2013; Johnson & Lorenz, 2015; Kralchevska et al., 2016; Licht, Naschitz, Halperin, et al., 2001; Prucek et al., 2015, 2013; Rai et al., 2018; Virender K. Sharma, 2010, 2011; Virender K. Sharma et al., 1997; Song & Ma, 2013; Zhao et al., 2014).

Treatments of water sources collected worldwide, as well as laboratory specimens and pilot implants, have demonstrated the ferrates capability of removing in milliseconds to minutes a wide range of organic and inorganic compounds (see Par. 1.1.4.). The Fe(VI) redox potential is superior to other oxidants/disinfectants (Tab. 1.2) while the additional benefit lies in the fact that during the oxidation/disinfection process the reaction with water leads to the in-situ formation of Fe(III) oxides/hydroxides/oxyhydroxides nanoparticles, which serve as efficient adsorbents for oxidized pollutants and suspended/colloidal materials (Prucek et al., 2013). Since pre-oxidation (addition of an oxidant to raw water) is a common step in various water treatments, ferrate(VI) has been proposed as a as multi-function water chemical, which can reduce the treatment cost with a single injection.

1.1.1. General properties

Iron is a ubiquitous element in the earth's crust, ranking fourth with about 5% by mass (Duarte, 2019). In the crust mineral environment and in biological systems, iron can be found in extremely varying concentration, from trace level up to 72% in magnetite. Under the Earth physio-chemical conditions, iron has an high versatility, being able to participate in ion mobility processes, forming solids, promoting redox reactions which have a great impact on the mobility of various species in the environment, e.g. arsenic (Duarte, 2019). The ferrous (Fe(II)) and ferric (Fe(III)) states are the most common in the natural environment; the most diffuse minerals are hematite, maghemite, magnetite and goethite (Duarte, 2019) (Tab. 1.1). Ferrite salts (FeO_2^-) have been synthesized for various industrial and environmental applications, together with other salts with iron in higher oxidation states (e.g. Tab. 1.1) (Casbeer et al., 2012; Jeannot et al., 2002; Kopelev et al., 1992; Perfiliev et al., 2007; Perfiliev & Sharma, 2008; Yates, Darlington, et al., 2014). Evidence for the existence of a tetraoxoferrate(VII) was produced by Zhou et al. in a recent work (J. B. Lu et al., 2016). Formed by co-condensation of laser ablated iron atoms and electrons with O_2/Ar mixtures at 4 K, the anion was studied through a combination of matrix-isolation infrared spectroscopy and theoretical calculations (J. B. Lu et al., 2016). Regarding Fe(VIII), a FeO_4 molecule is still considered a “non-existent compound”, that is to say all attempts to synthesize it were unsuccessful (Schmidbaur, 2018). As highlighted by the theoretical study of Huang et al. 2016,

the Fe(VIII) oxidation state seems not to be stable under "normal chemical conditions", being only possible for metastable FeO_4 in vacuum at "non-elevated temperatures" (W. Huang et al., 2016).

Formula	**Name**	**Mineral/salt**
Fe_2O_3	Ferric oxide	hematite, maghemite
Fe_3O_4	Ferroso-ferric oxide	magnetite
FeO(OH)	Ferric oxide monohydrate	goethite, akaganeite
FeO_2^-	Ferrite	$NaFeO_2$, $KFeO_2$
FeO_4^{4-}	Ferrate(IV)	Na_4FeO_4
FeO_4^{3-}	Ferrate(V)	K_3FeO_4
FeO_4^{2-}	Ferrate(VI)	Na_2FeO_4, K_2FeO_4
FeO_4^-	Ferrate (VII)	-
FeO_4	Ferrate(VIII)	-

Table 1.1: oxo-compounds of iron at different oxidation states.

Among the various higher oxidation states, the +6 is comparatively stable and easier to produce. Figure 1.1 shows the iron speciation depending on redox potential and pH conditions (Virender K. Sharma, 2011). Single solid lines separate species related by acid-base equilibria (e.g. line **a** indicates the pH at which half of the 1 M iron is Fe^{3+} and half is precipitated as $Fe(OH)_2$); solid double lines separate species related by redox equilibria (e.g. line **b** separate redox species involving hydrogen/hydroxide ions and so appears diagonal because part of an acid-base equilibria); internal dashed lines enclose the theoretical water stability region to oxidation or reduction (e.g. dashed line **c** represents the potential of O_2 saturated water at 1 atm, above which water is oxidized to oxygen) while external dashed lines enclose the practical water stability region (e.g. dashed line **d** defines the additional 0.5 V of potential necessary to overcome the overvoltage of oxygen formation). Figure 1.1 suggests how ferrate(VI) has an high potential under acidic conditions which strongly decreases at high pH; moreover, it emerges how ferrate(VI) is stable in water only under alkaline conditions and it oxidizes water about pH < 10.

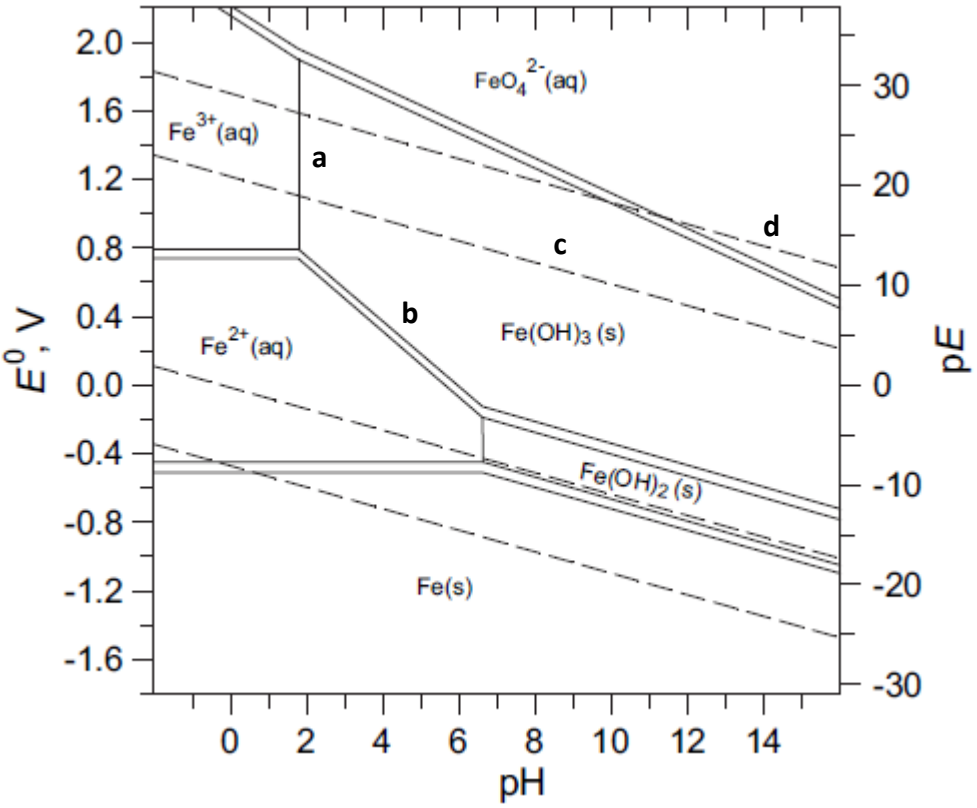

Figure 1.1: simplified Pourbaix diagram for 1 M iron solutions, from (Virender K. Sharma, 2011) modified.

Fe(VI) is a powerful oxidizing agent both in acidic and basic solutions, with redox potentials spanning from + 2.2 to + 0.7 V, respectively. In acidic conditions, its redox potential is superior to other oxidants/disinfectants, making it the strongest of all the products practically used for water/wastewater treatment (higher than that of ozone, which is 2.0 V) (Tab. 1.2) (J.-Q. Jiang & Lloyd, 2002).

Disinfectant/ oxidant	Reaction	E^o, V
Chlorine	$Cl_2(g) + 2e \leftrightarrows 2Cl^-$	1.358
	$ClO^- + H_2O + 2e \leftrightarrows Cl^- + 2OH^-$	0.841
Hypochlorite	$HClO + H^+ + 2e \leftrightarrows Cl^- + H_2O$	1.482
Chlorine dioxide	$ClO_2(aq) + e \leftrightarrows ClO_2^-$	0.954
Perchlorate	$ClO_4^- + 8H^+ + 8e \leftrightarrows Cl^- + 4H_2O$	1.389
Ozone	$O_3 + 2H^+ + 2e \leftrightarrows O_2 + H_2O$	2.076
Hydrogen peroxide	$H_2O_2 + 2H^+ + 2e \leftrightarrows 2H_2O$	1.776
Dissolved oxygen	$O_2 + 4H^+ + 4e \leftrightarrows 2H_2O$	1.229
Permanganate	$MnO_4^- + 4H^+ + 3e \leftrightarrows MnO_2 + 2H_2O$	1.679
	$MnO_4^- + 8H^+ + 5e \leftrightarrows Mn^{2+} + 4H_2O$	1.507
Ferrate(VI)	$FeO_4^{2-} + 8H^+ + 3e \leftrightarrows Fe^{3+} + 4H_2O^-$	2.20
	$FeO_4^{2-} + 4H_2O + 3e \leftrightarrows Fe(OH)_3 + 5OH^-$	0.76

Table 1.2: redox potential for the oxidants/disinfectants used in water and wastewater treatment (J.-Q. Jiang & Lloyd, 2002; J. Yu et al., 2023).

In aqueous solutions, Fe(VI) exhibits a distinctive red-violet color, which resembles permanganate; ferrate ions exhibits characteristic absorption peaks at 500 and 800 nm in the visible range along with several absorption peaks in the near-infrared (IR) region (Schmidbaur, 2018) (Fig. 1.2).

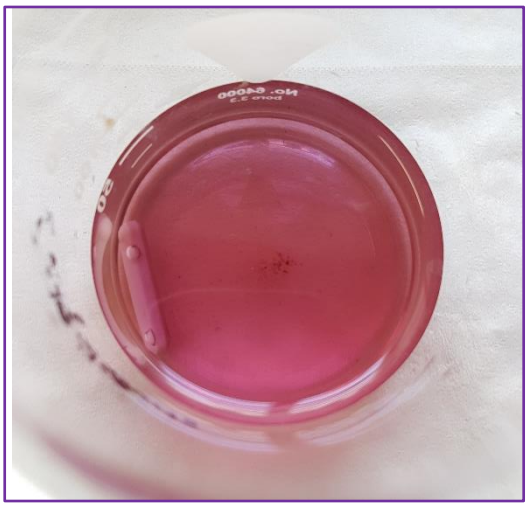

Figure 1.2: typical color of a Fe(VI) aqueous solution, freshly mixed.

The employment of common oxidizers and disinfectants such as chlorine (Cl_2) and ozone (O_3) presents some limitations such as formation of carcinogen by-products during the reaction with natural occurring organic matter in water treatments (e.g. trihalomethanes and

bromate). Fe(VI) treated waters did not produce mutagenic and carcinogenic by-products such as bromate due to Fe(VI) non-reacting with bromide ion, as demonstrated by the negative results of the Ames test (DeLuca et al., 1983). A more recent study compares the formation of Adsorbable Organic Haloids (AOX) as by-products of the ferrate(VI) and chlorine treatments of municipal secondary effluents (Gombos et al., 2013). The results show how a low Fe(VI) content is able to inactivate 99.9 % of the bacteria and largely removes dissolved phosphate while generating less AOX formation than chlorination (Gombos et al., 2013). Moreover, in another study, the toxicity of ferrate(VI) treated wastewater was evaluated and compared to the un-treated wastewater using the zebrafish embryos model (J. Jiang et al., 2013). The tests performed at various dilutions and [ferrate(VI)] showed the zebrafish embryos high mortality once added to the raw wastewater, while no adverse effect emerged from the addition to the ferrate(VI) treated samples (Fig. 1.3) (J. Jiang et al., 2013).

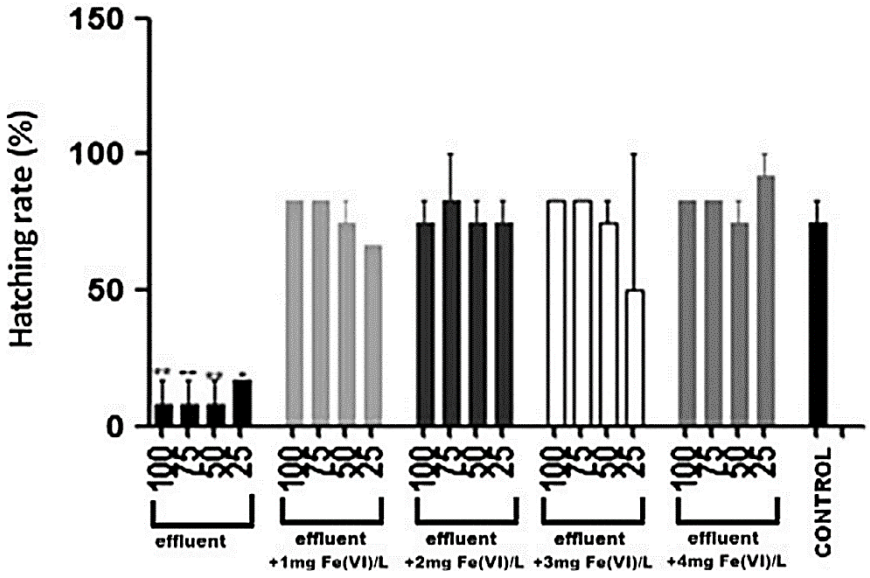

Figure 1.3: zebrafish embryos hatching rate after the treatment for 72 h in raw wastewater ("effluent") and ferrate(VI) (1, 2 or 3 mg Fe/L) treated effluents, at 100% and diluted to 75 %, 50 % and 25 %. Untreated zebrafish embryo water was as the control sample. Results are shown as the mean ± SD (n = 7). Error bar: standard deviation (SD). From (J. Jiang et al., 2013).

The Fe(VI) ion (FeO_4^{2-}) has a tetrahedral structure similar to its geometry in the solid state; it has three independent Fe-O bond distances with bond angles close to the 109.5° required for a perfect tetrahedron (Fig. 1.4). The M_2FeO_4 salts (M = K, Rb and Cs) are isomorphous with K_2SO_4, K_2CrO_4 and K_2MnO_4, sharing an orthorhombic Pnam cell (Audette et al., 1973; Hoppe

et al., 1982). Table 1.3 summarizes the general structural parameters of the studied ferrate (VI) salts.

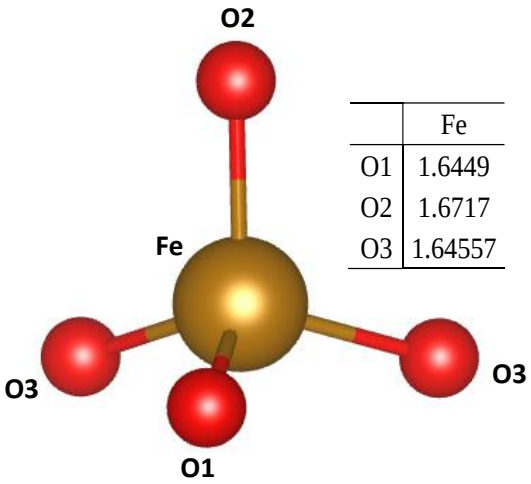

	Fe
O1	1.6449
O2	1.6717
O3	1.64557

O1-Fe-O2	110.1618
O2-Fe-O3	107.9576
O3-Fe-O3	110.0526
O1-Fe-O3	110.3249

Figure 1.4: FeO_4^{2-} anion structure realized with the Visualization for Electronic and Structural Analysis (VESTA); Fe-O bond distances in (Å) and angles in (°), data from (Hoppe et al., 1982).

1.1.1.1. Solubility and stability in water

The stability of ferrate(VI) is a problem which limits its storing, large-scale application and synthesis; once in contact with water molecules, ferrate(VI) will rapidly decompose, undergoing oxidation processes synthesized by eq. (1). Due to the release of hydroxyl ions, the resulting pH of the solution will be highly alkaline.

$$4FeO_4^{2-} + 10H_2O \rightarrow 4Fe(OH)_3 + 3O_2 \uparrow + OH^- \quad (1)$$

As reported in numerous studies and expressed in the eq. (1), "… ferrate(VI) ions will be reduced to Fe(III) ions or ferric hydroxide, and this generates a coagulant in the process simultaneously" (J.-Q. Jiang & Lloyd, 2002). This generic statement on the decomposition products nature of Fe(VI), often described as "Fe(III)", "ferric hydroxide", "ferric hydroxides" and/or "ferric oxide" in multiple state-of-the-art reviews (J.-Q. Jiang & Lloyd, 2002; J. Q. Jiang, 2007; Luo et al., 2011; V. K. Sharma, 2007), was deeply delved by Prucek et al., who used a broad variety of techniques onto the resulting products from ferrate(VI) decomposition alone and from pollutants removal at neutral and near-neutral pH (Kralchevska et al., 2016; Prucek et al., 2013, 2015). All the solid samples resulting from ferrate(VI) decomposition in deionized

water and from reaction with polluted solutions were turned to be X-ray amorphous on the basis of X-Ray powder Diffraction (XRD) measurements, with the only existing signals appearing in the maghemite (γ-Fe_2O_3) most intense diffraction lines (Kralchevska et al., 2016; Prucek et al., 2013, 2015). This information was then unambiguously confirmed by the 5 K ^{57}Fe in-field Mossbauer spectroscopy, while the particle size distribution through Transmission Electronic Microscopy (TEM) pointed out an average particle size between 3.92 ± 0.35 nm for the "ferrate(VI) in deionized water" nanoparticles and 2.41 ± 0.29 nm for the "ferrate(VI) in As solution" ones, with similar results coming from the phosphate removal study (Kralchevska et al., 2016; Prucek et al., 2013, 2015). The Selected Area Electron Diffraction (SAED) confirmed the poorly crystalline nature of the nanoparticles and 5 K hysteresis loop measurements and Zero-field-Cooled (ZFC) and Field-Cooled (FC) magnetization curves proved again to be compatible with poorly crystalline nanoparticles of γ-Fe_2O_3, while suggesting also a core-shell architecture (Prucek et al., 2013, 2015). This architecture was finally confirmed by 5 K ^{57}Fe in-field Mossbauer spectroscopy, which highlighted the presence of a γ-FeOOH shell surrounding the γ-Fe_2O_3 core, with evidences of pollutants being both incorporated in the crystalline sites of the γ-Fe_2O_3/ γ-FeOOH nanoparticles and/or adsorbed onto the surface (see par. 1.1.4) (Kralchevska et al., 2016; Prucek et al., 2013, 2015). A core-shell γ-Fe_2O_3/ γ-FeOOH nanoparticles formation was then proposed as the main model of Fe(VI) dissolution in water.

Using the dissociation constants from the previous literature, Sharma was able to calculate the speciation of the ferrate species (Fig. 1.5). Ferrate(VI) exists in four main forms, including $H_3FeO_4^+$, H_2FeO_4, $HFeO_4^-$ and FeO_4^{2-}; at neutral and alkaline pH, $HFeO_4^-$ and FeO_4^{2-} are the predominant Fe(VI) species while $H_3FeO_4^+$ and H_2FeO_4 dominate the acidic pH range.

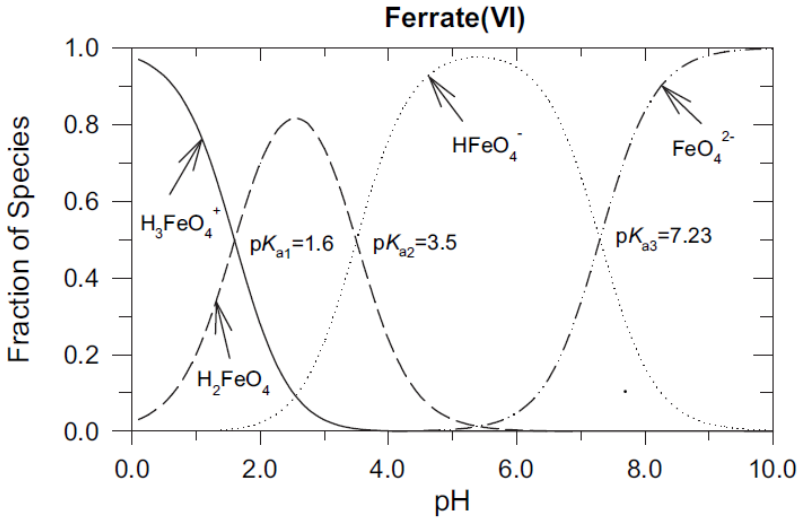

Figure 1.5: triprotonated, diprotonated, monoprotonated and deprotonated species of ferrate(VI) present in the acidic to basic pH range (Virender K. Sharma, 2011).

While being stable at higher pH, FeO_4^{2-} is extremely unstable at acidic pH, undergoing rapid exothermic degradation In aqueous solution of pH = 5, a [ferrate(VI)] solution = 1 mM was reported to completely degrade within 7 minutes (Tiwari et al., 2007). The main reactions under different environment are shown by eq. (2) and (3) (J. Yu et al., 2023):

$$Acidic: \quad FeO_4^{2-} + 8H^+ + 3e^- \rightarrow Fe^{3+} + 4H_2O \quad (2)$$

$$Alkaline: \quad FeO_4^{2-} + 4H_2O + 3e^- \rightarrow Fe(OH)_3 + 5OH^- \quad (3)$$

Therefore, the solubility and stability of Fe(VI) salts are among the most important characteristics when the potential practical synthesis and use of ferrate(VI) are considered. The solubility indicates how easily the Fe(VI) ion can be transferred from solution, where it is mostly produced, to the solid state. The solid state is necessary for long-term storage because of the negative influence of the moisture. In the case of drinking water treatment, the solid state is also preferred since addition of dissolved ferrate(VI), as opposed to solid, would increase the pH and salinity of the solution (because it is usually produced in highly alkaline solutions) (Mácová et al., 2009).

The first ferrate salt isolated and characterized is the potassium salt K_2FeO_4 (Fig. 1.6); other noteworthy examples include alkali ferrates(VI), M_2FeO_4 (M = Li, Na, Rb and Cs) and earth

alkaline ferrates(VI), M'FeO_4 (M' = Ca, Sr, Ba) together with the silver ferrate, Ag_2FeO_4 (Tab. 1.3) (Schmidbaur, 2018).

Potassium ferrate (K_2FeO_4) and **sodium ferrate** (Na_2FeO_4) are the two types of ferrate salts most often employed for water and wastewater treatment. K_2FeO_4 can be obtained in relatively high purity/quantity (see par. 1.1.3.), it is stable at ambient T° and it is an important precursor for the synthesis of some of the other ferrate salts by cation exchange and metathesis (Schmidbaur, 2018). More important, K_2FeO_4 is insoluble in a saturated KOH solution, so it can be isolated through a precipitation procedure (J.-Q. Jiang & Lloyd, 2002). Instead, Na_2FeO_4 is not accessible in pure crystalline form using conventional synthesis methods due to the fact that it remains soluble in aqueous solution saturated in NaOH; since the ferrate solution is unstable and it is convenient to prepare a solid product, the preparation of Na_2FeO_4 from aqueous solution is difficult (J.-Q. Jiang & Lloyd, 2002; Schmidbaur, 2018).

Lithium ferrate(VI) (Li_2FeO_4) has been prepared for the first time by cation exchange reaction on K_2FeO_4 and freeze drying of the resulting aqueous solution (Malchus & Jansen, 1998). Due to the hydrated nature of the compound, the resulting low stability makes a temperature-control environment mandatory (Malchus & Jansen, 1998).

Rubidium and cesium ferrates(VI) (Rb_2FeO_4 and Cs_2FeO_4 respectively) can be prepared using the corresponding hypochlorite and hydroxide, with a procedure similar to the wet synthesis adopted for K_2FeO_4 (see par. 1.1.3.) or by the already mentioned cation exchange (Audette & Quail, 1972; Licht et al., 2004). Together with a mixed Na-K ferrate salt, their use in super-iron ferrate batteries have been documented by Licht et al. (Licht et al., 2004). While ferrates of light earth alkaline metals are not known, **calcium ferrate** ($CaFeO_4$) has been recently synthesized with a purity sufficient to be properly characterized (71.5%); due to the presence of higher impurity content as Fe(III) and H_2O molecules, the stability of the resulting product is relatively low (Xu et al., 2007).

Strontium and **barium ferrate** salts ($SrFeO_4$ and $BaFeO_4$ respectively) can be synthesized using their respective acetate salts in a solution where K_2FeO_4 is added, exploiting their higher alkaline insolubility compared to that of potassium ferrate(VI) (Licht, Naschitz, Ghosh, et al., 2001). It is interesting to highlight the intrinsic complication of the ferrate salts syntheses, which the stability conditions of ferrate contribute to: e.g., in the same period of time, Dedushenko et al. claimed that they were "not able to prepare $SrFeO_4$ according to the procedures previously published" but, "in all cases, the mixed **$K_2Sr(FeO_4)_2$** salt precipitated"

(S. K. Dedushenko et al., 2001). Strontium ferrate was also tested as cathode in AAA batteries, showing an alkaline super-iron battery behavior intermediate to the equivalent potassium or barium cells (Licht, Naschitz, Ghosh, et al., 2001). Regarding the barium ferrate(VI), it is the least soluble of the ferrate salts in alkaline water, pointing to a great similarity with the barium sulfate (Schmidbaur, 2018). Being the second ferrate(VI) salt to be discovered in the mid-19th century, $BaFeO_4$ synthesis has improved after many different iteration, now approaching the stability of the most stable chemically synthesized K_2FeO_4 salts with purities ≥ 99.75 % (Audette & Quail, 1972; Licht et al., 2002; Licht, Naschitz, Ghosh, et al., 2001). **Silver ferrate** (Ag_2FeO_4) has been synthesized in attempts to design cathodes for super-iron batteries; the results indicate low purities products, sensitive to light but stable when kept in dark and low T° environment (Licht et al., 2005).

Sodium tripotassium bis-ferrate(VI) has been prepared via direct precipitation by adding solid potassium hydroxide to 40% NaOH solution containing 0.1 M FeO_4^{2-} or via electrosynthesis in concentrated NaOH electrolyte (S K Dedushenko et al., 2002; W.-C. He et al., 2007). It has also been studied in later investigations of materials for supe-iron batteries (Licht et al., 2004).

To be reported is the preparation of four novel Fe(VI) salts (**lead, zinc, cadmium and mercury ferrates**), which were singularly prepared by "rapid and simple" solid phase reactions between K_2FeO_4 and the respective metallic salts (grinding at room T°) (Kooti et al., 2010). No other literature references have been found in the literature.

	Space group	***a* /Å**	***b* /Å**	***c* /Å**	**Reference**
K_2FeO_4	*Pnma* (orthorhombic)	7.690(1)	5.855(1)	10.328(1)	(Audette et al., 1973; Herber & Johnson, 1979; Hoppe et al., 1982)
Na_2FeO_4	*Cmcm* (orthorhombic)	5.675(3)	9.349(4)	7.160(2)	(Malchus & Jansen, 1998)
Rb_2FeO_4	*Pnma* (orthorhombic)	8.015(1)	6.015(7)	10.619(2)	(Herber & Johnson, 1979)
Cs_2FeO_4	*Pnma* (orthorhombic)	8.399(2)	6.274(1)	11.064(2)	(Herber & Johnson, 1979)
$SrFeO_4$	*Pnma* (orthorhombic)	9.153(6)	5.398(3)	7.226(4)	(Herber & Johnson, 1979)

$K_2Sr(FeO_4)_2$	*R*3*m* (rhombohedral)	7.8	(α = 42.2°)		(Ogasawara et al., 1988; Yang et al., 2002)
$BaFeO_4$	*Pnma* (orthorhombic)	9.126(1)	5.456(7)	7.323(8)	(Herber & Johnson, 1979)
$K_3Na(FeO_4)_2$	*P*/3*m*1 (hexagonal)	5.827(3)		7.541(2)	(Sergey K. Dedushenko et al., 2005)

Table 1.3: crystal structure data of ferrate(VI) salts.

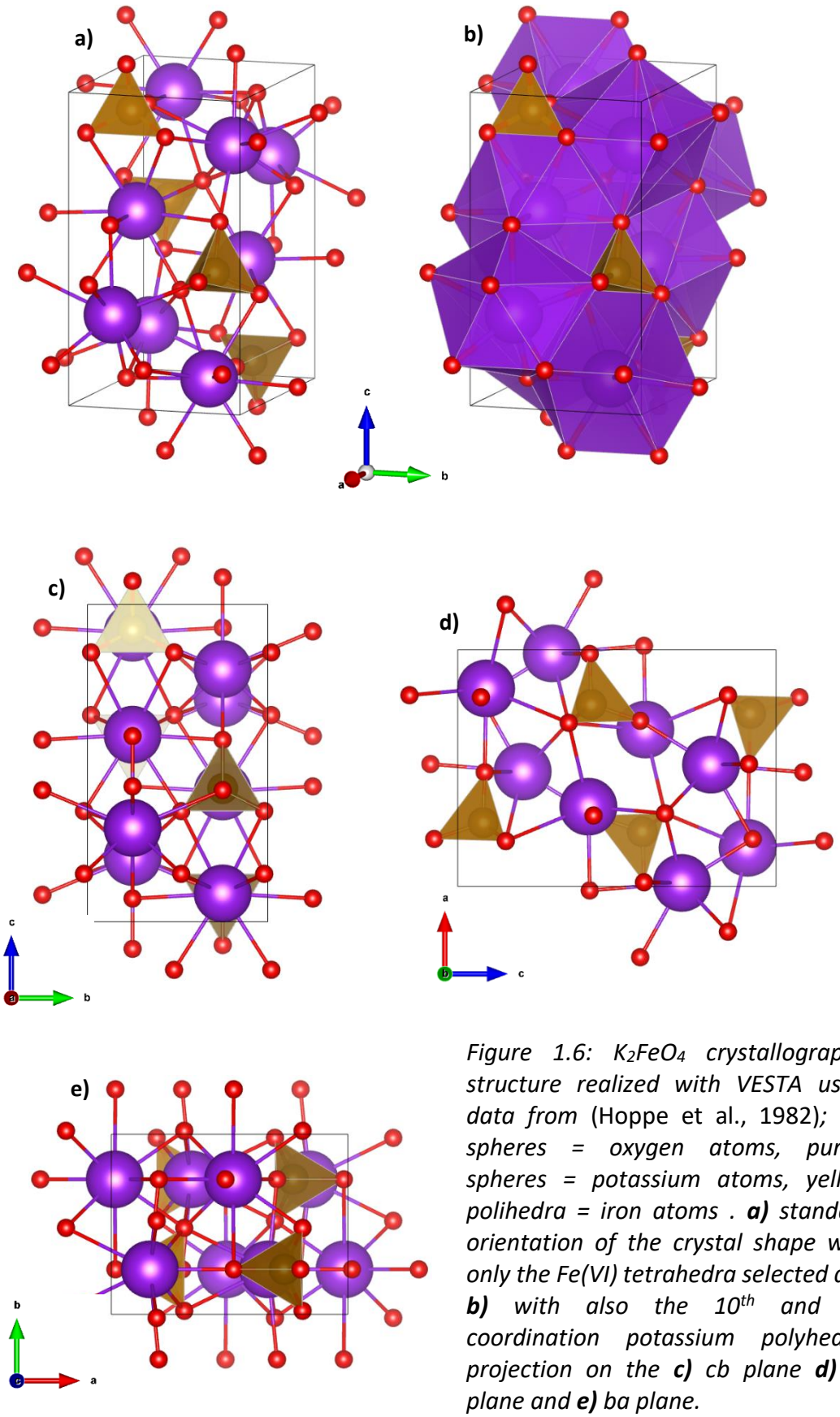

Figure 1.6: K_2FeO_4 crystallographic structure realized with VESTA using data from (Hoppe et al., 1982)*; red spheres = oxygen atoms, purple spheres = potassium atoms, yellow polihedra = iron atoms .* ***a)*** *standard orientation of the crystal shape with only the Fe(VI) tetrahedra selected and* ***b)*** *with also the 10th and 9th coordination potassium polyhedra; projection on the* ***c)*** *cb plane* ***d)*** *ac plane and* ***e)*** *ba plane.*

Due to its properties, potassium ferrate has become the most studied form of ferrate salt. Due to the absence of a downloadable Crystallographic Information File (CIF) of K_2FeO_4, a new one was made using the VESTA software and the parameters from Hoppe et al. (Fig. 1.6) (Hoppe et al., 1982). K_2FeO_4 crystallizes into the orthorhombic system, space group Pnma, with the iron atoms located into quasi-perfect tetrahedra and the potassium atoms into 9th and 10th coordination polyhedra (Fig. 1.6). When potassium ferrate is dissolved into water, the result is the evolution of oxygen and the final precipitation of ferric hydroxide which make the ferrate solution unstable (eq. (4)) (J.-Q. Jiang & Lloyd, 2002)).

$$4K_2FeO_4 + 10H_2O \rightarrow 4Fe(OH)_3 + 8KOH + 3O_2\uparrow \quad (4)$$

Wood measured its thermodynamic constants in an early work; with a $FeO_4^{2-}{}_{(aq.)}$ formation heat ΔH_f = - 115 ± 1 kcal/mol and an estimated entropy ΔS = - 9 ± 4 e.u., the resulting $FeO_4^{2-}{}_{(aq.)}$ energy formation is ΔG_f = - 77 ± 2 kcal/mol (Wood, 1958). Instead, the heat of dissolution of K_2FeO_4 was calculated by Bailie et al. as - 14.3 kJ/mol while studying the solubility of the mentioned salt in aqueous solutions of NaOH and KOH of 12 M total concentration and a KOH:NaOH molar ratios in the range 12:0 to 3:9 at (Bailie et al., 1996). During numerous trials, it was observed that the main factors affecting the decomposition rate are the initial ferrate concentration, the pH, the T° and the co-existence of other ions.

The diluted ferrate solutions were accounted to be more stable than the concentrated ones (Schreyer & Ockerman, 1951). For example, a solution with a starting ferrate(VI) content < 0.025 M, after 1 hour, will show about 89 % of that concentration, while almost all of the ferrate ions will decompose if the initial ferrate(VI) concentration is > 0.03 M after the same period of time (T = 26 ± 0.5°, pH = free to vary) (Schreyer & Ockerman, 1951). Wagner et al. found that a 10 mM potassium ferrate solution decomposes by 79.5 % in 2h30 while a 1.9 mM solution of the same salt shows a 37.4 % reduction after 3h50 (T = 25°, pH = free to vary) (Wagner et al., 1952).

Using potassium ferrate, the decomposition % of a solution with initial [ferrate(VI)] = 0.25 mM was tested over 10 minutes (Graham et al., 2004). For pH ~ 10, the stability of ferrate(VI) tends to be the maximum, while at pH > 10 starts to decrease (Fig. 1.7a). Taking also into account paragraph 3.1, it is confirmed how, for pH < 6, ferrate(VI) is highly unstable and is reduced within several minutes; however, it should be noted that, at high pH too, ferrate has a

significant positive oxidation potential (see par. 3.1.) and even if the reason for the apparent decrease in stability for pH > 10 is not clear, "it is believed to be associated with a different reduction pathway leading to the formation of anionic ion species (e.g. $Fe(OH)_4^-$ and $Fe(OH)_6^{3-}$) instead of $Fe(OH)_{3(s)}$ at the particular ferrate concentration used" (Graham et al., 2004). The results are consisted with Lee and Gai, who found the lowest rate of reduction of ferrate by water occurring at pH = 9.4-9.7 (Fig. 1.7b) and with Li et al., who showed that the decomposition rate constant of a 0.25 mM K_2FeO_4 solution, with pH controlled by different buffers, has a minimum between 9.2 < pH < 9.4 (D. G. Lee & Gai, 1993; C. Li et al., 2005). Li et al. observed also the typical change in color which join the ferrate decomposition in water, with the initial ferrate solution purple color which rapidly shifted to yellowish as decomposition occurs before the solution becomes colorless with yellowish precipitate at the bottom (C. Li et al., 2005).

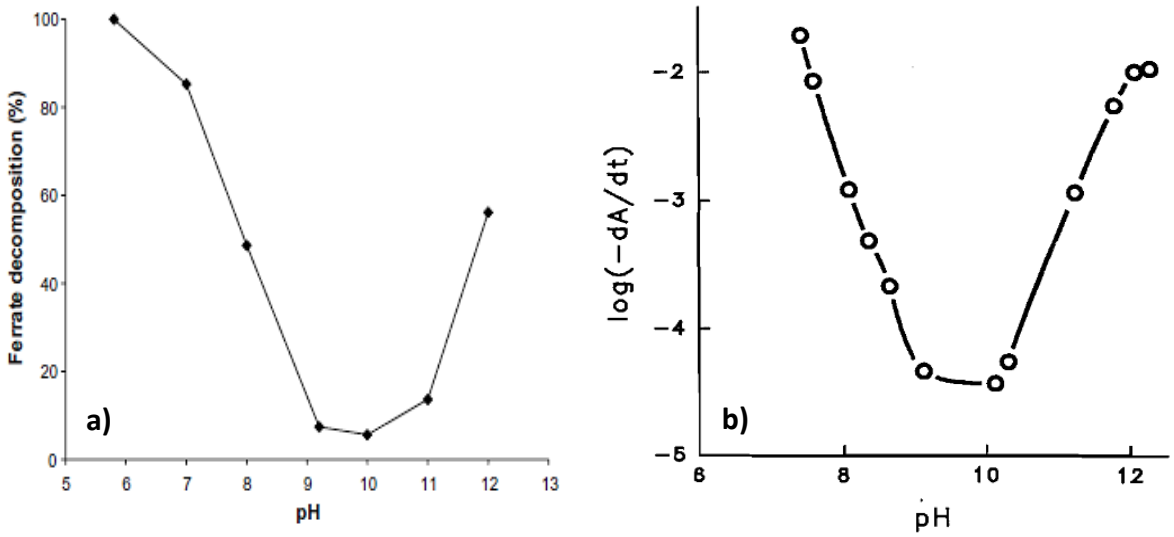

Figure 1.7: effect of pH on the aqueous decomposition of potassium ferrate. ***a)*** *% reduction over 10 min with initial ferrate concentration 0.25 mM (Graham et al., 2004);* ***b)*** *initial reduction rates of a "small portion of solid potassium ferrate", T = 25 ± 0.1° (D. G. Lee & Gai, 1993).*

Temperature also influences the stability of ferrate solutions; over the course of 2h, a 0.01 M potassium ferrate aqueous solution kept at 25° showed a 10 % decrease in potassium ferrate content, while, at a 0.5°, only a 2% decrease was observed (Wagner et al., 1952).

The effect of coexisting ions on the ferrate stability was investigated using a 0.04 M potassium ferrate solution in the presence of 0.5 M potassium chloride (KCl), potassium nitrate (KNO_3),

sodium chloride (NaCl) and hydrous ferric oxide (FeOOH) (Fig. 1.8) (Schreyer & Ockerman, 1951). It was found that potassium chloride and potassium nitrate accelerated the initial decomposition, while the remaining ferrate ions appeared to be relatively stable (decomposition retarders, as also Moeser predicted (Moeser, 1897)). Instead, addition of sodium chloride accelerated the decomposition, so as hydrous ferric oxide did (explaining the rapid decomposition of ferrate solutions after quantities of hydrous ferric oxide are produced by the decomposition itself) (Schreyer & Ockerman, 1951).

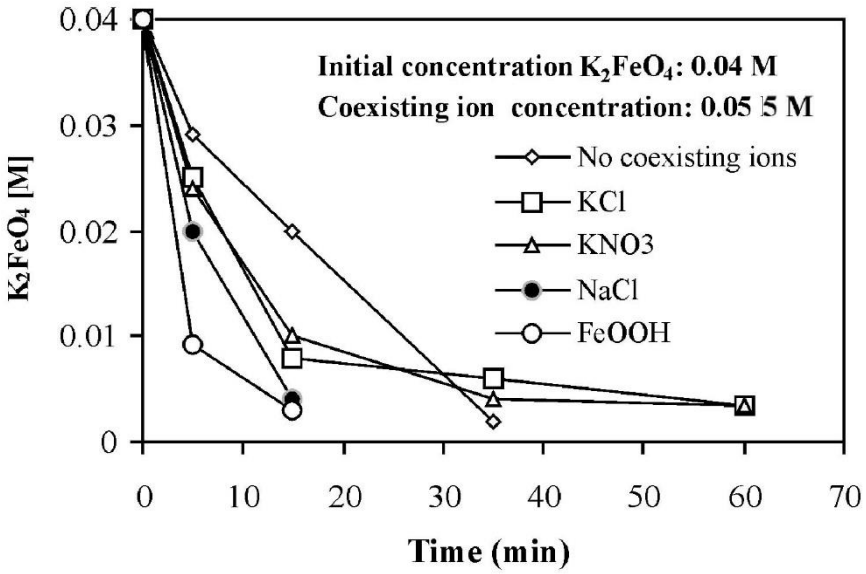

Figure 1.8: effect of coexisting ions on K_2FeO_4 stability at 26° ((J.-Q. Jiang & Lloyd, 2002), reproduced from (Schreyer & Ockerman, 1951)).

The stability of ferrate(VI) solutions increases also with increased alkalinity; the [potassium ferrate] decreased only 5 % over the 2h test in a 6 M KOH solution, while it rapidly diminished in 3 M KOH (Fig. 1.9) (Wagner et al., 1952). To show the combined effect of temperature and alkalinity, a 6 M KOH solution of potassium ferrate was placed at -20° and, after 31 days, showed a decrease in [ferrate] of 29.3 % while, another 6 M KOH potassium ferrate solution decomposed completely at room T° in 7 days.

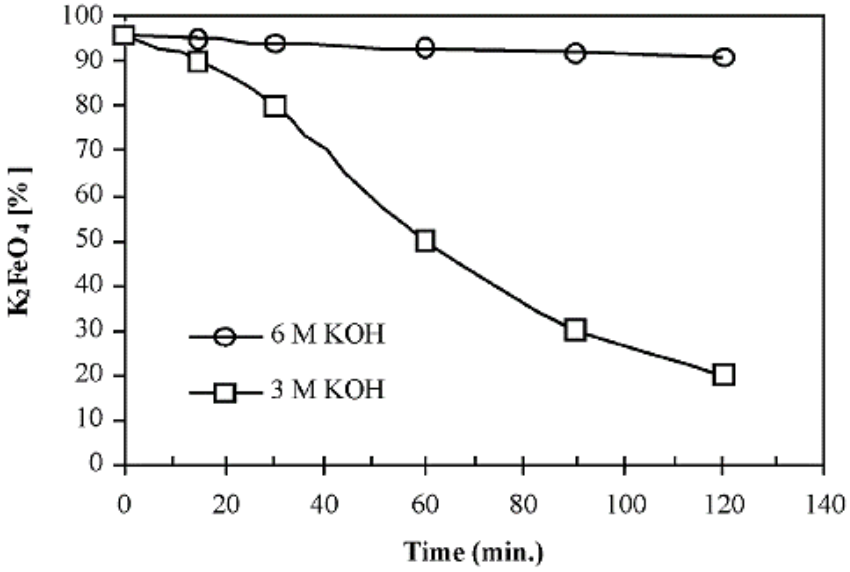

Figure 1.9: effect of alkalinity on the stability of 0.01 M K_2FeO_4 at 25° ((J.-Q. Jiang & Lloyd, 2002)*, reproduced from* (Wagner et al., 1952)*).*

Bailie et al. studied the solubility of K_2FeO_4 in KOH+NaOH mixtures at total concentration of 12 M but with various molar ratios KOH/NaOH in the range 12:0 to 3:9 (Bailie et al., 1996). They found out that the solubility of ferrate (VI) decreases with increasing K/Na, with a maximum at 1:0 (Fig. 1.10) (Bailie et al., 1996).

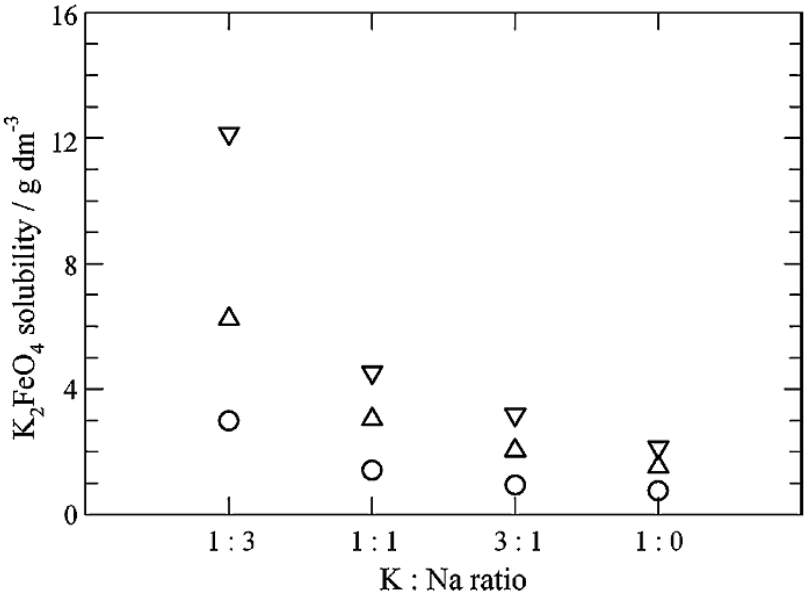

Figure 1.10: K_2FeO_4 solubility dependance on K/Na molar ratio and T° in KOH+NaOH solution at [OH^-] = 12 M (circles = 20°, upward-pointing triangles = 40 °, downward-pointing triangles = 60°). From (Mácová et al., 2009).

Licht et al. studied the stability of K_2FeO_4 by measuring Fe(VI) absorbance over 3 months, taking into account the possible presence of Ni(II) and Co(II) in traces (Fig. 1.11) (Licht et al., 1999). In 10 KOH, K_2FeO_4 stability is increased by an order of magnitude in comparison with 5 M KOH, while is almost perfectly stable in saturated KOH, with a decomposition rate of 10-9 M/s, equivalent, in 1 ml of the solution, to a monthly loss of 0.0005 g K_2FeO_4 (Fig. 1.11) (Licht et al., 1999). Regarding the impurities, the stability of K_2FeO_4 is increased by an order of magnitude in 10 M KOH (from hours to weeks) when the [Ni(II)] decreases from 100 µM to <0.1 µM (Fig. 1.11); Ni(II) and Co(II) exhibited analogous behaviors and the K_2FeO_4 stability is similar in KOH or NaOH electrolytes (Licht et al., 1999). Nitrate salts not containing Ni(II) or Co(II), including nitrate of Cu(II), Fe(III), Zn(II), Pb(II), Ba(II), Sr(II), Ca(II), Mg(II) and other salts including $K_2Zn(OH)_4$, KIO_4, $K_2B_4O_9$, K_3PO_4, $Na_4P_2O_7$, Na_2SiF_6, Na_2SiO_3, Na_2MoO_4, Na_2WO_4 have no effect on the stability of K_2FeO_4 (Licht et al., 1999).

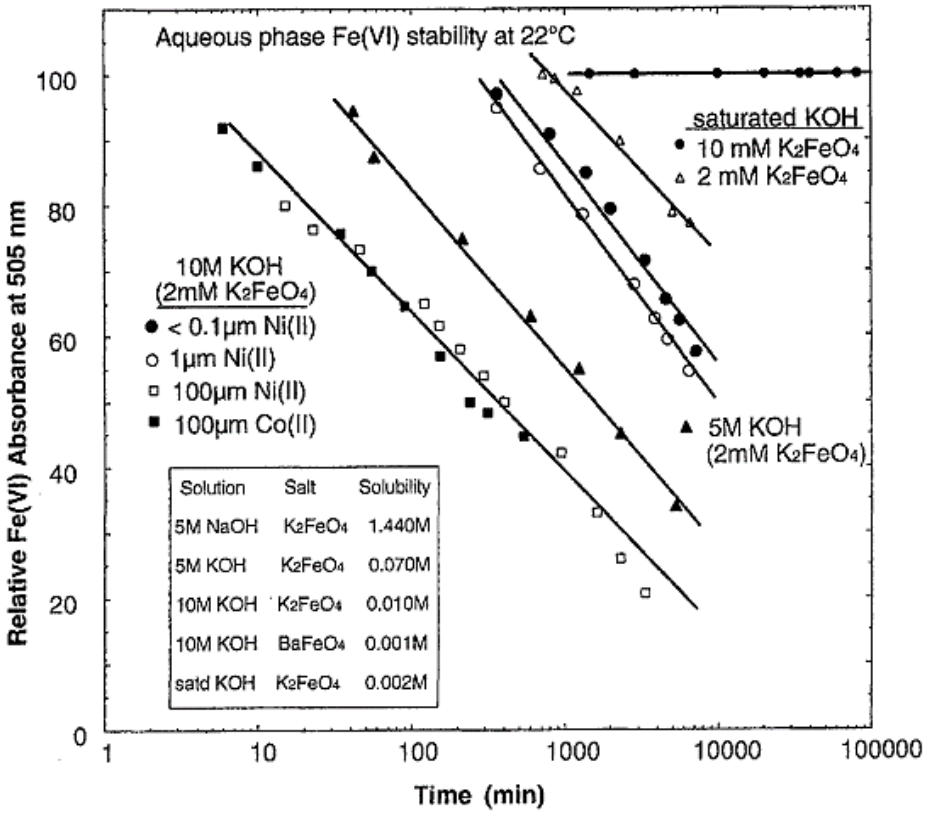

Figure 1.11: stability of Fe(VI) as variation of FeO_4^{2-} absorption at 505 nm and the 505 nm extinction coefficient, measured at 1.1 $mM^{-1}*cm^{-1}$. Relative absorption of 100 % = initial [Fe(VI)]. The interference from colloidal ferric oxide is minimized by a 385 nm baseline correction and solution centrifugation before spectroscopic analysis. The indicated [Ni(II)] and [Co(II)] are prepared as added nitrate salts (Licht et al., 1999).

An interesting factor influencing the ferrate stability was determined by Jiang et al. as the use of buffer chemicals (Y. Jiang et al., 2015). After validating the aforementioned Fe(VI) decomposition catalytic effect of Fe(III) decomposition products, they found that chemical buffers, used to maintain the solution pH, prevent the precipitation of Fe(III) through complex reactions, facilitating the spectrophotometric measurements of [Fe(VI)] on one hand but altering the Fe(VI) stability on the other (Y. Jiang et al., 2015). Chemical buffers can stabilize Fe(VI) in water complexing the Fe(III) precipitation products capable of surface-catalyzing Fe(VI) decomposition, together with other solutes that can have the same behavior, such as bicarbonates (Fig. 1.12) (Y. Jiang et al., 2015). Phosphate exhibited nearly complete inhibition across the entire concentration range investigated, while bicarbonate and borate were less effective in suppressing Fe(VI) decomposition (Fig. 1.12) (Y. Jiang et al., 2015). The results were in agreement with Su and Puls, who studied the effects of different chemicals relative to chloride on As(III) and As(V) removal by ZVI; because of the competitive adsorption of the anions on the iron surface, phosphate caused the highest decrease in the arsenic removal rate, followed by carbonate and borate (Su & Puls, 2001).

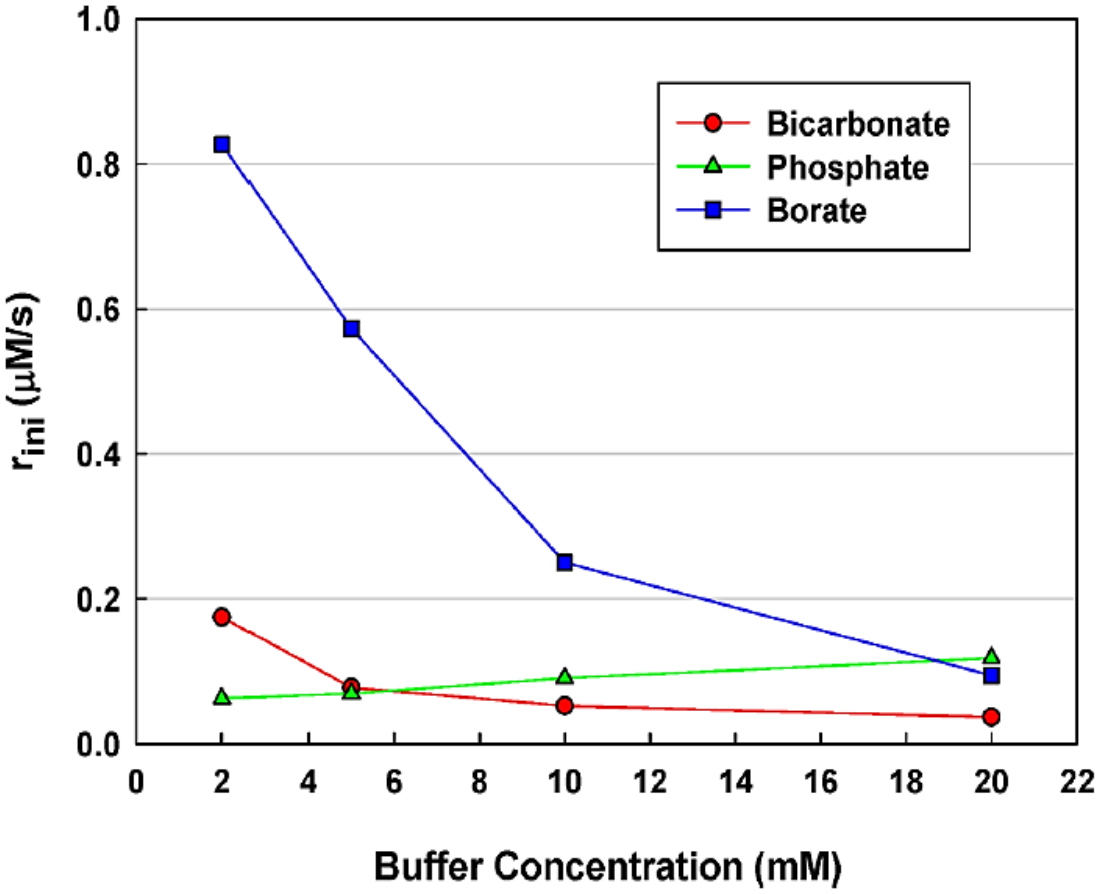

Figure 1.12: initial Fe(VI) decomposition rate at t=0 (r_{ini}) in the presence of different solutes. The symbols represent the calculated rates on the basis of the estimated decomposition constants using AQUASIM software. The lines connect sets of data points to show trends. Experimental conditions: pH = 7.5; T = 20°; 50 µM of Fe(VI) (Y. Jiang et al., 2015).

Another noteworthy interaction to be considered is the reaction with the Natural Organic Matter (NOM) ubiquitously present in natural waters. While NOM would be expected to incrementing Fe(VI) decomposition through redox reactions, Jiang et al. found that Fe(VI) decayed more rapidly in borate-buffered deionized water than in borate-buffered natural waters (Fig. 1.13) (Y. Jiang et al., 2015). The reason identified by the authors was the inhibiting action of the catalytic effect of Fe(VI) decomposition products by NOM, which alters the precipitate's surface area/coats the surface of the precipitate (Y. Jiang et al., 2015). But, as Deng et al. found in a more recent study, this may not be the case in Jiang et al. study, due to not ruling out the stabilizing effect of other matrix constituents of the natural waters while overestimating the NOM effect on the slow initial Fe(VI) decomposition rates (little iron oxides capable of catalyzing Fe(VI) produced in the beginning = low possibility for NOM to sequester

them) (Deng et al., 2018). Deng et al. instead conclude that NOM accounts for the major part of the initial Fe(VI) loss due to instant reaction with its reacting function groups (e.g. the hydrophobic fractions as fulvic acid and the humic acids), in direct proportion with the initial Dissolved Organic Carbon (DOC), which can reduce the effective Fe(VI) oxidant exposure and so the eliminating effectiveness of target pollutant (Deng et al., 2018).

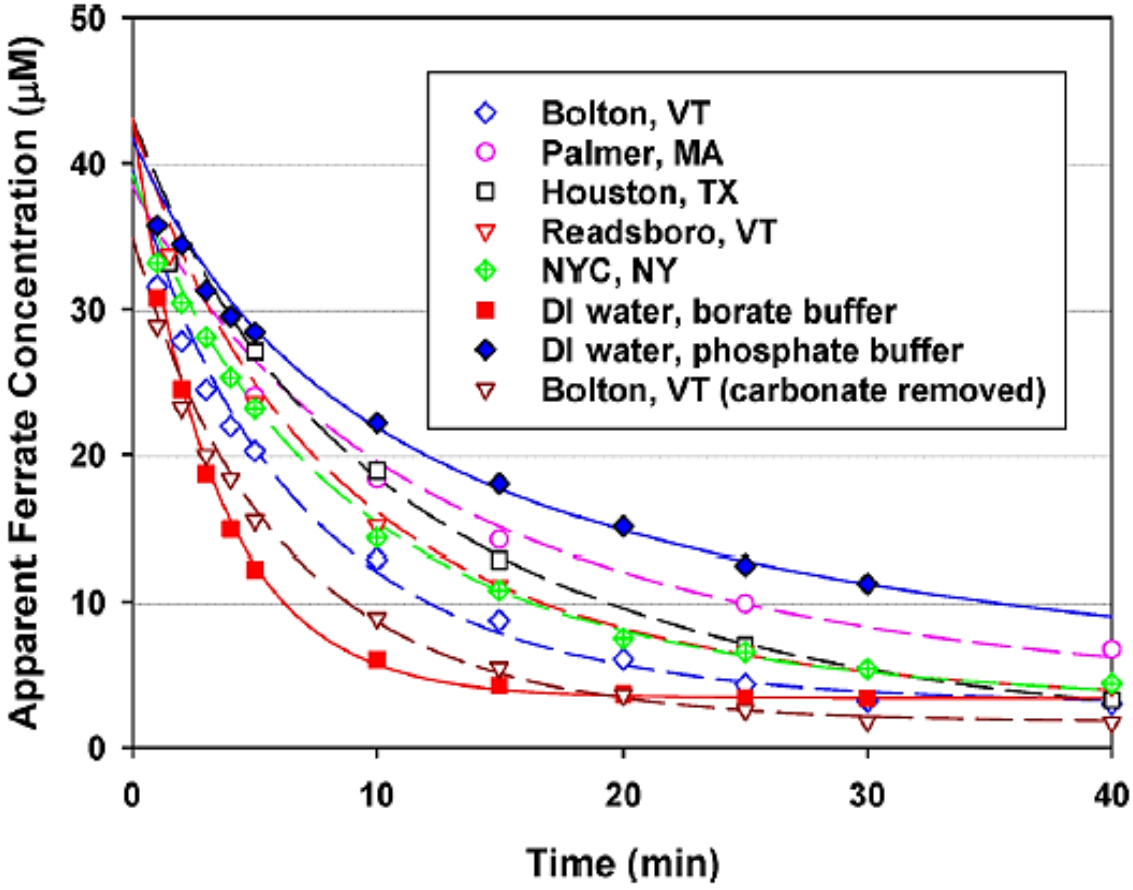

Figure 1.13: Fe(VI) decomposition in borate-buffered natural waters in comparison with borate and phosphate buffered deionized waters (DI). The symbols represent the measured data and the modeled Fe(VI) decomposition results. Bolton natural water was also tested after pre-acidification before buffering in order to remove carbonate ("carbonate removed"). Experimental conditions: pH = 7.5; T = 20°; 50 µM of Fe(VI); 10 mM of borate/phosphate (Y. Jiang et al., 2015).

In an early study, Moeser highlighted how potassium ferrate is insoluble and can be suspended in benzene, ether and chloroform without rapid decomposition but rapidly decomposes alcohols containing > 20 % of water forming aldehydes and ketones (Moeser, 1897). Williams and Riley, instead, pointed out how ferrate(VI) is able to slowly oxidize even benzene and ethyl ether, indicating that the oxidation begins at terminal OH groups of the alcohols (Williams & Riley, 1974).

1.1.2. Characterization techniques

A number of analytical techniques have been developed to study FeO_4^{2-} in water solutions including volumetric techniques (titration), spectrophotometric methods (UV-Vis, colorimetry using ABTS or I_3^-, fluorescence, Fourier Transform Infrared spectroscopy (FTIR), Mossbauer) and electrochemical techniques (cyclic voltammetry).

The quantitative determination of Fe(VI) can be performed by chromium(III) or arsenic(III) titration (equations (5) and (6) respectively) (Cataldo Hernández et al., 2016; Licht, Naschitz, Halperin, et al., 2001; Luo et al., 2011; Schreyer et al., 1950b, 1950a).

$$Cr(OH)_4^- + FeO_4^{2-} + 3H_2O \rightarrow Fe(OH)_3(H_2O)_3 + CrO_4^{2-} + OH^- \quad (5)$$

$$3AsO_3^{3-} + 2FeO_4^{2-} + 9H_2O \rightarrow Fe(OH)_3(H_2O)_2 + 3AsO_3^{3-} + 4OH^- \quad (6)$$

In the chromite method, chromate(VI) is formed from the reaction between Cr(III) and Fe(VI) (eq. (5)); the chromate(VI) solution produced is then acidified and the resulting dichromate is titrated with a standard ferrous ions solution (Cataldo Hernández et al., 2016; Licht, Naschitz, Halperin, et al., 2001; Schreyer et al., 1950b). The arsenite method use a similar procedure, where As(III) reacting with Fe(VI) produces As(V) (Schreyer et al., 1950a). Both methods are able to determine Fe(VI) contents at sub-molar to molar levels and are considered between the most accurate methods for quantification of ferrate(VI) with the obvious drawbacks of being not very convenient due to the hazardous materials involved, the necessity of relative high quantity of ferrate solution, the cost of the consumables (Cataldo Hernández et al., 2016). The chromite method was tuned and further developed in more recent works to be more suitable to different ferrate materials (e.g. electrochemical produced ferrate(VI)) (Cataldo Hernández et al., 2016; Licht, Naschitz, Halperin, et al., 2001).

FeO_4^{2-} has a distinctive UV-Vis spectrum. The UV-Visible spectroscopy method is used for quantitative analysis and can be conducted using visible absorption spectrum at a wavelength between 505-510 nm, where a maximum is shown. This method is commonly used in the kinetic and mechanistic studies on ferrate(VI) decomposition, as well as checking platform for synthesis procedures thanks to its general practicality and rapid execution (Bielski & Thomas, 1987; Cataldo Hernández et al., 2016; J.-Q. Jiang et al., 2018; Licht, Naschitz, Halperin, et al., 2001; Luo et al., 2011; Rush & Bielski, 1986; Wei et al., 2015). The molar absorptivity (ε) of

ferrate(VI) in different solutions has been extensively measured at different conditions in the 505-510 nm range, and multiple studies point to the two values of 1070 ± 25 $M^{-1}*cm^{-1}$ (Fig. 1.14a) and 1150 ± 25 $M^{-1}*cm^{-1}$ in concentrated alkali solution, independently of the alkali hydroxide cations and concentrations studied; to within 5 %, the ε_{505nm} of 2 to 200 mM K_2FeO_4 is the same in [MOH] = 5 M (with M = Li, Na, K) and in 5-15 M NaOH, 5-13.5 M KOH and 5-15 M CsOH (Licht, Naschitz, Halperin, et al., 2001). However, Hernández et al. found a Fe(VI) molar absorptivity ε_{505nm} equal to $1.5*10^3$ $M^{-1}*cm^{-1}$ (Fig. 1.14b) (Cataldo Hernández et al., 2016); the discrepancy could be due to the lower Fe(VI) concentration range investigated, with a maximum value of 692 µM in 14 M NaOH which is almost 3 times less the minimum Fe(VI) content tested by Licht et al. and which could be out of the linear response usually found. The limits of this method regards the tendency to decomposition of ferrate(VI) in water into colloidal Fe(III) oxides, which interfere with the spectral measurements, so as the tendency of Fe(VI) to decompose in aqueous solutions other than specific electrolytes such as concentrated KOH (Licht et al., 1999). However, this problem can be minimized through the subtraction of a 385 nm baseline correction and/or centrifugation prior to the analysis (Cataldo Hernández et al., 2016; Licht, Naschitz, Halperin, et al., 2001). Due to the low molar absorptivity of Fe(VI), relative higher quantity of ferrate(VI) solution are needed. This method provides more accurate measurements for [Fe(VI)] > 100 µM (e.g. for a 17.3 ± 0.1 mM concentration using the titration method, UV-Vis measurement produce a reasonable 16.9 ± 0.4 mM) (Cataldo Hernández et al., 2016).

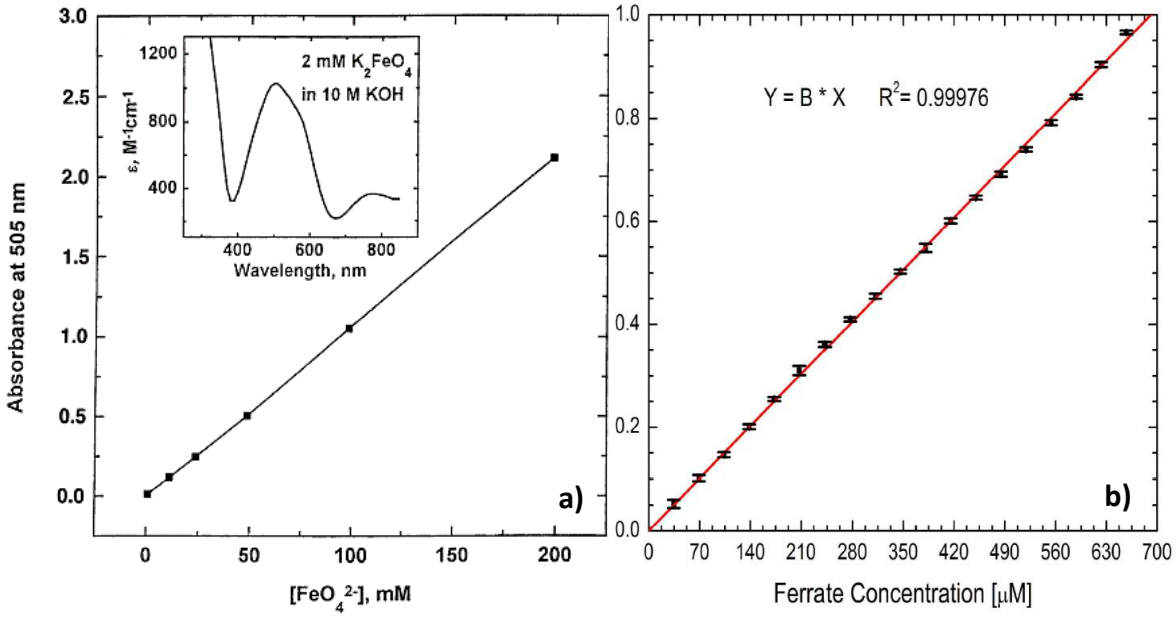

*Figure 1.14: the 505 nm absorbance of ferrate(VI) solutions of various concentration **a)** in concentrated alkaline solution (in the inset is presented the VIS spectrum of 2 mM K_2FeO_4 in 10 M KOH aqueous solution (from (Licht, Naschitz, Halperin, et al., 2001)) and **b)** in 14 M NaOH (from (Cataldo Hernández et al., 2016)).*

The molar absorptivity of ferrate(VI) at 505-510 nm is relatively low hence a method using 2,2-azino-bis(3-ethylbenzothiazoline-6-sulfonate) (ABTS) was proposed by Lee et al. to determine low ferrate(VI) contents (Y. Lee et al., 2005). Colorless ABTS reacts with ferrate(VI) with an 1:1 stoichiometry when ABTS is in excess, forming a green radical cation, $ABTS^+$ (eq. (6)), with an absorption peak at 415 nm (Fig. 1.15a) (Cataldo Hernández et al., 2016; Y. Lee et al., 2005).

$$Fe(VI) + ABTS \rightarrow Fe(V) + ABTS^+ \quad (6)$$

The $ABTS^+$ molar absorptivity ((3.40 ± 0.05) * 10^4 $M^{-1}cm^{-1}$) was found to be one order of magnitude higher than the ferrate(VI) one at 505-510 nm (Fig. 1.15b), allowing the determination of lower concentration than UV-Vis spectroscopy, with accuracy higher than the titration method (17.3 ± 0.1 mM with the titration method vs 17.32 ± 0.03 mM with ABTS) (Cataldo Hernández et al., 2016; Luo et al., 2011). The absorbance is linear with 0.03 µM < [ferrate(VI)] < 35 µM, with similar calibration slopes in natural waters than those run in synthetic buffer solutions (Luo et al., 2011). One of the major drawbacks of ABTS is the instability of the solution, which decompose significantly after 30 min at room T°, making

essential to prepare fresh ABTS solution for accurate determination (Cataldo Hernández et al., 2016).

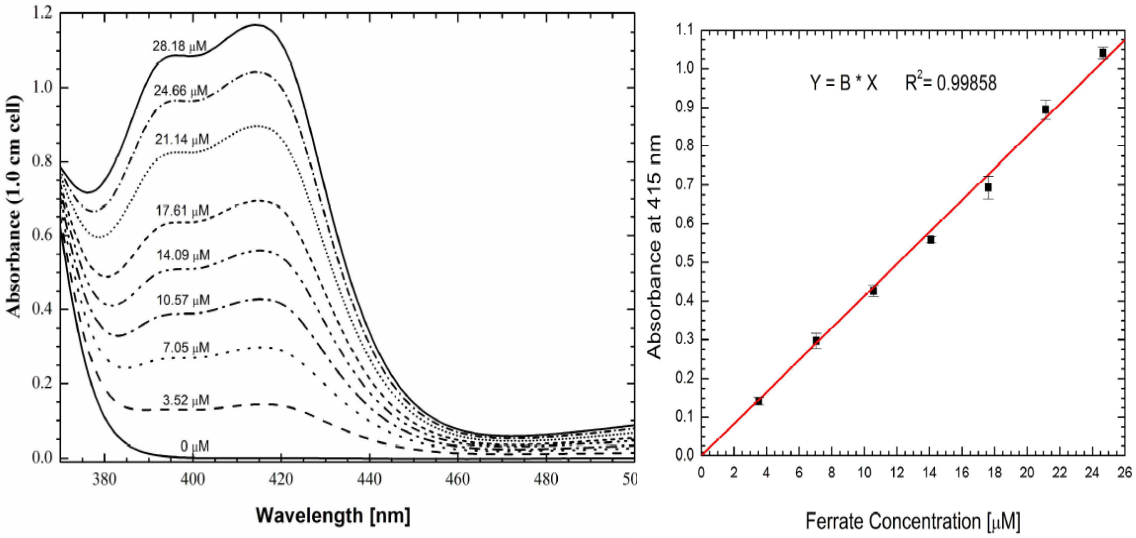

Figure 1.15: ***a)*** *absorption spectra for different [ferrate(VI)] using the ABTS method and* ***b)*** *the relative 415 nm absorbance plotted against [ferrate(VI)] (Cataldo Hernández et al., 2016).*

While the ABTS method presents advantages for the analysis of low ferrate(VI) concentrations, it may not be suitable for solutions containing products with similar absorption wavelengths. To overcome this scenario, a new fluorometric technique was developed by Noorhasan et al. to determine low ferrate(VI) amounts in water using a fluorescent agent known as scopoletin (7-hydroxy-6-methoxy coumarin) (Noorhasan et al., 2008). The technique was found to be accurate at low µM, rapid and allows to measure [Fe(VI)] al pH values below 6, where the absorption spectroscopy tends to fail due to interferences (Noorhasan et al., 2008). The simplicity of the method is the fixed values of excitation and emission wavelength values (335 and 460 nm respectively), independent of the pH, with a linear decrease in the fluorescence of scopoletin with increasing [ferrate(VI)] higher at low pH, which allows even more precise measurements in conditions where other method are ineffective (Fig. 1.16).

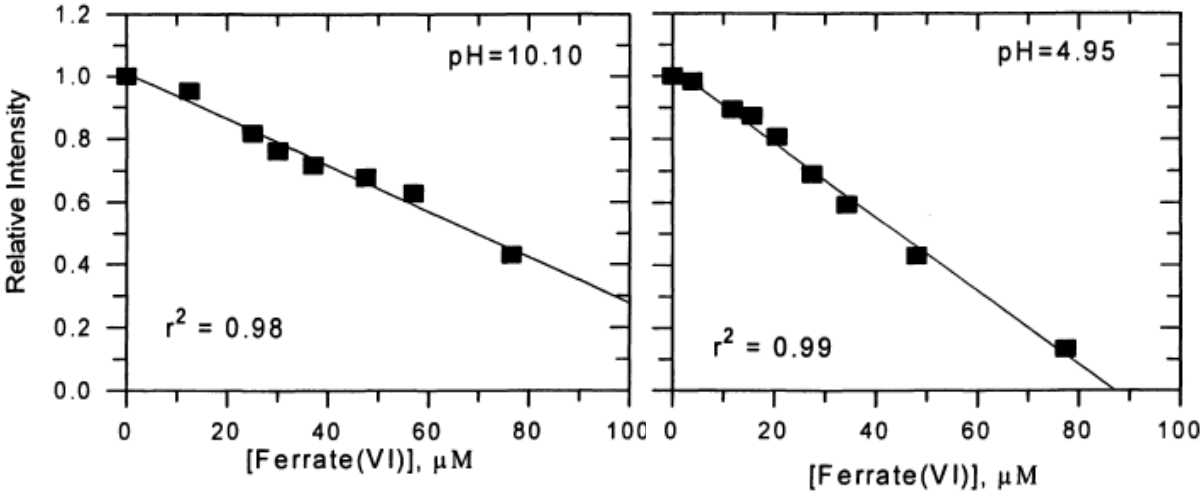

Figure 1.16: emission intensities of scopoletin vs [ferrate(VI)] at pH 10.10 and 4.95, modified from (Noorhasan et al., 2008).

While the ABTS and scolopetin methods use organic reagents, in a growing emphasis of using environmental friendly and more safe chemical compounds, a new spectrophotometric method was developed using sodium iodide (NaI) solution to determine [Fe(VI)] at low µM (< 10 µM) in water (Luo et al., 2011). Upon reaction with an excess amount of NaI, the purple color of Fe(VI) solution disappears instantaneously and a yellow solution appears, indicating the formation of I3- ions (eq. (7)) (Luo et al., 2011).

$$Fe(VI) + 3I^- \rightarrow Fe(III) + I_3^- \qquad (7)$$

The method is applicable for a pH range of 5.5 to 9.3 where the absorbance at 351 nm of the I_3^- species is linear with respect of the [Fe(VI)] (Fig. 1.17). The molar extinction coefficient ε_{351nm} was determine as $2.97*10^4$ $M^{-1}cm^{-1}$ (Luo et al., 2011).

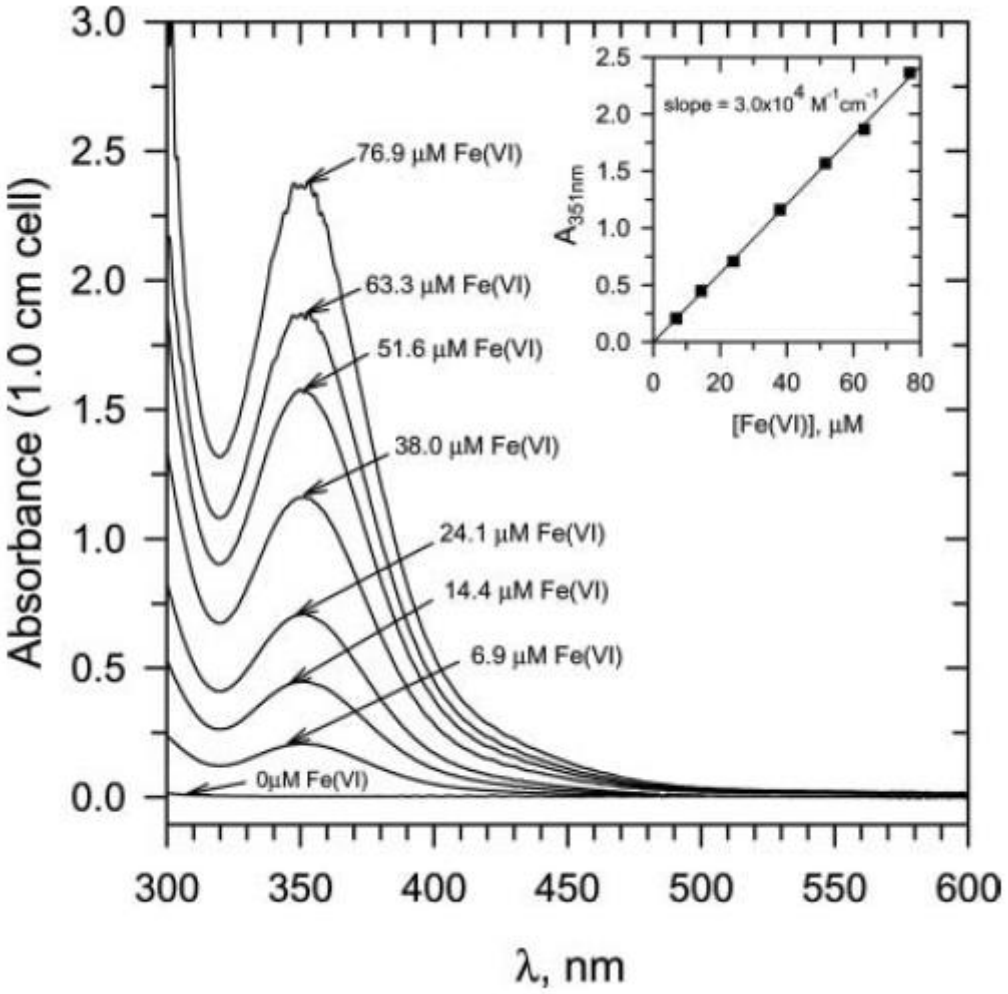

Figure 1.17: spectra obtained mixing 0.10 M NaI with Fe(VI) solution at pH 9 and 25°; the inset shows the absorbance plot of I_3^- species at 351 nm vs [Fe(VI)] (Luo et al., 2011).

Hernández et al. tested a modified NaI method, suitable for larger pH ranges, which taking advantages of the higher absorptivity of I_3^- compared to ferrate(VI) showed high accurate measurements ([Fe(VI)] = 17.27 ± 0.08 mM vs 17.3 ± 0.1 mM using the titration method) (Cataldo Hernández et al., 2016). The NaI solutions have the advantages over ABTS of being stable for extended periods of time without degrading or reacting but the possible presence of organic matter in the media has to be taken into account for proper spectroscopic measurements due to the possible absorption in similar visible region of the spectrum (baseline subtraction needed) (Cataldo Hernández et al., 2016; Luo et al., 2011).

Fourier Transform Infrared (FTIR) spectroscopy can be use to determine the Fe(VI) content of unknown samples using standard KBr pellets, as long as a proper standard is added as a constant fraction (Audette & Quail, 1972; Licht, Naschitz, Halperin, et al., 2001). The standard requires to be inert towards Fe(VI) compounds and with a distinct IR spectra, isolated from the Fe(VI) absorption bands (Licht, Naschitz, Halperin, et al., 2001; Luo et al., 2011). $BaSO_4$ was successfully used as a standar in measuring $BaFeO_4$; the $BaFeO_4$ absorbance at 780 cm^{-1} has a linear relationship with the $BaSO_4$ absorbance at 1079 cm^{-1}, allowing the quantitative analysis of [$BaFeO_4$] (Fig. 1.18) (Licht, Naschitz, Halperin, et al., 2001).

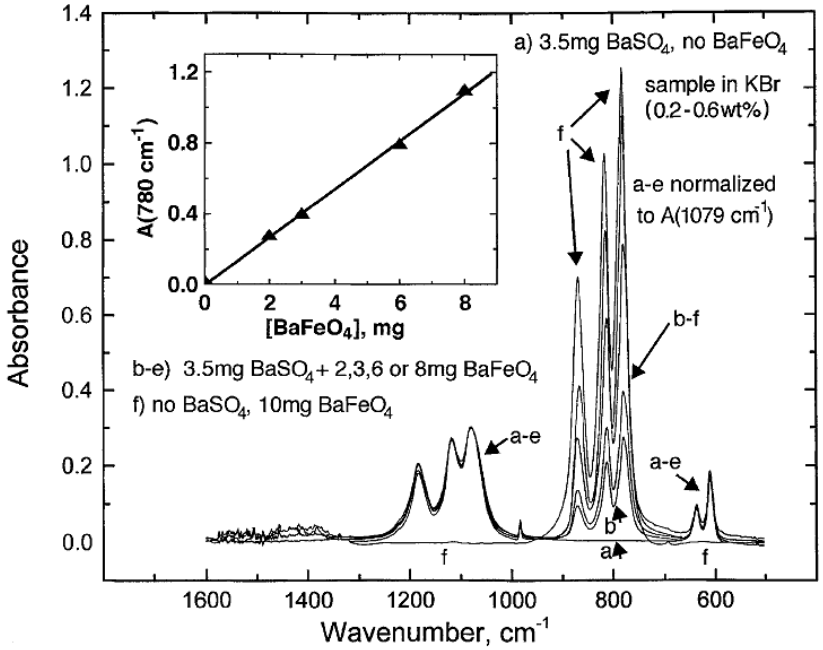

Figure 1.18: FTIR analysis of $BaFeO_4$ using $BaSO_4$ as a standard (Licht, Naschitz, Halperin, et al., 2001). A step-by-step suggested procedure is reported in the up-mentioned paper.

Mossbauer studies of Fe(VI) using the iron isotope ^{57}Fe have drawn lot of interest because important tools for obtaining informations on the iron oxidation states (throught the determination of the isomer shift, which varies with the valence state in the sample) and in the sourrounding symmetry of their local environment in solids, all at different T°/sourroundings conditions (Tab. 1.4). Due to its properties, ^{57}Fe Mossbauer is used for kinetic studies onto the decomposition of ferrates and as a quality control tool for synthesis procedure, e.g. the in-situ monitoring of the thermal behaviour and the aging effect at different ambient conditions on to K_2FeO_4 (Machala et al., 2007, 2008). Table 1.4 shows a summary of data from different studies on the ferrate(VI) salts.

	IS /mm·s^{-1}	QS /mm s^{-1}	T_N /K	Reference
K_2FeO_4	–0.90	0	4.2	(S. K. Dedushenko et al., 2001; Sergey K. Dedushenko et al., 2013; Herber & Johnson, 1979; Shinjo et al., 1970)
Rb_2FeO_4	–0.89	0	2.8	(S. K. Dedushenko et al., 2001; Herber & Johnson, 1979)
Cs_2FeO_4	–0.87	0	4.2	(S. K. Dedushenko et al., 2001; Herber & Johnson, 1979)
$SrFeO_4$	–0.86	0	n. o.	(Herber & Johnson, 1979; Shinjo et al., 1970)
$K_2Sr(FeO_4)_2$	–0.91	0.14	≈ 3.0	(S. K. Dedushenko et al., 2001)
$BaFeO_4$	–0.90	0.16	7	(S. K. Dedushenko et al., 2001; Sergey K. Dedushenko et al., 2013; Herber & Johnson, 1979; Shinjo et al., 1970)
$K_3Na(FeO_4)_2$	–0.89	0.21	n. o.	(S. K. Dedushenko et al., 2001; Sergey K. Dedushenko et al., 2005, 2013)

Table 1.4: ^{57}Fe Mössbauer spectroscopic data of ferrates(VI) (IS = Isomeric shift, QS = Quadrupole splitting, TN = Neél temperature of antiferromagnetic ordering).

Multiple electro-analytical techniques have been used in order to quantify Fe(VI), elucidate its synthesis mechanisms in the electrochemical methods (both in aqueous and in molten salt solutions) and monitor ferrate(VI) concentration in highly diluted contexts (Golovko et al., 2011; Híveš et al., 2008; Licht, Naschitz, Halperin, et al., 2001; Mácová et al., 2009; Venkatadri et al., 1971).

Cyclic voltammetry (CV) has been shown to provide a more sensitive method for determining lower [K_2FeO_4] than spectrophotometry (up to 2.5 µM); however, spectrophotometric methos remain more convenient in studying hours-long decompositions and it is still a reliable method for calibrating CV (Venkatadri et al., 1971). The peak cathodic current density was found to be proportional to [Fe(VI)] and it is proportional to the square root of the scan rate, indicating

that the Fe(VI) reduction is diffusion limited (Fig. 1.19) (Licht, Naschitz, Halperin, et al., 2001; Venkatadri et al., 1971).

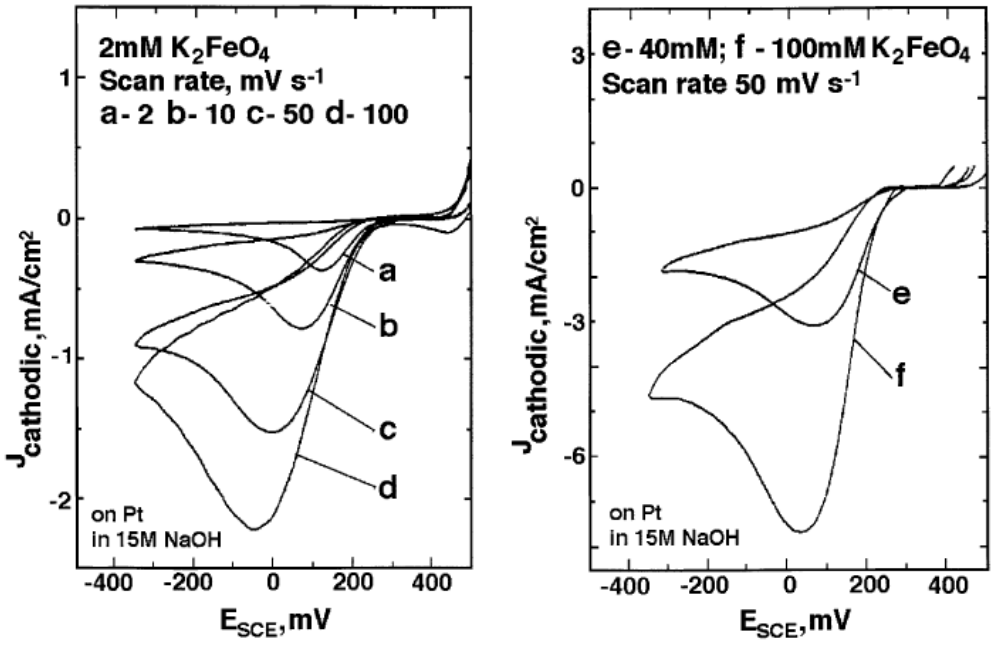

Figure 1.19: cyclic voltammetry of K_2FeO_4 solutions obtained in 15 M NaOH with a Pt electrode varying the potential scan rate (left) and the [ferrate(VI)] (right) (Licht, Naschitz, Halperin, et al., 2001).

1.1.3. Synthesis procedures

Nowadays, the preparation of ferrate(VI) products involves three different methodologies: the high temperature dry method, the low temperature wet method and the electrochemical method. The techniques differ for the specific medium and energy source used to drive the oxidation of lower-valence iron to the target Fe(VI).

The dry method combines a solid iron compound source with caustic alkali and peroxides in an high T° environment to get a final Fe(VI) containing product; the main advantage presented is the high quantities of ferrate(VI) produced with single batch synthesis. One of the first example of this kind of synthesis is based on the reaction between Na_2O_2 and anhydrous $FeSO_4$: when an appreciable excess of Na_2O_2 over $FeSO_4$ is present (molar ratio $Na_2O_2/FeSO_4 \geq 3$) and the temperature reaches 700° (maintained for 1h), the resulting solid containing sodium ferrate(VI) can be dissolved into concentrated NaOH before and KOH afterwards to make K_2FeO_4 precipitating (which can be washed with hexane, ethanol and dry ether to remove water) (Martinez-Tamayo et al., 1986). Kiselev et al. were able to reduce the

temperature needed by exploiting the calcination of a mixture of ferric oxide and potassium peroxide at 350-370° to obtain potassium ferrate(VI) or the oxidation of iron oxide with sodium peroxide at 370° to obtain sodium ferrate(VI) (Kiselev et al., 1989). Instead, Cici and Cuci proved that it is possible to produce ferric-iron (Fe_2O_3) and, consequently, sodium ferrate from galvanizing waste, using only Na_2O_2 while reaching T = 800° (Cici & Cuci, 1998). Due to the risk of detonation at elevated T°, the low yields, the high energy consumption and the costs of the alkali and peroxides used, the dry method has been considered a non-economic process (Jia Qian Jiang, 2014). More recently, Ninane et al. worked on new strategies in order to reduce the production costs and scale the dry method up to an industrial level, so to make it usable in real life applications (Ninane et al., 2008). The first technique, which development started in 2001 and resulted in a patented design, involves the use of residue $FeSO_4$ from metallurgy and titanium dioxide production processes as the iron source, solid $Ca(OCl)_2Ca(OH)_2$ as the oxidant and KOH pellets as the base for the potassium ferrate(VI) crystallization (Ninane et al., 2008). Using a rotating reactor, the method has the advantage of starting at room T°, employing small quantities of water (from the reagents) and producing large quantities of ferrate(VI) but the heat of the reaction is difficult to be controlled (temperatures of 45-175° spontaneously reached in the reactor due to the exothermic nature of the reaction itself), so as the mixing of the reagents, resulting in a 50 % yield, too low to scale-up the process at industrial size (Ninane et al., 2008). In order to improve the yield, improve the T° control and reduce the overall costs, fluid bed technology and chlorine were used, resulting in two more processes, both patented (Ninane et al., 2008). As a continuous of those previous works, Kanari et al. developed a unique manufacturing process which included mixing of industrial ferrous sulphate waste and sodium hydroxide in a rotary reactor under controlled conditions and T < 100° and fluidization of the obtained mixture in diluted chlorine (Kanari et al., 2019). The results showed yields between 30 and 55 %, a resulting product ready to be directly used and the reach of numerous green chemistry and sustainable development principles (Kanari et al., 2019).

The electrochemical procedures were heavily studied during the past decades due to the general high purity products, low demands for solvents and to their possibility for industrial scaling in continuous ferrate(VI) production. The two main approaches differ in terms of the low-valence iron source used, being a sacrificial iron anode or, more recently, a Fe(III) solution oxidized by an inert electrode.

The sacrificial anode approach involves the use of a dissolving solid iron anode and it is typically performed in high pH electrolyte where an applied electric current oxidizes the iron electrode into Fe(VI) ions according to the eq. (8) (M. A. Cataldo-Hernández et al., 2019):

$$Fe + 8OH^- \rightarrow FeO_4^{2-} + 4H_2O + 6e^- ; \; E^0 = -0.8\,V\ (vs\ SHE) \quad (8)$$

The efficiency of this kind of method is deeply linked to the passivation tendency of the electrode, that is the formation of a compact iron oxide layer (which can be identified as Fe_3O_4) directly on the metal surface, which inhibits the anode material dissolution process (Bouzek & Nejezchleba, 1999). Moreover, ferrate(VI) formation takes place in the transpassive potential region of iron dissolution which, in aqueous solution, corresponds to potentials which exceed the electrochemical solvent stability, making oxygen evolution a competitive factor influencing the synthesis (Mácová et al., 2009). An additional complication rises from the ferrate(VI) stability in water, which has to be considered in order to find the optimal production conditions. For example, increasing temperature has a de-passivating effect on the electrode surface but enhances the ferrate(VI) decomposition kinetics (Wagner et al., 1952). An optimal way of minimizing this effect is to combine different electrode materials with electrolytes compositions (Mácová et al., 2009). Bouzek et al., studying different iron anode materials, concluded that pure iron has the strongest tendency to form a compact oxide layer, requiring 30° < T < 50° to overcome the problem, while high iron carbide (Fe_3C, commonly call "white cast iron") ensures high current yields at 20° during prolonged electrolysis (Bouzek et al., 1996; Bouzek & Roušar, 1996, 1997). The positive effect of carbon in the carbide form on the anode dissolution is a general trend which finds agreement in literature (Mácová et al., 2009). On the electrolyte compositions, it was found that using a more [OH^-] solution increases both the electrode surface layer disintegration and ferrate(VI) ions stability (Bouzek & Nejezchleba, 1999; Mácová et al., 2009). Bouzek and Rousar, studying a [NaOH] range between 5 and 16 M at 20° using a white cast iron anode, found that the optimal results are achieved at 14 M (Bouzek et al., 1996). Exploiting the low solubility of K_2FeO_4 in concentrated KOH, He et al. were able to directly electro-synthesize solid K_2FeO_4 in one step with both high efficiency and low energy consumption, with the best results achieved at [KOH] = 14.5 M (W. He et al., 2005). An upper [MOH] ~ 15 M cap (with M = K, Na) corresponding to a significant decrease in current efficiency was found by multiple authors, probably due to the decrease of

free water, which slows down of the iron anode dissolution process, even if this cap can be increased up to 16-20 M in particular electrochemical configuration from more recent works (Barişçi et al., 2014; Barışçı, 2018; Bouzek & Roušar, 1997; W. He et al., 2005). Another important parameter is the geometry of the electrode, in particular the specific surface; increase the specific surface area exposed significantly increases the ferrate(VI) production rates (Mácová et al., 2009). Some notable examples of high specific surface electrodes are iron wire coils/gauzes (K. M. Wang et al., 2020), iron chunks (Lescuras-Darrou et al., 2002), iron plates and iron flakes (Barışçı, 2018), pressed iron powder pellets (De Koninck et al., 2003), porous magnetite electrodes (Ding et al., 2004). The last two substantial parameters to be controlled are the electrolysis time and the applied current density. Since ferrate(VI) is unstable in aqueous environment (par. 3.1) there will be an optimal time for a maximum production yield which is the best compromise between Fe(VI) decomposition/Fe(VI) formation kinetic/electrode passivation. Current density is related to the applied electrode potential and drives the reactions taking place at the electrode surface (Mácová et al., 2009). As mentioned above, ferrate(VI) formation takes place in the transpassive potential region of iron dissolution; higher potentials mean higher overall electric current consumption due to increasing oxygen evolution while insufficient potentials limit the rate of formation of ferrate(VI) intermediates which may be removed from the anode surface, decelerating the process (Mácová et al., 2009). For any set of T°, electrode material, electrolyte, electrode geometry but also electrode pre-treatment, number of electrodes, single or multiple chambers and consequent membrane-separation technology, chambers geometry, current waveforms, an optimal current density exists and, therefore, taking into account also the electrolysis duration, different current and ferrate(VI) production yields.

The inert electrode approach uses Fe(III) containing solutions as iron source and inert electrodes to eliminates the drawbacks caused by the passivation which are subjected the dissolving iron electrodes and the general kinetics of the dissolution process. Moreover, when Fe(III) is used, only three electrons are necessary to achieve the Fe(VI) oxidation state. The overall oxidation is expressed by the eq. (9) (M. A. Cataldo-Hernández et al., 2019):

$$Fe^{3+} + 4H_2O \rightarrow FeO_4^{2-} + 8H^+ + 3e^- ; \; E^0 = -2.2\,V\,(vs\,SHE) \quad (9)$$

The disadvantages of this strategy include the low solubility of iron species in the anolyte solution and the reduced stability of ferrate(VI) in Fe(III) solutions, which speed up the Fe(VI) decomposition kinetics. For this approach, then, it is necessary to account not only for oxygen evolution as a parasitic reaction but also for the notable mass transfer between bulk solution and anode surface (Mácová et al., 2009). As for the anode choice, materials with high oxygen overpotential were studied such as Pt (for stationary and rotating electrodes), SnO_2-Sb_2O_3/Ti, boron-doped diamonds (BDD) (Bouzek et al., 1997; Cañizares et al., 2007; Zhang et al., 2004). For the first time, ferrate(VI) production was studied under acidic conditions using BDD and ferrous sulphate solutions but the generated Fe(VI) ions rapidly decomposed to Fe(III) and oxygen, as expected from ferrate(VI) stability conditions (J. Lee et al., 2002). Thanks to BDDs properties, recently Cataldo- Hernández et al. successfully tested, for the first time, ferrate(VI) production at neutral pH in small and in large stirred reactors (5 and 100 cm^2 electrode area) (M. A. Cataldo-Hernández et al., 2018, 2019). Their works are part of the "REAS'EAU WaterNet Program, a federally funded research program aimed at studying drinking water issues currently affecting small rural communities across Canada" and exploited BDDs in order to avoid parasitic reactions such as oxygen evolution and, obviously, electrode passivation, using $FeCl^3$ as iron source (M. A. Cataldo-Hernández et al., 2018, 2019). Using a stirred flow reactor connected to an external electrolyte reservoir with a recirculating design and an ion exchange membrane, Cataldo- Hernández et al. demonstrated the feasibility of ferrate(VI) electrochemical generation at pH ~ 7 with high current efficiency values and proper resulting [Fe(VI)]; the product was also tested in treatment of synthetic waters containing 2,4-dichlorophenoxyacetic acid with good results (M. A. Cataldo-Hernández et al., 2019). As well as for the sacrificial anode method, the production of ferrate(VI) is strongly influenced by the electrolyte used, hydroxide content, T° and current density, as well as the iron content, with similar trends except for the current density, which seems to have a direct proportional effect on the ferrate(VI) production more than an optimal value (Cañizares et al., 2007). This evidence contributes to highlight how the availability of iron reagents around the electrode represents a crucial limiting factor for this kind approach. Ferrate(VI) can be also synthesized in molten hydroxides in order to overcome the product instability in the presence of water, obtaining a solid, dry Fe(VI) salt (Mácová et al., 2009). Direct anodic oxidation of the iron electrode or oxidation of the iron species in the molten electrolyte by the inert electrode are

both suitable with the main limitation being the limited stability of the product at high temperatures, which limits the electrolysis operational T° and duration (Mácová et al., 2009).

The low temperature wet method involves the oxidation of a solution containing iron, commonly in the form of Fe(III) (e.g. $FeCl_3$, $Fe(NO_3)_3$ etc), under high alkaline conditions to form a ferrate(VI) solution which is rapidly subjected to precipitation, purification and washing+drying with organic solvents to obtain a solid stable product. Since Na_2FeO_4 has relatively high solubility in NaOH solutions, solid sodium ferrate(VI) is difficult to isolate (with a 41.38 % Na_2FeO_4 content obtain in an optimized chlorine gas-flowing procedure) making potassium ferrate(VI) the easiest form achievable and, consequently, the most studied for this kind of synthesis (J.-Q. Jiang & Lloyd, 2002). Currently, the overall reaction often reported for potassium ferrate(VI) synthesis using ferric nitrate, potassium hypochlorite and potassium hydroxide is expressed by the eq. (10) (Delaude & Laszl, 1996):

$$2Fe(NO_3)_3 + 3KClO + 10KOH \rightarrow 2K_2FeO_4 + 3KCl + 6KNO_3 + 5H_2O \quad (10)$$

Although potassium ferrate was first synthesized in 1841, it was not until the 1950s that a viable wet procedure was developed for the synthesize of a stable, crystalline form with decent purity (Fremy, 1841; Moeser, 1897; G. W. Thompson et al., 1951). Production yields between 44.1 to 76.4 % of the theoretical and purities from 92.34 to 96.3 % (up to 99 % but with lower yields) were achieved for the first time by Thompson et al. in 1951 (G. W. Thompson et al., 1951). The procedure first involved the formation of sodium ferrate(VI) by reacting of ferric nitrate ($Fe(NO_3)_3$*$9H_2O$) with sodium hypochlorite (NaOCl) in the presence of sodium hydroxide (NaOH) and then the addition of potassium hydroxide (KOH) for the precipitation step, followed by filtrations and further washing + precipitations with KOH concentrated solutions in multiple passages (G. W. Thompson et al., 1951). Then benzene, 95 % ethyl alcohol and ethyl ether were used for the final washing and drying steps using a calcium chloride tube for protecting the K_2FeO_4 from the air moisture (G. W. Thompson et al., 1951). By substituting the NaOH with potassium hydroxide (KOH) and using potassium hypochlorite as the oxidizing agent, the intermediate formation of Na_2FeO_4 was avoided with consequent simplification of the process; 95 % ethanol and ether were used for the washing/drying steps (Williams & Riley, 1974). The yields increased up to 90 % for 40 % K_2FeO_4

content samples and 75 % for 99 % purity thanks to the precipitation procedure where K_2FeO_4 can be isolated by performing several dissolution and precipitation steps, which however consume lot of alkali solutions (Williams & Riley, 1974). Williams et Riley stated also that the use of ferric nitrate rather than any other iron salt produced the best results, probably due to nitrate ion being more stable towards oxidation by ferrate(VI) ion than the other anions tried (chloride, sulfate and phosphate) (Williams & Riley, 1974). In 1996, Delaude et Laszl further modified the procedure, leaving the reaction scheme unchanged while simplifying the purification part by reducing the number of filtering/precipitation/washing cycles and the volume of organic solvents used (Delaude & Laszl, 1996). In the final purification steps, after displacing the residual water from the precipitated product with n-pentane, which replaced the carcinogenic benzene of earlier procedures, methanol is used instead of ethanol for its better performance in removing KOH and other mineral impurities, while diethyl ether is used at the end for accelerating the drying of the salt (Delaude & Laszl, 1996). A proper removal of excess water with an inert hydrocarbon (n-pentane) is absolutely essential to the success of the purification; in fact, aqueous ferrate(VI) reacts readily with alcohols and K_2FeO_4 is quickly destroyed if it is not thoroughly dried before washing with methanol (Delaude & Laszl, 1996). Moreover, Delaude et Laszl tested commercial bleach solutions, pure potassium persulfate ($K_2S_2O_8$) and concentrated H_2O_2 solutions (30%) as alternatives to KClO but these failed to produce Fe(VI); meanwhile, only analytical grade KOH should be employed since technical grade reduces the cost but leads to rapid decomposition of Fe(VI) and gives very low purity (probably because of organic materials and metal traces contaminants) (Delaude & Laszl, 1996). The purities reached by the various batches were always > 97 %, with yield between 70-80 % of the theoretical (Delaude & Laszl, 1996). Li et al. furtherly improved the procedure by letting the ferrate solution resting 40 minutes before the starting the purification part of the synthesis (improving the “yield of potassium ferrate crystals”), introducing a double filtration with GF/A filters with 1.6 µm pore size and by using n-hexane together with n-pentane before the methanol purification part (C. Li et al., 2005). In all the procedures listed before, NaClO/KClO is prepared via chlorination of NaOH/KOH water solution, which is then filtrated in order to remove NaCl/KCl, leaving an alkaline hypochlorite solution where the iron reagent is then added for the oxidation. For the KCl removal, Li et al. used GF/C filters instead of the usual P-0 fritted glass because of the much smaller pore size (GF/C pore index = 1.2 µm vs 160 µm < P-0 pore index < 250 µm) which can decrease the impurity of the following ferrate

solution (C. Li et al., 2005). The yields achieved were between 50-70 % with very high purities (99 %) (C. Li et al., 2005). Other noteworthy examples are the employment of ozone instead of OCl^- for oxidation of Fe(III) in a alkaline solution (Perfiliev et al., 2007), the recycle of the waste alkali solution for preparing potassium ferrate with high purity/yield up to 10 times (Chengchun et al., 2008) and the usage of spent steel pickling liquid as iron source (93 % $FeCl_2*4H_2O$ + 7 % $FeCl_3*6H_2O$ once dried) for costs reduction (Wei et al., 2015).

A different approach was adopted by Sun et al. who tried to account for reduction in production cost of ferrate(VI); since in water treatments, having a pure solid ferrate(VI) product appears pointless, they decided to avoid the precipitation, purification and drying steps in order to produce a so called "liquid ferrate" using only chemicals which are often present in water treatment plants (X. H. Sun et al., 2013). The study tested the optimum [alkaline], reaction time, T° and water quality affecting the liquid ferrate product using ferric nitrate and sodium hydroxide and hypochlorite (X. H. Sun et al., 2013) (Fig. 1.20).

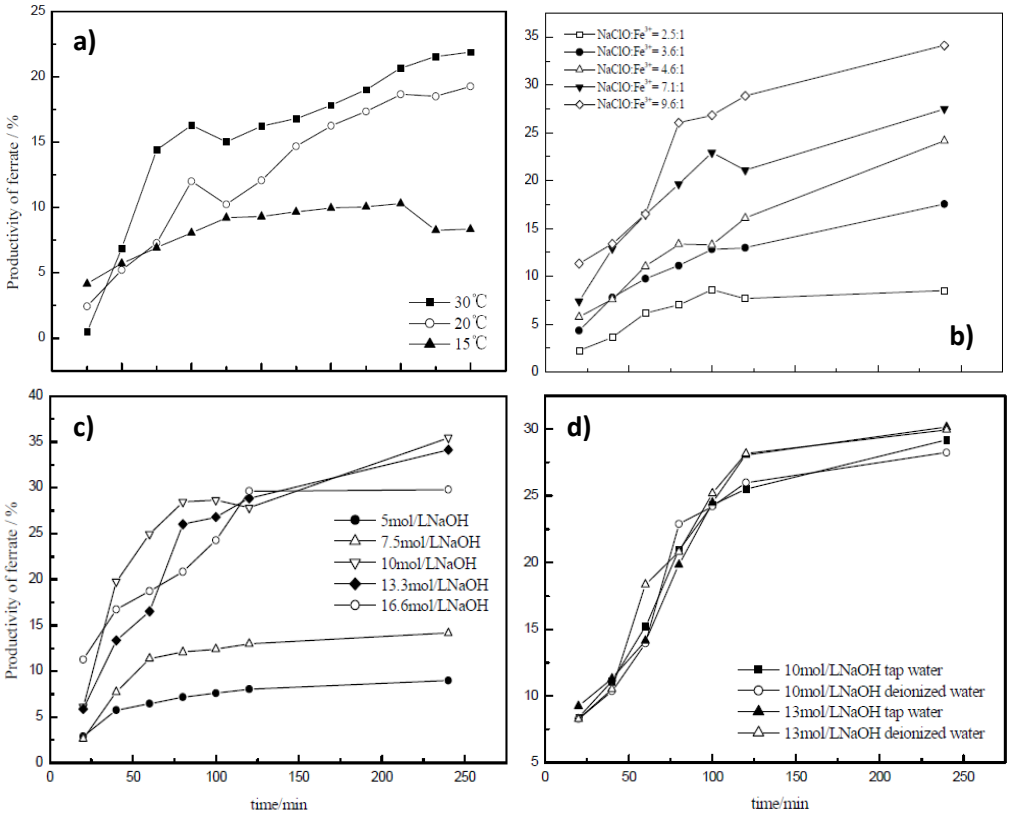

*Figure 1.20: effect of time and **a**) T°, **b**) mole ratio of NaClO/Fe(III), **c**) [NaOH] with 9.6 NaClO/Fe(III) molar ratio and **d**) water quality on the productivity of ferrate(VI) in liquid ferrate, where "productivity" is the % ratio between the amount of ferrate(VI) obtained experimentally and the amount produced theoretically, from* (X. H. Sun et al., 2013) *modified.*

The results showed an optimum 10 M [NaOH], a positive effect of the temperature between 15-30° and of time up to 250 minutes for ferrate(VI) productivity and no apparent difference between tap and deionized water (Fig. 1.20). Moreover, the larger the NaClO/Fe(III) mole ratio is, the higher the productivity is (Fig. 1.20b). Alshahri et al. prepared sodium liquid ferrate using $FeCl_3*6H_2O$, NaOH and NaClO following the conditions investigated by Sun et al. and obtaining a yield in agreement with the [NaOH] and NaClO/Fe(III) used (Alshahri et al., 2019; X. H. Sun et al., 2013). The final product was tested as a seawater treatment during algal bloom and it achieved higher removals of DOC, NOM and Algal Organic Matter (AOM) compared to $FeCl_3$ using equivalent [Fe], while efficiently inactivating the microorganisms (Alshahri et al., 2019).

1.1.4. Applications

Treatment of water sources collected worldwide by ferrates(VI), as well as laboratory specimens and pilot implants, have demonstrated their capability of removing a wide range of organic and inorganic compounds through 1) their oxidative power, 2) the absorbance strength of the coagulant secondary Fe(III) nanoparticles resulting from their decomposition in water 3) capability of embedding contaminants into the crystalline structures of the decomposition by-products, simultaneously (Tab. 1.5). The different case studies demonstrate that most of the inorganic contaminants can be degraded in milliseconds to minutes depending on the pH, T° and the co-presence of multiple of them (Virender K. Sharma, 2011). Another key factor is the high coagulation performance, which allows to reach better results with very low doses in comparison to the traditional coagulants, reducing the chemical demand as well as sludge production. Jiang et al., treating domestic sewage at pilot scale trials, found that a 0.1-0.2 mg Fe(VI)/L can achieve removal targets for total phosphorous, COD, BOD and suspended solids (whereas much higher dose of 25 mg Fe/L was required for ferric sulfate) with multiple additional pollutants removal and without generating bromate (unlike ozonated water) (J.-Q. Jiang et al., 2018). Kralchevska et al., studying ferrate(VI) phosphate removal from deionized water (DW) and real wastewater from the outlet of a sewage treatment plant (STP), found that complete removal of phosphates by K_2FeO_4 occurred in 30 min in DW at pH = 5.0-7.0 with Fe/P mass ratio of 3:1 to 5:1 by sorption on the surface of γ-Fe_2O_3/γ-FeOOH core/shell nanoparticles spontaneously formed from Fe(VI), while the sorbent-to-

phosphorous ratios typically vary between 1000:1 to 100:1 (Kralchevska et al., 2016). The calculated sorption capacity at pH=7 and Fe/P = 5:1 was 143.4 mg P per gram of sorbent (200 mg P per gram of Fe), being the highest capacity reported in the literature for phosphate removal up to that study. An higher Fe/P ratio of 20:1 at pH 7.3 was needed to achieve complete phosphate removal in STP samples; by using different STP dilution but keeping the same phosphate levels, it was shown how the presence of other inorganic and organic species affects the Fe(VI) removal efficiency (lower concentrations of calcium, magnesium, nitrates, chlorides, sulphates and NOM brought the complete phosphate removal back to a Fe/P of 5:1). The presence of the γ-Fe_2O_3/γ-FeOOH nanoparticles in the Fe(VI) by-products were studied by Prucek et al. through XRD, high resolution X-ray Photoelectron Spectroscopy (XPS), TEM and low-T° in-field Mossbauer (Prucek et al., 2013). The study tested As(III) and As(V) removal from deionized water by K_2FeO_4 focusing on the removal mechanisms using two approaches: an "in situ", where the ferrate(VI) is added to As contaminated waters and an "ex-situ", where the As contaminant is added to waters where only Fe(III) nanoparticles resulting from the K_2FeO_4 decomposition are present. Complete As removal occurs in the in-situ samples in less than 2 minutes at pH = 6.6 with Fe/As weight ratio 2:1, while common sorbents have comparable efficiencies at sorbent-to-arsenic rations typically between 1000:1 to 10:1 (w/w); the efficiency decreases to ~ 80 % increasing the pH up to 10.0. Meanwhile, only ~ 75 % removal after 4h of sorption was achieved in the ex-situ samples. This is because the arsenic removal mechanism by Fe(VI) cannot be solely explained by simple sorption but also by incorporation into the crystal structure of the in-situ formed Fe(III) nanoparticles, as highlighted by the multiple high resolutions techniques employed, which also pointed out the lack of this kind of information coming from the ex-situ resulting solids. As seen by XPS and Mossbauer, about 20 atomic % of arsenic enters the structure of the in-situ nanoparticles (while the rest is absorbed on their surface), which have a smaller average particle size than ex-situ ones, as expected from As(V)-for-Fe(III) substitution taking place. K2FeO4 showed same efficiency in As(V) and As(III) containing samples while only As(V) was detected in both in-situ and ex-situ resulting solids (Prucek et al., 2013). This is compatible with the As(III) to As(V) oxidation mechanisms of Fe(VI) which, contrary to all known competitive technologies: 1) is really effective in removing both arsenite and arsenate species at the same time (Fe(III) coagulants only adsorb As(V)); 2) firmly bound arsenic preventing its leaching back to the environment; 3) produces nanoparticles which are strongly magnetic, allowing their

separation from the solution by application of an external magnet, simultaneously (Y. Lee et al., 2003; Prucek et al., 2013). A similar study was realized and similar conclusions were drawn by Prucek et al. in 2015, regarding the Cd(II), Co(II), Ni(II), Cu(II) and Al(III) removal by K_2FeO_4 and the relative mechanisms (Prucek et al., 2015). The same in-situ and ex-situ design was adopted, so as the combination of XRD, high resolution XPS, in-field Mossbauer spectroscopy and magnetization measurements. At pH = 6.6, Co(II), Ni(II), Cu(II) and Al(III) were completely removed within 2 minutes with a Fe/Co and Fe/Cu weight ratios of 1:1, a Fe/Ni of 2:1 and a Fe/Al of 0.5:1; in the Cd(II) case, only a ~ 70 % removal was achieved at Fe/Cd weight ratio of 15:1. Regarding the pH effect, a positive correlation was highlighted between removal efficiency and pH increase between 5.0 and 10.0 (complete Cd(II) removal occurring at pH 10.0) while the starting metal concentrations tested (100, 10 and 1 ppm) seem not to influence significantly the Fe(VI) removal efficiencies. The use of $FeCl_2*4H_2O$ and $FeCl_3$ salts showed a ~ 40-60 % efficiency in comparison to K_2FeO_4 whit none of the metal ions removed at Fe(II)/M or Fe(III)/M of 2:1; moreover, a continuous leaching of the metal ions was observed within 1h, lowering the efficiency to ~ 20 % (no leaching back to the solution was observed for ferrate(VI)). XPS, magnetization measurements and Mossbauer showed that Co(II), Cu(II) and Ni(II) in the in-situ samples are removed largely by incorporation into the crystal lattice of the γ-Fe_2O_3/γ-FeOOH nanoparticles (octahedral sites) and by the simultaneously formation of MFe2O4 spinel phases, while only a tiny part is removed by sorption onto the nanoparticles surface. Ex-situ samples presented XPS spectra distinguishable different, where the predominant removal mechanism is adsorption. Regarding the smaller sized Al(III) ions (~ 0.39 Å ionic radius in the IV coordination) they appears to be incorporated easily in the tetrahedral positions of γ-Fe_2O_3 lattice with some contribution of the sorption phenomena. These evidences show the important advantages of Fe(VI) employment for Co(II), Cu(II), Ni(II) and Al(III) removal, as the leaching back in the environment prevented by the structural incorporation and formation of metal ferrites, together with the easy separation of the formed phases by application of an external magnet. In contrast, the Fe(VI)-induced Cd(II) removal occurred solely by adsorption, as showed by the XPS spectra of in-situ and ex-situ samples showing no significant differences, and confirmed by magnetization measurements and Mossbauer. The inability of Cd(II) of being incorporated into the nanoparticles crystal lattice could be explained by the Cd^{2+} ionic radius (~ 0.96 Å for coordination) exceeding the octahedral positions limiting size (~ 0.95 Å) in the γ-Fe_2O_3 structure

Some other notable applications of Ferrate(VI) in the environmental remediation fields include (Tab. 1.5): the total disinfection of bacteria and viruses (with Fe(VI) dosages between 0 to 50 ppm) (Rai et al., 2018; Song & Ma, 2013); the complete removal of total cyanide in rinse-water, gold mining and coke oven plants (Song & Ma, 2013); the rapid degradation of nitrogen-containing pollutants (Virender K. Sharma, 2010); the oxidation of Sb(III) to Sb(V) and the removal below the maximum levels for drinking waters using a mixture of Fe(II) and Fe(VI) (Johnson & Lorenz, 2015); the oxidative transformation and removal of micropollutants (e.g. estrogens, antibiotics, general Pharmaceutical and Personal Care Products (PPCPs)) (T. He et al., 2022; Karim et al., 2020; Rai et al., 2018; J. Yu et al., 2023); the degradation of phenolic compounds, pesticides and dyes (T. He et al., 2022; Karim et al., 2020; J. Yu et al., 2023); the removal of algae in drinking water (Alshahri et al., 2019; J. Yu et al., 2023); the simultaneously removal of SO_2, NO and Hg(0) from flue gas bubbling in a solution with 0.25 mmol/L of ferrate(VI) (Zhao et al., 2014); the elimination of various radionuclides from active and abandoned uranium mines and nuclear reactors (Rai et al., 2018).

Compound	Max removal (%)	Removal mode	References
Arsenic	100	Ox., inc., ads.	(Jain et al., 2009; Y. Lee et al., 2003; Prucek et al., 2013)
Cyanide	100	Ox.	(Filip et al., 2011; Song & Ma, 2013; Yngard et al., 2008)
Phosphorous	100	Ox., ads.	(J.-Q. Jiang et al., 2018; Kralchevska et al., 2016)
Copper (II)	100	Inc., ads.	(Filip et al., 2011; Murmann & Robinson, 1974; Prucek et al., 2015)
Nickel (II)	100	Inc., ads.	(Prucek et al., 2015)
Cobalt (II)	100	Inc., ads.	(Prucek et al., 2015)
Aluminum (III)	100	Inc., ads.	(Prucek et al., 2015)
Cadmium (II)	70	Ads.	(Murmann & Robinson, 1974; Prucek et al., 2015)
Mercury (II)	> 90	-	(Murmann & Robinson, 1974)
Elemental Mercury (from flue gas)	81.4	Ox., ads.	(Zhao et al., 2014)
SO_2 (from flue gas)	100	Ox., ads.	(Zhao et al., 2014)
NO (from flue gas)	64.8	Ox., ads.	(Zhao et al., 2014)
Lead (II)	Und. detec. Lim.	-	(Murmann & Robinson, 1974)
Manganese (II)	~ 99	-	(Murmann & Robinson, 1974)
Zinc (II)	> 90	Inc., ads.	(Filip et al., 2011; Murmann & Robinson, 1974)
Iron (II), Iron (III)	~ 80	-	(Murmann & Robinson, 1974)
Chromium (III)	> 60	-	(Murmann & Robinson, 1974)
Chromium (VI)	Not affected	-	(Murmann & Robinson, 1974)
Hidrogen Sulfide	99	Ox.	(Virender K. Sharma et al., 1997)

Antimony	98	Ads.	(Johnson & Lorenz, 2015)
Ammonia	~ 22	Ox.	(Virender K. Sharma, 2010)
Hydroxylamines, Hydrazynes, Azides	-	Ox.	(Virender K. Sharma, 2010)
Amines, Amino acids, Anilines, Sulfonamides, Macrolides, Dyes	-	Ox.	(Virender K. Sharma, 2010)
Ethanol	> 80	Ox.	(Schmidbaur, 2018)
Formaldehyde	> 80	Ox.	(Schmidbaur, 2018)
Carboxylic compounds	> 80	Ox.	(Schmidbaur, 2018)
Aliphatic sulfur	> 80	Ox.	(Schmidbaur, 2018)
Chlorine oxyanions	> 80	Ox.	(Schmidbaur, 2018)
Iodide	-	Ox.	(Schmidbaur, 2018)
Benzene	47	-	(J.-Q. Jiang & Lloyd, 2002)
Chlorobenzene	47	-	(J.-Q. Jiang & Lloyd, 2002)
allybenzene	100	-	(J.-Q. Jiang & Lloyd, 2002)
Phenol	70	Ox.	(Schmidbaur, 2018)
2-, 3- ring fluorescent aromatics	78	Ox.	(Schmidbaur, 2018)
Nitrobenzene	< 20	Ox.	(Schmidbaur, 2018)
TOC	35	-	(J.-Q. Jiang & Lloyd, 2002)
BOD	95	-	(J.-Q. Jiang & Lloyd, 2002)
Antibiotics	-	Ox.	(Schmidbaur, 2018)
Micropollutants	-	Ox.	(T. He et al., 2022; Karim et al., 2020; Rai et al., 2018; J. Yu et al., 2023)
Farmaceutical products	-	Ox.	(T. He et al., 2022; Karim et al., 2020; Rai et al., 2018; J. Yu et al., 2023)
Gross radioactive activity	10^3 pCi/l	-	(J.-Q. Jiang & Lloyd, 2002)
^{137}Cs(I), ^{90}Sr(II), ^{152}Eu(III), ^{243}Am(III), ^{239}Pu(IV), $^{237+239}$Np(V), $^{238+233}$U(VI)	-	-	(Schmidbaur, 2018)
Non-recombinant *Pseudomonas*, recombinant *Pseudomonas*	100	Ox.	(J.-Q. Jiang & Lloyd, 2002; Rai et al., 2018)
Escherichia Coli	99.9	Ox.	(J.-Q. Jiang & Lloyd, 2002; Rai et al., 2018)
Total *Coliforms*	99.9	Ox.	(J.-Q. Jiang & Lloyd, 2002; Rai et al., 2018)
Total viable Bacteria	97	Ox.	(J.-Q. Jiang & Lloyd, 2002; Rai et al., 2018)
All microorganisms in water	100	Ox.	(Rai et al., 2018; Schmidbaur, 2018)

Virus f2 *Coliphage*	99.9	Ox.	(J.-Q. Jiang & Lloyd, 2002; Rai et al., 2018)

Table 1.5: removal capability of ferrate(VI); "Ox." = oxidation, "Inc." = incorporation (in the structure of the by-products), "ads." = adsorption.

1.1.4.1. Real life applications

The United States Environmental Protection Agency (EPA), through its National Risk Management Research Laboratory, developed an environmental life cycle assessment and cost analysis to evaluate the environmental outcomes and costs associated with innovative disinfection water treatment technologies for drinking water. In 2014, EPA published a 104 pages study comparing a baseline life-cycle model developed using the infrastructure and operational datasets from the Greater Cincinnati Water Works Richard Miller Treatment Plant (GCWW), a 106 million gallon per day drinking water plant which uses granular activated carbon and gaseous chlorine as primary disinfectant, and four in-plant disinfection alternative models based on four different technologies (Cashman et al., 2014). The alternatives include the disinfection by conventional ultraviolets (UV), LED UV, plasma-bead UV and oxidation/disinfection using Fe(VI) produced on-site by the Ferrator® system, a reactor for municipal and industrial applications from Ferrate Treatment Technologies LLC (more information below). The final comparison between the GCWW baseline model (Base Case 1) and the alternative technology models is shown in Fig. 1.21. While conventional UV technology eliminates the formation of disinfection by-products (TTHM) and reduces hazardous chlorine usage, it implies higher electricity consumption and an elevated new capital investment; switching to LED UVs could reduce the energy expense but, when the study was published, it was only developed for point-of-use and not for large-scale facilities. Instead, "utilization of ferrate results in environmental, human health and cost benefits for combined use in the pre-disinfection and primary disinfection stages, since ferrate acts as both a coagulant and disinfectant and only small dosages are required for treatment". Figure 1.22 displays the annual impact % reduction derived by switching to Ferrator® technology, based on 1 m^3 water delivered to the customer and normalized over the 15 years expected lifetime of the reactor.

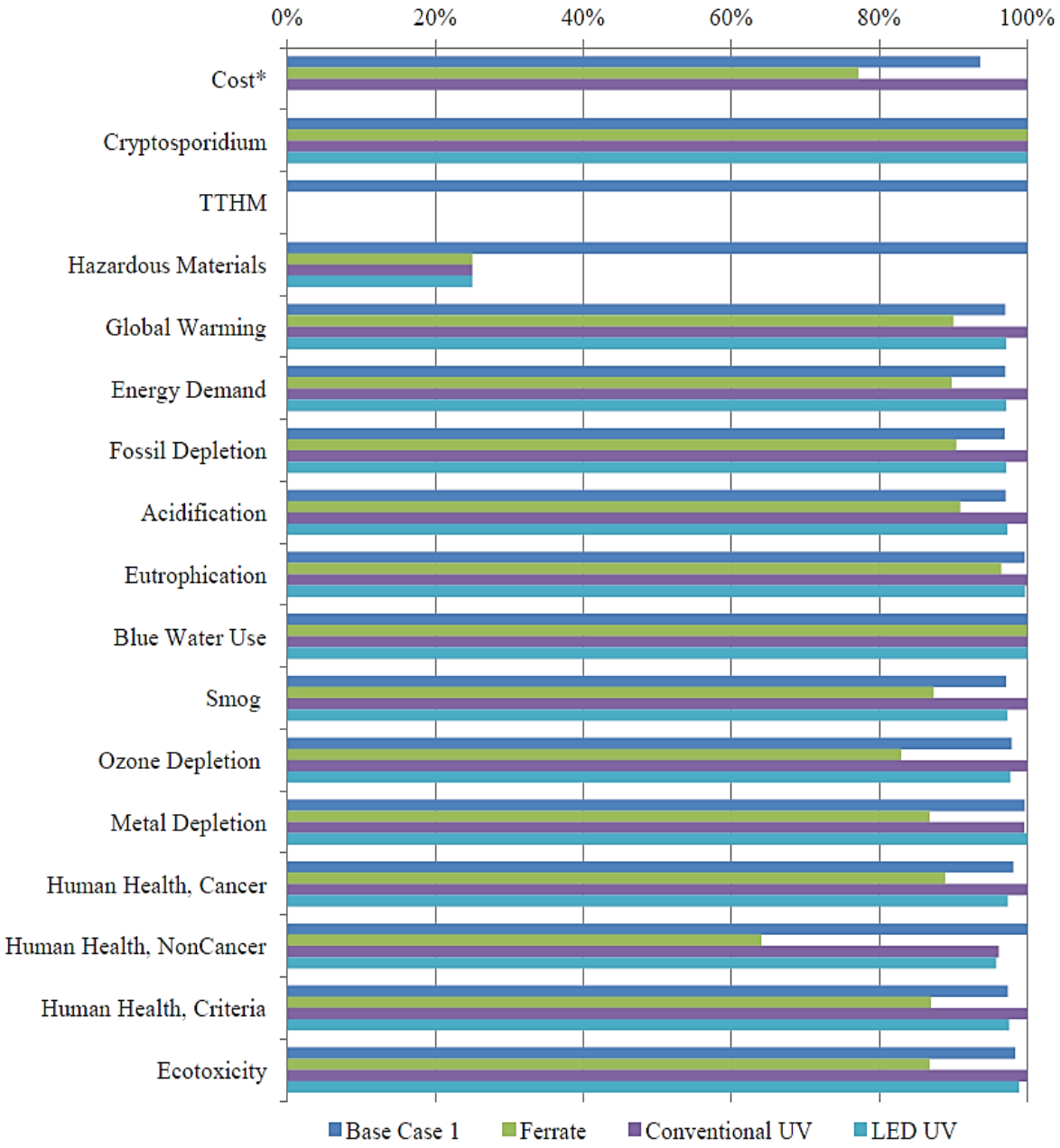

Figure 1.21: summary comparative results of standard and alternative disinfection technologies models (Cashman et al., 2014).

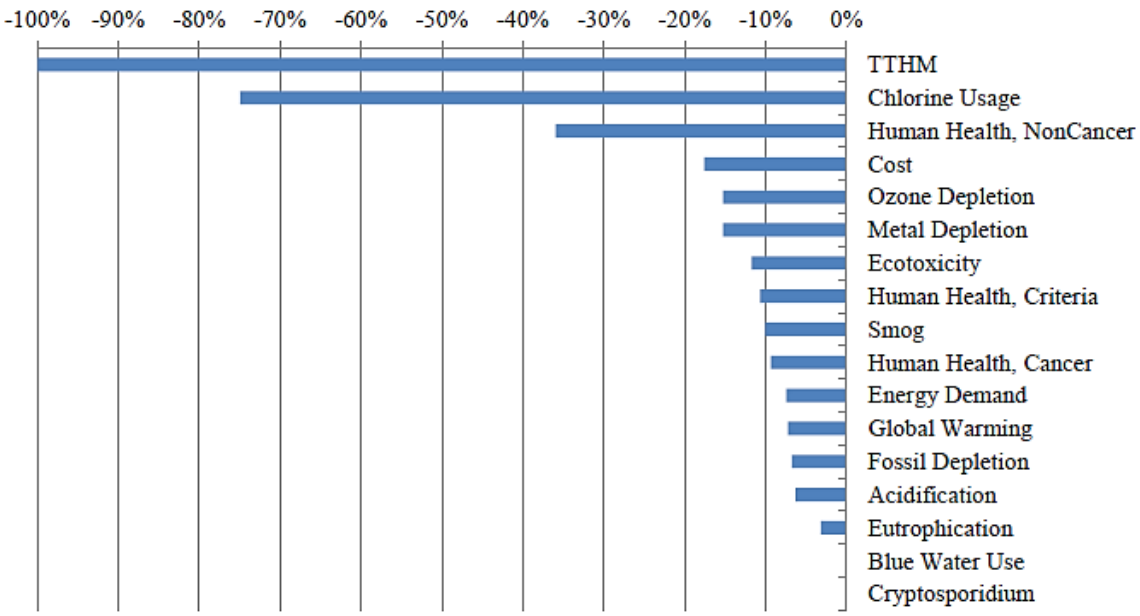

Figure 1.22: impact % reduction results between the plant model exploiting the on-site Fe(VI) production by Ferrate Treatment Technology LLC Ferrator® and the GCWW baseline model, using traditional gaseous chlorine gas and granular activated carbon (Cashman et al., 2014).

An example of ferrate(VI) transition from the laboratory to the real world is Ferrate Treatment Technologies LLC (FTT), a company from Orlando, Florida, founded in 2004 "to invent, develop, and commercialize innovative water and wastewater technologies on its proprietary iron chemistry platform" (Environmental XPRT, n.d.). It was the first company which developed and patented an on-site ferrate(VI) reactor for municipal and industrial water treatment applications called Ferrator®, which produces liquid ferrate through wet chemical synthesis from sodium hypochlorite, sodium hydroxide and ferric chloride that can be pumped directly into the treatment process streams. This transportable system, which can be scaled for multiple application, eliminates product handling, transport, distribution and reduces the traditional manufacturing costs (see as reference Fig. 1.23). Unfortunately, their website (http://www.ferratetreatment.com), which I consulted up to the end of 2019, is currently down and I couldn't retrieve any news on the current state of the company. FTT advertising videos, still online on Youtube, are currently displayed on the Recovered Earth Technologies LLC (RET) webpage and Youtube channel, as well as photos of a Ferrate Water Treatment (FWT) with analogous description, models and photos of the Ferrator® ones (Recovered Earth Technologies, n.d.). On the "Awards and Accolades" section of RET webpage, the three awards listed were all won by FTT, here reported as "strategic partner" but without specific mention.

RET is “a global leader in the recovery of natural resources utilizing a combination of licensed and patented technologies” located in Reno, Nevada. Thus, for any further data on on-site ferrate(VI) production systems for municipal and industrial applications, please refer to RET website (Recovered Earth Technologies, n.d.).

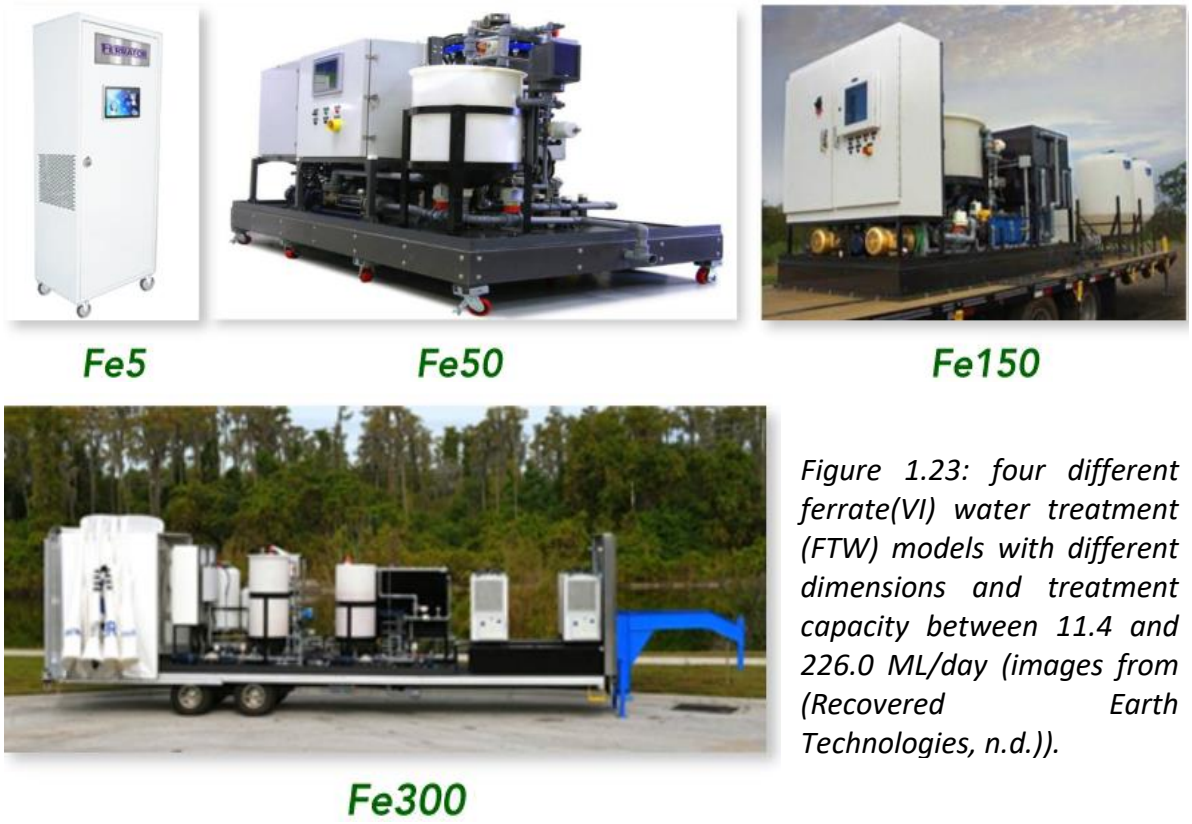

Figure 1.23: four different ferrate(VI) water treatment (FTW) models with different dimensions and treatment capacity between 11.4 and 226.0 ML/day (images from (Recovered Earth Technologies, n.d.)).

A more recent example of ferrate(VI) application into the real world is Ferrate Solutions® Inc. (FS), a company launched in 2019 and located in West Melbourne, Florida, which “designs, fabricates, installs and maintains site-specific equipment that creates and delivers ferrate-based treatments” for “drinking water, domestic and industrial wastewater, sludge and gasses” (Ferrate Solutions® Inc, n.d.). Similar to FTT, FS provides scalable on-site synthesizers which wet-synthesize liquid ferrate(VI) using sodium hypochlorite, sodium hydroxide and ferric chloride in “proprietary blends” which “are now available at a commercial scale for < $ 5.00 per pound of FeO_4^{2-}“. Some notable application of FS technology are the pilot-tests in Amman, Jordan (Ferrate Solutions® Inc, 2019), the realization of a facility for blue-green algae-feeding phosphorus and nitrogen remediation at Lake Okeechobee (Florida) (Treadway, 2020) and the full-scale treatment of muck dredge water on the Indian River Lagoon (Florida) (Ferrate Solutions® Inc, 2021).

Looking to Europe, Ferr-Tech, a Dutch start-up officially launched in 2020, is currently producing sodium or potassium liquid ferrates(VI), sodium ferrate(VI) in "cake form" and powder sodium ferrate(VI) for industrial water treatments in the agrifood, dairy, steel, oil and gas and polymer recycle sectors (Ferr-Tech, n.d.; Netherlands Enterprise Agency, 2022). In 2022, at the Consumer Electronics Show (CES), the world's largest technology show held each year in Las Vegas, Ferr-Tech was selected for the CES 2022 Innovation Award in the "Sustainability, Eco-Design & Smart Energy" category for its FerSol® product (sodium or potassium liquid ferrate (VI)) while on the 28th of March 2023, the same product was awarded with the Aqualia Innovation Award during WEX Global 2023 in Spain (Consumer Technology Association, 2022; Water and Energy Exchange Global, 2023).

1.2. Mercury: overview

Mercury is an heavy metal of the transitional element series and it is considered by the World Health Organization (WHO) "one of the top ten chemicals or groups of chemicals of major public health concern" (World Health Organization, 2017). It is highly toxic to human health, which may be affected by an exposure to mercury with severe (even death), subtle or invisible effects depending on the form of mercury, the amount in the exposure, the duration and the mechanism of the exposure, the age and the health of the person exposed (United States Environmental Protection Agency, 2023). Being a local, regional and global pollutant, mercury is a natural occurring element which has been directly mobilized by humans for millennials into aquatic and terrestrial ecosystems through mining, precious metal extraction, energy production (coal burning), use in products (e.g. paints, electronic devices) and industrial processes (e.g. catalysis) (Driscoll et al., 2013). Mercury has three oxidation states (Hg(0), Hg(I) and Hg(II)) and can exists in soils, oceans, atmosphere, plants and other living organisms in a variety of different states and species with different properties (Fig. 1.24) (O'Connor et al., 2019). While Hg(I) is not stable under typical environmental conditions, being an intermediate product of Hg redox processes, Hg(0) is typically found as atmospheric particulate due to its high volatility and susceptibility to oxidation (Gaseous Elemental Mercury, GEM, > 95 % of total atmospheric Hg with a lifetime of 0.5-1 year), and in localized heavy polluted soils (e.g. spillages), where typically is oxidized to Hg(II) forming inorganic salts and minerals (e.g. HgS, HgO, $HgCl_2$) or organo-Hg compounds (Edwards et al., 2021; O'Connor et al., 2019). With the

primary anthropogenic emissions greatly exceeding the natural geogenic ones, mercury in natural reservoirs is constantly increasing with different response times, concentrating over the course of centuries in soil pools, deep ocean waters and sediments (Driscoll et al., 2013). Regarding the human health, the two most highly adsorbable Hg-species are Hg(0) and the organic methyl-mercury (CH_3Hg), with the latter being readily assimilated by the gastrointestinal tract in the lipid tissues, having a low excretion rate and so accumulating into the food chain, especially in fishes, up to toxic levels (bioaccumulation) (Tchounwou et al., 2012). Due to the diffusion of methylation processes all over the ecosystems, exposure to methyl-mercury represents the primary health risk for humans and wildlife, making Hg(0) and Hg(II) health impacts linked to their net conversion to CH_3Hg (Driscoll et al., 2013). In terrestrial and freshwater ecosystems, methylation occurs in reducing zones, largely mediated by SO_4^{2-} and, to a lesser extent, Fe reducing bacteria and influenced by a large variety of factors (organic matter, supply of bioavailable Hg(II), T°, hydrology, presence of wetlands, riparian zones etc.); CH_3Hg can then be supplied to downstream and adjacent aquatic environments and/or bio-accumulates in fishes (Driscoll et al., 2013). Mercury is highly attracted to organic matter and mineral surfaces in soils, where it can reacts with sulfide to form the stable cinnabar, relatively immobile and insoluble under normal environmental conditions and poorly subjected to methylation (O'Connor et al., 2019). However, certain DOM substances (e.g. fulvic acids), excess of sulfide ions and presence of nano-sized HgS particles can increase the bioavailability of HgS (O'Connor et al., 2019). Regarding oceans, riverine and coastal CH_3Hg inputs are small in comparison to the in-situ production; while the ultimate source of methyl-mercury has still remained uncertain, water-column methylation of inorganic Hg(II) mercury seems to be an important source of CH_3Hg in pelagic marine food webs in the Artic and perhaps in the oceans in general (Lehnherr et al., 2011). Concentrations of CH_3Hg are low in surface ocean waters due to photochemical and biotic demethylation, increase in subsurface/subthermocline waters and are low in the deep ocean, presenting a [CH_3Hg]/depth profile in conjunction with the decomposition of organic matter (O'Connor et al., 2019).

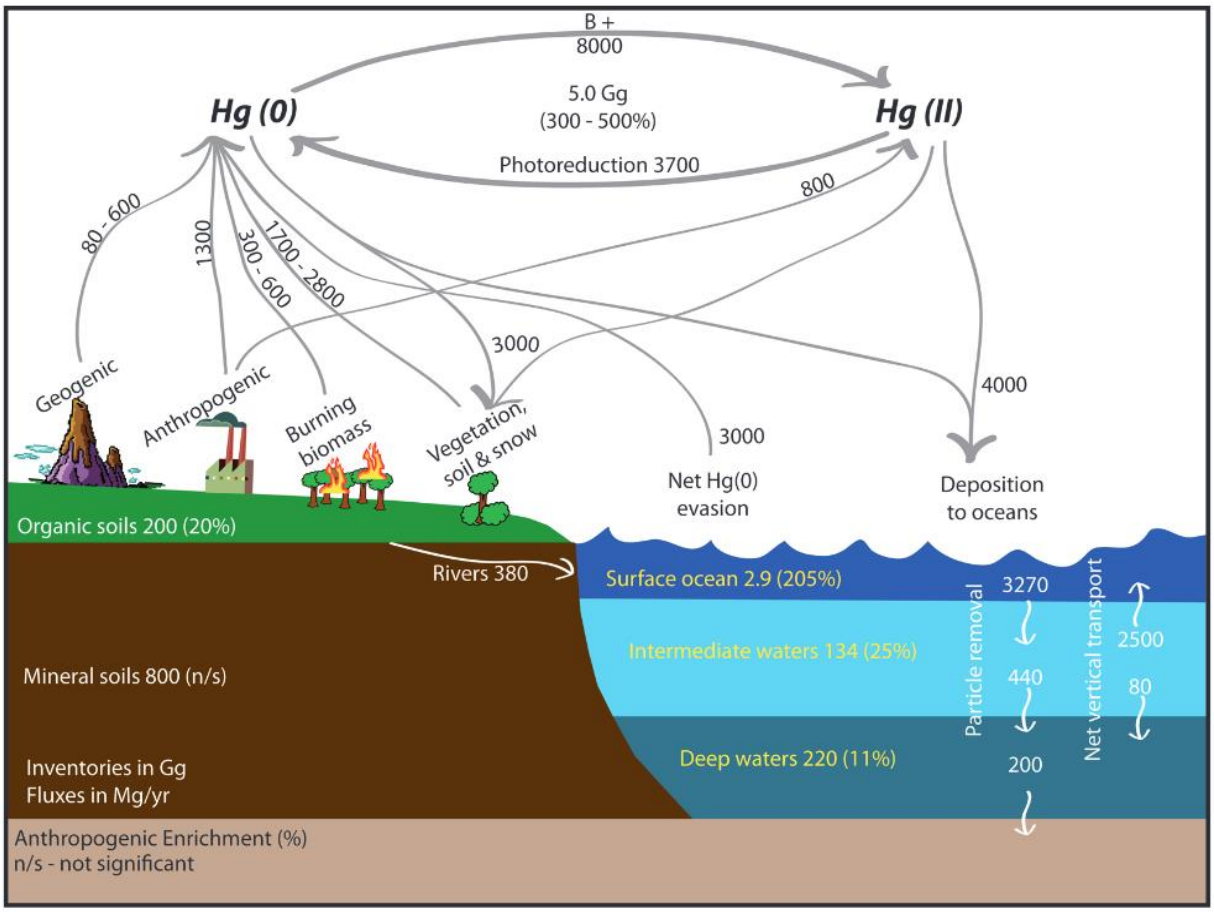

*Figure 1.24: primary and secondary mercury fluxes and pools estimates from the work of Driscoll et al. 2013 (references therein); Hg(II) includes both gaseous and particulate forms and a negligible 1 Mg contribution from inert particulate mercury. The (%) are estimated increases in pools due to anthropogenic activities over the past 150 years. Fluxes are in Mg*year^{-1} while reservoirs in Gg. From (Driscoll et al., 2013).*

1.2.1. Mining primary production

Over the past few decades, mercury geochemical cycle has increasingly been decoded, thanks to the considerable insights on Hg pathways from local to global scales (e.g. Hg stable isotopic research is a rapidly developing field which helps in elucidating Hg fractionate processes) (Driscoll et al., 2013; Edwards et al., 2021; Lehnherr et al., 2011; Nannoni et al., 2022; O'Connor et al., 2019). While the primary contribution from natural sources (~ 500 ton/year) is still uncertain (e.g. the volcanic activity, considered an important but poorly understand Hg source, gives global output flux estimates between 45 and 700 ton/year), anthropogenic atmospheric emissions are relatively constrained (2500 ± 500 ton/year), currently leaded by the coal-fired electricity generation in the developing world (Driscoll et al., 2013; Edwards et al., 2021). Regarding the primary production of mercury, mining activities have consistently

decreased since early 1980 due to the increasing recognition of environmental problems up to the global treaty of the Minamata Convention on Mercury (United Nation Environmental Programme, 2013); currently Hg mining is limited to China and Kyrgyzstan (Nannoni et al., 2022). Accounting for the low efficiency of the past technology involved in those activities, the Hg lost in the environment have been enormous and the Hg releasing from the still contaminated sites is an on-going problem at different scales. The world production of mercury has largely come from mercury-bearing ores concentrated in globally distributed mercury mineral belts (Tab. 1.6). About three quarters of the total production has come from the five districts of (in order from highest to lowest) Almaden (Spain), followed by Idrija (Slovenia), Mt. Amiata (Italy), New Almaden (California Coast Range) and Huancavelica (Peru) (Fig. 1.25, 1.26) (Hylander & Meili, 2003; Nannoni et al., 2022). Table 1.6 was compiled using data from statistical yearbooks, historical registers, scientific articles, exported quantities or were estimated when the information were scarce or not available (e.g. Algeria and China); due to that, Tab. 1.6 has to be regarded as a lower limit of the mined mercury instead of actual quantities, which could be much larger.

Year	Europe[b]				America			Former USSR[k]	Asia[b]		Africa	Other	Globally
	Spain[c]	Slovenia[d]	Italy[e]	Other[f]	North[g,h]	S&C[g,i]	Mexico[j]		China[l]	Other[m]	Algeria[n]	countries[o]	mined
1501–1550	2601[p]	2449	0	0	0	0	0	0	>0?[q]	0	0	0	5050
1551–1600	4138	3931	0	0	0	8091	0	0	>0?	0	0	1	16 161
1601–1650	8740	6062	0	0	0	11 255	0	>0?	>3	0	0	0	26 060
1650–1700	5372	4111	0	0	0	11 628	0	>0?	>2	0	0	0	21 113
1701–1750	14 437	4241	0	0	0	9460	0	>0?	>0?	0	0	0	28 138
1751–1800	32 708	14 815	0	0	0	9887	0	>0?	>0?	0	0	0	57 410
1801–1850	35 544	11 299	0	0	266	1968	0	>0?	>0?	0	0	0	49 077
1851–1860	9330	2371	4	0	8464	>0?	0	>0?	>0?	0	0	0	20 169
1861–1870	10 879	2841	55	0	14 603	>0?	>0?	>0?	>0?	0	0	0	28 378
1871–1880	11 228	4327	744	25	17 975	>0?	>0?	>0?	>0?	0	0	93	34 392
1881–1890	17 434	5249	2566	279	12 794	>0?	>0?	892	1000	0	0	398	40 612
1891–1900	15 785	5521	2457	0	10 193	>0?	983	3253	6000	0	0	011	44 203
1901–1910	11 428	5740	4812	164	9400	>0?	905	2267[r]	1758	0	0	1136	37 610
1911–1920	10 627	6309	9373	693	8099	>10	398	79[r]	1241	136	0	2063	39 028
1921–1930	14 801	5955	11 719	626	4190	621	679	703[s]	314[r]	241	24	1962	41 835
1931–1940	12 086	3810	12 082	817	6547	699	2338	2049	549	344	99	1057	42 477
1941–1950	16 729	3972	16 058	635[s]	11 946	747	5575	400	769	1235	239	2280	60 585
1951–1960	16 226	4821	19 180	294	8041	934	5962	5949	4348	3164	21	858	69 798
1961–1970	20 601	5517	18 170	898	10 126	1806	6634	13 578	8992	5030	49	147	91 548
1971–1980	14 782	3409	6842	3309	8386	694	4717	21 300	8100	3236	7150	0	81 925
1981	1560	7	252	296	962	3	240	1700	800	204	30	0	6054
1982	1540	7	159	275	888	2	295	1200	800	246	386	0	5798
1983	1416	58	0	209	864	4	221	1200	850	162	828	0	5812
1984	1520	78	0	232	657	2	384	1220	800	182	586	0	5661
1985	1539	7	0	288	570	1	394	1200	800	226	801	80	5906
1986	1471	82	0	315	470	0	185	2250	700	262	764	0	6499
1987	1553	74	0	308	100	0	124	2300	700	211	756	0	6126
1988	1499	77	0	303	379	0	345	2300	940	97	662	0	6602
1989	967	57	0	291	428	0	651	2300	880	202	587	0	6363
1990	962	44	0	266	460	0	735	2100	800	60	639	0	6066
1991	52	16	0	149	58	0	340	1900	700	25	431	0	3671
1992	36	14	0	145	64	0	21	1900	392	5	476	0	3053
1993	636	7	0	148	70	0	12	1190[s]	520[s]	0	459	0	3042
1994	386	12	0	133	70	4	12	534	470	0	414	0	2035
1995	1497	11	0	140	70	13	15	520	780	0	292	0	3338
1996	1024[t]	5	0	108	30	13	15	709	510	0	368	0	2782
1997	389[t]	5	0	83	15[u]	15	15	725	835	0	447	0	2529
1998	474[t]	0	0	74	15[u]	24	15	725	225	0	224	220	1996
1999	433	0	0	40	15[u]	33	15	705	200	0	240	380	2061
2000[v]	236[t]	0	0	45	15[u]	48	25	640	200	0	240	400	1849
Sum	304 666	107 311	104 473	11 588	137 230	57 962	32 250	77 788	45 978	15 268	17 212	11 086	922 812
% of total	33.0	11.6	11.3	1.3	14.9	6.3	3.5	8.4	5.0	1.7	1.9	1.2	100

Table 1.6: global historical primary production of mercury from mining activities, in tons of Hg, until 2000, from (Hylander & Meili, 2003). [b] excluding former USSR countries; [c] mainly Almaden, [d] Idrija, the mine(s) belonged to Austria-Hungary 1867–1918, Italy 1919–1945, Yugoslavia 1945–1991; [e] mainly Mt. Amiata, Hg produced at Idrija 1919–1945 is listed under Slovenia; [f] Austria 47 t, Czechoslovakia 5883 t, Finland 2090 t, Germany 2081 t, Hungary 1160 t, Ireland 264 t, Romania 104 t; Sweden 1 t; [g] excluding Mexico; [h] mainly New Almaden and several other mines in California, a few in Nevada, Virginia; Canada 6124 t; [i] mainly Huancavelica, Peru; [j] small, not reported quantities of Hg produced during colonial time; [k] mainly Nikitovka in Ukraine, Russia, Khaydarkan in Kyrgyzstan, and Jijikrut in Tajikistan (an antimony-Hg mine); [l] mainly in south-western China, data estimated if not otherwise indicated; [m] Japan (mainly Hokkaido) 6810 t, Philippines (Palawan) 2138 t, Turkey 6179 t; [n] Incl. Tunisia 109 t, South Africa 9 t; [o] Australia 101 t, New Zealand 41 t, the rest is estimates for not identified countries; [p] reference therein (Hylander & Meili, 2003) ; [q] Hg produced but not quantified; [r] exported quantity; [s] former USSR countries 1700 t, China 468 t; [t,u] references therein (Hylander & Meili, 2003); [v]estimated quantity in reference.

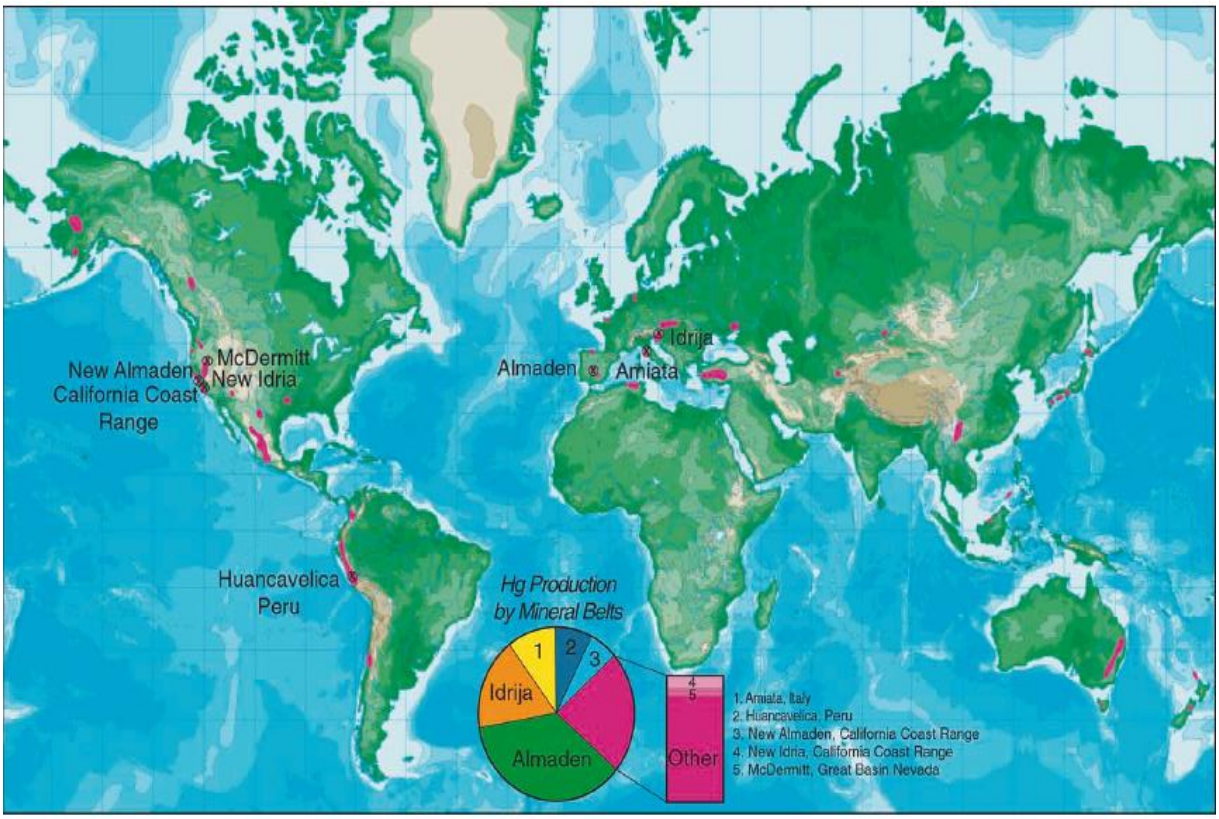

Figure 1.25: global distribution of mercury mineral belts with significant mercury production (in red) and the relative mining sites. From (Rytuba, 2003).

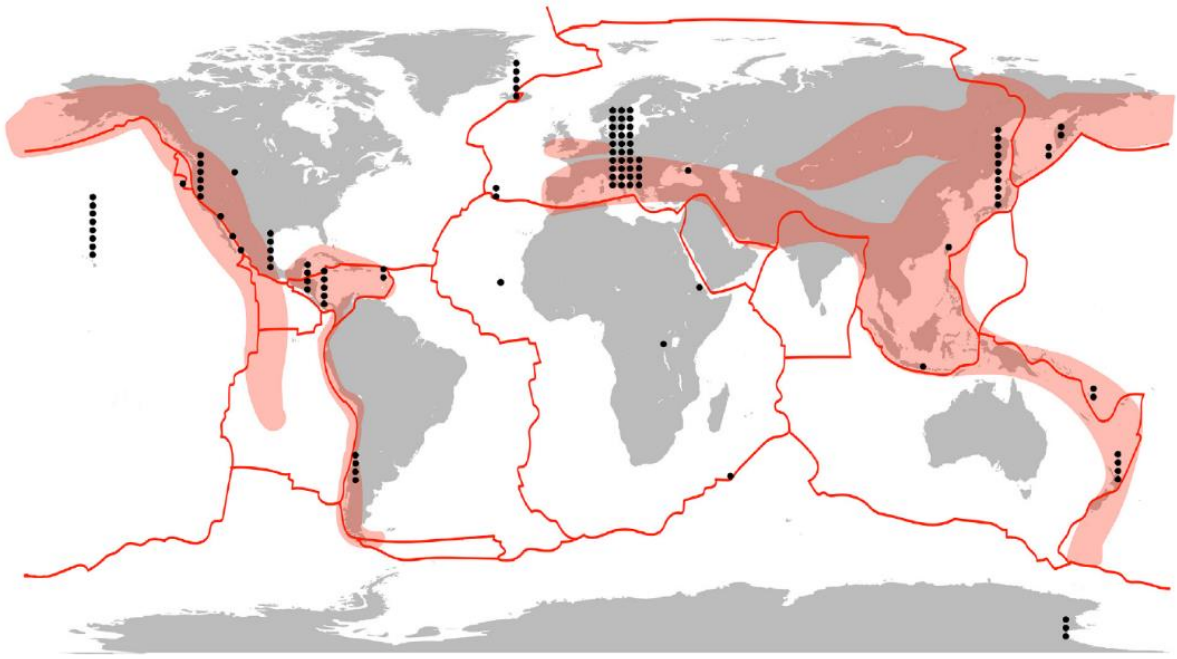

Figure 1.26: locations of the global mercury belts (light red areas) in relation to the major tectonic boundaries (red lines) and all the volcanic Hg emissions field studies published (black dots). From (Edwards et al., 2021).

The mercury mineral belts comprise mercury deposits, occurrences and areas of altered rocks containing high [Hg] (Rytuba, 2003). Mercury deposits are usually cogenetic within each mineral belt and reflect the tectonic and/or volcanic processes that contribute to the Hg enrichment (e.g. California Coast Range mercury belt formed along a boundary plate as the tectonic regime changed from convergent to transform) (Fig. 1.26) (Rytuba, 2003). Instead, the Mediterranean belt deposits aren't usually co-genetic but rather consist localized accumulates formed at different times/geological settings (e.g. Almaden, which consists of 11 deposits in a 10x20 km area) (Rytuba, 2003). Three types of deposits occur in the mercury belts: Almaden type, silica-carbonate type and hot-spring type (Rytuba, 2003). The Almaden type occurs mostly in Almaden, central Spain, and comprehend deposits which forms when submarine mafic centers occur adjacent to Hg-enriched marine sediments (e.g. Las Cuevas, which is localized in a submarine caldera); such deposits usually form along continental margins, where black shales are disrupted by volcanic activity (Hazen et al., 2012; Rytuba, 2003). Silica-carbonate type is referred to mercury ores hosted in silicate and carbonate minerals formed during low-T° hydrothermal alteration and replacement of serpentinite, which due to its common location along faults and its low-permeability, acted as a trap for CO_2-rich fluids which deposited Hg (e.g. New Almaden and New Idria in the California Coast Range); as for the other types, the Hg-rich fluids derived from nearby marine sedimentary basins (Hazen et al., 2012; Rytuba, 2003). The hot-spring type, the most diffuse, gathers all the shallow to low-depth deposits formed due to often silicic, near-surface waters circulation in geothermal systems, which vapor-precipitate Hg minerals in the coolest shallow environments; many of this kind of deposits are generally young and active and ore located in or adjacent to intermediate to felsic volcanic centers (e.g. McDermitt, the largest deposit of this type) (Hazen et al., 2012; Rytuba, 2003). The rock hosting the mercury ores are typically hot-spring silica deposits and hydrothermal altered sedimentary and volcanic rocks (Rytuba, 2003). Mercury exploitation as by-product has interested also other mineral deposits with sufficient [Hg] such as several types of gold-silver and massive sulfide deposits (Rytuba, 2003).

1.2.2. State-of-the-art on ferrate studies for mercury removal

Today, thanks to the global concern drawn over mercury toxicity and environmental pollution, several paths of action have been taken and have still to be adopted fully to contrast, contain and coexists with this ubiquitous threat. Some of these strategies include: reducing and limiting the direct use of mercury and its compounds while researching alternative technologies; replacing the fossil fuels in favor of renewable energy sources; monitoring the mercury diffusion in and into the environment to regulate human activities and avoid its invasion of the food chains; contrasting its mobilization and the methylation process. Developing new advanced strategies based on high capacity, fast, sensitive, low price and easy to produce mercury removers is an integral part of those processes, having an important role in reducing Hg contents in waste-products and industrial emissions, direct environmental removal or limiting its mobilization. The most studied removal methods based on different removal mechanisms are: precipitation through chemical complexation (e.g. usage of sulfide, lignin derivatives, hybrids nanomaterials); adsorption (e.g. activated carbon, zeolites, clays, metal and non-metal oxides, metal-organic frameworks such as resin with nanocomposites and nanoparticles); membrane separation (polymer networks, engineered filter membranes); biological treatment, that is the passive adsorbing or matching metal ions with biomass (e.g. bacteria, yeasts, molds, seaweeds); ion exchange (e.g. chelating resins, nanocrystals) ((Babel & Kurniawan, 2003; Hua et al., 2019; J. G. Yu et al., 2016) and references therein) (Tab. 1.7).

Methods	Advantages	Defects	Mechanism
Precipitation	Process simple, low cost	Secondary pollution, Sludge treatment, poor selectivity	Chemical reaction
Adsorption	Operation simple, Cost-effective, low second pollution, high adsorption rate	Contaminant sensitivity fouling and plugging, spent media disposal	Chemical or physical adsorption
Membrane separation	High separation selectivity and efficiency, small space requirement	Membrane clogged/fouling, decay faster, high energy consumption	Selective permeability of the membrane
Biological treatment	Low cost, continuous operation, simple process, high selectivity, environmental friendly	Technical complexity, pre-treatment requirements, time-consuming	Transformation, degradation and adsorption
Ion exchange	Low time consumption and technical uses, simple process	High capital cost	Reversible chemical reaction

Table 1.7: synthetic summary of the main advantages, disadvantages and mechanisms of the principal Hg removal methods. From (Hua et al., 2019), (Zeng et al., 2020).

From a deep literature search, there are only two published studies which delve into Hg removal in water using ferrate(VI) compounds and both of them are not-flawless without proper indications of the removal mechanism involved (Bartzatt et al., 1992; Murmann & Robinson, 1974). In 1974, Murmann and Robinson studied the reduction of metal ion contents in river, tap and deep well waters spiked with solutions of the relative metal ion (Pb(II), Cu(II), Zn(II), Fe(II), Fe(III), Hg(II), Cd(II), Mn(II), Cr(III) and Cr(VI)) using most-likely K_2FeO_4 (Murmann & Robinson, 1974). Unfortunately, while "K_2FeO_4" is the kind of ferrate(VI) salt reported along the majority of the study, "Na_2FeO_4" is mentioned as the added Fe(VI) reagent both in the abstract and in part of the experimental section. Moreover, some inconsistencies are present, such as: the Zn(II) reported as "slightly affected by the treatment" while in the relative table almost a 94 % removal is shown; Mn(II) is not mentioned in the abstract while being tested; in the experimental section the procedure isn't quite clear (e.g. the addition moment of ferrate(VI) is not specified, the metal ions reagents used to spike the natural waters are not indicated). Concerning the Hg(II), the addition of 50 and 100 ppm of FeO_4^{2-} to Missouri river water enriched up to 0.37 ppm Hg(II) in solution at pH = 7.6 (assuming the final pH didn't change) produces about 94 % mercury removal, which is consistent with the results of this study. In 1992, Bartzatt et al. realized a similar experiment, using K_2FeO_4 to test the removal of a variety of metal cations (Ag(I), Cd(II), Al(III), Cu(II), Ce(III), Sn(II), Pb(II), Ba(II), Co(II), Mg(II), Mn(II), Hg(II), Tl(III), Ca(II), K(I)) and anions (SO_3^{2-}, SO_4^{2-}, SiO_2^{2-}, Cl^-, CrO_4^{2-}, SeO_3^{2-}, MoO_4^{2-}, PO_4^{3-}) from test solutions made using distilled water (Bartzatt et al., 1992). This study presents multiple inconsistencies which compromise the significance of its results. The most important is the lack of the [metal ions] values after the ferrate(VI) treatment; "30-50 % of substances was removed with the reported quantities of potassium ferrate" and "In the cases where initial metal cations were diluted (ppm), potassium ferrate quantitatively removed them from solution (to less than ppb)" are the only poorly-accurate information to the supposed K_2FeO_4 efficacy. Moreover, no mention on the analytic method used to determine the starting and the final amounts of cations/anions is made.

More in-depth Hg-ferrate studies are published when we move to alternative technologies for removing Hg(0) from coal-derived flue gas. In 2014, Zhao et al. published the first report on the application of ferrate(VI) as oxidant for the removal of SO_2, NO and Hg(0) from a coal burning simulated flue gas (Zhao et al., 2014). The three gases mixture was introduced with a

1 L/min flow in a bubbling reactor containing a K_2FeO_4 solution, stabilized and pH controlled by NaOH addition. The removal efficiency was studied as a function of ferrate concentration, pH and T (K) and the optimal conditions of [ferrate(VI)] = 0.25 mmol/L, pH = 8 and T = 320 K allow for a 100 %, 64.8 % and 81.4% of SO_2, NO and Hg(0) simultaneous removal respectively by oxidation and coagulation (Fig. 1.27). These conditions represent the best balance between stability of Fe(VI) in higher pH values but reduction in redox potential (Fig. 1.27b) and improved diffusion and absorption of NO and Hg(0) in ferrate(VI) with increasing T up to 320 and 313 K respectively but also increasing desorption for higher T, together with increasing Fe(VI) decomposition (Fig. 1.27c). Accounting for ferrate speciation over pH, the standard electrode potentials of Fe(VI) compared with SO_2, NO and Hg(0) ones and the analysis results of the reaction products, the following oxidation reactions were proposed (eq. 11-17):

$$HFeO_4^- \leftrightarrow FeO_4^{2-} + H^+, \ pK_a = 7.3 \quad (11)$$

$$SO_2 + 3FeO_4^{2-} + 5H_2O \leftrightarrow SO_4^{2-} + 3Fe(OH)_3 + OH^- + 5/2\, O_2 \quad (12)$$
$$SO_2 + 3HFeO_4^- + 7/2\, H_2O \leftrightarrow SO_4^{2-} + 3Fe(OH)_3 + OH^- + 7/4\, O_2 \quad (13)$$

$$NO + 3FeO_4^{2-} + 4H_2O \rightarrow 3Fe(OH)_3 + NO_3^- + 2OH^- + 3/2\, O_2 \quad (14)$$
$$NO + 2HFeO_4^- + 3H_2O \rightarrow 2Fe(OH)_3 + NO_3^- + 2OH^- + 1/2\, O_2 \quad (15)$$

$$Hg^0 + 2FeO_4^{2-} + 4H_2O \leftrightarrow Hg^{2+} + 2Fe(OH)_3 + 2OH^- + 2O_2 \quad (16)$$
$$Hg^0 + 2HFeO_4^- + 5H_2O \leftrightarrow Hg^{2+} + 2Fe(OH)_3 + 6OH^- + 1/2\, O_2 \quad (17)$$

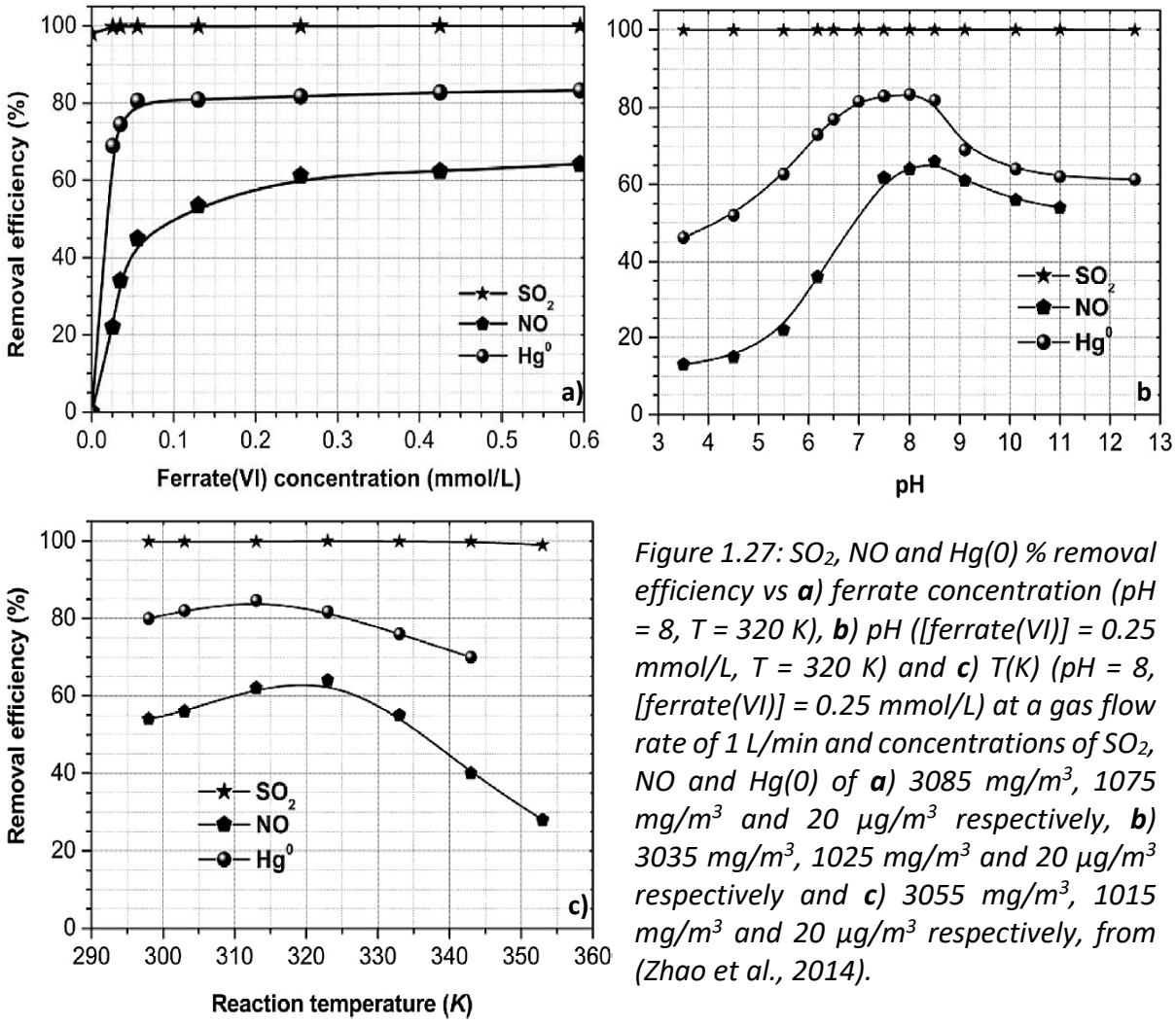

*Figure 1.27: SO_2, NO and Hg(0) % removal efficiency vs **a**) ferrate concentration (pH = 8, T = 320 K), **b**) pH ([ferrate(VI)] = 0.25 mmol/L, T = 320 K) and **c**) T(K) (pH = 8, [ferrate(VI)] = 0.25 mmol/L) at a gas flow rate of 1 L/min and concentrations of SO_2, NO and Hg(0) of **a**) 3085 mg/m^3, 1075 mg/m^3 and 20 µg/m^3 respectively, **b**) 3035 mg/m^3, 1025 mg/m^3 and 20 µg/m^3 respectively and **c**) 3055 mg/m^3, 1015 mg/m^3 and 20 µg/m^3 respectively, from (Zhao et al., 2014).*

In 2015, Han et al. explored deeply the vapor-phase Hg(0) removal by K_2FeO_4 solution in various conditions, with particular attention to species analysis and thermodynamic calculations (Han et al., 2015). Through the data from multiple experimental tests and statistical analysis validations, a Response Surface Methodology Model was also developed which can serve as a prediction tool for Hg(0) removal efficiency by Fe(VI). As with the Zhao et al. study, high removals were achieved for optimal values of pH, T° and [ferrate(VI)] which synergistically affect the Fe(VI) performance and the Hg(0) diffusion and binding power; through Multiple Linear Regression (MLR) technique and ANOVA analysis the synergistic effects were represented in a 3D surface graph and a 2D contour plot which bounds the optimum conditions for maximum Hg(0) removal (Fig. 1.28). Thanks to the speciation data available of Fe(VI) and Hg in aqueous solution, in moderately alkaline conditions the overall reaction between Fe(VI)-Hg(0) is expressed by eq. (18):

$$2FeO_4^{2-} + 3Hg^0 + 5H_2O \rightarrow 2Fe(OH)_3 + 3HgO + 4OH^- \quad (18)$$

Thus, the resulting Gibbs free energy change of - 120.03 kJ/mol reveals the spontaneity of the reaction and the direct dependance from [FeO_4^{2-}].

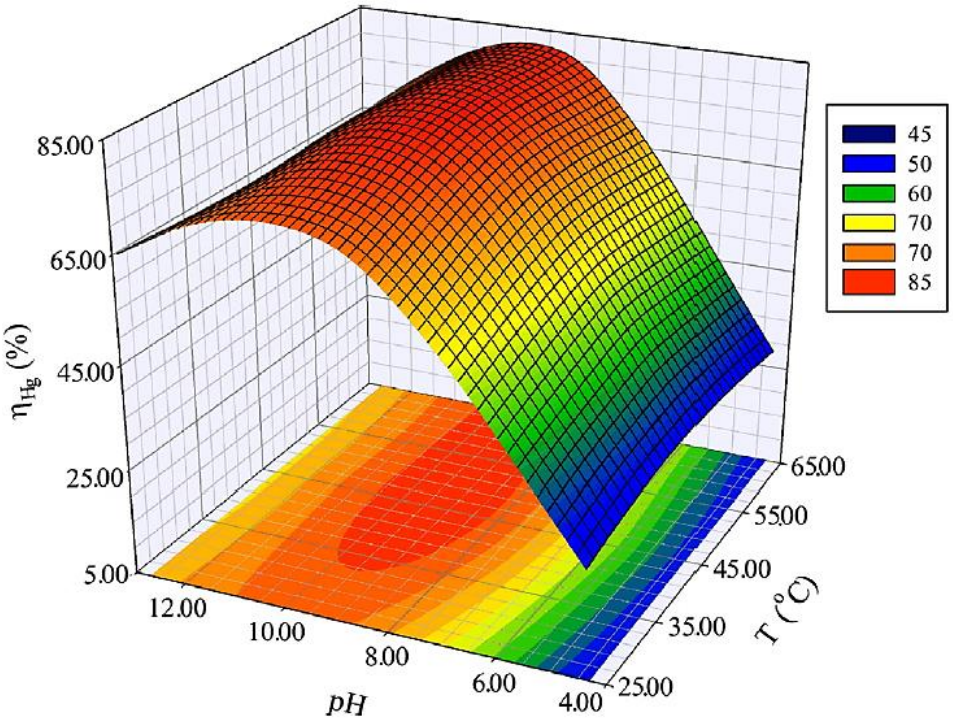

Figure 1.28: 3D surface and 2D contour plot of the interaction effects between initial pH and reaction T° on the % efficiency removal of Hg(0) (initial [Hg(0)] = 20 µg/m^3, initial [Fe(VI)] = 0.35 mM, flow gas rate = 1 L/min) (Han et al., 2015).

Another strategy for ferrate(VI) employment in Hg(0) removal from flue gas was tested by Zhou in 2017, who used K_2FeO_4 as a modification reagent to "upgrade" bio-chars, the pyrolysis products of renewable biomass, regarded as a more economical alternative to Activated Carbon (AC) (Zhou et al., 2017). The impregnation by ferrate(VI) solution greatly improves the pore structure of the bio-char from wheat straw with new active sites generated on its surface, resulting in a superior capacity for Hg(0) removal in comparison to raw char. Moreover, Hg(0) may be firstly oxidized to Hg^{2+} by FeO_4^{2-}, which is often more readily adsorbed in comparison with Hg(0) in flue gases.

1.3. The Monte Amiata area and its exploitation: overview

The southern Tuscany enrolls the oldest magmatic activity of the Italian peninsula such as the volcanism of the Tuscany Magmatic Province (TMP) (Cadoux & Pinti, 2009). The TMP is characterized by abundant silicic volcanisms (silicic rocks defined as SiO_2 > 65 wt%), comprising of a large number of intrusive and extrusive bodies having peraluminous character (Alumina Saturation Index > 1) and moderate variations of major and trace elements at a given silica level (Peccerillo, 2005). The mafic magmatism (mafic rocks defined as MgO > 3 wt%) is mostly limited to small monogenetic intrusive and effusive bodies, ranging from calc-alkaline and shoshonitic to potassic and ultrapotassic (Peccerillo, 2005). The Tuscan ultrapotassic rocks are slightly undersaturated to oversaturated in silica, in contrast with the ultrapotassic rocks from the Roman Province, which are strongly undersaturated (Peccerillo, 2005). The TMP silicic magmatism occurs as: occasional outcrops of lava flows and domes at San Vincenzo, Roccastrada, Mt. Amiata, Mts. Cimini and Tolfa-Manziana-Cerite complex; ignimbrites only occurring at Mts. Cimini and Tolfa-Manziana-Cerite complex; plutons in Mt. Capanne in Elba island, Montecristo and Giglio islands and at Campiglia, Gavorrano, Monteverdi and Roccastrada (Fig. 1.29) (Cadoux & Pinti, 2009; Peccerillo, 2005). Mafic rocks occur as: high-silica lamproitic hypabyssal and volcanic rocks at Sisco (in Corsica, as the 14 Ma old mafic ultrapotassic dyke of Sisco is traditionally included into the TMP), Montecatini Val di Cecina, Orciatico, Torre Alfina and Campiglia; calc-alkaline, shoshonitic and potassic volcanics at Capraia island, Radicofani and among the latest eruped products of the prevailingly silicic volcanoes of Mts Cimini and Mt. Amiata; enclaves in several acid intrusive and extrusive rocks (Peccerillo, 2005).

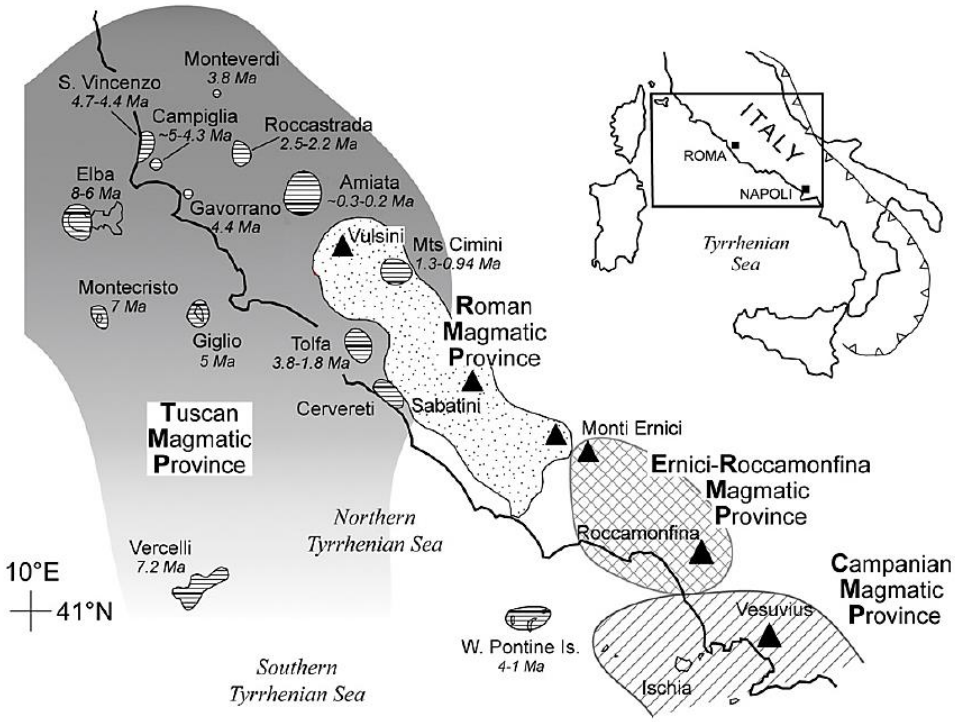

Figure 1.29: main silicic volcanic centers outcropping in the Northern–Central Italy. The fields of the Tuscan (TMP), Roman (RMP), Ernici-Roccamonfina and Campanian Magmatic Provinces are delimited. The radiometric age ranges of the silicic centers are also reported, From (Cadoux & Pinti, 2009), modified.

Mt. Amiata is a 1738 m-high late Pleistocene volcano built over a horst, which is delimitated at East by the Siena–Radicofani structural depression and is located 40 km Nord-West of Vulsini volcanoes (Ferrari et al., 1996). The volcanic complex covers an area of ~ 90 Km^2 dominated by trachydacitic lava flows and domes, with a few late-erupted shoshonites and latites (Peccerillo, 2005). The volcanic activity developed in three main phases, in relation with a magma body emplaced at 6–7 km depth: the Basal Trachydacitic Complex (BTC), the trachydacitic to trachytic and latitic Dome and massive Lava flows Complex (DLC) and the Olivine Latitic final Lavas (OLF) (Gianelli et al., 1988; Laurenzi et al., 2015). Mt. Amiata is traditionally considered part of the TMP due to its leucite-free potassic rocks but it can be considered belonging neither to TMP nor to the RMP because of the outpouring period of its products well within the RMP epoch (between about 300 and 230 ky, from ^{40}Ar-^{39}Ar dating on sanidine crystals and groundmasses) and the transitional mineralogical, chemical and isotopic characteristics (Laurenzi et al., 2015). Mt. Amiata area presents the following units (from bottom to top): Tuscan Units of the Tuscan Nappe (Late Triassic – early Miocene), Ligurian and

Subligurian Units (Jurassic – Oligocene), continental sedimentary successions (Miocene), marine sediments (Pliocene), volcanic and volcano-sedimentay successions (upper Pliocene – upper Pleistocene) and continental deposits, debris and alluvional deposits (Quaternary) (Fig. 1.30a) (Nannoni et al., 2022; Rimondi et al., 2015). Many deposits, at the local scale, show a geological control associated with the Apenninic Mts. chain structures, although the tectonic evolution of the region is still debated (Cretaceous to Quaternary compression vs Middle Miocene-Quaternary extension, (Laurenzi et al., 2015) and references therein). The hydrography of the area, controlled by Apennine tectonic features as the Siena-Radicofani graben, shows a drainage network radially developed around the mountain (Fig. 1.30b); the average annual precipitation of 1480 mm (reference period: 1925-2000) is for the two-thirds concentrated in the autumn-winter season (Nannoni et al., 2022).

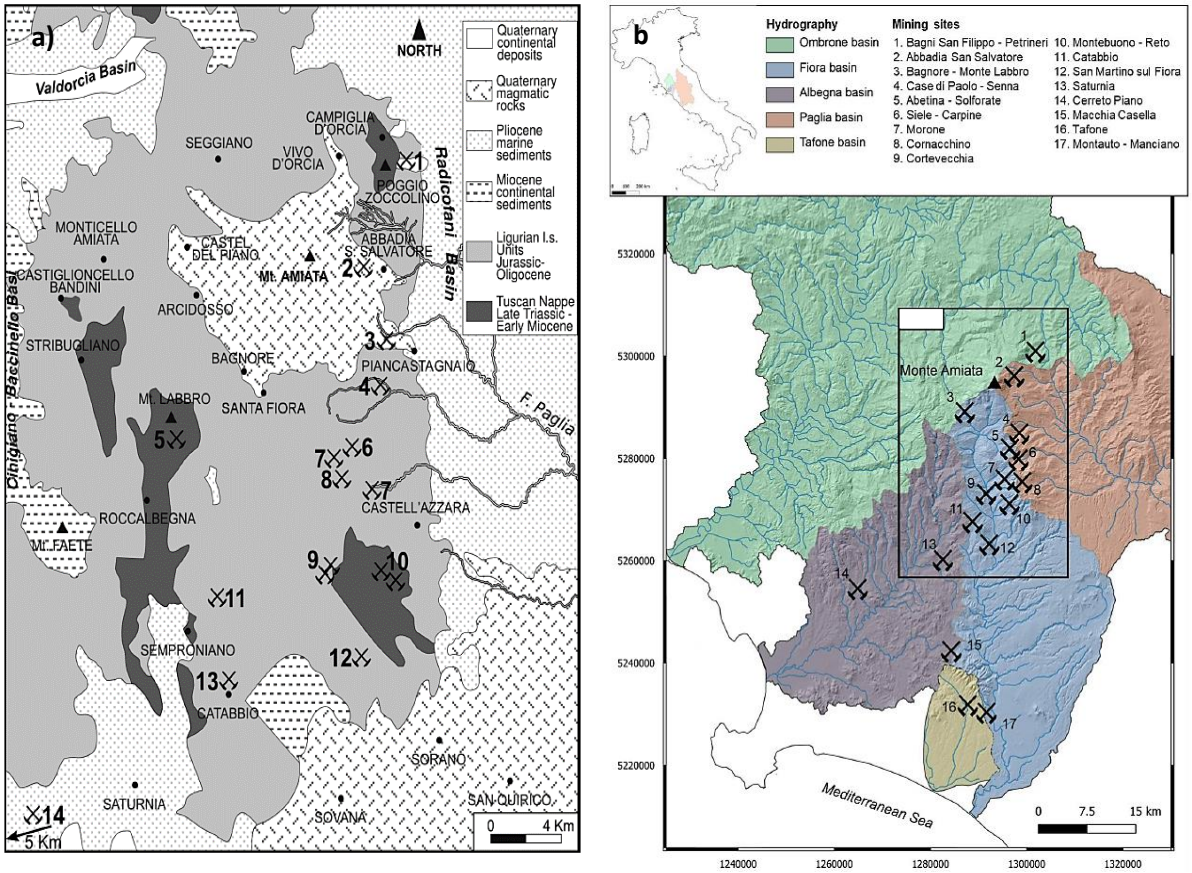

*Figure 1.30: **a**) geological map of the Mt. Amiata area, with location of the main exploited Hg mines and the Paglia river basin. The numbers indicate the following Hg mines: 1) Pietrineri; 2) Abbadia San Salvatore; 3) Cerro del Tasca and Cipriana; 4) Senna; 5) Bagnore and Monte Labbro; 6) Abetina; 7) Siele and Solforate Rosselli; 8) Solforate Schwarzenberg; 9) Morone; 10) Cornacchino; 11) Cortevecchia; 12) Montebuono; 13) Catabbio, and 14) Cerreto Piano. From (Rimondi et al., 2015). **b**) Principal hydrographic catchments of southern Tuscany/central Italy and main Hg mining sites. The box highlights the Mount Amiata Mining District (MAMD). From (Nannoni et al., 2022).*

The Mount Amiata Mining District (MAMD), part of the Hg bearing mineralization in Tuscany, is located in the southern Tuscany in close association with the homonymous magmatic centre (Fig. 1.30b). MAMD was the third largest mercury producer worldwide, with a cumulative production of 100000 tons spanning between 1870 and 1982, when all the activities ceased (Tab. 1.7) (Nannoni et al., 2022). This mining district appears almost unrelated to other ore deposits of the Tuscan metallogenic province, whereas presents a logical affinity with the supra-regional Mediterranean Hg belt (which hosts 65% of the world's cinnabar deposits) (Fig. 17d) that includes the supergiant Almadén (Spain) and the second largest Idrija (Slovenia) (Rimondi et al., 2012, 2015). In the MAMD there were up to 42 mining sites including Cerreto Piano (the number 14 in Fig. 1.30), which is traditionally considered part of the district due to its mineralization style similarities and historical ground (Rimondi et al., 2015). While the main sites are reported in Fig. 1.30b, Abbadia San Salvatore mine (ASSM) was by far the most productive, accounting for ~50 % of the MAMD total production and being one of the most important smelting centers of the district, together with Siele (the number 6 in Fig. 1.30b) (Nannoni et al., 2022; Vaselli et al., 2015). Ore bodies are usually confined in hosts with comparable permeability such as limestones, sandstones and marls, by overlying less-permeable formations; few examples are in volcanic rocks without impermeable formation caps (Fig. 1.30a) (Rimondi et al., 2015). The mineralization is constituted by: cinnabar (α-HgS) as the only ore mineral, with metacinnabar (β-HgS) and elemental Hg (Hg(0)) being rare and montroydite (HgO) reported at Morone (the number 7 in Fig. 1.30b); pyrite and/or marcasite (FeS_2) ubiquitous, locally abundant; realgar and orpiment (As_4S_4 and As_2S_3) diffuse; stibnite (Sb_2S_3) sparse; chalcopyrite and nickel sulfides ($CuFeS_2$ and NiS, NiS_2) localized (Rimondi et al., 2015). The typical gangue is constituted by calcite with scarce quartz (Rimondi et al., 2015). At a local scale, MAMD presents analogies with the hot-spring and silica-carbonate type deposits, in particular with the Western US ones such as the close relation between Hg deposits and hydrothermal activity (e.g. proximity of some of the mines to geothermal phenomena and recent to present-day cinnabar deposition from gas emissions) and the mineralization often occurring along structures of the recent post-orogenic extensional tectonics at the interface between two rock formations with marked different permeability (Rimondi et al., 2015). However, there are some marked differences in the hosting rocks and diffuse alteration. In the MAMD deposits, silica is comparatively rare since hot springs in the area have been deposited prevalently travertine, while in the Western US ones, amorphous

and opaline silica is a common gangue together with the widespread acid sulphate alteration which, except for minor gypsum, isn't common at Mt. Amiata (Rimondi et al., 2015). However, since a proper model for the origin of MAMD is not established, many unknown details are still present and, in particular, the level of knowledge is insufficient for a definitive hypothesis on the original mercury source (Nannoni et al., 2022; Rimondi et al., 2015). The two main hypotheses include:

1) a pre-eruption stage of magma degassing throughout basement fractures before the BTC effusive emplacement, as proposed by Cadoux and Pinti (Cadoux & Pinti, 2009). This could provoke Hg segregation and enrichment in the magmatic fluids and would explain the Hg contents of magmatic rocks, considered too low for these to be a viable source (Rimondi et al., 2015);
2) the interaction of hydrothermal cells with the siliciclastic formations of the Tuscan Paleozoic basement, as black shales are typically identified as involved into the formation of large Hg deposits and Paleozoic schists in Alpi Apuane host Hg deposits (Rimondi et al., 2015). Even if some evidence from drilling in Mt. Amiata geothermal field have revealed the presence of graphitic phyllites able to host Hg, no clear evidence that these rocks were a source of Hg has been provided (Rimondi et al., 2015).

About 40 years after the MAMD exploitation ceased, the environmental heritage of such a world-class district can be mainly identified in the contamination of waters interacting with dumps of the mining and smelting activity (e.g. circulating through mine tunnel systems) and of the surrounding sediments (Meloni et al., 2021; Pattelli et al., 2014; Rimondi et al., 2012, 2015; Vaselli et al., 2015, 2021). The regional impact of such contamination occurs at multiple levels. On the one hand, it clearly afflicts the local surroundings, e.g. enriching Hg contents well above the national limit for drinkable water (1 μg/L) (Vaselli et al., 2015). On the other hand, the Hg anomaly is transferred downstream in the main regional river, the Paglia River, and from it to the Tiber River (Fig. 1.31), which may be considered as one of the main contributor to the total Hg budget of the Mediterranean Sea, considering the total estimation of 20000 tons of Hg dispersed in the environment by the MAMD mining/smelting activities (Nannoni et al., 2022; Pattelli et al., 2014; Rimondi et al., 2015).

Figure 1.31: hydrological relationships between mining sites and the main regional tributary of the Tiber River, where the Hg anomaly is transferred. Only the Hg mines belonging to the Paglia basin are shown. From (Rimondi et al., 2015).

In this macroregional context, a prevailing role of the sediments, which ultimately determine the mobility rate of Hg, has been ascertained. Stream sediments (as well as soils and rocks) in the Mt. Amiata region contained elevated [Hg]; furthering away from MAMD, in Paglia and Tiber Rivers stream sediments, the [Hg] was found to decrease in a range between 0.21 to 14 µg/g (Tab. 1.8); the Hg probable effect concentration (PEC) in sediments ("concentration above which harmful effects are likely to be observed in sediment-dwelling organisms") is 1.06 µg/g, the Italian limit for residential and industrial soils are 1 and 5 µg/g respectively. Samples collected from a tributary not interested by the MAMD runoff showed low [Hg] (20-90 ng/g) (Tab. 1.8). Regarding the Tiber River sediments, a marked increase in [Hg] was found downstream from the Paglia confluence, while downstream from the Alviano Lake damn it was lower, pointing to the sediment sink effect of the lake (Fig. 1.32). The correlation between Hg and methyl-Hg founded in the MAMD stream sediments wasn't found in the Tiber River (Fig. 1.32), thus indicating different methylation mechanisms (Rimondi et al., 2015). Regarding the fishes, the freshwater fish muscle samples revealed [methyl-Hg] higher than the EPA guidelines, pointing to active methylation in the systems since the fish population sampled is the herbivorous, bottom-feeder one, which contains lower Hg contents than the carnivorous predatory species (Tab. 1.8) (Rimondi et al., 2015).

Location	*Unfiltered water*		*Sediment, calcine, or soil*		*Fish (muscle)*
	Hg (ng/L)	*methyl-Hg (ng/L)*	*Hg (µg/g)*	*methyl-Hg (ng/g)*	*Hg (µg/g, wet weight)*
Paglia River basin					
Downstream from mines	3.8-1400	0.10-3.0	0.26-14	0.20-6.4	0.16-1.2
Mine-waste calcine	–		25-1500	0.34-26	–
Soil	–		0.64-400	7.9-45	–
Lakes	55-290	0.67-0.77	11-15	4.7-8.7	0.49
Overbank sediment			2-905		
Tiber River basin					
Downstream from mines	2.9-19	0.061-0.53	0.21-1.7	0.15-0.52	0.052-0.44
Upstream from mines	2.6-2.9	<0.02-0.16	0.02-0.092	0.12-0.28	
Comparative guidelines					
Italian industrial soil limit			5		
Italian residential soil limit			1		
Italian drinking water standard	1000				
International drinking water standard	6000				
Probable effect concentration sediment			1.06		
USEPA, residential soil limit			2.3	780	
USEPA, industrial soil limit			31	10,000	
USEPA, drinking water standard	2000				
USEPA, acute aquatic life water standard	2400				
USEPA, chronic aquatic life water standard	770				
USEPA, methyl-Hg standard fish muscle					0.3

Table 1.8: Hg and methyl-Hg contents in mine wastes, and sediments and waters from the Paglia and Tiber River basins. From (Rimondi et al., 2015), references therein.

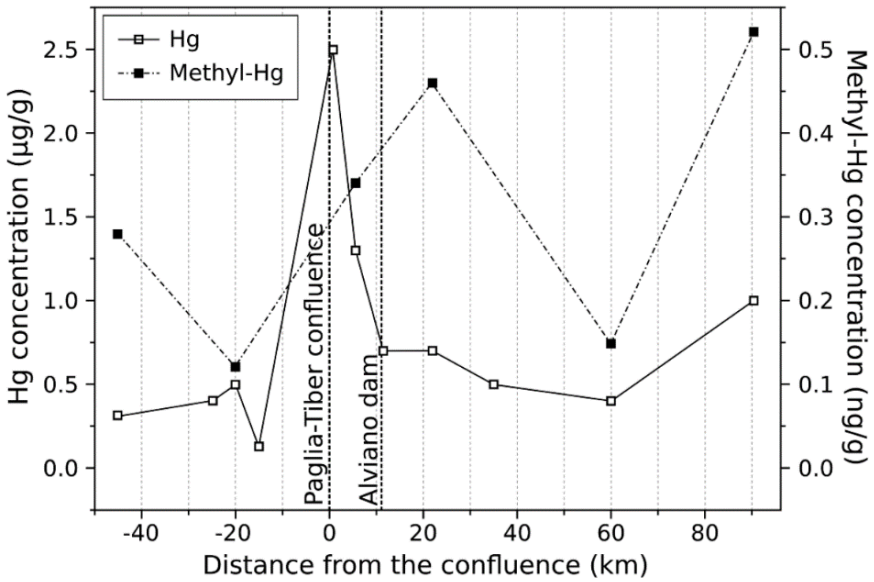

Figure 1.32: Hg and methyl-Hg concentrations along the Tiber River in stream sediments sampled in 2012. Negative numbers indicate the distance from the Paglia-Tiber confluence moving toward the river headwaters (generally northward) while positive numbers indicate the distance from the confluence to the mouth of the river (generally southward). From (Rimondi et al., 2015).

A criticality concerning the extreme meteorological events (e.g. floods) has been pointed out by Pattelli et al., who studied the effects of the extreme flood event of November 2012 (328 mm of precipitation in 48h at Piancastagnaio) on the mobilization of Hg in the Paglia River

basin (Pattelli et al., 2014). According to these authors, the sediments, where Hg is "stored", could be easily mobilized during flood events, determining a physical transfer downstream. Bank erosion and remobilization lead to an increase of Hg contents in stream sediments up to an order of magnitude after the flood (March-May 2013), showing the re-mobilization effect of this kind of events rather then a possible dilution. The study confirmed the sediment-sink function of the Alviano dams which limited the Hg transfer downstream; however, accounting for climate change and the increasing occurrence of this extreme events, such dams could have a consistent barrier as well as an extraordinary source of pollution.

1.3.1. The situation in Abbadia San Salvatore

The two largest deposits of MAMD, where the ore had Hg contents between 0.6 and 2 wt%, where discovered at ASS between 1897 and 1909 and exploited up to 400 m depth (Meloni et al., 2021). The ASSM is located on the eastern flank of Mt. Amiata and, with its 65 ha, accounted for ~ 50 % of the MAMD total production, hosting a complete facility for mercury processing deeply integrated into the urban center (Fig. 1.33, 1.35b) (Meloni et al., 2021). The mining activity started in 1850 while the Cermak-Spirek shaft roasting furnaces were firstly ignited in 1899; as the request of mercury increased, new Cermak tower furnaces (later dismantled) and then rotary horizontal Gould and vertical Nesa ones were installed, along with new dryers, condensers and conveyor systems (Vaselli et al., 2019). The exploitation was managed by private companies and the closure was carried out in 1982 by E.N.I. (National Agency for Hydrocarbons, AGIP Division) (Vaselli et al., 2019). In 2008 the Municipality of ASS signed an agreement with the former owner of the mining concession becoming the responsible of the reclamation of the mining area (Vaselli et al., 2019). The mining complex hosted complex and impactful operations, which legacy still affect the air, water and soils surrounding the area (e.g. the ASSM tunnels, entirely underground, were sealed and refilled with the mine waste) (Vaselli et al., 2019). The entire ASSM area was divided into 7 sectors on the basis of the heterogeneous distribution of Hg and the reclamation activities to be performed; each of the sector presents different criticalities on top of the mercury contamination (e.g. presence of asbestos, Polychlorinated Biphenyls (PCB)) (Fig. 1.33) (Vaselli et al., 2019). The reclamation, still ongoing, has currently seen many interventions, with the aim of mitigating, remediating and converting more and more area to the open-air mining-

park museum. Some of the achieved results are: the reclamation, with physical barrier and waterproof covering, of a small portion (ca. 4500 m²) of the mining area dedicated afterwards to playgrounds (Fig. 1.35b); the construction of a channel passing through the mining area, which conveys the surface waters in order to decrease the interaction between Hg-contaminated terrains and meteoric waters (Fig. 1.35); the removal of the mechanical workshop roof, containing asbestos, and installation of photovoltaic solar panels in its place; the removal of different materials (e.g. furniture, cinnabar-bearing rocks) and cleaning of many buildings (e.g. workshops, headquarters); the improvement of the environmental impact knowledge through studies and monitoring of the area (Nannoni et al., 2022; Vaselli et al., 2019). The intervention currently undergoing/planned are aimed at: cleaning-up the metallurgic facilities and their rehabilitation; reclamation of the most contaminated material, such as terrains and waste piles distributed to throughout the area and its delivery on a designed landfill; ground sealing through impermeabilization of the contaminated soils to contrast the percolation of meteoric water to the water table; realization of an hydraulic barrier and a water treatment plant to improve the quality of underground waters, studying the Hg removal efficiency of different technology through a small-scale pilot implant (Nannoni et al., 2022; Vaselli et al., 2019)

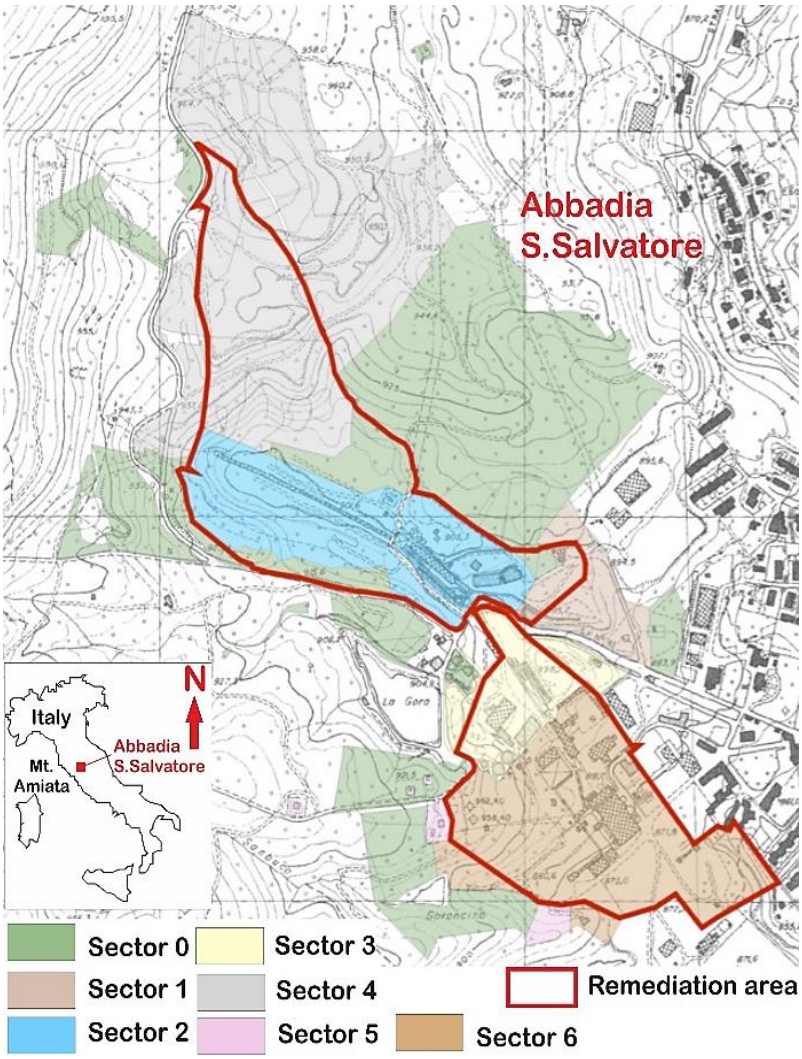

Figure 1.33: division into 7 sectors of the ASSM area. Sector 0 = large areas dominated by local vegetation. Low [Hg], no remediation activities expected; sector 1 = easternmost entrances of the mining site, low [Hg]; sector 2 = host buildings for miners and management executives + grinding area + conveyors and Garibaldi well; sector 3 = electrical cabin, mechanical workshops and old furnaces, dryers and condenser buildings; sector 4 = "Le Lame" dump site; sector 5 = armory and guardians house; sector 6 = close to ASS urban center, hosts Gould and Nesa furnaces, new dryers, condensers and the main mining material storage area. Most contaminated area. Scale 1:15000. From (Meloni et al., 2021).

Cinnabar was the main mineral ore while metacinnabar was also found during the drilling of the new piezometers (Vaselli et al., 2015). The ore bodies are located in Eocene marls and marly limestones ("Sopranummulitico"), Eocene calcarenites ("Bancone Nummulitico") and in altered Quaternary volcanic rocks (Fig. 1.34). As in the majority of MAMD sites, the gangue of such process consists mostly of calcite, quartz and rare celestite, gypsum, native sulphur and hydrocarbons (Rimondi et al., 2015). Mercury in its liquid elemental form was obtained

through roasting of the dried, crushed and sorted ore inside the retort and rotary furnaces at 600-700° under oxygen. The cinnabar reacted with O_2 at high T° following the eq. (19):

$$HgS + O_2 \rightarrow Hg^0 + SO_2 \quad (19)$$

Sulfur dioxide was then removed by water washing, the mercury vapors were condensed by cooling systems and then bottled, while the roasted waste material (calcine) stored into nearby buildings before being dumped (Meloni et al., 2021). It is estimated that more than 10 % of the total production was released into the environment during cinnabar roasting (Vaselli et al., 2015).

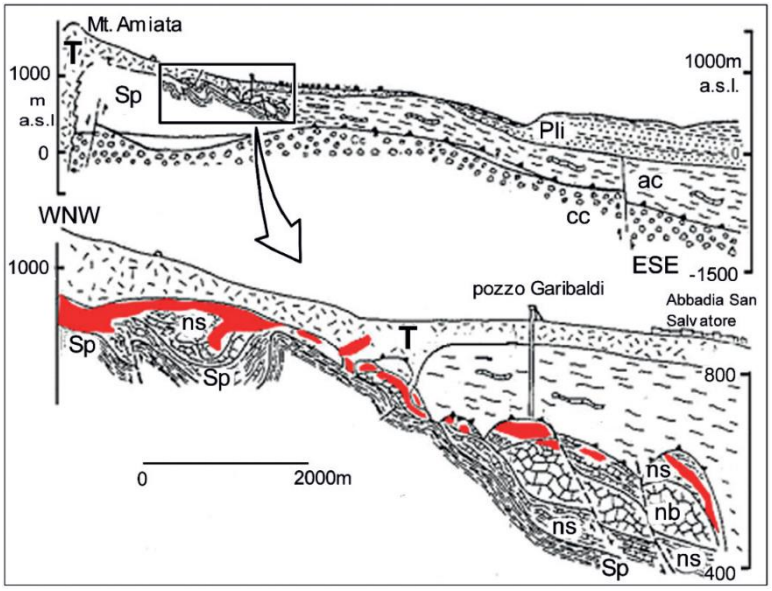

Figure 1.34: schematic cross section of ASSM Hg deposits geological locations (in red); cc = "Calcare Cavernoso" (carbonate/dolomitic unit with vacuolar structure), Sp = "Scisti Policromi" (clay shales of various colors), ns = "Sottonummulitico" and "Sopranummulitico" (marls and marly limestone), nb = "Bancone Nummulitico" (massive calcarenite), ac = Cretaceous Flysch (Ligurian Units), Pli = Pliocene sandstones, T = Quaternary volcanic rocks. From (Rimondi et al., 2015) modified.

From mid-1950, the calcine materials were mostly accumulate in a 120000 m² area few kms north of ASS called "Le Lame" (Meloni et al., 2021). Rimondi et al. determined Hg concentrations in a wide range between 25 and 1500 µg/g in calcine samples collected from waste piles adjacent the ASS town while Meloni et al. found a similar range of 4 to 1910 µg/g in top-soil samples from Le Lame (Italian limit for residential and industrial use = 1 and 5 µg/g) (Meloni et al., 2021; Rimondi et al., 2012). The broad distribution of values is due to the use

of older and less efficient Cermak-Spirek furnaces, later substituted by the more recent and efficient Gould and Nesa ones (Meloni et al., 2021). Elemental mercury concentrations > 50000 ng/m^3 in air were measured out- and indoor the air-shafts of Spirek and Cermak-Spirek furnaces while the stream and lake sediments in the surrounding area achieved contents up to 1900 µg/g (Rimondi et al., 2012; Vaselli et al., 2015). Surface waters showed concentrations of 1,400 mg/L (Rimondi et al., 2012), although when the mining operations were active the concentrations of Hg in the waste waters reached values up to 180,000 mg/L (Vaselli et al., 2015). High [Hg] were found also in beets, lettuce, rosemary and sage in samples cultivated near the ASSM (Nannoni et al., 2022). Values up to 28.8 mg/kg were found in the Pinus nigra outer bark grown near ASSM, compared to 5-98 ng/kg in the trees from Florence taken as a baseline; mercury concentration decreased exponentially with distance from the mine (Nannoni et al., 2022).

Ground waters were the object of a monitoring campaign, described by Vaselli et al., on the setting of which also this study is ground (Vaselli et al., 2015). In that study, a geochemical mapping of major and minor dissolved species, along with Hg, As and Sb, was realized all over the 65 ha of the ASSM area in 4 different sampling campaigns between February 2013 and January 2014. The sampling sites were located within and nearby the former industrial site; a schematic map of the sampling sites (excluded S110 and S111 piezometers), coupled with an aerial view of the site before the beginning of remediation procedures is shown in the Fig. 1.35. The main results obtained by the 1-year geochemical monitoring are summarized in the Tab. 1.9 to 1.12 and Fig. 1.36. The study, realized about 30 years after mine closure, found really variable geochemical conditions, both spatially and temporally. The geochemical facies spanned from Ca(Mg)-SO_4 to Ca(Mg)-HCO_3 and Na-HCO_3; the presence of Ca(Mg)-SO_4 waters is really interesting, since it suggests the contribution of sulfate hydrolysis processes, corroborating the dumping of waste materials from other MAMDs such as Siele and Morone, where gypsum and anhydrite were present, as opposed to the ASS ore. Regarding As and Sb, their concentrations had values below the maximum allowable concentrations, with very few exception, and narrow variations. Hg contents fell into a large interval, dominated by values above the law limit independently from the sampling period, with only the waters from areas peripherical to the mine having a [Hg] < 1 µg/L (Fig 1.36). In particular, among all sites considered in the study, the S6N piezometer was recognized as one of the most heavily contaminated. The high heterogeneity in geochemical conditions found is likely to be

attributed to the heterogeneous filling material which constituted the terrain where part of the mining structures lie. In fact, during the drilling of new piezometers, were found calcines, cinnabar and metacinnabar, slag, tailings, gypsum and anhydrite fragments, various anthropogenic materials and other exotic products. This implies that the dissolved mercury in the groundwater comes from different contributions.

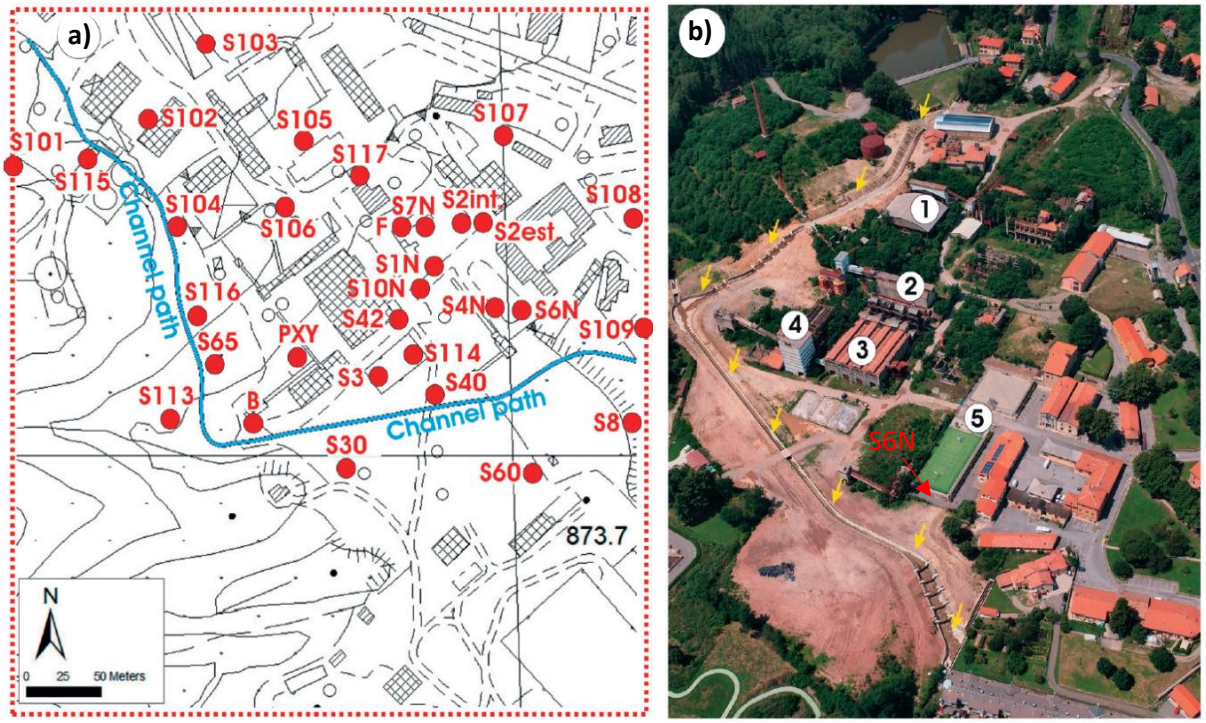

*Figure 1.35: **a**) location of the piezometers ("S-") from where the water samples were collected (red circle) and the artificial channel (blue line), whose construction commenced in March 2013 and terminated at the end of 2013; **b**) aerial photo of the previous ASSM area near ASS urban center (July 2014) from an ultra-light vehicle after the completion of the artificial channel (yellow arrows) with the location of the S6N piezometer (red arrow). The numbers refer to the main mining structures: 1) dryers; 2) Cermak condensers; 3) the building hosting the Spirek and Cermak-Spirek shafts and 4) Nesa furnaces and 5) the sports ground, which was the very first reclamation action undertaken when the site was the sole area of public property. From (Vaselli et al., 2015) modified.*

ID	CX	CY	Water table depth	T	pH	E.C. 20 °C	HCO_3^-	CO_3^{2-}	F^-	Cl^-	NO_3^-	SO_4^{2-}	Ca^{2+}	Mg^{2+}	Na^+	K^+	NH_4^+	TDS	As	Hg	Sb
	Easting	Northing	(m)	(°C)		(µS cm^{-1})	(mg L^{-1})	(mg L^{-1})	(mg L^{-1})	(mg L^{-1})	(mg L^{-1})	(mg L^{-1})	(mg L^{-1})	(mg L^{-1})	(mg L^{-1})	(mg L^{-1})	(mg L^{-1})	(mg L^{-1})	(µg L^{-1})	(µg L^{-1})	(µg L^{-1})
B	1717566	4751026	6.77	12.5	6.32	454	44		0.61	20	6.5	88	26	8	18	13	0.05	225	6.1	6.6	1.0
PXY	1717593	4751065	3.10	10.0	7.43	n.d.	305		0.28	14	31.8	126	86	33	8	71	0.04	676	1.6	1.0	5.9
S1N	1717693	4751137	4.75	12.0	7.38	218	65		0.18	6	1.8	18	15	2	7	10	0.03	124	1.9	4.9	3.3
S2 est.	1717713	4751155	5.09	13.0	4.87	649	1		2.00	25	39.1	234	74	5	30	15	0.09	427	1.9	433.0	0.1
S2 int.	1717703	4751154	6.38	12.0	8.43	703	121	5	0.38	12	3.5	196	83	18	9	16	0.07	464	1.0	28.3	0.2
S4N	1717725	4751096	7.78	11.0	6.91	99	21		0.18	4	1.5	4	4	1	3	5	0.06	43	0.3	1.0	0.3
S6N	1717748	4751093	5.60	12.0	8.97	351	75	4	1.57	8	0.6	46	31	0.1	9	20	0.16	196	11.5	240.0	31.0
S7N	1717674	4751155	2.45	10.0	6.04	499	49		0.89	12	5.9	135	49	10	11	9	0.14	281	1.2	4.7	1.8
S7N	1717674	4751155	2.75	13.0	5.84	625	127		0.40	15	5.7	144	79	8	10	8	0.03	398	3.5	2.1	2.6
S8	1717816	4751018	15.02	10.0	6.09	2370	26		0.41	25	10.3	1005	367	22	21	60	0.04	1537	1.8	1.0	1.1
S10N	1717681	4751119	3.35	12.5	6.03	382	90		0.30	8	5.2	61	48	4	4	5	0.25	226	1.2	3.2	3.4
S30	1717629	4750990	10.06	12.0	6.64	509	87		0.52	10	0.1	89	38	8	12	8	0.04	253	4.9	3.9	0.1
S40	1717682	4751033	8.40	11.0	6.07	1694	155		0.33	13	0.1	633	213	54	16	26	0.16	1111	0.6	1.1	0.2
S42	1717658	4751088	4.00	11.5	6.54	860	79		0.09	12	20.2	280	115	10	10	16	0.05	542	0.6	22.5	0.7
S60	1717751	4750985	15.12	11.0	5.99	535	26		0.26	9	3.9	125	27	12	13	12	0.10	228	1.1	35.5	0.3
S65	1717529	4751057	6.86	11.0	5.87	510	30		0.48	29	1.3	116	35	10	22	5	0.05	248	1.6	4.7	1.0
S101	1717397	4751187	10.32	11.0	6.57	436	96		0.48	12	1.5	42	45	3	6	5	0.36	211	2.4	0.2	0.7
S102	1717491	4751224	7.74	10.5	6.25	644	127		0.58	10	0.1	139	60	14	13	7	0.11	370	2.9	0.2	0.1
S103	1717531	4751282	13.75	11.0	6.13	1358	94		1.10	11	0.9	511	218	25	5	12	0.14	878	9.5	<0.1	1.3
S104	1717507	4751155	10.54	9.5	6.99	545	207		0.28	10	0.1	30	68	6	7	4	0.10	334	1.0	0.2	0.3
S105	1717595	4751211	5.84	10.0	7.38	461	176		0.36	13	1.7	72	75	6	8	4	0.10	356	2.6	0.8	1.4
S106	1717582	4751167	3.75	10.0	6.88	538	152		0.13	13	7.0	118	95	5	6	4	0.04	400	0.6	19.2	0.4
S107	1717732	4751213	6.62	12.5	5.83	921	67		0.64	20	6.8	288	121	8	16	12	0.10	539	1.0	1.7	0.2
S108	1717826	4751152	4.17	13.0	9.94	578	144	14	0.24	12	1.1	59	38	6	32	28	0.05	334	3.4	0.1	0.5
S109	1717839	4751070	7.63	12.0	7.30	460	84		0.33	11	1.5	71	45	4	7	9	0.04	232	1.2	<0.1	2.3
S110	1717947	4751129	7.50	14.0	7.45	437	156		0.20	18	0.2	26	52	4	13	3	0.07	273	2.8	<0.1	1.5
S111	1718079	4750879	4.88	12.0	7.85	387	99		0.85	11	0.1	40	30	9	8	7	0.04	205	2.2	<0.1	2.5
S112	1717781	4751046	11.69	n.d.	6.78	n.d.	136		0.35	11	20.7	1061	447	47	14	25	0.07	1763	n.d.	n.d.	n.d.
S113	1717509	4751022	6.85	12.5	5.82	526	35		0.30	12	10.3	130	42	9	11	9	0.08	259	0.9	17.6	0.3
S115	1717450	4751206	6.57	11.0	7.05	685	256		0.33	12	2.2	60	108	5	6	5	0.02	455	1.4	0.2	0.5
S116	1717525	4751087	6.11	11.5	5.66	528	24		1.70	11	24.7	143	50	9	9	9	1.34	283	0.8	22.4	0.3
S117	1717632	4751189	5.21	11.5	6.96	737	161		0.26	12	6.9	181	112	7	9	8	0.08	499	0.7	1.1	0.8
			Mean value	11.6	6.37	657.1	104		0.53	13.2	6.97	196.0	90.6	11.6	11.7	14.1	0.13	449.1	2.4	31.7	2.1
			Max. value	14.0	9.94	2370.6	305		2.00	28.7	39.05	1061.0	447.2	54.0	32.0	71.0	1.34	1762	11.5	433.0	31.0
			Min. Value	9.5	4.87	99.7	1		0.09	3.6	0.05	4.2	4.0	0.1	3.0	3.0	0.02	43	0.3	0.1	0.1

1.9)

ID	CX	CY	Water table depth	T	pH	E.C. 20 °C	HCO_3^-	CO_3^{2-}	F^-	Cl^-	NO_3^-	SO_4^{2-}	Ca^{2+}	Mg^{2+}	Na^+	K^+	NH_4^+	TDS	As	Hg	Sb
	Easting	Northing	(m)	(°C)		(µS cm^{-1})	(mg L^{-1})	(mg L^{-1})	(mg L^{-1})	(mg L^{-1})	(mg L^{-1})	(mg L^{-1})	(mg L^{-1})	(mg L^{-1})	(mg L^{-1})	(mg L^{-1})	(mg L^{-1})	(mg L^{-1})	(µg L^{-1})	(µg L^{-1})	(µg L^{-1})
B	1717566	4751026	6.95	13.50	6.20	372	39		0.30	12	3.2	91	24	8	11	12	0.24	202	4.9	6.8	0.3
F	1717665	4751153	2.70	15.50	6.51	598	90		0.45	14	6.4	131	66	10	10	8	0.05	337	3.6	4.1	1.3
PXY	1717593	4751065	3.08	10.50	7.07	1213	369		0.51	10	34.8	152	104	40	5	67	0.03	782	1.1	3.7	2.9
S1N	1717693	4751137	4.10	12.50	7.66	419	110		0.42	9	7.4	48	45	3	8	8	0.02	239	1.3	1.5	3.8
S2 est.	1717713	4751155	4.35	13.00	5.69	401	16		1.45	11	19.4	272	96	10	13	13	0.80	452	1.3	126.0	0.6
S2 int.	1717703	4751154	5.62	12.50	8.08	239	41		0.30	3	1.1	30	16	3	3	7	0.90	104	0.3	5.2	0.2
S3	1717643	4751052	5.68	12.00	6.46	1297	126		1.40	18	11.5	441	151	39	14	23	n.d.	826	0.7	3.4	0.8
S4N	1717725	4751096	8.55	12.50	7.33	299	38		0.30	6	1.5	19	10	1	4	12	0.90	93	0.3	<0.1	0.4
S6N	1717748	4751093	6.45	12.50	9.55	299	81	6	1.07	7	2.8	39	26	0.1	9	22	0.12	194	14.9	695.0	31.4
S7N	1717674	4751155	1.73	13.00	5.84	826	44		0.35	15	2.4	270	86	19	13	12	0.07	462	1.9	4.7	0.4
S8	1717816	4751018	15.56	11.50	4.84	2630	6		0.61	15	12.0	1185	469	36	14	32	0.02	1770	5.2	1.1	0.6
S10N	1717681	4751119	3.55	12.50	6.03	634	43		0.49	12	18.4	172	68	10	8	14	0.20	346	2.4	10.0	0.5
S30	1717629	4750990	9.80	13.00	6.60	425	92		0.20	13	0.3	72	37	7	11	8	0.02	240	4.9	2.7	0.2
S40	1717682	4751033	9.30	12.50	6.07	1124	43		0.30	10	0.07	389	85	37	20	21	0.75	607	8.5	0.9	<0.1
S42	1717658	4751088	3.38	11.00	6.89	822	83		0.15	9	20.3	234	104	8	10	15	0.89	484	0.7	23.1	0.6
S60	1717751	4750985	15.15	12.00	6.07	521	21		0.32	6	3.7	134	32	13	13	13	0.08	236	1.1	49.7	0.2
S65	1717529	4751057	6.84	11.50	5.64	344	15		0.30	14	2.1	86	19	9	11	4	0.04	161	1.0	5.1	<0.1
S101	1717397	4751187	7.42	11.00	6.57	411	98		0.43	13	3.5	46	53	4	6	4	0.03	227	2.3	0.1	0.3
S102	1717491	4751224	6.75	10.50	6.07	606	72		2.27	16	0.3	113	39	12	14	7	0.77	276	7.5	0.5	0.3
S103	1717531	4751282	12.8	11.00	6.16	1321	100		2.46	15	1.9	469	195	22	4	10	0.10	819	6.1	<0.1	0.4
S104	1717507	4751155	9.25	10.50	6.88	493	178		0.68	14	0.2	22	66	3	5	3	0.10	292	1.1	0.3	0.3
S105	1717595	4751211	4.20	10.50	7.35	884	187		0.43	10	2.8	169	109	10	10	6	0.08	504	2.6	<0.1	0.9
S106	1717582	4751167	3.55	10.50	6.53	872	135		0.39	14	17.4	156	109	6	6	5	0.01	448	0.4	29.7	0.2
S107	1717732	4751213	4.40	12.50	4.38	1005	4		1.90	12	8.1	385	118	10	15	21	1.31	577	3.3	7.0	0.1
S108	1717826	4751152	3.70	13.00	10.63	260	64	10	0.21	8	0.6	16	18	1	10	16	0.52	143	1.4	0.3	0.3
S109	1717839	4751070	7.66	11.50	6.86	651	128		0.62	16	5.0	155	104	5	8	10	0.03	432	1.3	0.1	2.2
S110	1717947	4751129	7.26	13.00	7.37	472	195		0.31	20	7.0	104	103	5	14	4	0.06	452	1.8	0.4	0.9
S111	1718079	4750879	5.20	12.00	7.79	521	137		0.72	12	0.03	64	49	11	11	7	0.03	292	6.7	0.1	1.1
S113	1717509	4751022	6.83	12.50	5.82	467	23		1.10	13	10.1	113	35	9	10	8	0.70	222	1.3	21.0	0.1
S114	1717660	4751061	5.62	11.50	7.02	1045	288		0.41	26	5.7	159	124	23	12	15	n.d.	654	0.8	8.0	0.3
S115	1717450	4751206	6.22	11.00	6.99	797	256		0.21	14	11.5	80	118	4	5	5	0.01	494	0.9	<0.1	0.3
S116	1717525	4751087	5.83	11.50	5.15	455	8		2.90	9	18.0	130	40	8	9	6	0.91	231	1.0	39.7	0.1
S117	1717632	4751189	4.83	11.00	6.96	760	149		0.33	11	4.6	145	98	6	7	8	0.06	429	0.5	<0.1	0.3
			Mean value	11.97	6.7	712	99		0.74	12.3	7.4	184.6	85.4	11.9	9.7	12.8	0.32	425.0	2.8	37.5	1.7
			Max. value	10.63	10.63	2630	369		2.9	26	34.8	1185	469	40	20	67	1.31	1770	14.9	695.0	31.4
			Min. Value	4.38	4.38	239	4		0.15	3	0.03	16	10	0.1	3	3	0.01	93	0.3	0.1	0.1

1.10)

ID	CX	CY	Water table depth	T	pH	E.C. 20 °C	HCO_3^-	CO_3^{2-}	F^-	Cl^-	NO_3^-	SO_4^{2-}	Ca^{2+}	Mg^{2+}	Na^+	K^+	NH_4^+	TDS	As	Hg	Sb
	Easting	Northing	(m)	(°C)		(µS cm^{-1})	(mg L^{-1})	(mg L^{-1})	(mg L^{-1})	(mg L^{-1})	(mg L^{-1})	(mg L^{-1})	(mg L^{-1})	(mg L^{-1})	(mg L^{-1})	(mg L^{-1})	(mg L^{-1})	(mg L^{-1})	(µg L^{-1})	(µg L^{-1})	(µg L^{-1})
S1N	1717693	4751137	5.32	13.0	7.23	720	142		0.07	15	0.9	160	82	12	14	17	0.11	443	5.8	6.2	6.5
S2 est.	1717713	4751155	5.57	14.0	5.83	828	17		1.10	10	13.0	314	105	13	15	12	1.10	501	2.2	3.0	0.1
S2 int.	1717703	4751154	7.10	14.5	6.72	1249	77		0.33	12	3.3	370	124	36	12	17	0.30	652	1.8	29.6	0.2
S4N	1717725	4751096	6.70	13.5	7.50	175	44		0.14	5	2.1	15	9	1	6	15	0.20	98	0.4	0.2	1.7
S6N	1717748	4751093	8.45	12.5	6.23	610	179		0.50	7	7.1	120	77	2	16	39	0.14	447	6.8	121.0	30.5
S7N	1717674	4751155	3.35	13.0	6.62	815	48		0.40	14	1.7	260	87	20	14	11	0.11	456	2.0	3.1	0.4
S10N	1717681	4751119	5.40	13.0	6.96	614	44		0.15	11	5.5	179	66	11	8	13	0.08	338	2.6	5.0	0.3
S40	1717682	4751033	9.96	13.0	6.54	933	43		0.70	10	1.4	317	63	35	21	21	0.95	513	15.6	0.7	<0.1
S42	1717658	4751088	4.72	12.5	6.62	754	51		0.10	9	20.0	202	85	7	10	16	0.03	400	0.7	24.9	<0.1
S60	1717751	4750985	15.33	13.5	6.68	454	28		0.20	7	5.1	123	22	16	14	13	0.40	229	1.0	52.5	0.3
S101	1717397	4751187	9.62	11.0	7.63	349	74		0.21	13	0.9	36	33	3	6	3	0.10	169	1.5	<0.1	0.2
S102	1717491	4751224	8.82	11.0	6.68	573	66		0.70	9	1.9	117	34	13	14	7	0.15	264	13.2	0.2	<0.1
S103	1717531	4751282	15.01	12.0	6.70	1346	121		0.96	10	1.2	473	208	24	5	13	0.60	857	5.4	<0.1	0.5
S104	1717507	4751155	11.29	11.0	7.13	573	227		0.20	12	0.2	24	75	5	7	5	0.08	356	1.5	<0.1	0.2
S105	1717595	4751211	5.92	12.0	7.48	946	195		0.15	9	3.6	214	134	14	11	8	0.58	590	2.3	0.1	0.2
S106	1717582	4751167	5.07	11.5	6.39	651	43		0.20	13	16.0	177	84	6	6	6	0.53	351	1.2	72.3	<0.1
S107	1717732	4751213	6.50	12.5	3.98	1902			2.70	9	9.8	390	116	11	13	25	0.10	577	4.8	8.8	0.2
S108	1717826	4751152	5.25	13.5	9.62	291	58	4	0.10	8	4.2	26	12	1	12	20	0.40	145	2.0	0.4	0.5
S109	1717839	4751070	8.55	11.5	6.41	1045	135		0.30	18	7.9	217	119	9	10	18	0.02	535	1.2	0.4	0.3
S110	1717947	4751129	9.00	13.5	6.94	955	215		0.30	43	42.0	98	124	11	14	7	0.40	555	0.5	0.2	0.3
S111	1718079	4750879	5.89	12.5	6.99	825	151		0.40	11	0.1	123	64	18	13	12	0.03	393	3.3	0.2	0.6
S113	1717509	4751022	7.13	12.5	6.07	443	20		0.24	12	12.0	112	32	9	11	10	0.46	218	1.2	41.0	0.1
S114	1717660	4751061	6.05	14.0	8.06	840	198		1.00	9	2.1	214	133	13	8	9	0.16	588	13.3	1.3	199.0
S116	1717525	4751087	6.71	12.5	6.13	526	7		1.90	11	24.0	143	44	8	9	13	1.40	262	1.1	233.0	0.3
S117	1717632	4751189	6.86	12.5	7.26	825	142		0.20	12	5.1	219	131	8	12	10	0.5	540	0.7	0.3	0.5
			Mean value	12.6	6.82	770	97		0.53	12	7.6	186	83	12	11	14	0.36	419	3.7	27.5	11.6
			Max. value	14.5	9.62	1902	227		2.70	43	42.0	473	208	36	21	39	1.40	857	15.6	233.0	199.0
			Min. Value	11.0	3.98	175	7		0.07	5	0.1	15	9	1	5	3	0.02	98	0.4	0.1	0.1

1.11)

ID	CX Easting	CY Northing	Water table depth (m)	T (°C)	pH	E.C. 20 °C (µS cm⁻¹)	HCO_3^- (mg L⁻¹)	CO_3^{2-} (mg L⁻¹)	F^- (mg L⁻¹)	Cl^- (mg L⁻¹)	NO_3^- (mg L⁻¹)	SO_4^{2-} (mg L⁻¹)	Ca^{2+} (mg L⁻¹)	Mg^{2+} (mg L⁻¹)	Na^+ (mg L⁻¹)	K^+ (mg L⁻¹)	NH_4^+ (mg L⁻¹)	TDS (mg L⁻¹)	As (µg L⁻¹)	Hg (µg L⁻¹)	Sb (µg L⁻¹)
PXY	1717593	4751065	3.83	11.0	7.05	1209	245		0.25	8	26.4	214	98	30	6	41	0.08	669	0.7	10.1	0.5
S1N	1717693	4751137	5.25	11.0	10.87	473	89	12	0.25	9	2.8	58	16	1	24	43	0.14	255	3.2	6.3	16.7
S2 est.	1717713	4751155	n.d.	n.d.	n.d.	n.d.	8		1.18	10	19.4	374	124	22	17	16	0.12	591	12.8	456.0	0.1
S2 int.	1717703	4751154	7.02	11.0	9.11	187	36	6	0.04	11	1.0	6	13	0.3	5	5	0.21	83	0.3	14.1	0.9
S3	1717643	4751052	6.38	12.0	7.41	933	265		0.52	27	7.2	195	153	16	10	17	0.32	690	0.5	1.5	1.3
S4N	1717725	4751096	7.70	11.5	7.16	713	39		0.06	11	1.9	23	10	1	10	13	0.08	109	0.4	1.3	0.3
S6N	1717748	4751093	6.48	11.5	6.23	283	90		0.66	4	0.9	19	26	0.3	7	16	0.47	164	14.4	471.0	28.2
S7N	1717674	4751155	3.28	11.0	6.84	349	55		0.11	7	1.5	110	51	9	7	8	0.04	248	2.4	6.3	7.9
S8	1717816	4751018	16.75	10.0	5.11	2178	2		0.53	10	21.8	993	380	32	14	30	0.14	1483	2.9	9.5	0.7
S10N	1717681	4751119	4.90	12.0	7.54	582	143		0.52	5	2.8	111	82	3	3	6	0.19	358	2.5	5.3	18.1
S40	1717682	4751033	9.02	10.5	6.59	1314	43		0.27	9	0.5	455	135	40	18	20	0.15	721	1.2	3.3	0.4
S42	1717658	4751088	4.70	11.0	6.77	735	173		0.14	9	10.1	138	95	8	6	14	0.03	453	1.0	25.9	0.9
S60	1717751	4750985	15.28	10.5	6.09	493	29		0.08	6	4.4	121	27	13	13	12	0.08	225	1.8	67.4	0.3
S101	1717397	4751187	9.16	10.0	6.93	384	107		0.09	9	0.4	37	43	3	6	3	0.16	209	1.5	0.5	0.3
S102	1717491	4751224	8.55	11.0	6.15	561	73		0.23	7	0.04	116	30	14	13	9	0.09	263	14.6	0.9	<0.1
S103	1717531	4751282	15.88	11.0	6.50	1246	195		0.53	6	0.7	415	180	37	5	19	0.13	857	2.4	<0.1	0.5
S104	1717507	4751155	11.59	9.5	6.82	611	232		0.36	9	0.4	24	76	5	12	4	0.09	362	1.5	1.8	0.2
S105	1717595	4751211	6.22	10.5	7.07	935	165		0.12	8	3.8	198	121	11	10	9	0.15	525	2.0	4.0	2.0
S106	1717582	4751167	5.22	10.0	5.88	615	61		0.13	9	10.1	122	67	5	7	7	0.09	288	1.3	70.1	7.2
S107	1717732	4751213	6.98	12.0	3.98	1164			2.84	9	7.9	391	118	11	13	25	0.99	579	5.5	15.5	<0.1
S108	1717826	4751152	5.43	12.0	6.51	800	85		0.15	8	0.02	197	72	15	14	23	0.24	414	2.8	2.2	0.2
S109	1717839	4751070	8.33	10.5	6.65	897	148		0.19	14	8.0	216	112	8	9	14	n.d.	530	1.2	0.5	0.1
S110	1717947	4751129	9.10	11.5	7.20	909	210		0.06	42	47.5	95	124	10	13	4	0.16	546	0.3	0.9	0.2
S111	1718079	4750879	5.40	11.5	7.63	664	165		0.37	10	0.2	105	66	16	13	10	n.d.	385	4.2	0.5	0.9
S113	1717509	4751022	7.20	11.5	5.70	430	6		0.15	11	10.2	107	30	8	11	7	0.06	190	1.5	92.8	0.1
S116	1717525	4751087	7.19	11.0	5.61	660	1		0.49	10	23.2	144	45	9	9	15	0.94	256	1.6	853.0	0.2
S117	1717632	4751189	7.04	10.0	6.13	807	79		0.19	18	11.6	194	99	9	10	14	0.10	434	3.0	16.7	0.2
			Mean value	11.0	6.6	769	104		0.37	11	7.3	188.8	89.8	11.8	9.9	12.7	0.2	432	3.0	72.4	3.2
1.12)			Max. value	12.0	9.11	2178	265		2.84	42	47.5	993.0	380.0	40.0	18.0	30.0	1.0	1483	14.6	853.0	28.2
			Min. Value	9.5	3.98	187	1		0.04	4	0.02	6	10	0.3	3	3	0.03	83	0.3	0.5	0.1

Tables 1.9 to 1.12: sample name, geographical coordinates, water table depth and physical and chemical parameters with mean, maximum and minimum values of the ground waters collected in the ASSM area in 7) February 2013, 8) May 2013, 9) September 2013 and 10) January 2014, with indication of the S6N piezometer. From (Vaselli et al., 2015) modified.

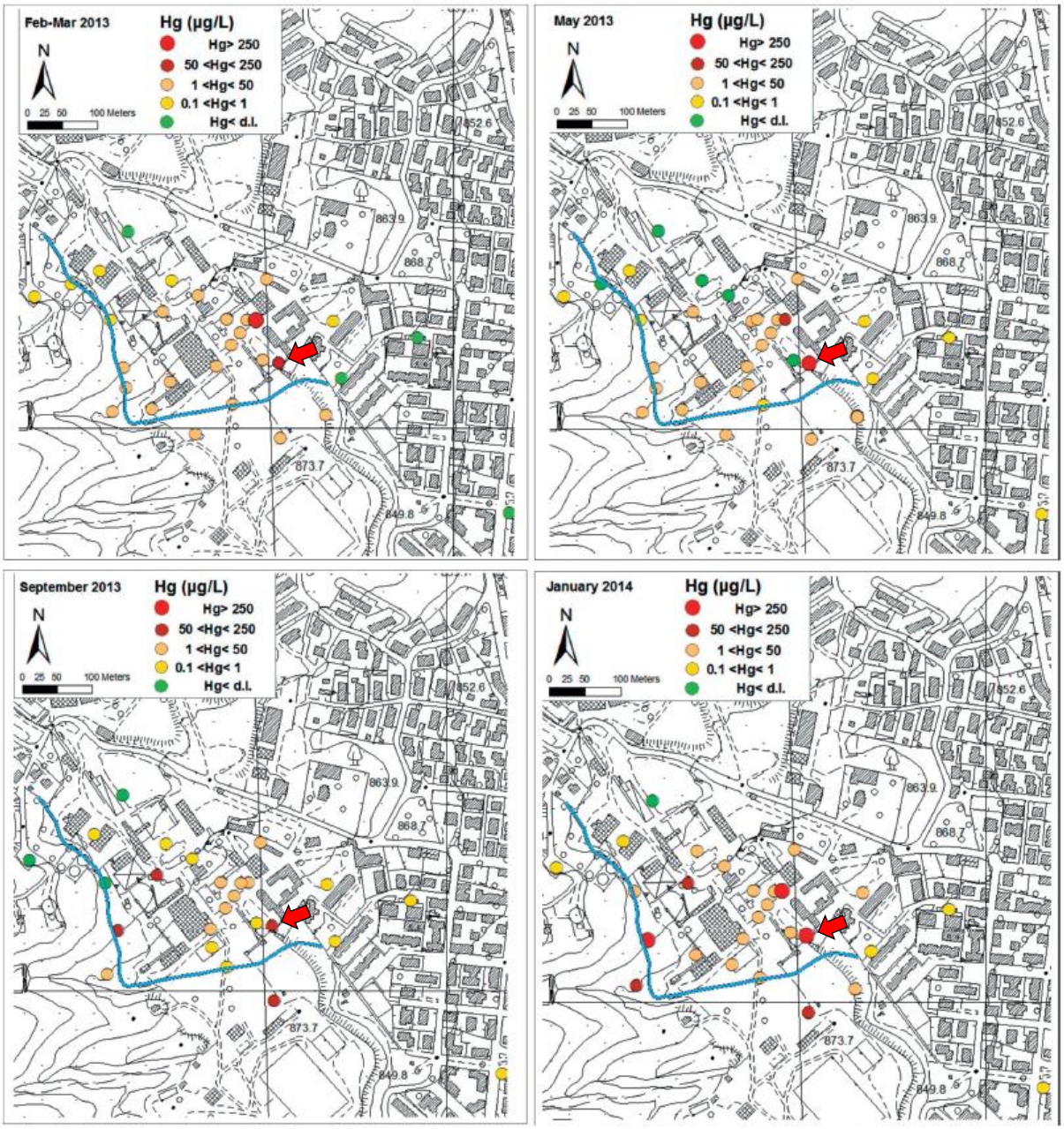

Figure 1.36: dot Hg distribution maps of the [Hg] ranges retrieved by the four different sampling campaigns of Tab. 1.09-1.12, with indication of the S6N piezometer. From (Vaselli et al., 2015), modified.

A very long geochemical monitoring of the water discharge from Galleria Italia, the output of the main mining tunnels drainage system (whose accesses were cemented), reveals circumneutral waters with Hg contents generally < 1 µg/L (maximal Hg load of the Galleria Italia samples = 25.6 µg/L) (Vaselli et al., 2021). However, it is also shown that most mercury is stored in the Galleria Italia sediments (1.2 mg/kg). This confirms the abandoned calcines and other contaminated objects and surfaces as the main source of Hg in the groundwater.

- Materials and methods -

2.1. Materials

Potassium hydroxide, KOH, (pellets, ≥ 85%, J.T. Baker, CAS 1310-58-3), potassium hypochlorite, KClO, (solution, ~ 19%, Laborchimica, CAS 7778-66-7) and anhydrous iron(III) chloride, $FeCl_3$, (powder, > 98%, Merck-Schuchardt, CAS 7705-08-0) were used as reactants to prepare the liquid ferrate and to straight interact with the investigated solutions. N-hexane (> 95 %, AnalaR NORMAPUR, VWR Chemicals BDH®, CAS 110-54-3) and methanol (anhydrous, CAS 67-56-1) were used during the separation and purifications steps during the attempts to synthesize solid ferrate(VI). A Fe(VI) and Fe(III) containing solid product, together with Fe(0) and Fe(0)+Ag(0) nanoparticles provided by the Regional Centre of Advanced Technologies and Materials (RCPTM) of Olomouc, Czech Republic, were also tested. All the different reagents are illustrated in the sections below, as well as main steps of their synthesis procedures are briefly summarized. A solution of $Hg(NO_3)_2*H_2O$ in HNO_3 0.5 M (10 ppm as Hg, ROMIL PrimAg®) was used as a source of Hg(II) for the laboratory prepared Standard Solutions (SS), to further tests the Hg removal efficiency. All solutions in this study were prepared with MilliQ water. All chemicals were used as received without any further purification.

2.1.1. LFe(VI)

Over the course of this PhD, a ferrate(VI) product was obtained using an original wet chemical synthesis, developed and tuned at the Geochemical Laboratory of the Earth Department (University of Florence). The final product falls into the liquid ferrate category and it was the result of multiples trials and optimization steps made based on the available facilities and equipment. The main advantages of the liquid variant of ferrate(VI) products is the reduce cost and complexity of the synthesis, thanks to the utilization of the Fe(VI) containing mixture directly without further steps and having the unreacted chemicals reagents still contributing. After a deep literature review, the solid potassium ferrate synthesis of Li et al. (C. Li et al., 2005) and the optimized parameters set up by Sun et al. (X. H. Sun et al., 2013) were chosen as the starting point (refer to paragraph 1.1.3. for further details on synthesis procedures).

Under appropriate cooling, KOH was slowly added to an about 19% KClO solution up to 10 M concentration. After that, $FeCl_3$ was gradually added in precise amounts to the alkaline solution, and solubilized under continuous stirring; the final product became dark purple, testifying the Fe(III) oxidation to Fe(VI) (ferrate anion, FeO_4^{2-}) (Schmidbaur, 2018). To reduce the amount of chemical used and the complexity of the synthesis procedure, the separation and purification steps were avoided, obtaining the liquid ferrate final product in which the ferrate is present in solution in the anionic form, mixed with the "unreacted" reagents.
Ferrate anion concentrations were measured using the spectroscopy method in the UV-Visible range using the Lambert Beer relation (eq. (20)):

$$[ferrate] = \frac{A}{\varepsilon * c} \quad (20)$$

where "A" is the UV/Vis absorbance in the sample, "ε" is the molar absorption coefficient ($M^{-1}cm^{-1}$) and "c" is the light path (cm) relative to the cell used. Interference of colloidal ferric oxide was minimized by using high dilutions and a 385 nm baseline correction (Alshahri et al., 2019; C. Li et al., 2005; Schmidbaur, 2018). In order to check the measurement reliability, multiple acquisitions were performed at different dilution ratios to build a calibration curve to further minimize interferences (see par. 3.2.). UV-Vis measurement were carried out using a DR/2010 spectrophotometers from Hach® and 1" cuvettes.

2.1.2. SFe(VI)

After the liquid ferrate synthesis, the further separation, purification and drying steps were undertaken in order to produce a more pure solid product with an higher K_2FeO_4 content and lesser of a contribute from the initial reagents. The procedure, devised from a review of all published methods, involves adding KOH to liquid ferrate in a specific time-frame for promoting K_2FeO_4 deposition, soaking the product in hexane to remove the contained water and using methanol to remove the contained impurities, such as KCl, all with multiple filtrations steps in between. An appropriate borosilicate filtering equipment was used. The final product was then preserved in a vacuum desiccator.

2.1.3. MixFer

A solid Fe(VI) containing product, kindly provided by the RCPTM of Olomouc, Czech Republic, was tested as a comparison in the Hg removal experiment. The product, called "MixFer", is a ferrate(VI)/(III) composite material constituted by a mixture of Fe(VI) and Fe(III) phases, namely K_2FeO_4 and $KFeO_2$ respectively, which can then achieve oxidation, coagulation and disinfection simultaneously with a singular dose, as already seen in previous paragraphs. MixFer was synthesized starting from the optimized method patented by Thompson in 1983 (J. A. Thompson, 1983). As described by Zboril et al., in this method, which falls into the dry-synthesis category, a mixture of Fe(III) oxide (in this case hematite α-Fe_2O_3 powder) and potassium nitrate in a 1:4 molar ratio was homogenized in an agate mortar and thermally treated for 30 minutes at 1000° under nitrogen gas stream. The final product, due to the unstable and hygroscopic nature of the phases contained, was then stored in a vacuum desiccator (Zboril et al., 2012). The method was chosen due to its scaling potential to large production amounts, typical of dry synthesis methods. Phase composition, studied by XRD and transmission ^{57}Fe Mossbauer spectroscopy acquired at room T°, revealed a 31 wt % of potassium ferrate(VI) and a 69 wt % of potassium ferrite. However, the Fe(VI)/Fe_{tot} atomic ratio coming from Mossbauer was 0.24, due probably to the formation of $KFeO_2$ phase both in several micrometer sized crystals to nanometer sized particles, evidenced as a superparamagnetic doublet fraction and confirmed by SEM images (Zboril et al., 2012). A Chemical Warfare Agents (CWAs) removal experiment was performed using MixFer, which completely and quickly removed bis(2-chlorethyl) sulfide (sulfur mustard), (3,3'-imethylbutan-2-yl)-methylphosphonofluoridate (soman) and S-[2-(diisopropylamino)ethyl] methylphosphonothiolate (O-ethyl) (Zboril et al., 2012). The oxidation promoted by MixFer revealed higher effectiveness in removing those CWAs than the reduction by nanoscale Zero Valent Particles (nZVI). The Fe(VI) content for the "Mixfer 31", which is the name of the origin batch name from which the Mixfer used in this study came, is indicated in Tab. 2.1, as well as the % of Fe in other oxidation states. From this point on, the term "Mixfer" will be only used to indicate the reagent coming from this batch.

Oxidation state	Molar ratio in total Fe
Fe(III)	72,9 ± 1 %
Fe(IV)	< 3 %
Fe(V)	18,7 ± 1 %
Fe(VI)	8,4 ± 1 %

Element	Mass concentration [%]
K	22,7
Fe	18.5

Specie	Mass ratio
Fe(III)	13,5 ± 3 %
Fe(IV)	–
Fe(V)	3,5 ± 3 %
Fe(VI)	1,6 ± 3 %
$KFeO_2$	30,6 ± 3 % [1)]
K_3FeO_4	14,7 ± 3 % [1)]
K_2FeO_4	5,5 ± 3 % [1)]
K_2O	2,7 ± 3 % [1)]
Fe(III)	13,5 ± 3 %

*Table 2.1: (**left**) % of Fe oxidation states determined by Mossbauer spectroscopy; (**center**) elementary analysis by AAS/flame photometry and (**right**) percentage of active species for the "MIXFER 31" batch of Mixfer reagent, provided by the RCPTM.* [1)] Sum of the individual components is 53.5 %. Difference to do 100 % is caused by content of oxide impurities (ca 5 – 10%) and content of unidentified components with different stoichiometry

2.1.4. Nanoscale iron-based reductants

Over the past twenty years, there has been an increasing interest over the study of new materials with higher specific surface area for inactivation and removal of hazardous components in the broad environmental remediation field. Starting from the Zero Valent Iron particles at the micro-scale (ZVIs), well researched and engineering and conventionally used in permeable reactive barriers (Tratnyek & Johnson, 2006), we arrive to more modern active metal nanoparticles (e.g. Fe, Ni, Pd, Ag, bimetallic nanoparticles) (Markova et al., 2013; Singh et al., 2020) up to new approaches such as the integration of nanoparticles with bioremediation (Singh et al., 2020). Two nanoscale iron-based reagents were provided by RCPTM and tested for Hg removal: a nZVI and a bimetallic Fe-Ag nanoparticles (nZVIs and Fe-Ag NPs).

2.1.4.1. Zero Iron Valent nanoparticles (nZVI)

Due to their smaller size, nanoscale ZVI particles (nZVIs) have significantly larger specific surface area than ZVIs, which leads to higher adsorption and reactivity tendencies and higher mobility into porous media such as soils, sediments and aquifers. Moreover, they are considered a sustainable remediation technology due to the environmental compatibility of the iron-containing reaction products (Kašlík et al., 2018). In laboratory and pilot-scale tests using lab solutions, ground- and waste-waters, nZVIs have proven to significantly remove a

large number of inorganic compounds such as heavy metals (e.g. As(III), As(V), Cr(VI), Zn(II), Ni(II), Pb(II), Cu(II), Zn(II), Cd(II) Ag(I), Hg(II)), metal oxyanions and nitrate as well as organic compounds (e.g. chlorinated organic and nitroaromatic compounds, dyes, phenol and its derivative) and more novel contaminants (e.g. CWAs, antibiotics, contrast agents, viruses) (Chizitere Emenike et al., 2023; Fu et al., 2014; Gil-Díaz et al., 2021; Kašlík et al., 2018; Klimkova et al., 2011; S. Li et al., 2014; Yates, Zboril, et al., 2014; Zboril et al., 2012; Zou et al., 2016). Standard nZVI exhibit a core-shell structure with the Fe(0) core surrounded by a Fe(II)/Fe(III) mixed oxide shell which protect the core from rapid oxidation while being disordered and defective enough to make it very reactive, in contrast with the typical passive oxide layer formed in bulk iron (Monga et al., 2020). The metallic core is the electron source which gives to the nZVI its reducing power while the oxide shell provides sites for the adsorption, chemical reactions and/or electrostatic interactions (Fig. 2.1) (Li et al., 2014; Monga et al., 2020). Some disadvantages have limited the nZVIs application at full-scale such as their tendency to form agglomerates in aqueous media due to their intrinsic magnetic and Van der Waals attractive interaction (which limits mobility and decreases the available particle surface area, thus their reactivity) and their reactivity in air (which affects storage, transportation, utilization) (Kašlík et al., 2018). Stabilization through organic and/or inorganic amendments and creation of an organic or inorganic shell are used to counteract the agglomeration, aging and instability connected with nZVIs (Kašlík et al., 2018).

The nZVIs used in this study come from a commercially viable product called NANOFER 25N, provided by the Czech company NANOIRON, a pure (Fe(0) ≥ 80 %, Fe_3O_4 ≤ 20 %) nanopowder of zero-valent iron in the dry state preserved in the inert atmosphere which was subjected to aging in water environment by RCPTM, with the same conditions (T° and time) as the Fe + Ag NPs, but without the Ag-salt (see below). This resulted in a partly oxidation and passivation of the surface which stabilized the sample, letting possible to exposure it to air for longer period of time. See (Markova et al., 2013) for characterization of data.

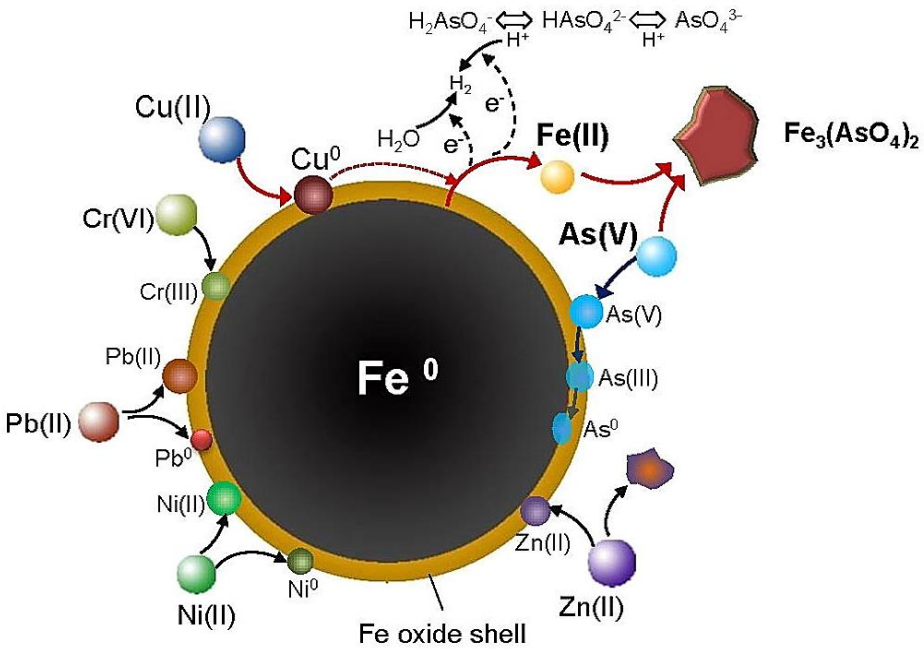

Figure 2.1: Li et al. nZVI proposed removal mechanism of metal contaminants in industrial wastewater; Cu(II),Cr(VI) = reduction + deposition onto the nZVI surface, Pb(II),Ni(II) = reduction + deposition and adsorption, As(V) = adsorption + reduction and co-precipitation as arsenate with the ferrous ions generated by neutralization of protons from dihydrogen arsenate, Zn(II) = adsorption and co-precipitation with nZVI corrosion products (ferrous ion or iron oxide/hydroxides). Cu deposition enhances the redox effect of the nZVI. From (S. Li et al., 2014).

2.1.4.2. Fe+Ag nanoparticles

The Fe+Ag NPs were firstly reported by Markova et al. in 2013 (Markova et al., 2013). The preparation of bimetallic NPs is one of the strategies to eliminate the tendency of nZVIs to react with surrounding media and spontaneously aggregates, resulting in loss of their reactivity. The choice of silver was made in order to possibly improve the antibacterial and antifungal properties of the resulting Fe+Ag NPs in respect to nZVIs or Ag NPs alone. Fe-Ag NPs were obtained by addition of $AgNO_3$ solution to commercially available nZVIs (the NANOFER 25N by NANOIRON, Ltd.), followed by sonication, shaking, magnetic separation and washing. The reduction of Ag(I) in aqueous solution oxidized partially the nZVIs, producing a lepidocrocite (γ-FeOOH) and magnetite (Fe_3O_4) shell together with almost spherical Ag(0) NPs onto the nZVI surface, as pointed out by XRD, TEM and Mossbauer spectroscopy (Fig. 2.2a). The uniformity of Ag NPs distribution on the nZVIs surface was confirmed by elemental mapping (Fig. 2.2c). The Fe-Ag NPs resulted stable while stored as dry powders in air for 21

days and the adsorption of silver was verified by strong sonication up to 300 hours, which didn't show any Ag:Fe variation above the error for all the samples. The Fe+Ag NPs were tested as phosphate remover and antibacterial and antifungal agent against nZVIs. The addition of Ag seemed to negatively impact phosphorus removal acting as a passivation layer when present in higher amounts; instead, the formed lepidocrocite enhanced the phosphate degradation even further the nZVIs performance since iron oxyhydroxides represent a stronger adsorbed than iron oxides. On the other hand, Fe+Ag NPs showed antimicrobial activity thanks to the Ag content while no antibacterial or antifungal effects were manifested by nZVIs. Lastly, the saturation magnetization of Fe+Ag NPs revealed the possibility of magnetic separation, thus control over its action in the environment.

The Fe+Ag NPs tested in this work were prepared using the above illustrated method (from (Markova et al., 2013)), starting from the NANOFER 25N by NANOIRON, and presented an Ag(0) content of 7.1 %, over a 82.9 % of Fe(0), 1 % of FeO and 9 % of Fe_3O_4 (data analyses provided by RCPTM).

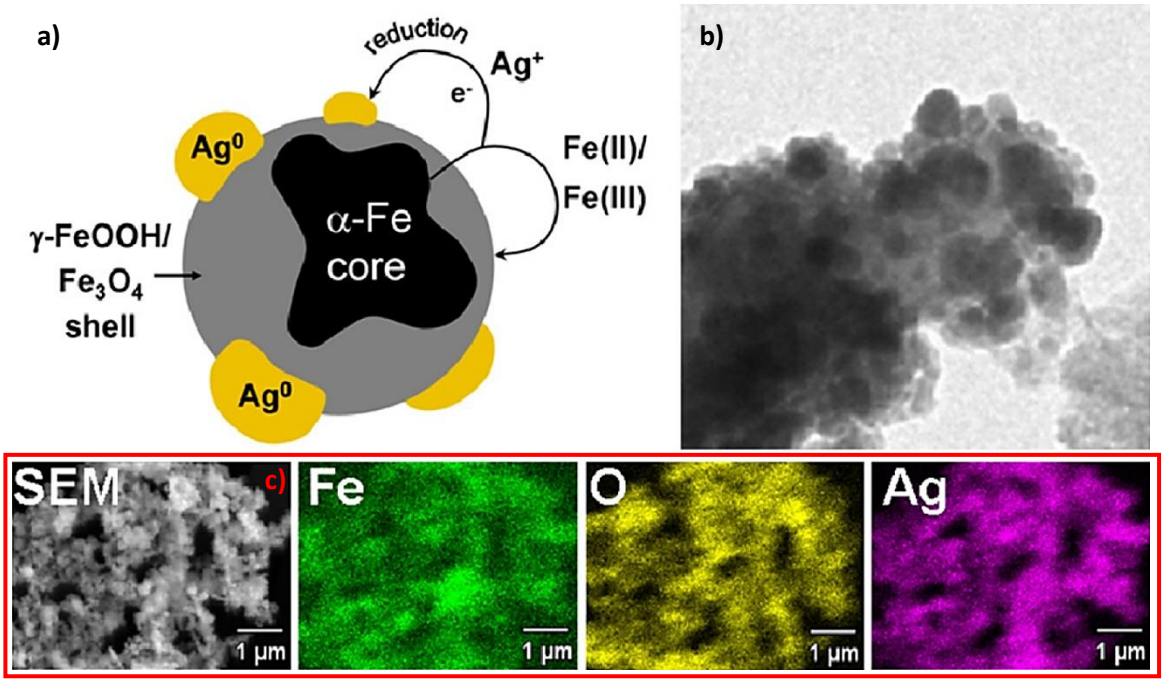

*Figure 2.2: **a**) schematic illustration of a Fe+Ag NP model, **b**) SEM image of a Fe-Ag NPs sample and **c**) Fe-Ag NPs SEM image and relative x-ray elemental maps of Fe, O and Ag distribution. From (Markova et al., 2013).*

2.2. Experimental procedures

In order to test, for the first time, the feasibility of using several modern products for the removal of mercury in solution, an analysis routine was developed based on a series of preliminary tests performed during the course of this PhD. The routine found was the best in addressing issues such as limiting-time frame (e.g. analysis has to be completed in the least amount of time after the natural water collection), limited resources and lack of experience in the usage of some of the new products, as well as complications implied in some of the techniques used (e.g. low Hg signal coming from X-ray measurements). The routine includes the analysis of the residual Hg content and the characterization of the resulting solids obtained from the filtration post-treatment. The waters and solids characterizations were performed through different techniques, schematically summarized in Figure 2.3.

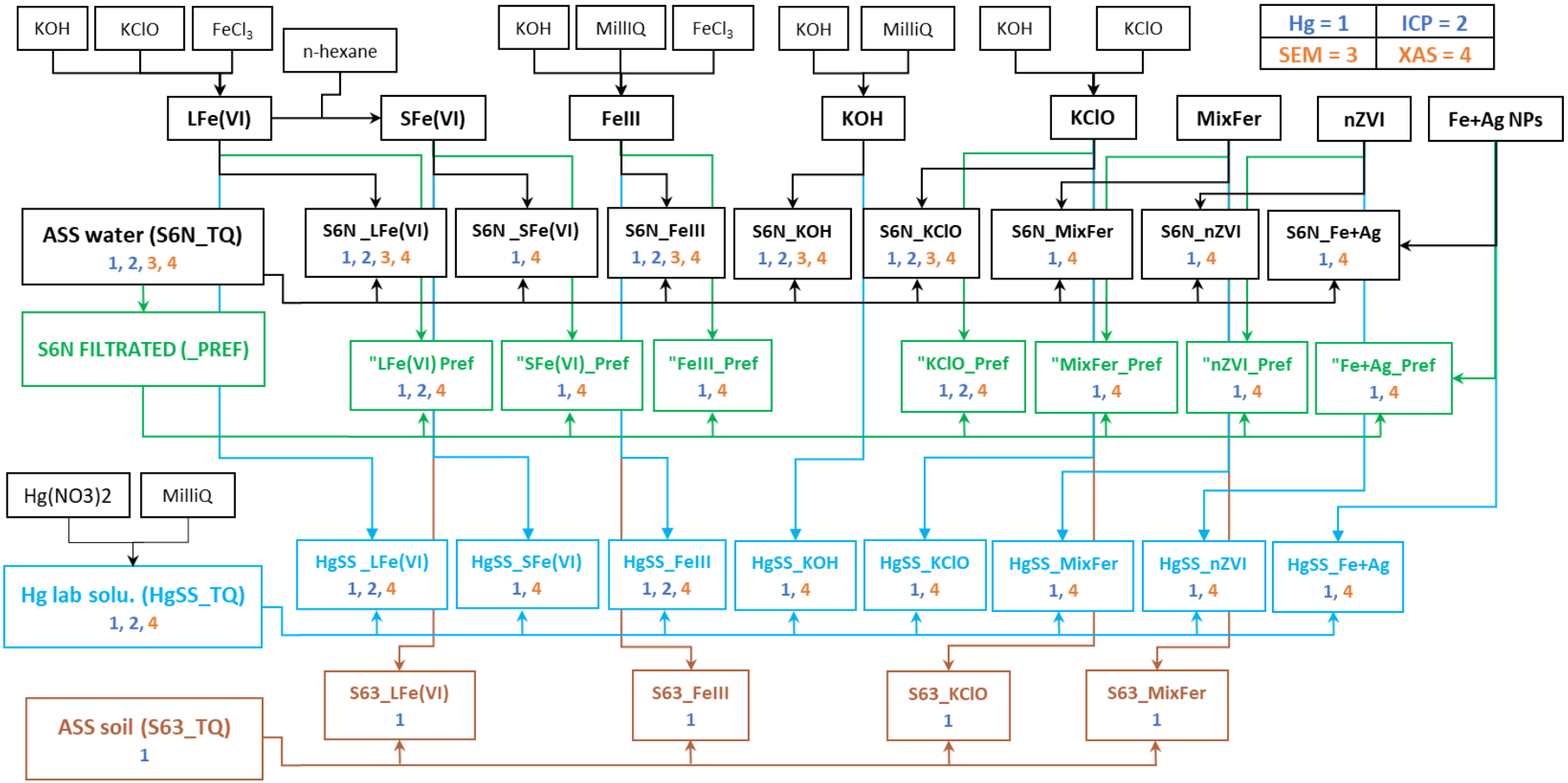

*Figure 2.3: conceptual map outlining the different kind of samples prepared during this study, combining both natural waters from ASS (S6N) and Hg lab prepared solutions (HgSS) with the different reagents tested. The maps summarized the techniques used for characterizing the samples (the **resulting waters** and the **solid by-products**). The map doesn't account for the trials done at half or quarter reagents dosages, complementary analysis on the starting chemicals (KOH, KClO etc.), as well as minor preliminary tests (e.g. XRD on the SFe(VI)) which will be specified when needed in the text.*

Two different kinds of Hg-containing waters were used to verify the efficacy in Hg removal of the different reactants:

- Hg(II) solutions, prepared properly diluting $Hg(NO_3)_2*H_2O$ 10 ppm in MilliQ water (HgSS), at a 500 ppb and a 1 ppm final Hg concentration, labelled as "HgSS_500ppb" and "HgSS_1ppm", respectively;

- natural water samples from the ASS mining catchment, collected at the S6N piezometer (Fig. 1.35, 1.36, Tab. 1.9-1.12) in May 2021 and April 2022, labelled as "S6N_May21" and "S6N_Apr22" respectively.

Moreover, Hg contaminated soil from Petrineri mine in Bagni San Filippo (points 1 in Fig. 1.30) collected by Meloni Federica during her PhD study, labelled as "S63"(Meloni et al., 2021), was also tested by addition in MilliQ water, together with the different reactants. The S63 Hg content in the soil sample was around 657 mg/kg while mercury speciation estimated in about 76 % cinnabar, 12 % metacinnabar and Hg bound to humic acids (personal communication). No further Hg was added to any of the samples.

The S6N was sampled through a pump system developed and normally used by the geochemical research team of the Earth Department of the University of Florence. After routinely T°, pH and electrical conductivity measurements performed on site, the water was stored into 2 liters plastic containers, prepared and provided by the Earth Department team. After few hours from the sampling, the containers were placed into a fridge and used within 24 h after in order to prevent as much as possible the natural sedimentation and the Hg loss into the container walls. The S6N was used without acidification or filtration, except in the "_Pref" samples, where it was filtered using 0.45 µm cellulose filters by manual syringes immediately before the addition of the reagents. Another S6N trial (labelled as "S6N_Oct20") and discharge waters from Galleria Italia (see par. 1.3.1.), labelled as "GITA", were also used in the early stage of the project. GITA was used to test the efficiency of the products on an As-contaminated water representative (GITA As contents are usually the highest among the ASSN waters, see (Vaselli et al., 2015; 2021)). Unfortunately, the initial inexperience mainly linked to performing experiments after a too long time-span from the sampling, affected the significance of the obtained results (reported only sporadically in the paragraphs below). The experiments were all performed in 50cc glass flasks (Fig. 2.4), where the different reagents have been added to the different Hg source material without any pretreatment ("TQ" which

means “tal quale”, namely “as it is”, is the sample used as reference) or to the _Pref variant for the S6N. The only exception is referred to the S63 experiments, where 100 cc flasks were used.

Figure 2.4: photo of some HgSS samples in 50 cc flasks after the addition of different reagents. The typical violet color resulting from the ferrate addition is clearly visible on the right flasks.

The different reagents were added to the flasks in comparable amounts, accounting for about 400 ppm of total added Fe and about 80 ppm as Fe(VI) (see par. 3.2.) in the iron-containing ones. Regarding the nZVI and the Fe+Ag NPs addition, about 120-130 ppm of the respective pure products were used in S6N trials, 250 in HgSS_1ppm, together with testing done at about half and a third of that quantity, due to the high efficiency emerged in lab tests done by RCPTM (personal communication). The addition to the raw waters of the following solutions was performed to compare respectively the different treatment processes of alkalinisation, redox, or adsorption alone against the combined effects of the unreacted reagents contained into the LFe(VI): a 10 M KOH MilliQ water (labelled as “KOH”), 10 M KOH in about 19 % KClO (“KClO”) and $FeCl_3$ as 400 ppm of Fe in 10 M KOH MilliQ water (“Fe(III)”). The amounts added in the KOH, KClO and FeIII samples are proportional to the amounts of the respective reagent added in the LFe(VI) samples. The KClO, Fe(III), LFe(VI), SFe(VI), MixFer, nZVI and Fe+Ag NPs were double tested using both S6N_TQ and S6N_Pref aliquots to evaluate the interaction effect between any natural precipitate/suspended solid phase contained. In the S63 experiments, the TQ sample was the only one where the test was performed in a 50 cc flask using 155 mg of soil; in all the other samples, the soil was introduced in 100 cc flask of MilliQ water one 1h prior, followed by the addition of the specific reagent in double the amount, to

keep the concentrations used in the S6N trials. The S63 added amounts were: 313 mg for S63_KClO; 318 mg for S63_Fe(III); 290 mg for S63_LFe(VI); 302 mg for S63_Mixfer. The complete list of successfully prepared samples is reported in Tab. 2.2 while the amount of each of the reagent added are reported in Tab. 2.3. The lack of some combination, easily noticeable in Tab. 2.2, is due to strategic choices (e.g. no useful data coming from KOH treated samples), timeframe constrains (e.g. availability of some of the reagents) as well as technical accidents (e.g. lost of some of the samples during transportation to an external lab for analysis) which will be addressed in the next paragraphs.

Hg SOURCES	**REAGENTS**												
	TQ	KOH	KClO	Fe(III)	LFe(VI)	SFe(VI)	Mixfer	nZVI			Fe+Ag NPs		
								1	1/2	1/3	1	1/2	1/3
S6N_May21	✓	✓	✓	✓	✓								
S6N_May21_Pref			✓		✓								
S6N_Apr22	✓		✓	✓	✓	✓	✓	✓	✓	✓	✓	✓	
S6N_Apr22_Pref			✓	✓	✓	✓	✓	✓	✓		✓	✓	✓
HgSS_500ppb	✓	✓	✓	✓	✓								
HgSS_1ppm	✓		✓	✓	✓	✓	✓	✓			✓	✓	
S63	✓		✓	✓	✓		✓						

Table 2.2: lists of the different trials performed, resulting from the combination of different Hg sources and reagents.

TQ =	the water (or soil + water for S63) has been left standing without any treatment
KOH =	addition of 0.90 g solution of 10 M KOH in MilliQ
KClO =	addition of 1.00 g solution of 10 M KOH in 19% KClO
Fe(III) =	addition of 0.95 g mixture of FeCl3 in 10 M KOH (about 400 ppm as Fe(III))
LFe(VI) =	addition of 1.08 g of liquid ferrate (about 400 ppm as Fe total, 80 ppm as Fe(VI))
SFe(VI) =	addition of about 151 mg of solid ferrate (153 mg in S6N, 152 mg in S6N_Pref, 148 mg in HgSS)
Mixfer =	addition of 18.3 mg in S6N, 15.7 in S6N_Pref, 144 mg in HgSS, 58 mg in S63
nZVI 1 =	addition of 6.6 mg in S6N, 5.6 mg in S6N_Pref, 12.7 mg in HgSS
nZVI 1/2 =	addition of 3.4 mg in S6N, 3.3 mg in S6N_Pref
nZVI 1/3 =	addition of 2.0 mg in S6N
Fe+Ag NPs 1 =	addition of 6.6 mg in S6N, 6.4 mg in S6N_Pref, 12.1 in HgSS
Fe+Ag NPs 1/2 =	addition of 3.5 mg in S6N, 3.3 mg in S6N_Pref, 6.4 mg in HgSS
Fe+Ag NPs 1/3 =	addition of 1.8 mg in S6N_Pref

Table 2.3: amount of reagent added in each of the different category of samples, expressed in grams/milligrams over 50 cc of starting Hg source (except for S63_Mixfer, where the mg over 100 cc flask are reported).

After the addition of the different reagents, the flasks were positioned on a vibrating shaker for 10 minutes at maximum power and then left to interact for 48h at ambient T°. Afterwards, the resulting solutions were filtrated with a vacuum system (Fig. 2.5a) using 47 mm diameter, 0.45 µm porosity cellulose acetate filters from Sartorious Stedim Biochem (Fig. 2.5b), and the different aliquots were withdrawn and properly acidified for the following determinations (the different procedures are described below). The filters were collected, dried at ambient T° overnight and positioned in plastic bags for further studies.

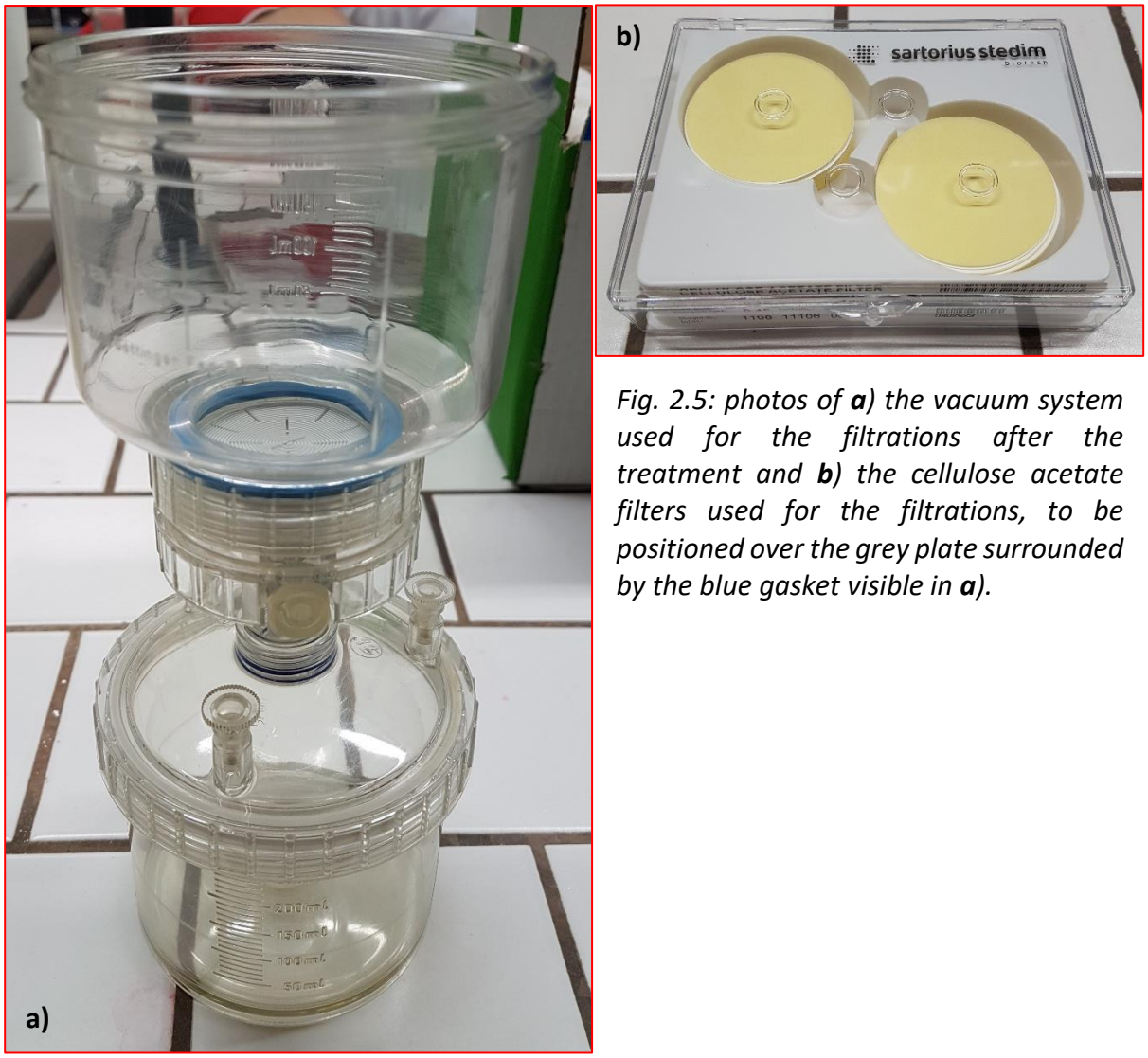

*Fig. 2.5: photos of **a**) the vacuum system used for the filtrations after the treatment and **b**) the cellulose acetate filters used for the filtrations, to be positioned over the grey plate surrounded by the blue gasket visible in **a**).*

2.2.1. Analytical characterization of waters

The HgSS, S6N and S63 samples, after the treatment, were filtered using the equipment from Fig. 2.5 and the resulting solutions placed in plastic beakers. The pH and electrical conductivity, together with T° were then measured using a PC 70 Vio professional portable multiparameter

equipped with 201T electrode (for pH) and 2301T cell (for conductivity) from XS Instruments© (Fig. 2.6), properly calibrated and cleaned with MilliQ water between each measurement.

Figure 2.6: photo of the PC 70 Vio multimeter used for pH, electrical conductivity and T° of the treated samples.

From the filtered solutions in the plastic beakers, 10 cc aliquots were then collected in plastic vials. The 10 cc samples were properly acidified (with hydrochloric or nitric acid), diluted (only for trace elements analyses), and stored in the fridge before the Hg and other trace elements content measurements.

For the dissolved mercury contents, samples were sent to the C.S.A. Research Institute (Rimini, Italy), where they were analyzed following the EPA 7473 2007 method (U.S. EPA, n.d.), with a detection limit < 0.1 µg/L. The samples were acidified beforehand using 1-4 % of Suprapur® Supelco® hydrochloric acid 30% from Merck Millipore.

The trace elements investigation was performed at the Department of Earth Sciences of the University of Florence, using a 7800 ICP-MS with autosampler module from Agilent Technologies, calibrated standards and own laboratory solutions to properly calibrate the instrument before the analysis (Fig. 2.7). For each of the elements analysed, the detection limit corresponds to the lowest analysis point with a ratio between measured/expected value of 1 ± 0.1 in the calibration line made from the calibrated standards measurement and will be made explicit during the presentation of the results. The samples were acidified using 3 % of

Suprapur® Supelco® nitric acid 65 % from Merck Millipore and diluted 1:100 with MilliQ water to be within the measurement salinity range.

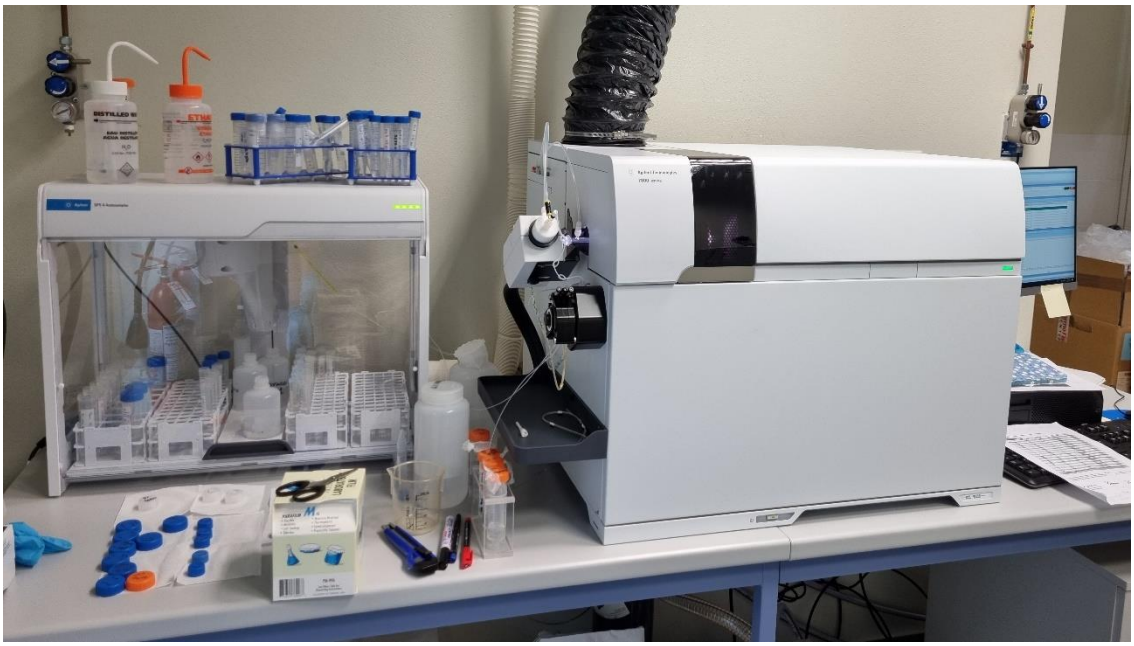

Figure 2.7: photo of the Agilent 7800 ICP-MS and Agilent autosampler at the Department of Earth Sciences of the University of Florence.

2.2.2. Analytical characterization of precipitates

The solid by-products from the interaction between starting waters/lab solutions and the different reactants were collected over 0.45 µm cellulose acetate filters by vacuum filtration (Fig. 2.8); dried overnight and properly weighted before and after, they were used to perform different kind of determinations.

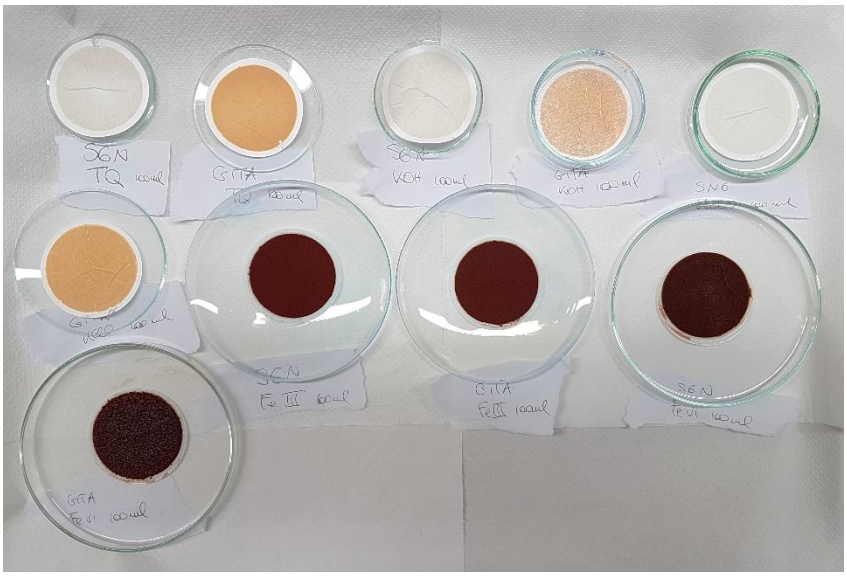

Figure 2.8: photo of some of the cellulose acetate filters immediately after one of the first filtration round.

Portions of the 0.45 µm cellulose filters covered by the precipitates were gently fixed over the stubs for Scanning Electron Microscopy (SEM) analysis, using a double-sided conductive carbon tape, and coated with a graphite layer to ensure their electrical conductivity (Fig. 2.9b). SEM analyses were performed to study the nature of the resulting solids. Samples were analysed at M.E.M.A. laboratory ("Centro di Servizi di Microscopia Elettronica e Microanalisi") of the Earth Department of the University of Florence using a SEM ZEISS EVO MA15 equipped with the Oxford INCA 250 Microanalysis (Fig. 2.9a). Backscattered and secondary electron micrographs were registered while the mineral identification was carried out by means of point and raster Energy Dispersive X-ray (EDX) microanalysis. Measurements were carried out at an accelerating voltage of 15 KV up to 2200X magnification.

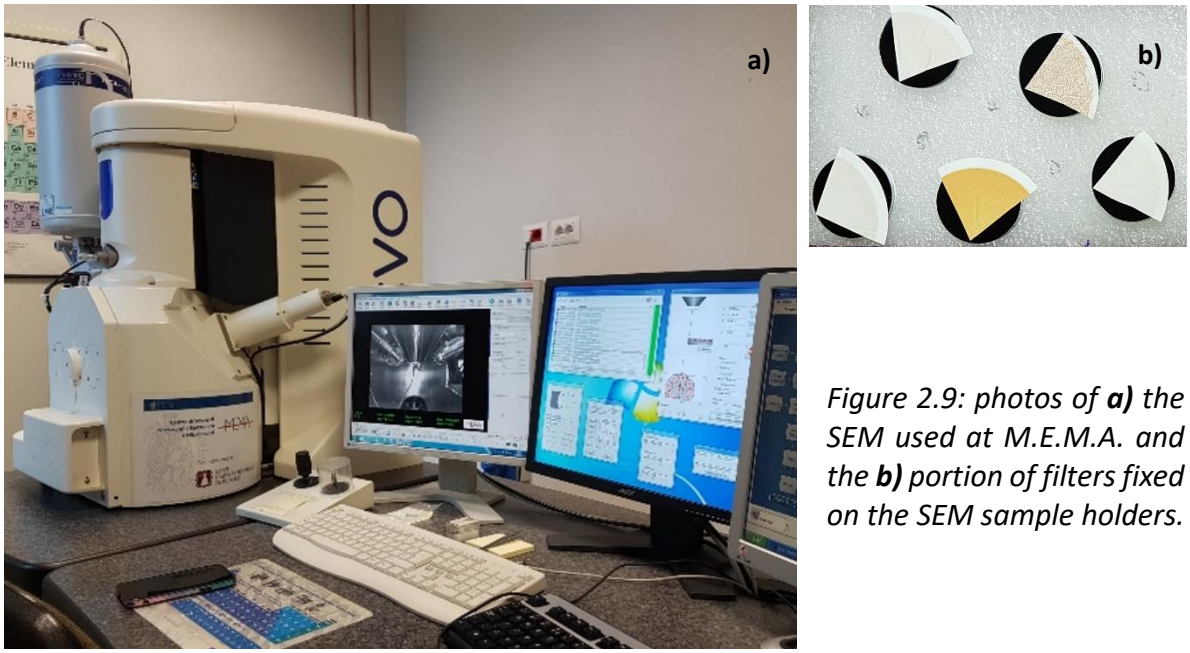

*Figure 2.9: photos of **a)** the SEM used at M.E.M.A. and the **b)** portion of filters fixed on the SEM sample holders.*

Using other filters portions, a detailed study on the solid by-products from the mercury removal tests were performed by means of X-ray Absorption Spectroscopy (XAS). Given the non-routine nature of the technique and the importance of this experimental phase, the following chapters will be devoted to an introduction to XAS and the parameters of the experiment.

2.2.2.1. X-ray Absorption Spectroscopy (XAS) measurements

XAS is a local-structure sensitive and element specific technique based on the measurement of the variation of the absorption coefficient as a function of the applied X-ray energy. It can provide important information about the phase distribution inside a sample, the relative oxidation state, so as quantitative data on the nature of the ligands and the interatomic distances between a central atom and its neighbors. Due to its properties, XAS was identified as the perfect technique to provide insights about the Hg removal mechanisms using different chemicals. The experiment described in this text was carried out at the LISA - BM08 line of the European Synchrotron Radiation Facility (ESRF) in Grenoble, dedicated to the structural characterization of materials and the occurring relation with their macroscopic properties. Thanks to characteristics such us high photon flux and radiation quality, the synchrotron light is the ideal source for XAS characterizations, which allows to perform low-concentration experiments and relatively fast acquisitions. The data for the S6N_Apr22 samples were

acquired during the experiment A08-1-1089 carried out between the 13th and the 19th of April 2022 while preliminary in-house tests performed during a long-term stay traineeship between June 2021 and March 2022 were used to investigate the S6N_May21 precipitates and to design and tune the proposal experiment, awarded with the above-mentioned 7 days worth of synchrotron time by the Central European Research Infrastructure Consortium, CERIC.

2.2.2.1.1. The European Synchrotron Radiation Facility (ESRF) and the LISA-BM08 beamline

The ESRF is a European research centre of excellence resulting from the international cooperation of 21 countries, hosting 44 different laboratories, the "beamlines", each equipped with state-of-the-art instrumentation and operating 24h a day, 6 days a week (European Synchrotron Radiation Facility, 2023a). ESRF is the world's first fourth-generation high-energy synchrotron, featuring the world's most intense X-ray source (ESRF-Extremely Brilliant Source, EBS), exploited by thousands of scientists every year to explore the complexities of materials and living matter in key areas such as health, environment, energy and new industrial materials, cultural heritage (precious artifacts and paleontological treasures), earth science, nanotechnologies (European Synchrotron Radiation Facility, 2023a). The entire facility is divided into (Fig. 2.10) (European Synchrotron Radiation Facility, 2023b):

- electron gun and Linac (LIN(ear) AC(cellerator)): an electron gun produces electrons that are "packed" and accelerated by the Linac to energies of 200 MeV, guided along the transfer line by steerer magnets before entering the booster;

- booster synchrotron: a 300-m-long, 10 Hz circular accelerator where electrons reach energies up to 6 GeV and are then injected into the main ring after passing another transfer line;

- storage ring: upgraded to the EBS status with a 150 M€ investment over the 2015-2022 period, it is a ring 844.4 m in circumference, where 6 GeV electrons are stored and delivered to the beamlines. Maintained at pressures of 10^{-9} mbar it includes 32 linear (where the insertion devices are located and, consequently, the "ID-" beamlines) and 32 curved sections (where the "BM-" beamlines are found) (Fig. 2.10c). Each curved section possesses 2 magnets that force the electrons to follow a closed circular trajectory. Each linear section possesses

several focusing magnets, which ensure the high spatial coherence, as well as insertion devices called undulators or "wigglers" which force the electron beam into sinusoidal trajectories, stimulating the production of X-rays (synchrotron light);

- beamlines (Fig. 2.10d): structures tangential to the storage ring, 25 to 100 m long, each equipped and designated for a specific technique/type of research, which exploit the synchrotron light produced by the trajectory changes of the electron beam through the curved section or the insertion devices. A beamline consists of a chamber (called "hutch") with optics for beam conditioning (selection of desired wavelengths/energy, focusing, etc.) and multiple other hutches where the samples interact with the beam and the data are collected, and the entire experiment is safely controlled.

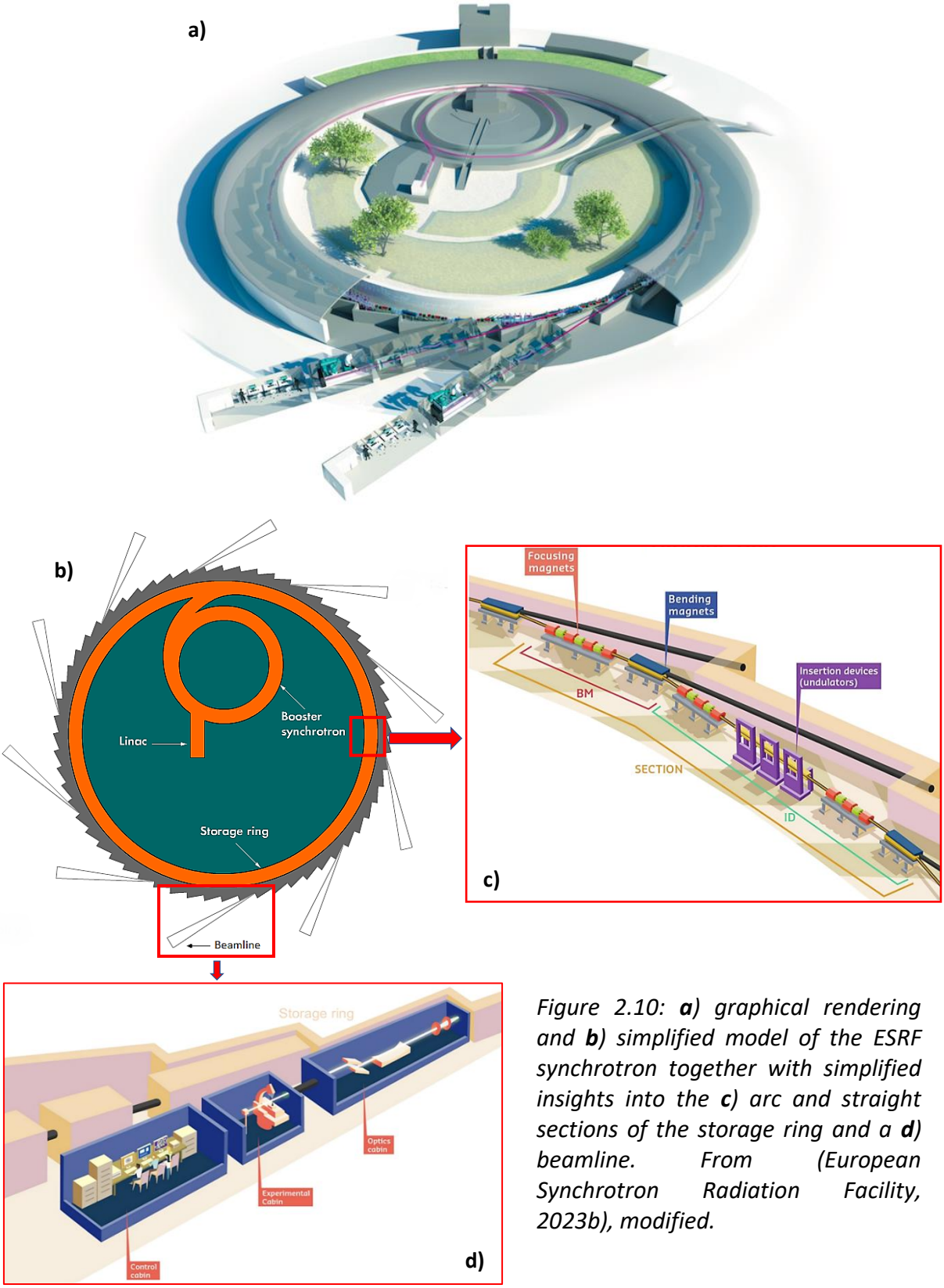

*Figure 2.10: **a**) graphical rendering and **b**) simplified model of the ESRF synchrotron together with simplified insights into the **c**) arc and straight sections of the storage ring and a **d**) beamline. From (European Synchrotron Radiation Facility, 2023b), modified.*

LISA (Linea Italiana per la Spettroscopia di Assorbimento di raggi x, BM08) is the new Italian beamline contributing to the Collaborating Research Group (CRG) at the ESRF (Fig. 2.11), fully presented in the papers from D'Acapito et al. and Puri et al. (D'Acapito et al., 2019; Puri et al., 2019). It is the results of the refurbishment of the former GILDA (General Purpose Italian beamline for the Diffraction and Absorption, (D'Acapito et al., 2014)), and it has been opened to the external users since April 2018. All the optics (mirrors and monochromator) were fully upgraded and improved, being also fully compatible with the new EBS ring (Fig. 2.11b). LISA is dedicated to XAS and related techniques, which can be exploited over a wide energy range (4 to 90 keV), allowing to probe the K- and/or L-edges of most of the elements heavier than calcium. The double crystal monochromator allows to work with a photon flux up to 10^{11} ph/s using a Si(111) crystal pair or in higher resolution with a Si(311) one. Through collimating and focusing mirrors it is possible to achieve high beam stability during scans (beam movement < 10 % of the beam size over an angular range of 30 for both crystals pairs) and a variable spot size (defocused up to millimetric scale or focused down to < 200x200 μm) which allow the study of small crystals and fibers. The energy resolution (ΔE/E) in the range of energy achievable varies between 10^{-4} and 10^{-5}, depending also on the crystal pair used, and can be also enhanced "on the go" by calibration with standards. The first experimental hutch (EH1) is equipped with a vacuum sample chamber and two ionization chambers used to measure the intensity of the incident (I_0) and transmitted (I_1) beam (Fig. 2.11c). This hutch is dedicated to measurements in transmission mode with an unfocused millimetric beam, since the position of the chamber is far from the second mirror focal point. The second experimental chamber (EH2) is the principal experimental hutch featuring a vacuum sample chamber in between two ionization ones for transmission acquisition, a smaller chamber for the contemporary and continuous standard acquisition (usually foils of the element analyzed in the sample chamber) and a final ionization chamber (I_{ref}) for the acquisition of the reference transmission signal (Fig. 2.11d). Moreover, the EH2 is equipped with swapable fluorescence detectors (a 12 elements high purity germanium detector or a 4 channels SDD silicon one, optimized for the lower energy range) which allow to perform fluorescence acquisitions and the analysis of diluted samples, such as trace elements in geological matrices and/or highly diluted liquids in the 10 ppm-range. EH1 and EH2 sample chambers and sample holders are equipped with motorized motors for translations and rotations, vacuum systems and the possibility of mounting a variety of manipulators hosting cold fingers/cryostats for low-T°

measurement (up to liquid He T°), high-T° reactor cells, electrochemical cells and custom ones. Recently, an outstation for X-Ray Powder Diffraction (XRPD) was developed and tested, which enables long-range structural analysis ideally complementing the local-range structural information achievable through XAS characterization (Lepore et al., 2022).

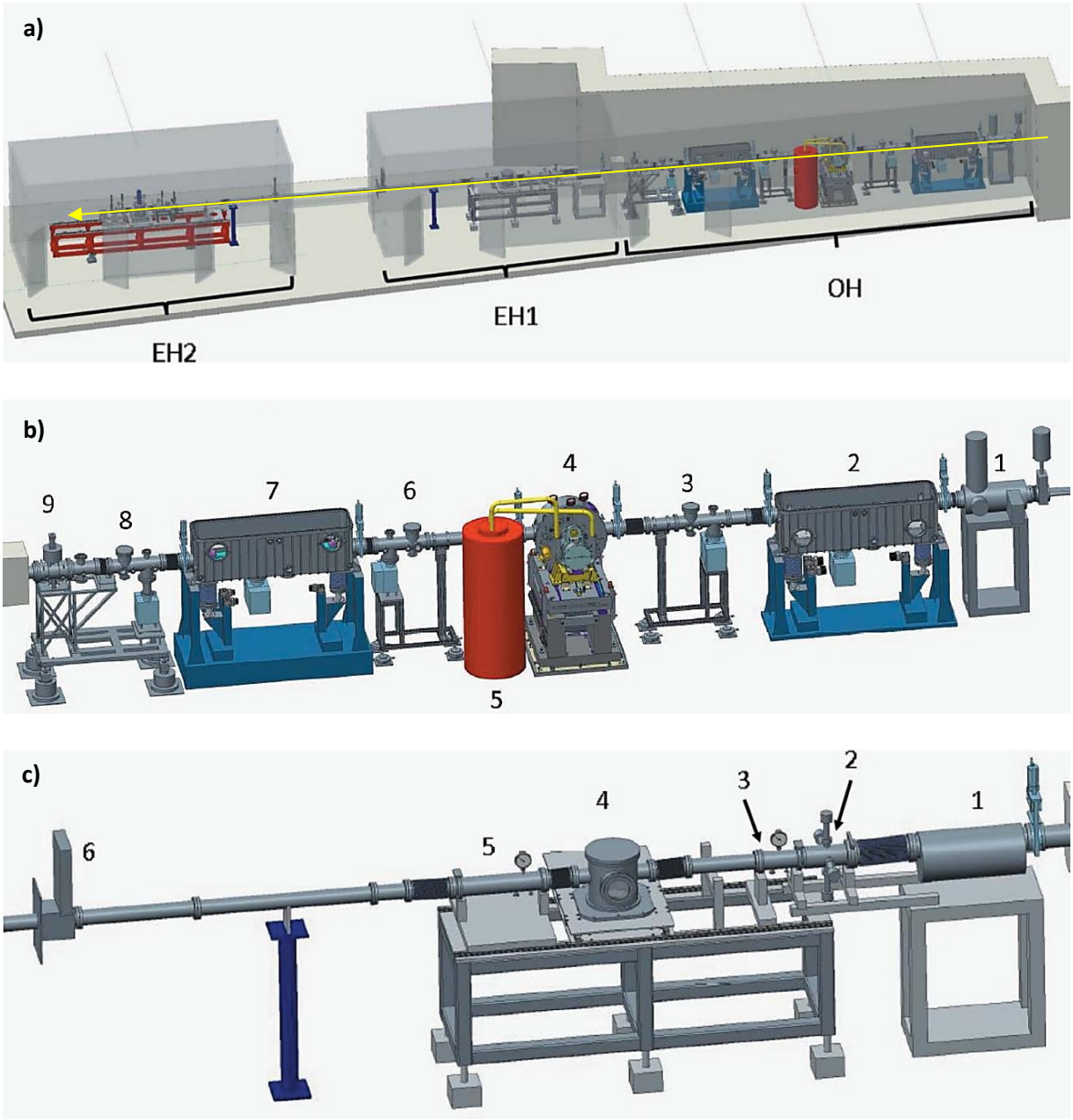

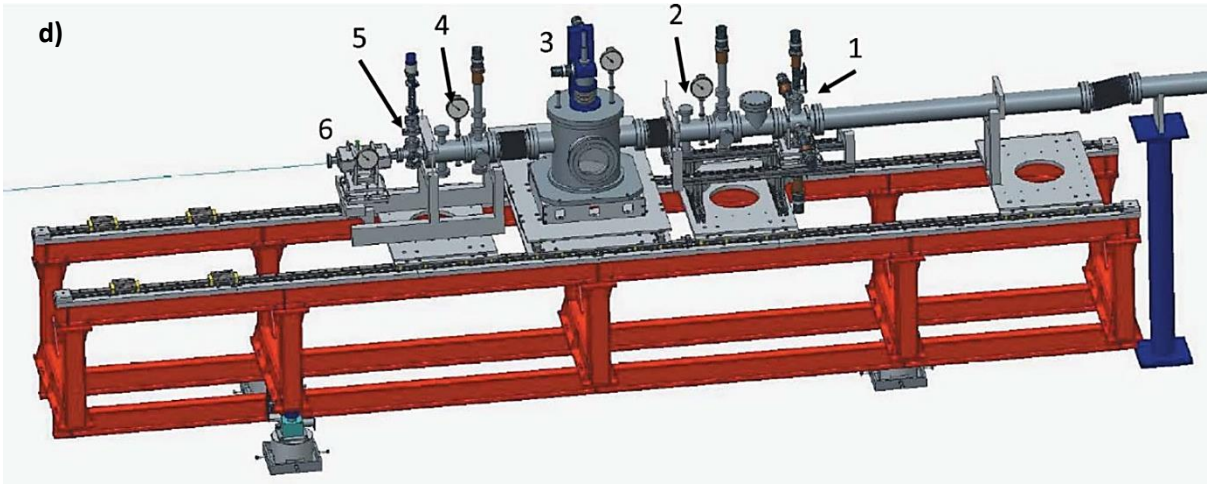

Figure 2.11: rendering of the LISA-BM08 and its hutches. ***a)*** *General layout of the beamline. The center of the first hutch (optics hutch, OH) is about 28 m from the source, the first experimental hutch (EH1) is at 37 m and the second experimental hutch (EH2) is at 49 m with indication of the beam path (yellow arrow).* ***b)*** *Side view of the OH. The numbers label the different elements: 1) chamber with principal slits, attenuators and white beam monitor; 2) first collimating mirror M1; 3, 6, 8) beam monitors; 4) monochromator; 5) cryocirculator; 7) second focusing mirror M2; 9) beam shutter.* ***c)*** *Side view of the EH1. 1) chamber with low-energy mirrors; 2) secondary slits; 3) ion chamber I_0; 4) sample chamber; 5) ion chamber I_1; 6) shutter.* ***d)*** *Side view of the EH2. 1) secondary slits; 2) ion chamber I_0; 3) sample chamber; 4) ion chamber I_1; 5) reference foils holder; 6) ion chamber I_{ref}. From (D'Acapito et al., 2019), modified.*

2.2.2.1.2. XAS introduction

A specific expertise on XAS technique was personally developed through a long @LISA internship in which I learned the basics of the technique and XAS data treatment, performed preliminary tests and finally, with beamtime awarded, acquired the measurements that will be discussed in this study. The examples that will be shown in this paragraph were personally realized during the above-mentioned internship.

XAS is a local-structure sensitive and element specific technique based on the measurement of the variation of the absorption coefficient as a function of the applied X-ray energy (μ(E)). XAS has been an important tool to gather structural information at the atomic level in the last decades, while being importantly promoted by the discover and diffusion of the synchrotrons in the second part of the 20th century. Its properties are due to the fact that the absorption energies and the energy of the emitted fluorescence photons are characteristic for an element and depend on its electron configuration. When their energy is sufficient, the X-ray photons

absorbed by a target element cause some of its core electrons to leave the atom or to be promoted to higher energy levels, leaving the absorber atom in an unstable excited state. The so created vacancy is filled by an electron from higher shells resulting in an excess of energy, which is then released internally as a photon. The photon can be internally converted, forcing an outer shell electron to be ejected as an Auger electron, or can exit the atom as characteristic X-rays, whose energy equal the difference between the core hole and the higher shells from which the substituting electron came (photoelectric effect). The energy level origin of the excited electron gives the name to the phenomena and the eV position of the edge observed in the resulting energy spectra (K-edge absorption for the electrons from the 1s level, L_I-, L_{II}- and L_{III}-edge for the ones in the 2s, $2p_{1/2}$ and $2p_{3/2}$ respectively and so on). The absorption coefficient variation of a sample can be measured either directly or indirectly. The direct method monitors the intensity of the beam transmitted through the sample (I_1) in respect to the incident one (I_0) (transmission mode) while indirect methods commonly record the fluorescent emission (I_f) (fluorescent mode); the resulting spectra are generally comparable but the carried information differ in terms of analytical depth (the transmission mode probe all the sample in its thickness, the fluorescence mode has a lower penetration and an higher response from the sample surface) (eq. (21)).

$$\mu(E) = \log\left({I_1}/{I_0}\right) \propto {I_f}/{I_0} \qquad (21)$$

XAS experimental spectra can be divided into 2 main sections, processed through 2 separate spectroscopic techniques: X-ray Absorption Near the Edge Structure (XANES) and the Extended X-ray Absorption Fine Structure (EXAFS) (Fig. 2.12). In a simplified way, the XANES region corresponds to the energy region in which the electron is excited in mainly allowed transitions to unoccupied molecular orbitals while in the EXAFS region the electron is ionized and the photoelectron wavevector bounces off of nearby atoms (Andrews, 2006). For the sake of this study, the pre-edge region, where the electrons can be excited to the lowest energy unoccupied molecular orbital in un-allowed transitions, will be included as a part of the XANES one. However, it is important to highlight that pre-edge analysis of first-row transition metal K-edges has become an important technique for the evaluation of their electronic structures and local geometry, becoming in an effective method on its own (Getty et al., 2008). Since

the phenomena behind XANES and EXAFS are different, so are the information that can be extracted.

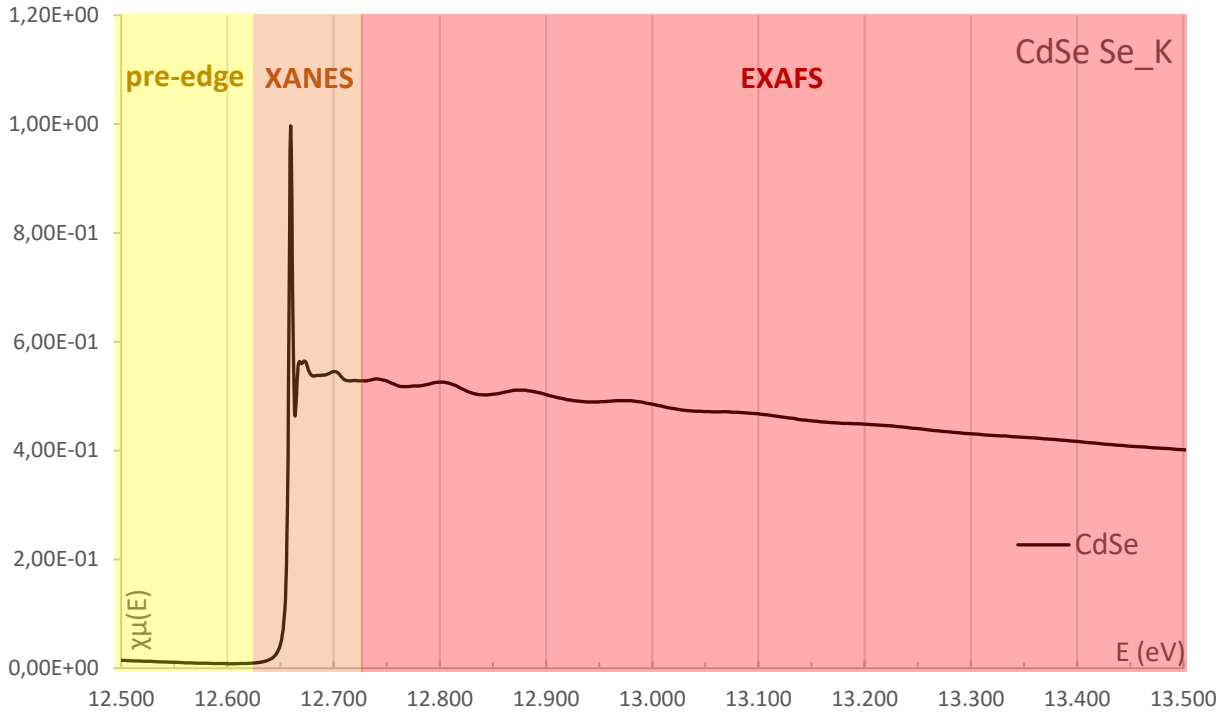

Figure 2.12: XAS spectrum of a synthetic pure CdSe sample, acquired at the Se K-edge during a tutorial at the Hercules 2022, with the different XAS sections highlighted.

XANES investigates the low-energy portion of a spectrum, from the start of the edge (including nearby pre-edge features) up to about 50 eV from the edge. XANES cannot be easily used for structural optimization due to the wavelength of the photoelectron being larger than the interatomic distances at low energy, requiring really complex simulation studies in order to create theoretical model to be adapted to the experimental data. Moreover, while the phenomena contributing to the EXAFS signal are properly understood and theorized, XANES lacks a "simple" analytic expression and a "straightforward" physical interpretation, making difficult to properly interpret all its spectral features. Despite that, XANES signal carries important chemical information about the oxidation number of an element, the local geometry of an atomic site and the consequent phase distribution inside the samples (Fig. 2.13). The valence state of an element directly affects the position of the edge, requiring more energy to promote/rip electrons the higher is the number of already missing ones, which can be observed in few eV shifts; this is particularly appreciable for 3d and 4d transitional metals (Fig. 2.13a). Information regarding the local geometry of an atomic site can instead be

obtained by the analysis of pre-edge features, which usually result from bound state transitions (such as the 1s to 3d transition in the 3d metals); the more distorted from a centrosymmetric site is the location of the probe element atoms, the more the pre-edge features will be evident (Fig. 2.13b). A typical example is the manganese which, in aqueous solution, shows no pre-edge features due to the typical octahedral coordination, while has an intense pre-peak when found in tetrahedral polyhedra. Due to these characteristics, XANES can be used to understand the phase distribution of an element inside a sample; assuming to know which phases are possibly present, the single pure-phases spectra can be acquired as standards and, through Linear Combination Fits (LCF) analysis, the sample spectrum can be decomposed into its component with semi-quantitative precision (see par. 3.3.2.1.). The larger XANES signal (comparately to EXAFS), can be used for measuring features in much more diluted and less ideal samples (e.g. high absorption matrix).

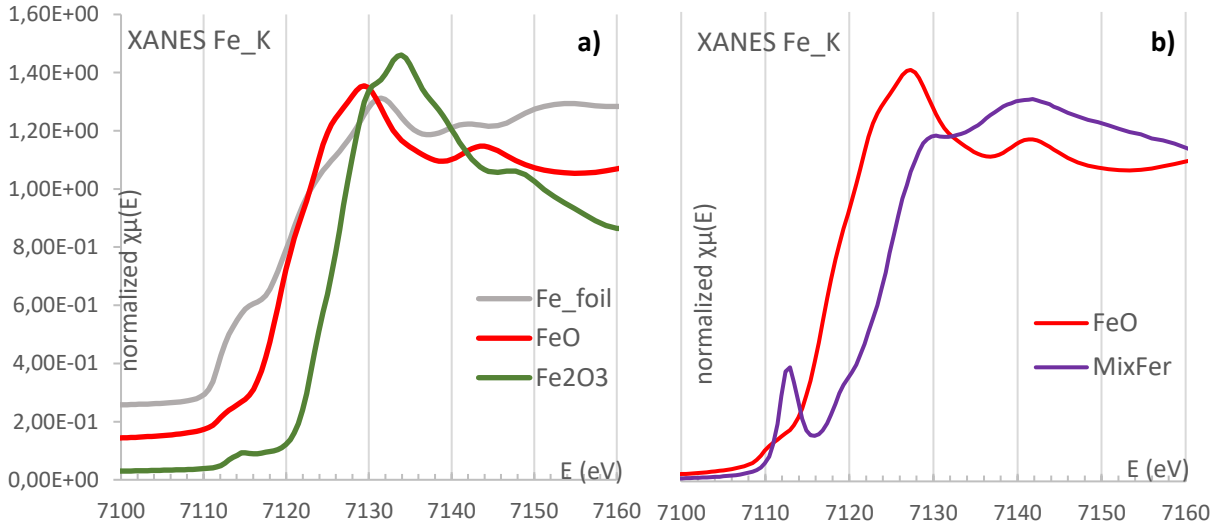

*Figure 2.13: XANES spectra acquired at the Fe K-edge of **a**) reference samples consisting of a pure iron metallic foil, a FeO and a Fe_2O_3 pellets, where it is easily noticeable the shifts at higher energies due to the increasing Fe valence state and **b**) a FeO pellet vs a freshly prepared MixFer one, where the presence of a pre-peak feature originating from the Fe(VI) in a tetrahedral coordination is compared to the absence of that feature in a wustite-structure, where the iron is located in perfect octahedra.*

EXAFS deals with the high energy portion of a spectrum, above about 50-100 eV to the end of it, and exploits the photoelectric effect illustrated above when the scattering from the electrons of the neighboring atoms is considered. The scattered photoelectron can return to the absorbing atom through different paths, altering the absorption coefficient, which represents the XAS phenomenon. Starting from the assumption that in the EXAFS region, the

spectrum is obtainable as individual path signals, the general EXAFS formula is expressed by eq. (22):

$$\chi(k) = S_0^2 * \sum_{j=shells} \frac{N_j}{kR_j{}^2} * f_j^{eff}(k) * e^{\frac{-2R_j}{\lambda}} * \sin\left(2kR_j + \phi_j^{tot}(k)\right) * e^{-2k^2\sigma_j^2} \quad (22)$$

Where the sum runs over all the paths of single or multiple scattering. The red parameters are the ones to be fitted, the blue ones are calculated with dedicated codes, such as FEFF. $f^{eff}(k)$ is the backscattering amplitude, with a different shape in k depending on the Z of the backscatterer element/ion, and $\phi^{tot}(k)$ the phase-shift of the neighboring atom in the j shell generated by the FEFF program from a theoretical model chosen in the beginning of the fit procedure. The amplitude reduction factor (S_0^2), the path half length (R, bond length in single scattering paths) and coordination number (N) of neighboring atom and the mean-square disorder of neighbor distance (σ^2, the Debye-Waller factor) are the parameters to be refined in order to match the experimental $\chi(k)$ signal through a series of transformation and step-by-step decisional making procedure, starting from the acquired μ(E) variation spectra in the energy domain (Fig. 2.14). In order: extract the oscillating part, the $\chi(k)$ function, from μ(E) (Fig. 2.14a); filter the desired $\chi(k)$ signal (red window in Fig. 2.14b); fit the resulting $\chi(R)$ (Fig. 2.14c) to a suitable model through a shell-by-shell procedure; double checking the fit results and the experimental signal transforming back the selected portion of the fitted R spectra into the $\chi(q)$ signal (Fig. 2.14d). Among the information attainable, there are: the number of neighbors atoms surrounding the central one, the chemical nature of the ligands and, more important, the interatomic distances at high precision.

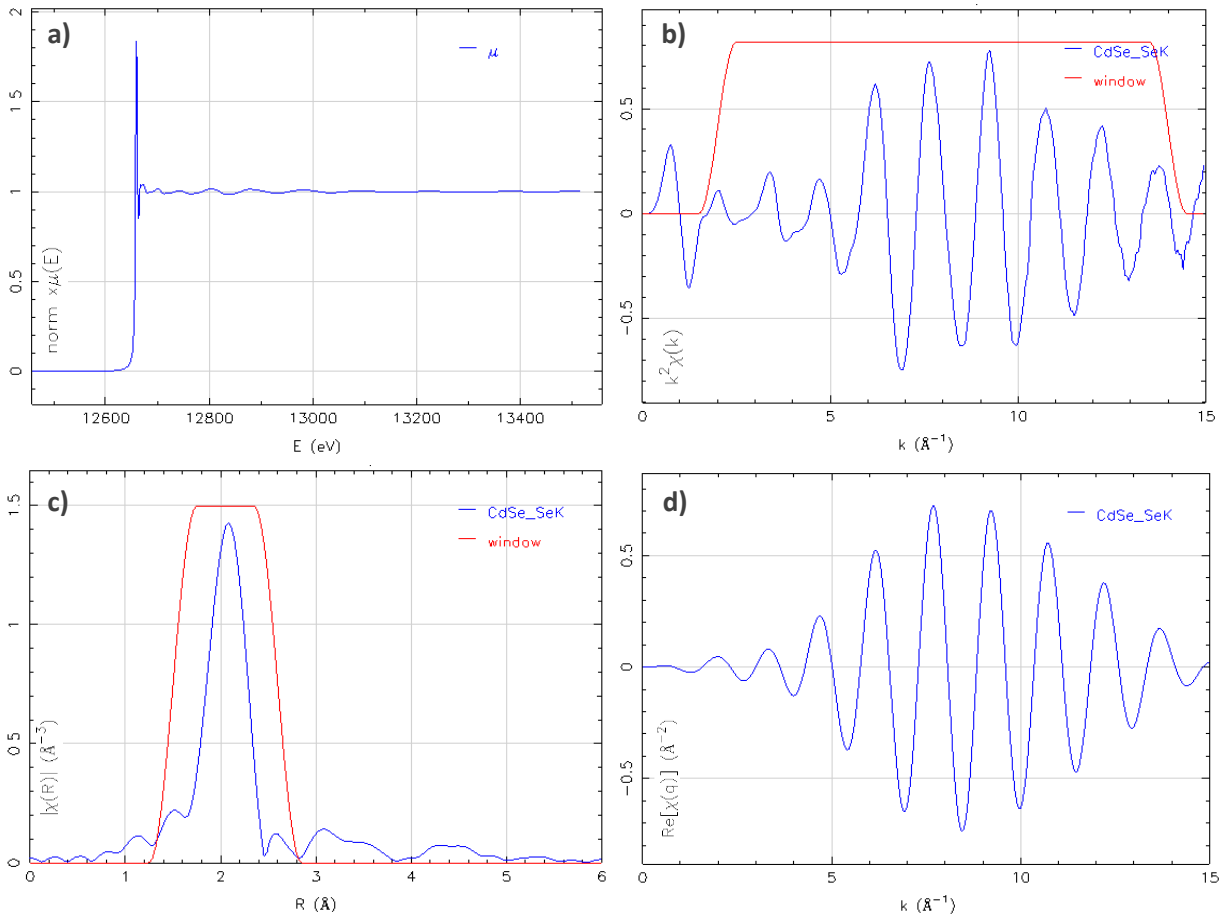

*Figure 2.14: XAS spectra of a synthetic pure CdSe sample, acquired at the Se K-edge, processed for EXAFS analysis as **a**) normalized absorption coefficient vs energy, **b**) wave vector space (with k weight = 2 to amplify oscillation at high values), resulting from the energy space converted to the photoelectron wavenumber one, showing the combination of the multiple scattering contribution from the atoms surrounding the selenium ones, **c**) radial distance space (R), resulting from the Fourier transformation of the wave vector portion of space selected through the window in Fig. 2.14b) (red line), which shows the scattering contributions coming from the different shells surroundings the selenium atoms up to 6 Å (distances which need to be fitted using a theoretical model to be quantitative accurate) and **d**) the inverse Fourier transform of the portion of radial distance space selected through the window in Fig. 2.14c) (red line), which shows the isolated scattering contribution of the selected shell.*

2.2.2.1.3. Design of the XAS experiment

Portions of the filters were cut and enclosed in Kapton tape, before being mounted on the sample holders (Fig. 2.15). The Kapton tape is commonly used in all kinds of X-ray analysis thanks to its thermal stability and high transmittance of X-rays.

Figure 2.15: photo of one of the 47 mm filter cut, with the cut portion enclosed in Kapton tape and mounted over one of the free slots available in the aluminum sample holders.

The XAS measurements were performed in the near-edge region of the spectra by means of X-ray XANES and, when possible, EXAFS. The experiment was performed in the Experimental Hutch 2 (EH2) of the BM08. Data were collected in fluorescence mode due to the low Hg contents inside the samples except for the high-concentrated standards, acquired in transmission mode. The different acquisitions were performed around the Hg L_{III}-edge (12284 eV, (Merritt, n.d.)) since, for larger elements such as Hg, the K-electrons require really high energies to be properly excited due to the larger positive charge influence of the Hg nucleus (Hg K-edge = 83102 eV (Merritt, n.d.)). The samples were measured at ambient temperature, with the exception of the nanoparticle ones measured at 80 K (nZVI and Fe+Ag NPs, plus a S6N_TQ sample for comparison), using a pair of Si [111] flat crystals. Higher harmonics rejection is obtained through Si coated collimating/focusing mirrors (with E_{cutoff} ~ 15 keV). Spectra were acquired with a fixed 5 eV step in the pre-edge region, 0.5 eV step around the edge and a k step of 0.05 $Å^{-1}$ up to a maximum value of k_{max} = 12 $Å^{-1}$ during the S6N_May21 trial and k_{max} = 14 $Å^{-1}$ during the S6N_Apr22 one (only for samples analyzed at 80 K, otherwise k_{max} = 8 $Å^{-1}$ to save time and focus on XANES acquisitions). Up to 6 consecutive scans per

sample were acquired for the S6N_May21 precipitates in order to increase statistics in the EXAFS region, while only 3 consecutives for the S6N_Apr22 ones, in order to be able to process a larger number of samples while still extracting clear-enough XANES signals. The number of scans was brought up to 4 for the S6N_Apr22 samples analyzed at 80 K, whose EXAFS spectra were identified as one of the main priorities during the A08-1-1089 experiment. In order to improve the Hg-signal/noise ratio, a very long acquisition time per point was always set (20 seconds per point). The samples consisted in portion of the 0.45 µm cellulose filters used to filter the treated waters and pellets of standard compounds. The procedure to extract the structural XANES signal followed the standard steps of: pre-edge background removal, followed by a spline modeling of bare atomic background, edge step normalization through a polynomial function interpolated far above the edge region and edge energy calibration. All these steps were realized using the software Athena (version 0.8.061) (P. A. Lee et al., 1981; B. Ravel & Newville, 2005). The procedure to extract the structural EXAFS signal ($k*\chi(k)$) started in an analogous way as the XANES signal extraction, with the pre-edge background removal, spline modeling of bare atomic background, edge step normalization and energy calibration performed using Athena. Afterwards, the modelling of atomic clusters centered on the absorber atom was obtained by the ATOMS routine using atomic coordinates from Cristallographic Information Files (CIFs) (Bruce Ravel, 2001), while the theoretical amplitude and phase functions were generated using the FEFF6 code (Rehr et al., 1992). Both ATOMS and FEFF6 macros were integrated in the Artemis software (version 0.8.014) (B. Ravel & Newville, 2005). Finally, EXAFS spectra were fitted using Artemis, both in the wave vector k and Fourier transform R space. Together the above-mentioned samples, a series of 8 Hg standards (montroydite (HgO); synthetic HgO; cinnabar (α-HgS, hexagonal); metacinnabar (β-HgS, cubic); calomel (Hg_2Cl_2); $HgCl_2$; Hg_2SO_4; Hg(0)) was also analyzed in transmission mode in order to obtain information about the Hg phase distribution inside the resulting samples through the Linear Combination Fit (LCF) procedure, also implemented in Athena, applied to the XANES spectra. The standard samples, part of the LISA-BM08 standard stash, were primarily provided by Valentina Rimondi, a researcher of the Department of Earth Sciences of the University of Florence, who prepared them in her previous experiments on the beamline. Finally, spectra of cinnabar mounted in the reference chamber were also measured in transmission simultaneously at each spectra acquisition, in order to monitor possible energy

shifts during consecutive data acquisitions and as a reference for energy alignment during the following data treatment.

- Results and Discussion –

3.1. pe-pH stability diagrams

The pe-pH stability diagrams (namely the "Pourbaix diagrams") are powerful tools to predict the form in which an element will be present in an aqueous solution or in contact with it. Any point of the diagram gives the thermodynamically most stable (and theoretically the most abundant) form of the element, based on the species equilibria considered, the pH and the reduction potential conditions of its environment ("pe", where pe = E_H/0.05916, "E_H" being the voltage potential with respect to the Standard Hydrogen Electrode (SHE), measured in volts).

Despite the huge number of studies on the iron phases equilibria, the Pourbaix diagrams directly involving ferrate species are pretty outdated and generally realized using the line-method (here referred as "LM") (Fig. 3.1) (M. Cataldo-Hernández et al., 2018; Virender K. Sharma, 2011). During the first part of this PhD course, a revision of the Fe-O-H system was performed (Fig. 3.2, 3.3) using a state-of-the-art point-by-point mass balance approach (here referred as "MB") (H. H. Huang, 2016), thanks to the knowledge acquired through PhD courses. This method performs equilibrium calculations over an array of points representing each one pH and one pe value of the entire pH-pe range of the system, and then combines the areas with different dominant species for building the diagram, being "dominant species" the ones with the highest absolute element-content (in moles) among the species considered. The diagrams presented in this study were realized using a 550x550 points grid and computed within the boundaries provided by the water stability field in the 0-14 pH range. The point-by-point MB approach allows for the consideration of secondary and tertiary abundant phases too, which was useful for visualizing the otherwise hidden ferrate stability fields, as well as other variables such as gas pressure and T°. The calculation was performed using *Phreeplot* (Kinniburgh & Cooper, 2011), version 1*,* a program for making geochemical plots and studying geochemical models exploiting the *PHREEQC* chemical engine (Parkhurst & Appelo, 2013), in this case the 3.6.2-15100-x64 version. The database used was the *wateq4f* (Ball & Nordstrom,

1991), in the "6895 2012-08-21 18:10:05Z" version, and the thermodynamic properties of Fe(VI) and Fe(V) compounds have been checked and added to the *wateq4f.dat* file (FeO_4^{2-}, FeO_4^{3-} and their protonated species respectively, using (Virender K. Sharma, 2011; Wood, 1958) and references therein). Whenever the solids precipitation is accounted, the additional phases/minerals considered were: mackinawite, magnetite, hematite, maghemite, goethite, $Fe(OH)_3$ (2-line ferrihydrite), greigite and $Fe_3(OH)_8$.

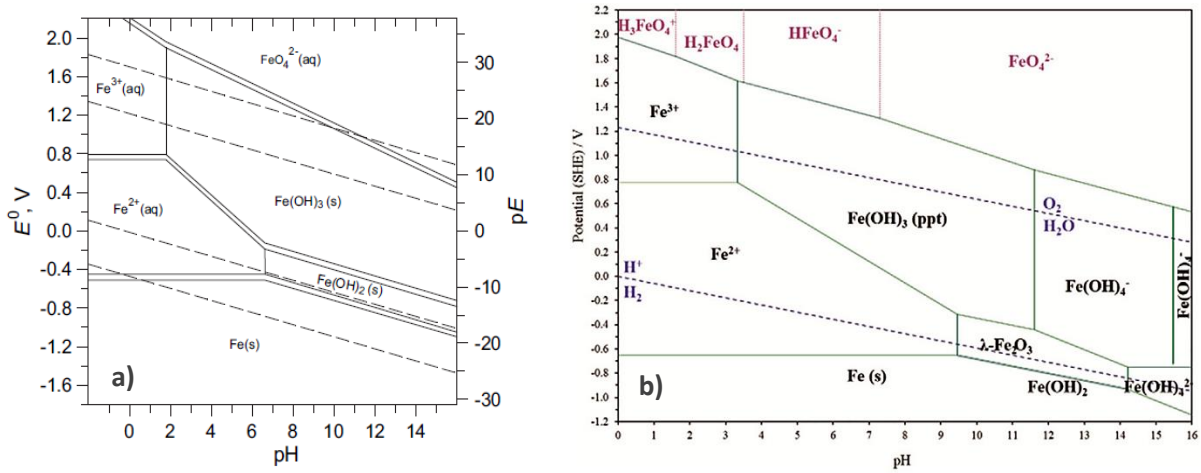

*Figure 3.1: simplified Pourbaix diagram for iron solutions obtained with the line-method, from **a**) (Virender K. Sharma, 2011) and **b**) (M. Cataldo-Hernández et al., 2018).*

Figure 3.2 shows the effect of different starting [Fe] in aqueous solution on the final iron phases equilibria, both with and without the solid precipitation accounted.

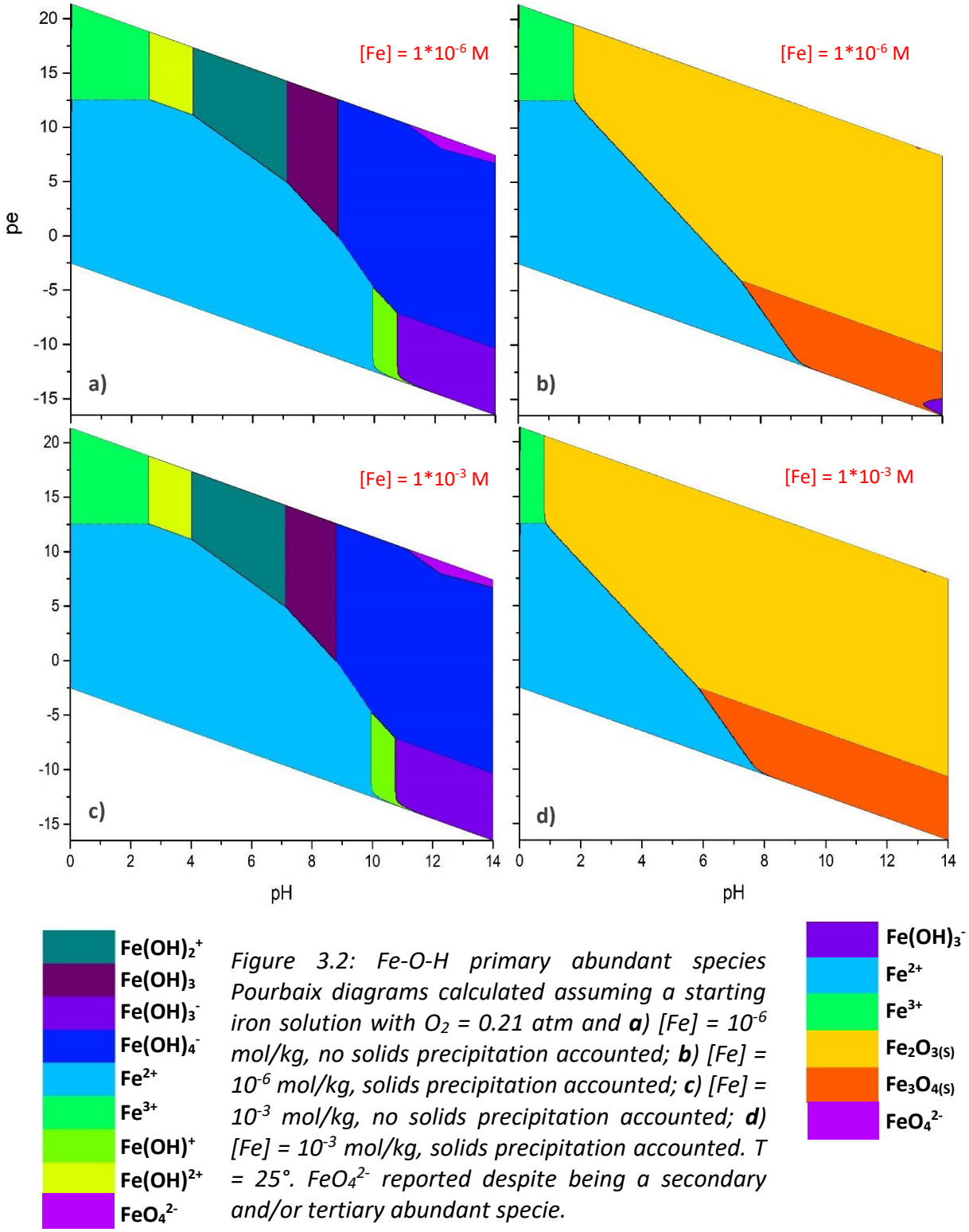

*Figure 3.2: Fe-O-H primary abundant species Pourbaix diagrams calculated assuming a starting iron solution with O_2 = 0.21 atm and **a**) [Fe] = 10^{-6} mol/kg, no solids precipitation accounted; **b**) [Fe] = 10^{-6} mol/kg, solids precipitation accounted; **c**) [Fe] = 10^{-3} mol/kg, no solids precipitation accounted; **d**) [Fe] = 10^{-3} mol/kg, solids precipitation accounted. T = 25°. FeO_4^{2-} reported despite being a secondary and/or tertiary abundant specie.*

Since the spontaneous decomposition of ferrate(VI) in water leads to formation of molecular oxygen (eq. (1)), the effect of the O_2 partial pressure was also taken into account, using a water solution with an iron content of 10^{-6} mol/kg and pO_2 = 0.21 and 1 atm, both with and without the solids precipitation accounted (Fig. 3.3).

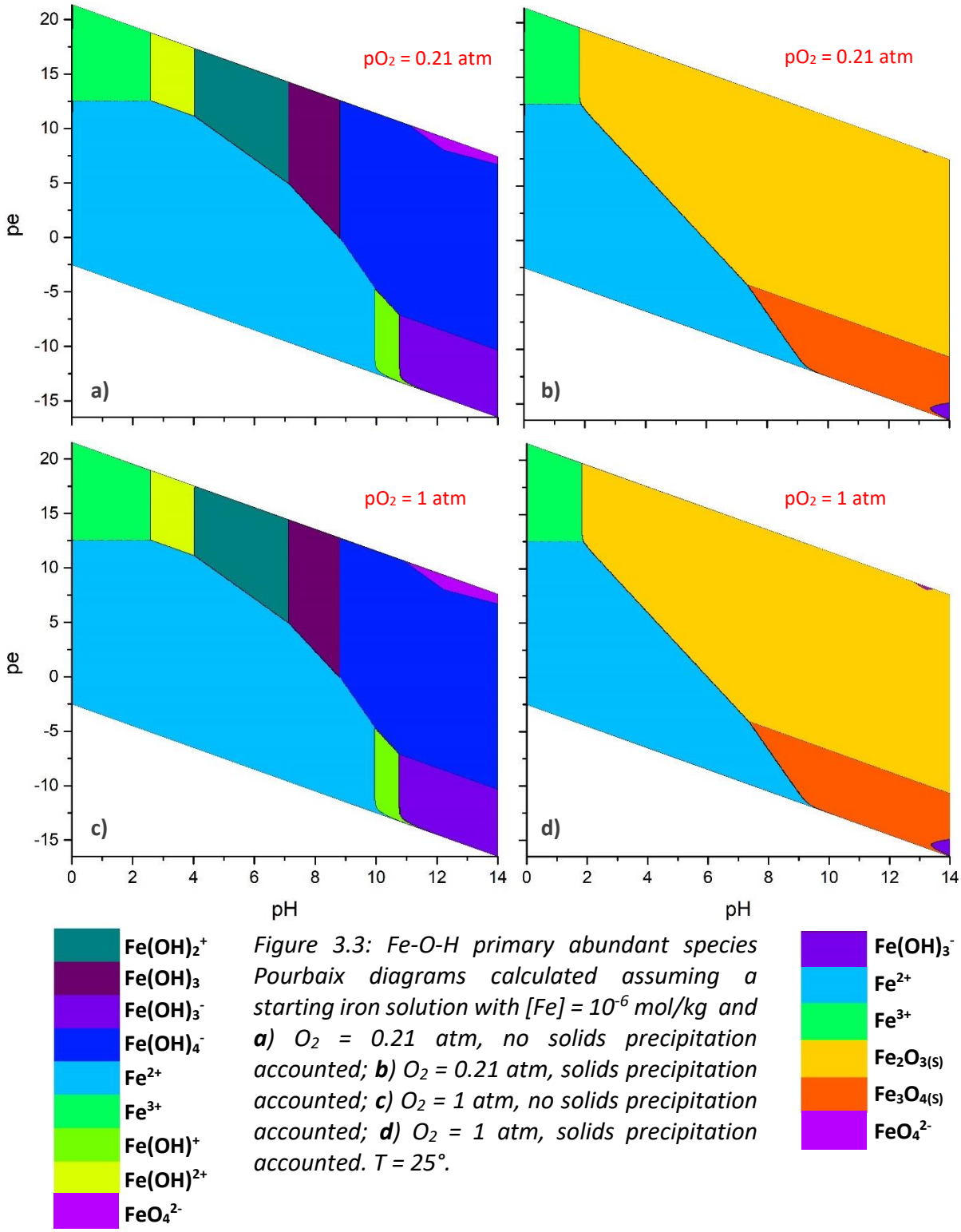

*Figure 3.3: Fe-O-H primary abundant species Pourbaix diagrams calculated assuming a starting iron solution with [Fe] = 10^{-6} mol/kg and **a)** O_2 = 0.21 atm, no solids precipitation accounted; **b)** O_2 = 0.21 atm, solids precipitation accounted; **c)** O_2 = 1 atm, no solids precipitation accounted; **d)** O_2 = 1 atm, solids precipitation accounted. T = 25°.*

The Pourbaix diagrams presented in this study represent an appreciable improvement over the ones published even in recent studies (Fig. 3.1). While the LM allows for an easy-to-read and immediate interpretation of the different iron phases stability fields, the point-by-point MB approach used here accounts for multiple equilibria, calculated simultaneously for each point in the pe-pH grid, allowing a deeper multi-level consideration of less abundant phases. In this way, it was possible to identify a small area at high pe and high pH values (Fig. 3.2, 3.3) where Fe(VI) is actually stable as a secondary or tertiary phase between the resulting species with the highest absolute iron-content and to study the direct influence of other parameters on its magnitude (Fig. 3.4). On the contrary, the LM diagrams do not show any possible presence of Fe(VI) inside the water stability field, confining it in the above outside region and not accounting for any modification of the relative Fe(VI) fields with different occurring conditions (Fig. 3.1). The obvious division of "oxidized species" residing in the high Eh areas (from low to high pH: Fe^{3+}, $Fe(OH)^{2+}$, $Fe(OH)_2^{+}$, $Fe(OH)_3$, $Fe(OH)_4^{-}$ and FeO_4^{2-} in solution and Fe_2O_3 (hematite) as solid product) and "reduced species" in the low Eh areas (from low to high pH: Fe^{2+}, $Fe(OH)^{+}$ and $Fe(OH)_3^{-}$ in solution and magnetite (Fe_3O_4) as solid product) is respected, even if the higher number of phases equilibria considered is evident when accounting for the greater subdivision of the larger fields (Fig. 3.1 vs . Fig. 3.2, 3.3). Moreover, while the straight separation lines in the LM Pourbaix diagram revolve around single electrochemical and/or acid-base reaction, MB method simultaneously solves all thermodynamic equations, equilibria and mass balances at each given point, returning more realistic separation curves depending on the resolution given. While this is evident in the comparison between Fig. 3.1 and Fig. 3.2, 3.3 it is not so pronounced using a 550x550 grid, adopted here for relatively fast calculation outputs. The fact that in some calculation the solids precipitation is suspended (Fig. 3.2a, 3.2c, 3.3a, 3.3c, 3.4) was a choice made to emphasize the aqueous solution environment without accounting for precipitation kinetics or reaction rates in order to calculate intermediate metastable equilibria. In this way it is possible to obtain a model situation more closely representing the timespan of ferrate(VI) syntheses. The found Fe(VI) pe-pH position in the point-by-point MB diagrams is compatible with the conditions sought during the various synthesis methods involving iron solutions, which aim to create a strong oxidizing environment in concentrated OH^- liquids (par. 1.1.3.). The extension of the Fe(VI) stability field is reduced when solids precipitation is accounted into the equilibria (Fig. 3.2b, 3.2d, 3.3b, 3.3d).

The effect of the iron dilution on the final speciation is marked in the "solid precipitation accounted" case, while being negligible into the "no solid precipitation accounted" one (Fig. 3.2); 10^{-6} M and 10^{-3} M iron contents were chosen as representatives of poor and enriched water respectively at the extremes of the natural iron content normally found (about 56 ppb vs 56 ppm respectively). It is evident that, in a more diluted solution, the soluble species have larger predominance areas and a reduction in total [Fe^{2+}] and [Fe^{3+}] reduces the driving forces of magnetite and hematite, as testified also from the $Fe(OH)_3^-$ stability field, disappearing at the higher total iron content.

The effect of the O_2 partial pressure, instead, has no visible effect on the shapes of the different stability fields while considering a water in equilibrium with atmosphere or an enriched one, regardless of the case (Fig. 3.3). The only visible effect is the upward translation of the superior limit of the water stability region, which defines the condition beyond which water is oxidized to oxygen. This directly impact the Fe(VI), as discussed below.

The combined effect of iron content and pO_2 onto the Fe(VI) field is depicted in Fig. 3.4, both in terms of extension and resulting FeO_4^{2-} concentrations; the plots show the conversion % of FeO_4^{2-} over the different total Fe contents, point-by-point over a pe-pH range focused on the ferrate(VI) stability conditions. Increasing the total iron content from 10^{-6} (Fig. 3.4a) up to 10^{-3} M (Fig. 3.4b) has no marked effect onto the extent of Fe(VI) stability field nor on the conversion %, pointing up to a proportionate rising in the final FeO_4^{2-} concentrations. Conversely, the pO_2 extending upwards the water stability region, extends the Fe(VI) ones too as a secondary and/or tertiary abundant phase at equal [Fe] total, offering at equal pH values more favorable oxidizing conditions (Fig. 3.4c, 3.4d). Interestingly, bringing the total iron content up to 1 M (which is a value closer to the iron concentrations used in the wet synthesis procedures) sensibly increases the conversion % in the 13.5 to 14 pH range.

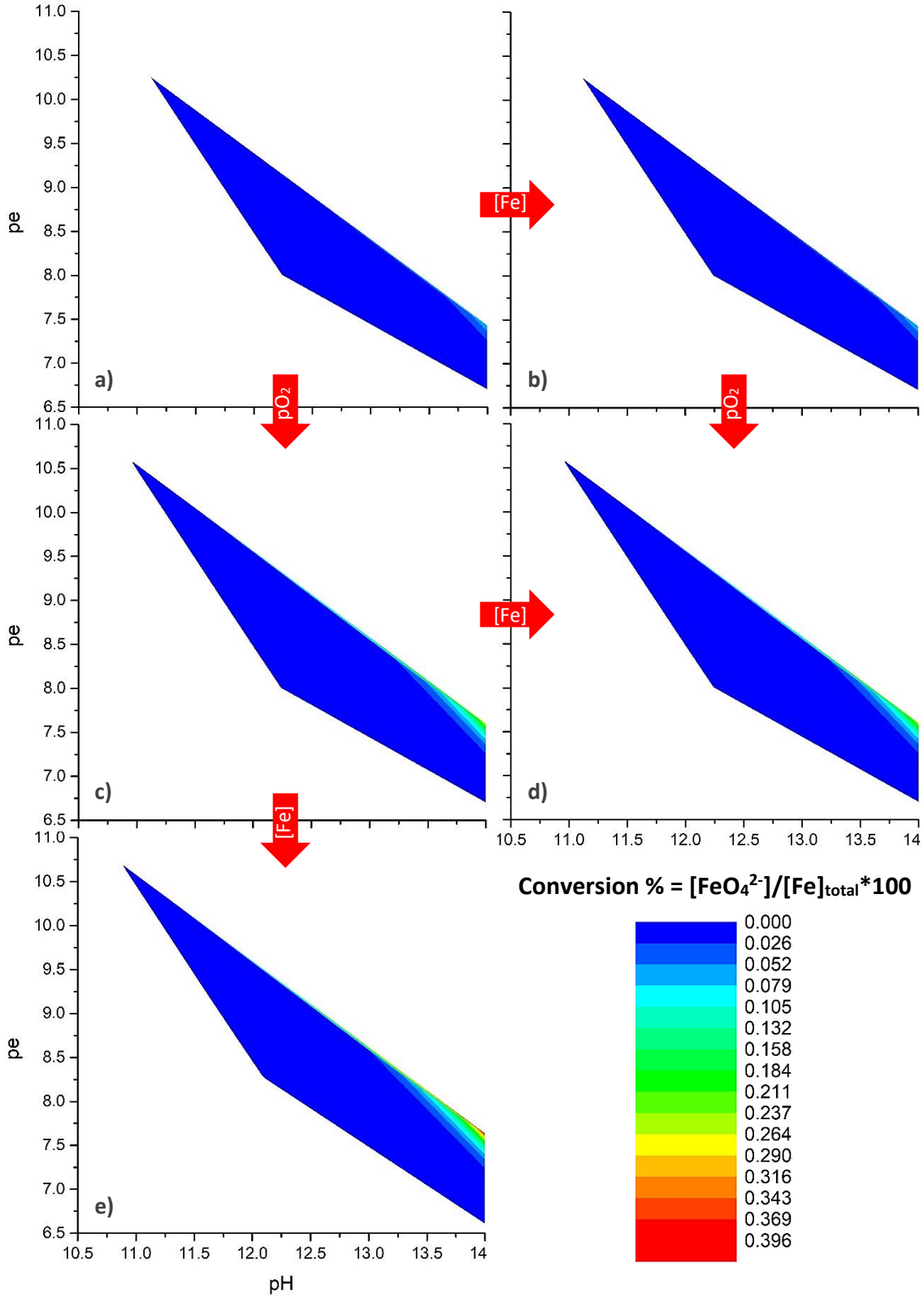

*Figure 3.4: focuses on the Fe(VI) stability field of the Fe-O-H Pourbaix diagrams plotted as FeO_4^{2-} % over the total [Fe], calculated assuming a starting iron solution with **a**) [Fe] = 10^{-6} mol/kg, O_2 = 0.21 atm; **b**) [Fe] = 10^{-3} mol/kg, O_2 = 0.21 atm; **c**) [Fe] = 10^{-6} mol/kg, O_2 = 1 atm; **d**) [Fe] = 10^{-3} mol/kg, O_2 = 1 atm; **e**) [Fe] = 10^{0} mol/kg, O_2 = 1 atm. T = 25°, no solids precipitation accounted.*

3.2. Liquid and solid ferrates(VI) syntheses

Over the course of this PhD study, liquid ferrate was generated through an original wet chemical synthesis, developed and tuned at the Geochemical Laboratory of the Earth Department (University of Florence) (par. 2.1.1.). The final product has the appearance of a dense dark purple fluid (Fig. 3.5a) which easily dissolves into water, immediately turning it brightly violet, a clear evidence of the presence of FeO_4^{2-} (Fig. 3.5b). Addition of around 0.50 g of liquid ferrate into 25 cc MilliQ flask and subsequent agitation, drastically increases the turbidity of the water (Fig. 3.5c), largely due to the presence of unreacted Fe(III) in this kind of ferrate(VI) product since the precipitation, separation and purification steps were avoided. After few minutes, the turbidity decreases due to the deposition of the unreacted Fe(III) and the Fe(III) produced by Fe(VI) decomposition, until revealing a clear violet solution in few hours whose color slowly vanishes over time (Fig. 3.5d).

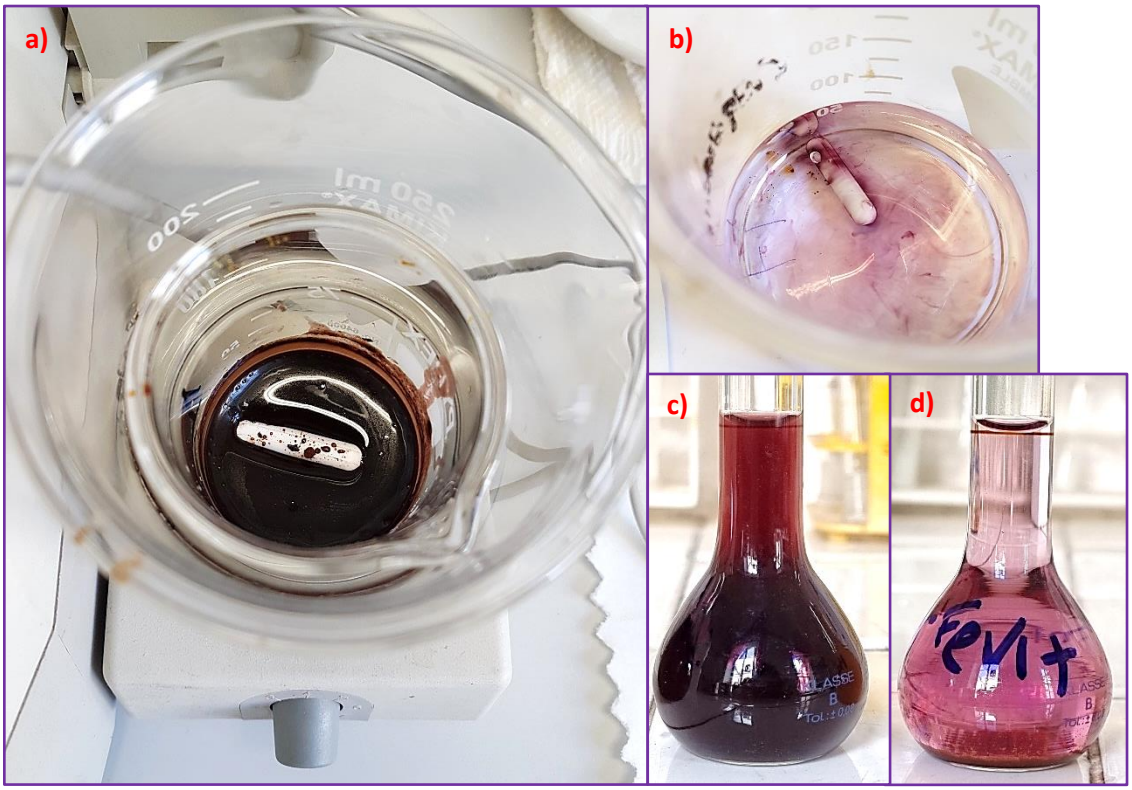

*Figure 3.5: photos of **a**) a batch of liquid ferrate at the end of the synthesis procedure (the white pill at the center of the image is the agitator of the magnetic stirrer underneath); **b**) the agitator transferred into about 50 cc of pure MilliQ water, whose residual drops of liquid ferrate stuck to its surface immediately dissolve into the water, turning it violet; c) MilliQ water in 25 cc flask, after the addition of about 0.50 g of liquid ferrate and subsequent agitation and **d**) the same flask after 4 hours.*

Concentrations of Fe(VI) in the obtained product were measured through the spectroscopy method in the UV-Visible range using a DR/2010 spectrophotometer from Hach® (Fig 3.6a), 1" cuvettes and the eq. (20). Mixfer was used to test the method since its Fe(VI) content was previously analyzed by the RCPTM (Tab. 2.1). In order to obtain a proper linear response from the instrument, high dilutions in MilliQ water were employed to keep the absorbance values between 0 and 1. The instrument was first set at 510 nm and a cuvette filled with only MilliQ water was used to calibrate the zero; Fig. 3.6b shows the resulting calibration curve. Given the low Fe(VI) concentration utilized in the various dilutions (between 10^{-5} and 10^{-6} M), a molar extinction coefficient (ε) equal to 1500 $M^{-1}cm^{-1}$ was considered as the best fit for our scenario (Cataldo Hernández et al., 2016). With an optical path of 2.54 cm, the obtained average value for the Fe(VI) content in the Mixfer was 4.8 ± 0.5 %, which is in the same order of magnitude of the 1.6 ± 3 % given in the attached analyses report, especially when considered the heterogeneous nature of the material, a 0-1 mm black-ish powder constituted by a 18.5 % of iron in various oxidation states.

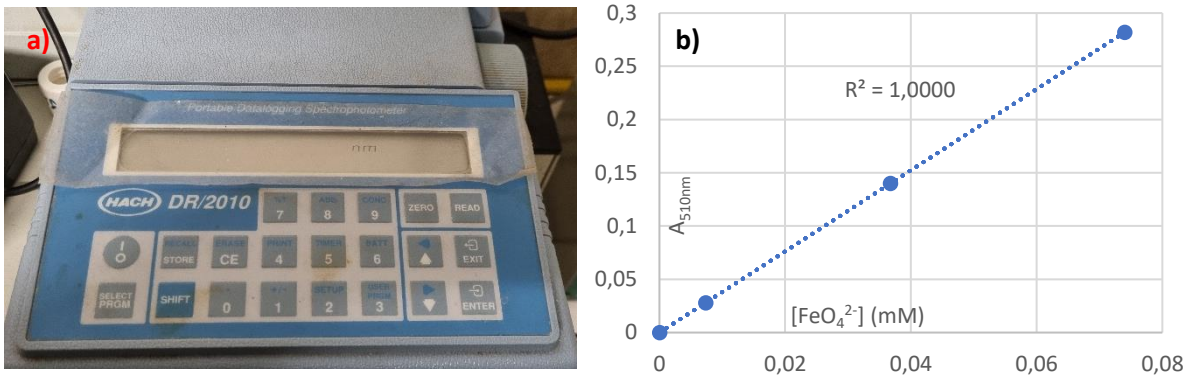

*Figure 3.6: **a**) photos of the DR/2010 spectrophotometer from Hach® and **b**) calibration curve (absorbance at 510 nm vs Fe(VI) concentration in mM) obtained using Mixfer at 1:50, 1:10 and 1:5 dilutions.*

Using the same procedure, the Fe(VI) content in the liquid ferrate produced in this study was attested to be around 20 ± 0.2 %. Considering the amount of reagents used and the conditions employed, this is in line with the results obtained by Alshahri et al. using NaClO, NaOH and $FeCl_3$ and Sun et al. using NaClO, NaOH and $Fe(NO_3)_3$ during their liquid ferrate syntheses (Alshahri et al., 2019; X. H. Sun et al., 2013).

In an attempt to produce a more pure, more stable solid ferrate(VI) product, with lesser of a contribute from the unreacted reagents (and lesser of an impact on the pH of the treated water), the separation, purification and drying steps were tested on the liquid ferrate. One of the main goals was to develop a method not relying on multiple dissolution-precipitation cycles, commonly suggested in the published works, which employ normally hundreds of ml of high concentrated alkali solution (up to saturation), with consequent high costs. The procedure initially involved using n-hexane as a water remover and methanol as a purifier for KOH, KCl and other impurities removal, without the employment of a drying agent to keep the costs low. To speed up the drying step, the product was spread on glass fiber filters (Fig. 3.7a) to absorb the remaining moisture and placed in a vacuum desiccator (Fig. 3.7b) at 30-35° overnight. Unfortunately, the complexity of this entire last part was soon discovered. The slow addition of KOH suggested to increase the nucleation of K_2FeO_4 before the first filtration step increased the viscosity of the liquid ferrate too, making it paste-like and preventing an easy displacement of the inside residual water by flushing n-hexane. Excluding the KOH supplementation, on the other hand, resulted in low amounts of solid deposition, with consequent low production yields. A big improvement came from the submersion of the KOH-enriched and filtrated product into n-hexane, subsequent strong stirring up to fragmentation of the paste and further filtration repeated up to 5 times which, however, did not prove sufficient in the removal of water. A proper removal of excess water with an inert hydrocarbon is absolutely essential to the success of the purification due to the aqueous ferrate(VI) high reactivity with alcohols and consequent K_2FeO_4 decomposition. During the numerous attempts, methanol always reduced the newly formed Fe(VI) almost instantly, turning the product brown; the purification step was then abandoned. At the same time, the high moisture still present in the sample batches ruined the final product during all the attempts, making it unstable and decomposing the ferrate(VI) into Fe(III) in a matter of few days, defeating the very purpose of producing a solid product. Only one small batch (~ 1g of final product) was able to be properly stabilized, revealing an high Fe(VI) content even 3 months after the synthesis (Fig. 3.7c). Regrettably, this was not sufficient to recognize the developed procedure as reliable and reproducible and the obtained product worth of proper chemical characterization (except for a preliminary XRD acquisition during a new X-Ray diffraction platform test at LISA-BM08, more on that below). The low-quantity solid ferrate(VI) produced was still used in the Hg removal experiments as a direct comparison to the Mixfer, but the

results obtained have to be considered in the light of that. The Fe(VI) content from UV-Visible spectroscopy was comparable to the Mixfer one, even if repeated measurements were affected by the high impurity content (probably in the form of Fe(III) oxides/hydroxides) which hindered their replication due to the solids scattering and the rapid degradation of Fe(VI) to Fe(III), visibly occurring in tens of seconds. Due to that, the [Fe(VI)] was only qualitatively taken as equal to the Mixfer one.

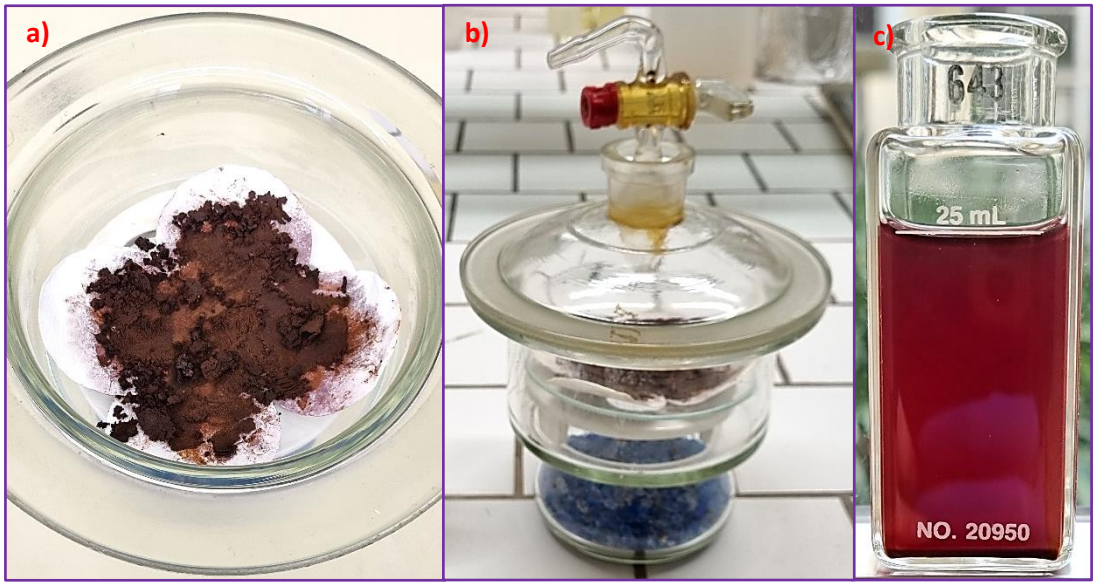

*Figure 3.7: photos of **a**) the successful batch of solid ferrate(VI), just synthesized, spread over fiber-glass filters; **b**) the solid ferrate(VI) inside the vacuum desiccator and **c**) 0.15 g of solid ferrate(VI) in MilliQ water.*

In the Fig. 3.8, the experimental synchrotron radiation XRPD pattern of the solid ferrate(VI) sample used for the Hg removal experiment is shown, compared with the calculated pattern obtained from the CIF file of K_2FeO_4 built using the data of Hoppe et al. during this PhD course (Fig. 1.6) (Hoppe et al., 1982). The XRPD acquisition was performed using the outstation recently build and tested on the LISA-BM08 beamline in the ESRF of Grenoble, France (Lepore et al., 2022). It is easily observable that the pattern is largely dominated by bands due particles having a nanometric size or, at least, a nanometric structural coherence. Among the most important features, those occurring at 7.5 and 12.5 2θ degrees can be assigned to a cryptocrystalline Fe oxyhydroxide phase such as 2-line ferrihydrite (Bardelli et al., 2023). Conversely, the main reflection, narrower than those already described, occurring at 6.2 2θ degrees, exhibits a very good agreement with the most intense reflection of the K_2FeO_4 pattern. Instead, the poor agreement between the experimental set of small intensity reflections in the 5-15 degrees range and the calculated potassium ferrate one suggests the

presence of additional phases. A tentative assignment operated with a search match procedure by *QualX2* software (Altomare et al., 2015) resulted in the suggestion of a spinel phase, such as magnetite. Accordingly, one can conclude that the Fe speciation in the considered sample is distributed over at least three phases, the main one being the cryptocrystalline 2-line ferrihydrite, while presenting experimental evidence of the appearance of the potassium ferrate(VI) phase too.

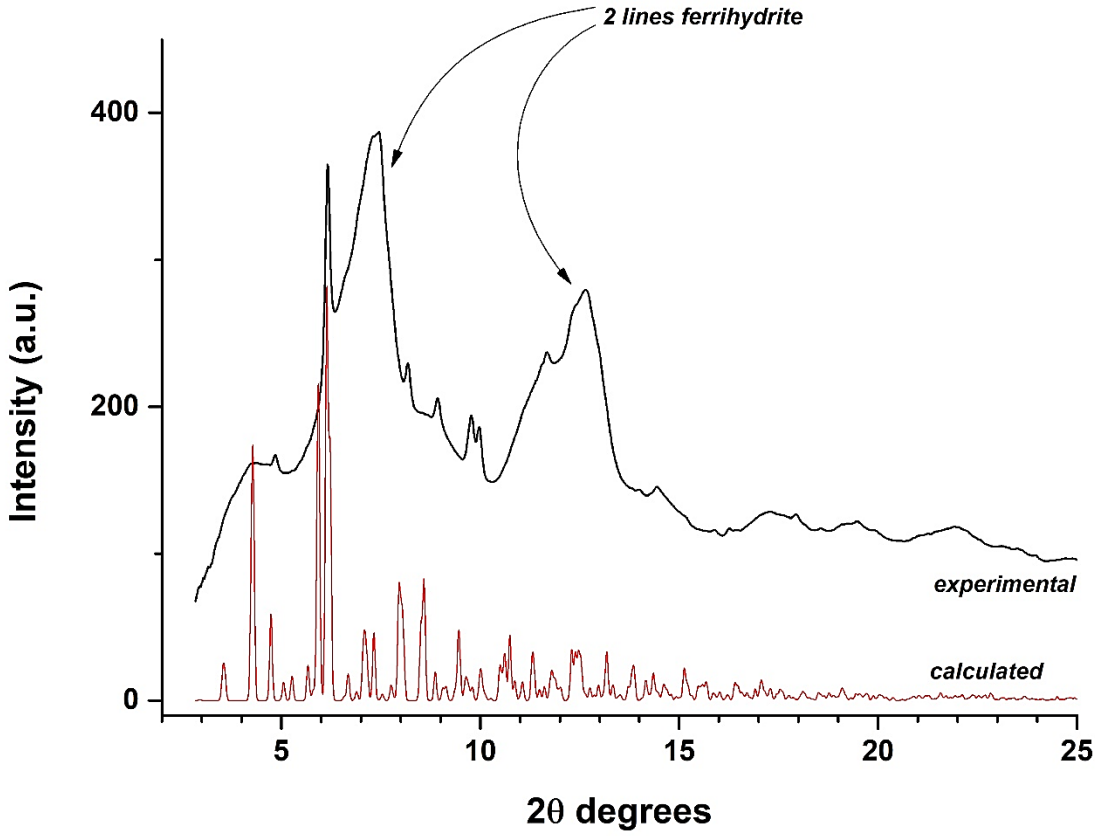

Figure 3.8: experimental XRPD pattern of solid ferrate(VI) in comparison with the K_2FeO_4 calculated one. The two features attributed to a ferrihydrite nanomaterial phase are indicated.

3.3. Mercury removal through ferrates and competitive nanoparticle reagents

For the first time, after the controversial studies published in the only two papers existing on laboratory solution exclusively (par. 1.2.2.), the results of the mercury removal experiments using ferrate-based products are shown in Figure 3.9 to 3.14, along with those of the other reagents. A summary with all the values and errors is given in Table 3.2. In Table 3.3 are shown the pH and Electrical Conductivity (EC) values of the treated waters. From Figure 3.15 to 3.17 some of the few significant ICP-MS data are displayed while in Table 3.4 are reported the ICP-MS analysis of the trace metals in S6N and GITA conducted in the earliest part of the PhD project, during a brief re-opening of the laboratories in the Covid pandemic spreading period.

3.3.1. Hg removal efficiency

Starting with the Hg(II) solution trials, Fig. 3.9 shows the results achieved during the HgSS_500ppb tests with different reagents. First of all, the TQ value endorsed the accuracy of the Hg solution preparation, with a value of 484 and an analytical error of ± 73 µg/L, which appears to be fixed at about 15 % for all the results provided by the C.S.A. Research Institute analyses. The application of the KOH reagent alone showed how alkalinization produced about a 32 % of Hg content decrease, not replicated by the KClO solution addition, which did not show significant variation from the starting HgSS_TQ. Fe(III) showed really high efficacy, scoring the highest mercury removal result of about 96 %. Liquid ferrate showed an high removal result too, lowering by about 91 % the starting mercury content of the TQ solution.

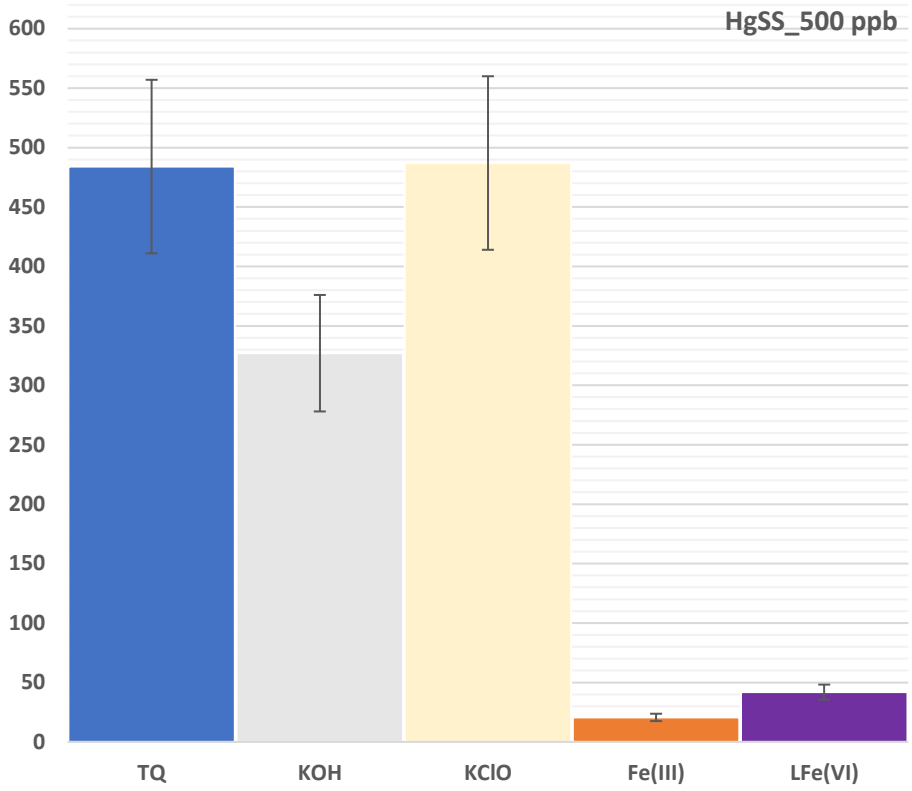

Figure 3.9: Hg content, in µg/L (ppb) in the treated HgSS_500ppb solution using different reagents. The error bars size results from the analytical errors given by the C.S.A. Research Institute.

The HgSS_1ppm trial saw the arrival of the RCPTM reagents and the starting Hg(II) content was raised up from 500 ppb to 1 ppm (Fig. 3.10). This time, the TQ analysis revealed a less accurate initial solution preparation, with a [Hg] value of 880 ± 130 µg/L reaching the target value of 1000 µg/L only due to the wide margin of error provided by the external laboratory. As with the HgSS_500ppb trial, the KClO treatment seemed to not have any significant removal effect towards mercury, with an about 11 % reduction post-treatment well within the analytical uncertainty. Conversely, Fe(III) and liquid ferrate presented high removal results, both lowering the initial Hg content by about 91 %, confirming the results of the previous trial. In contrast, solid ferrate and Mixfer appeared to have no effect on the mercury in solution, while the nZVI scored about 29 % removal. Unfortunately, the nZVI/2 sample was lost during the lab. transportation so no data are available for the half-concentration reagent case. Fe+Ag NPs achieved an about 70 % removal at full dose while decreasing down to about 61 % when half of the amount was used.

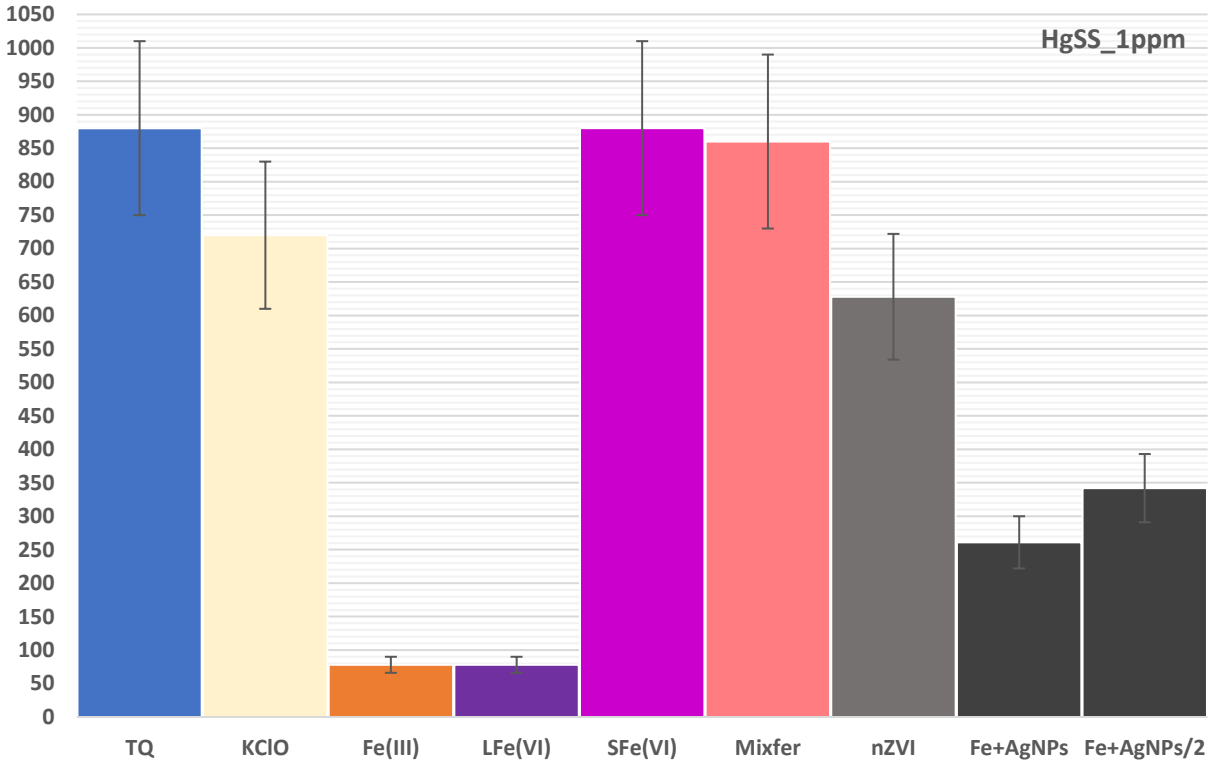

Figure 3.10: Hg content, in µg/L (ppb) in the treated HgSS_1ppm solution using different reagents. The error bars size results from the analytical errors given by the C.S.A. Research Institute.

Switching to ASS natural waters (Fig. 3.11), the first trial on S6N_May21 showed a starting Hg content value of 167 ± 25 µg/L, with the untreated S6N_TQ sample taken as reference. This value, as well as the pH and EC ones, falls within the broad range of values emerging from previous sampling campaigns, in agreement with the geochemical heterogeneity observed in the area, while positioning in the lower part of that range ((Vaselli et al., 2015) and personal communications). The addition of a solution of KOH-only did not produce any significant effect on the Hg content, suggesting that the mere strong alkalinization effect did not have a relevant impact in the natural water case. On the contrary, the inclusion of KClO changed significantly the scenario, even compared to the HgSS solutions, more than doubling the Hg outcome in the KClO sample while producing only a mild increase in the KClO_Pref variant, still within the analytical error when compared to S6N_TQ. The reasons behind these values do not lie in impurities possibly contained in the starting chemical reagents, which showed Hg contents of < 0.1, < 1 and < 0.1 µg/L for sole KOH, KClO and $FeCl_3$, respectively (added to MilliQ water at the same amounts than those used in the various samples and analyzed in the same external

lab with the same technique). The most plausible explanation found in this study for this evidence, as well as the widespread observable difference between post-treatment samples using unfiltered S6N water as the Hg source and those using the filtered variant, lies in the interaction between various components of the natural water and will be discussed in paragraph 3.4.3.. Proceeding ahead, the Fe(III) sample showed the best Hg removal efficiency with about 68% removal, confirming the known validity of ferric-base compounds for Hg remediation and the best overall scored registered with HgSS trials. Surprisingly, at this time, the liquid ferrate appears to have had no effect at all, producing only a mild increase in Hg content in the S6N_LFe(VI) sample, well within the analytical error; on the contrary, it lowered the mercury in solution by an about 40 % when the filtered S6N_May21 was used.

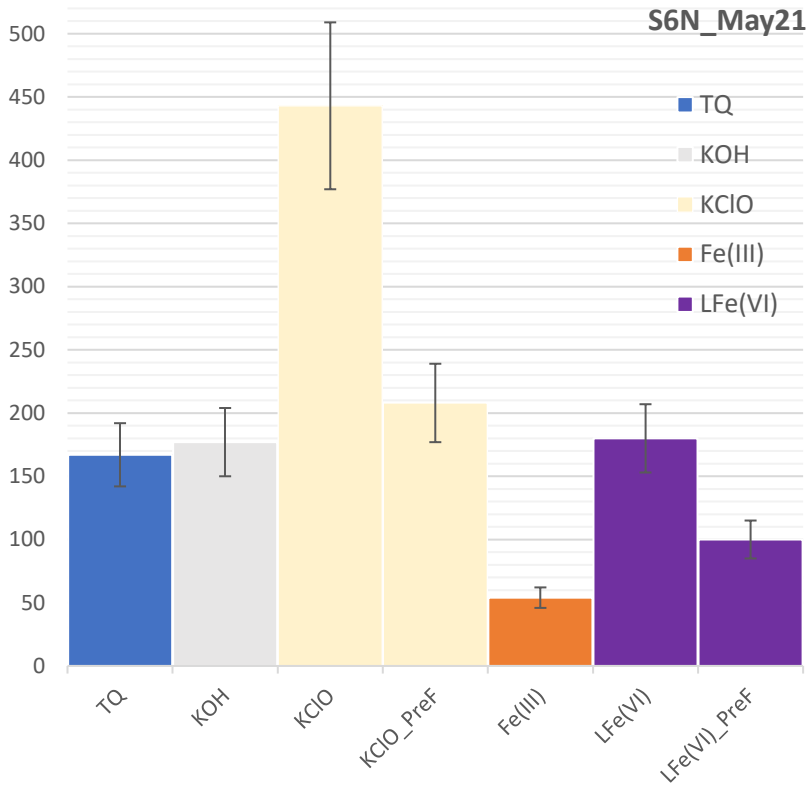

Figure 3.11: Hg content, in µg/L (ppb) in the treated S6N_May21 waters using different reagents. The error bars size results from the analytical errors given by the C.S.A. Research Institute.

A second test-trial was performed using the S6N water collected in April 2022 (Fig. 3.12). The test using the filtered S6N_Apr22 variant, was extended to all the reagents, which saw the arrival of the ones provided by RCPTM. In particular, the nanoparticle reagents were tested in progressively lower amounts (1, 1/2, 1/3), following the high performances reported by RCPTM in personal communications. This time, the TQ water showed a higher Hg content value of 202 ± 30 µg/l and no KOH only was tested to decrease the net amount of analyses to be performed. Again, the KClO reagent produced a marked increase in Hg content of about +58 %, which decreased to about +27 % in the KClO_Pref case, still within the uncertainty range. The Fe(III) reagent confirmed its high performances, with about 77 to 80 % mercury removal considering the two Hg source variants. Liquid ferrate achieved about a 38 % removal when S6N_Apr22 was used as a matrix, while improving not as much as in the S6N_May21 trial when switching to the filtered water, achieving about 51 % removal. The solid ferrate, employed 3 months after its synthesis, didn't promote any apparent decrease of the starting Hg content in the S6N_Apr22, scoring rather a mild increase (about +17 %) in the S6N_SFe(VI) case; however, an about 21 % removal was observed in the prefiltered variant, which represents a significant difference. The Mixfer treatment didn't produce a noticeable effect at the low amount used, except when exploiting the prefiltered water, where an about 11 % reduction was noticed, falling within the uncertainty range. Lastly, the nanoparticles materials showed two different interesting behaviors. The nZVIs removed about 41 % of the mercury in solution in the S6N_nZVI sample, confirming the average result from HgSS_1ppm trial, while showing an apparent small decreasing trend when lower amounts were employed, even if masked by the high uncertainties (Tab. 3.2). A similar trend can be observed in the prefiltered samples, which presented lower removal efficiency than the non-prefiltered ones, in contrast to what we have seen so far. In contrast with the HgSS_1ppm case, the Fe+Ag NPs achieved the best overall results, with a maximum removal of about 82 and 87 % in the S6N_Apr22 and S6N_Apr22_Pref waters respectively; a more distinct decreasing trend with the lower amounts used was observable, with higher removal efficiency per mg of reagent employed (Tab. 3.1). As in most of the other cases, the use of a filtered water showed lower final Hg contents.

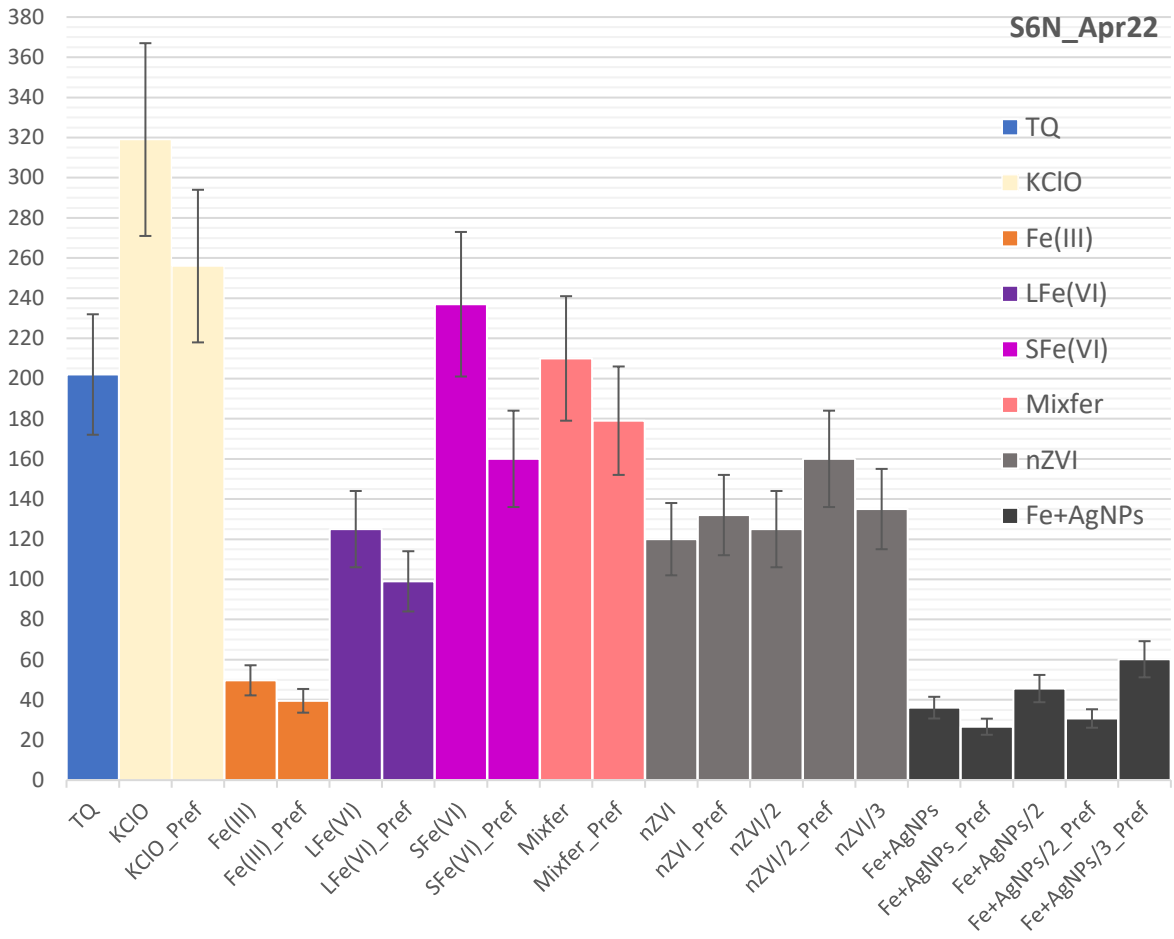

Figure 3.12: Hg content, in µg/L (ppb) in the treated S6N_Apr22 waters using different reagents. The error bars size results from the analytical errors given by the C.S.A. Research Institute.

	nZVI			Fe+Ag NPs		
	1	1/2	1/3	1	1/2	1/3
	Amount used (mg)			Amount used (mg)		
S6N_Apr 22	66	34	20	66	35	-
S6N_Apr22_Pref	56	33	-	64	33	18
	Amount used (%)			Amount used (%)		
S6N_Apr 22	100	51	30	100	53	-
S6N_Apr22_Pref	85	50	-	97	50	27
	Removal (%)			Removal (%)		
S6N_Apr 22	41	38	33	82	77	-
S6N_Apr22_Pref	35	21	-	87	85	70
	Efficiency (ppb_{Hg}/mg_{NPs})			Efficiency (ppb_{Hg}/mg_{NPs})		
S6N_Apr 22	1.2	2.3	3.4	2.5	4.5	-
S6N_Apr22_Pref	1.3	1.3	-	2.7	5.2	7.9

Table 3.1: amounts used (in mg and in % of the highest one), removal achieved (in %) and efficiency (expressed in ppb of Hg removed / mg of reagent used) for the nZVI and Fe+Ag NPs in their different trials at different amounts per 50 cc of water.

Lastly, a simple trial using the Hg contaminated soil from Petrineri, the S63, was attempted, which will help defining the interaction mechanism between various reagents and natural component mentioned earlier (Fig. 3.13). The analysis made on the water resulting from the interaction with the S63 without any other reagents addition, revealed a modest mercury leaching, as testified by the 1.03 ± 0.15 µg/L of mercury content. In contrast, treatment with KClO was successful in extracting a high amount of mercury from the soil, which reached 308 ± 46 µg/L in the post-treatment water. Liquid ferrate and Mixfer presented similar outcomes, even if with lower magnitude, since slightly less than half of the S63_KClO Hg content were reached. Fe(III) was the only reagent which appeared not to significantly interact with the S63, with a Hg concentration in the treated water of 2.7 ± 0.4 µg/L. Unfortunately, the solid ferrate treated sample was lost during transportation to the lab., even if an outcome similar to the Mixfer can be expected.

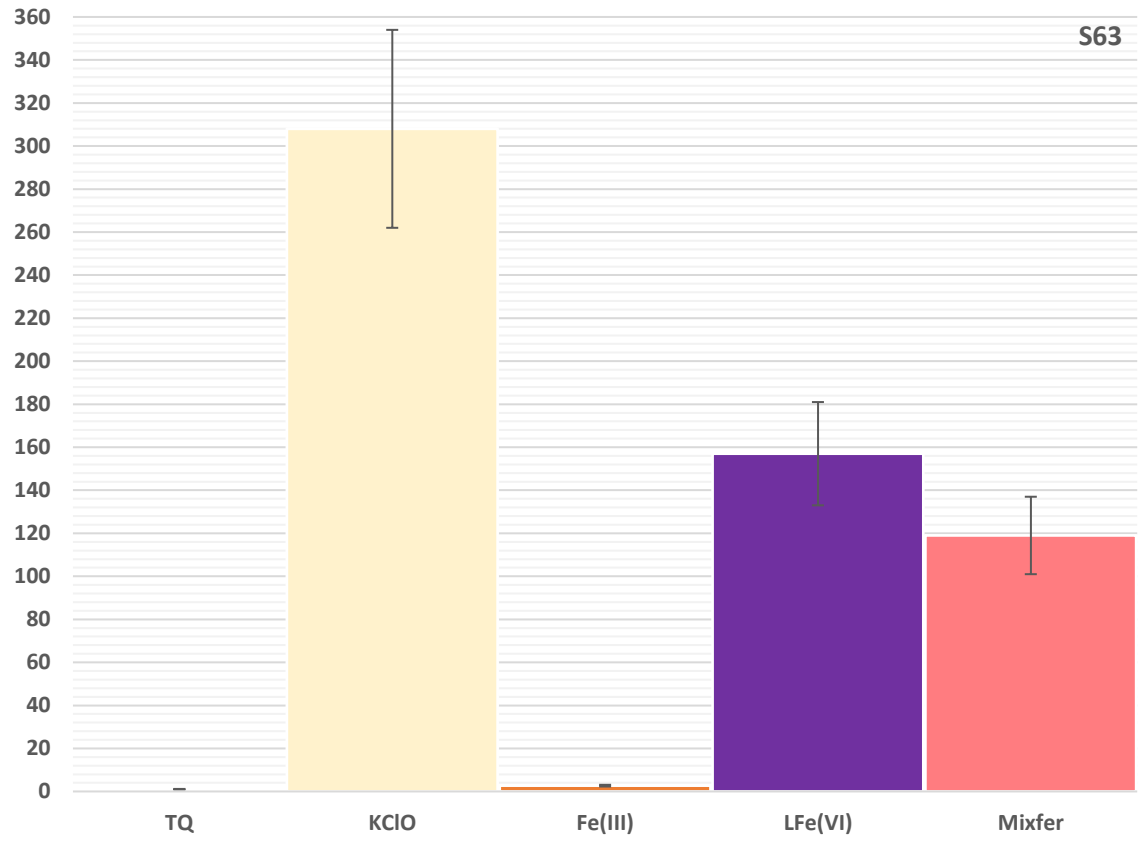

Figure 3.13: Hg content, in µg/L (ppb), in the treated S63 soil in MilliQ water, using different reagents. The error bars size results from the analytical errors given by the C.S.A. Research Institute.

Hg source	TQ		KOH		KClO		FeIII		LFe(VI)		SFe(VI)		MixFer		nZVI						Fe+Ag Nps					
															1		1/2		1/4		1		1/2		1/4	
	[Hg] (µg/L)	± (µg/L)	[Hg] (µg/L)	± (µg/L)	[Hg] (µg/L)	± (µg/L)	[Hg] (µg/L)	± (µg/L)	[Hg] (µg/L)	± (µg/L)	[Hg] (µg/L)	± (µg/L)	[Hg] (µg/L)	± (µg/L)	[Hg] (µg/L)	± (µg/L)	[Hg] (µg/L)	± (µg/L)	[Hg] (µg/L)	± (µg/L)	[Hg] (µg/L)	± (µg/L)	[Hg] (µg/L)	± (µg/L)	[Hg] (µg/L)	± (µg/L)
S6N_May21	167	25	177	27	443	66	54	8.1	180	27																
S6N_May21_Pref					208	31			100	15																
S6N_Apr 22	202	30			319	48	50	7.5	125	19	237	36	210	31	120	18	125	19	135	20	36	5.4	46	6.8		
S6N_Apr22_Pref					256	38	40	5.9	99	15	160	24	179	27	132	20	160	24			27	4	31	4.6	60	9
HgSS_500ppb	484	73	327	49	487	73	21	3.1	42	6.3																
HgSS_1ppm	880	130			720	110	78	12	78	12	880	130	860	130	628	94					261	39	342	51		
S63	1	0.2			308	46	2.7	0.4	157	24			119	18												

Table 3.2: summary of all the Hg contents from all the different trials with the relative analytical error (all in µg/L), coming from all the analyses performed by the C.S.A. Research Institute external laboratory.

Hg source	Sample	pH	Electrical conductivity (mS)
S6N_May21	TQ	7.1	0.352
	KOH	13.5	22.8
	KClO	13.5	29.2
	FeIII	13.4	21.4
	LFe(VI)	13.3	26.3
S6N_Apr22	TQ	8	0.401
	KClO	13.4	29.1
	FeIII	13.3	23.1
	LFe(VI)	13.3	25.6
	SFe(VI)	11.5	4.66
	Mixfer	10.4	0.589
	nZVI	8.3	0.401
	nZVI/2	8.4	0.409
	nZVI/3	8	0.388
	Fe+AgNPs	8.2	0.398
	Fe+AgNPs/2	8.2	0.387
S6N_Apr22_Pref	FeIII_Pref	13.4	23.4
	LFe(VI)_Pref	13.3	27.8
	SFe(VI)_Pref	11.5	4.56
	Mixfer_Pref	10.1	0.516
	nZVI_Pref	8.2	0.396
	nZVI/2_Pref	8.2	0.4
	Fe+AgNPs_Pref	8.4	0.397
	Fe+AgNPs/3_Pref	8	0.401
HgSS_1ppm	TQ	1.4	18.39
	KClO	13.2	21.2
	FeIII	13	15.4
	LFe(VI)	12.9	20.3
	SFe(VI)	1.7	18.31
	Mixfer	2.2	7.67
	nZVI	1.5	17.61
	Fe+AgNPs	1.5	18.23

Table 3.3: pH and conductivity measurements performed on the samples post-treatment and before their acidification for the following Hg content and ICP-MS analytical determinations.

The trace elements analyses were realized in the earliest part of the PhD project on a batch of S6N and GITA waters collected in October 2020 (S6N_Oct20 and GITA_Oct20 respectively) and on the S6N_May21. Unfortunately, the initial lack of experience regarding the system to be analyzed, an "in-progress" procedure still to be properly tested and designed in order to extract meaningful information, and the poor initial comprehension of the raw-material behavior severely undermined the significance of the results obtained. An example of this is shown in the analyses on the two waters sampled in October 2020 (Tab. 3.4) which were done at the same time as they were used for the initial testing of the various reagents (liquid ferrate

primarily) five months after being collected. This lapse of time visibly altered the concentrations of the various metals in solution and, first and foremost, of Hg, which is normally present in S6N water in concentrations of hundreds of ppb while here it borders on the Detection Limit (DL).

	DL (µg/l)	GITA_Oct20_TQ		S6N_Oct20_TQ	
		(µg/l)	± (%)	(µg/l)	± (%)
Hg*	0.1	< DL		0.7	15
As*	0.1	< DL		3.3	14.8
Al	1	90.2	2.8	4.2	9.3
Cr	0.2	0.18	10.2	0.6	4.7
Mn	0.02	331.53	1.1	0.28	9.4
Fe	2	7.8	3.9	6.5	1.2
Co	0.02	8.06	1.1	0.07	5.9
Ni	0.02	34.48	1.1	0.35	8.4
Cu	0.02	0.58	4.7	0.90	1.8
Zn	2	63.0	2.1	12.0	2.6
Rb	0.02	52.30	1.1	37.67	0.6
Sr	0.02	377.01	0.7	635.06	1
Ag	0.02	0.20	7.7	< DL	
Cd	0.02	1.13	6.4	0.04	32.5
Sb	0.1	< DL		20.5	1.6
Ba	0.2	51.58	2.3	26.215	1.5
W	1	< DL		1.0	3.5
Tl	0.2	< DL		< DL	
Pb	0.2	1.3	1.9	< DL	

*Table 3.4: ICP-MS trace metal analyses performed at the Department of Earth Science of the University of Florence on the GITA and S6N natural waters, 5 months after their sampling; the different concentration values (in µg/L), error percentages and Detection Limits (DL) are indicated for each of the analyzed element. *Hg and As analyses where performed at the C.S.A. Research Institute external laboratory using the EPA 7473 2007 and EPA 6020B 2014 method respectively.*

The most significant information coming from this round of experiment is about the variation of mercury content in S6N_Oct20 after the treatments with the different reagents seen before (Fig. 3.14). The large increase in mercury concentration in samples treated with KClO and

liquid ferrate even with a TQ water presenting such a low Hg content confirms what was seen in the tests presented earlier, although the absolute values cannot be quantitatively valid given the high probability of some of the mercury leaking from the container during the 5 months. Another important information concerns the arsenic contamination in the KClO reagent, which reached 16.8 ± 2.5 µg/L in a reference sample made mixing the same KClO amount used in the various experiments with MilliQ (analysis performed at the C.S.A. Research Institute external laboratory using the EPA 6020B 2014 method). Considering the typical ASSM As contents (Vaselli et al., 2015, 2021) this contamination invalidated any possible consideration regarding As removal efficiency trials while pointing out the importance of having pure and safe chemicals.

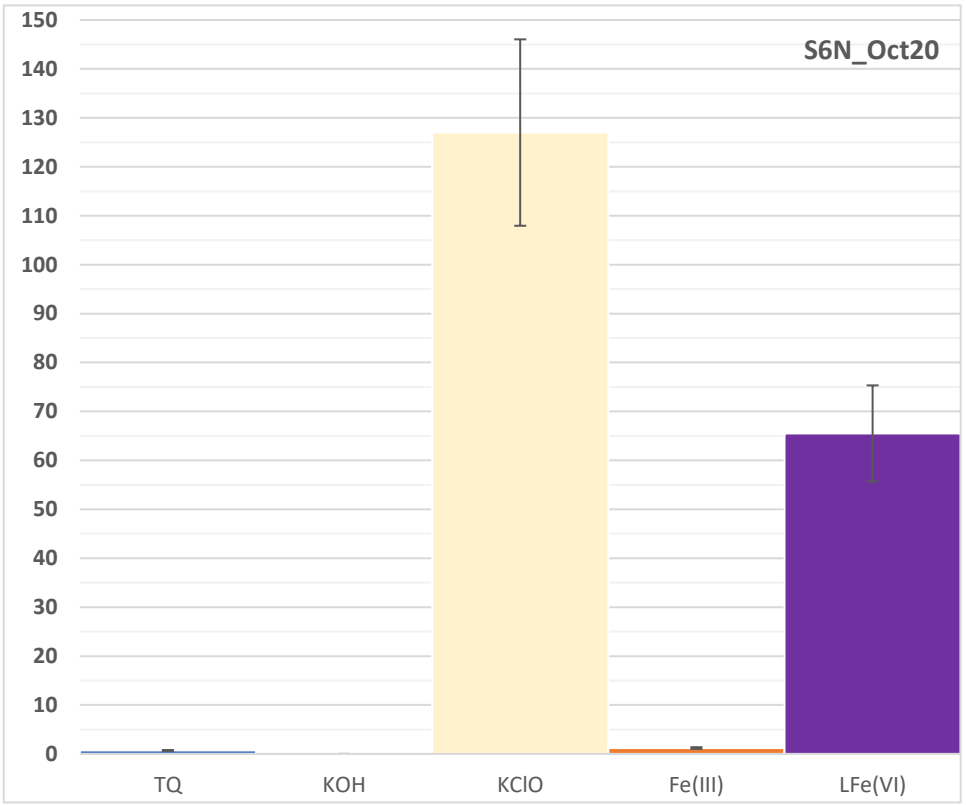

Figure 3.14: Hg content, in µg/l (ppb), in the treated S6N_Oct20 using different reagents. The error bars size results from the analytical errors given by the C.S.A. Research Institute.

The round of analyses performed on S6N_May21 was intended to check for any trends in the variation of trace metals among those with a particular enrichment in the water in relation to the different treatment. Taking into account the 1:100 dilution required for analysis given the salinity limit imposed by the instrument (waters with EC < 400 µS) and the high salinity of post-treatment waters (Tab. 9), the elements with overall relevant concentrations and interesting

information carried on were: Fe, Sr and Sb. Unfortunately, Rb and Al analyses, which reached abundant measurable concentrations in the S6N_May21_TQ, were affected by contamination from the KOH reagent while Pb showed no apparent effect linked to the different treatments. Fe analyses showed an initial iron content in the S6N_May21_TQ of 1184.5 ± 16.6 µg/L (DL = 1 µg/L). While the addition of the different reagents greatly lowered the initial iron concentration, liquid ferrate appeared to have little effect on it (Fig. 3.15), probably due to the increase in pH that created an environment positive to the stabilization of a small percentage of the added Fe(VI), as pointed out by the Pourbaix diagrams (par. 3.1.). No contamination in Fe above natural threshold levels is found.

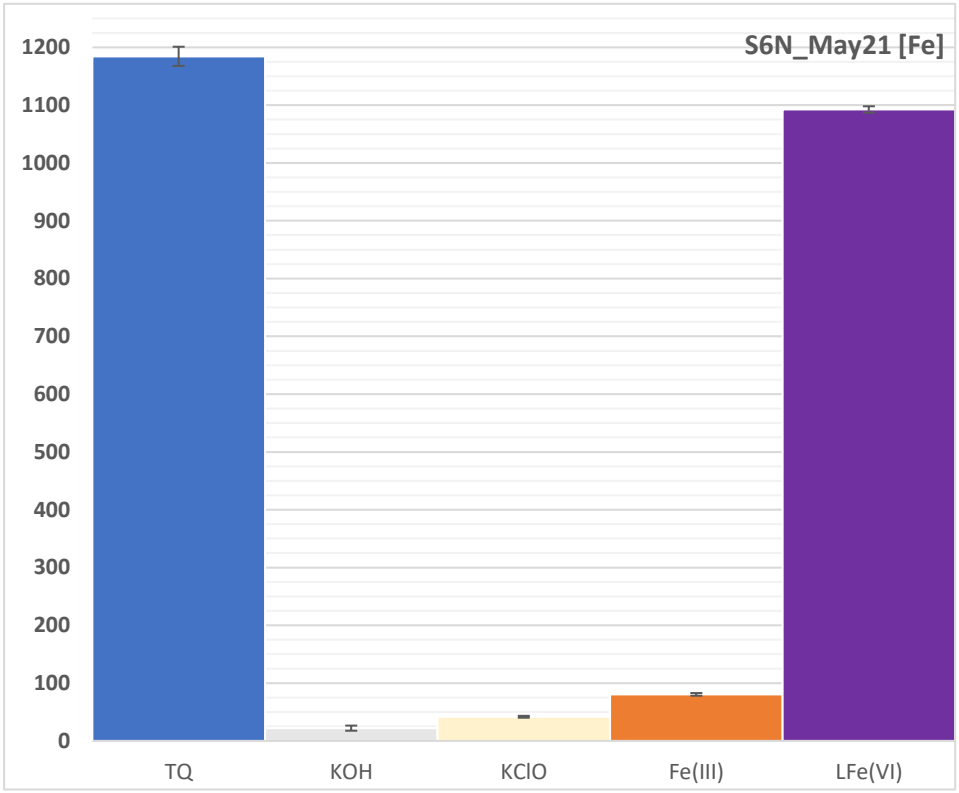

Figure 3.15: Fe content, in µg/L (ppb), in the treated S6N_May21 using different reagents. Results from the ICP-MS analyses conducted in the Department of Earth Sciences of the University of Florence.

The presence of strontium in water, also testified by the solid deposit analysis (see paragraph below), resulted in a concentration in the S6N_May21_TQ of 721.9 ± 10.8 µg/L (DL = 0.1 µg/L). Being Sr a common substituent of Ca, its origin could be ascribed to gypsum/anhydrite dissolution, which is an important component of the geochemical facies of ASSM groundwaters (par. 1.3.1.). While the application of different reagents lowered the Sr content,

a net removal was performed by the addition of the iron-based reagents, which reduced the initial concentration to around 5 % and below (Fig. 3.16).

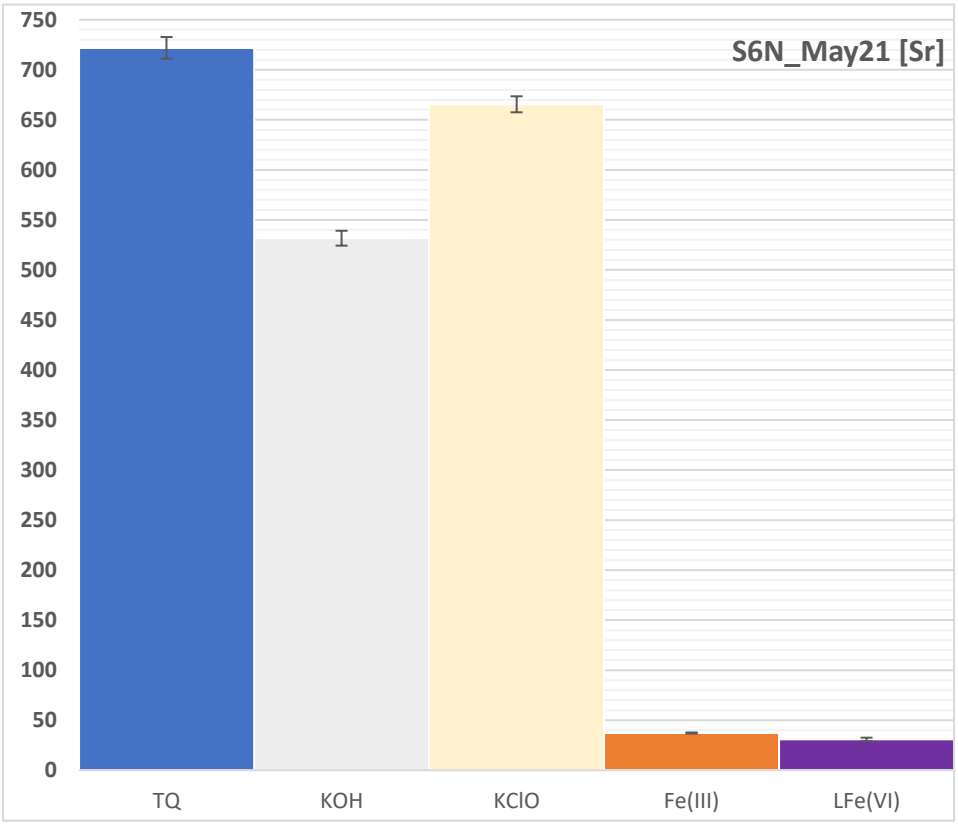

Figure 3.16: Sr content, in µg/L (ppb), in the treated S6N_May21 using different reagents. Results from the ICP-MS analyses conducted in the Department of Earth Sciences of the University of Florence.

Finally, probably the most significant information comes from the analyses of the antimony content. While uncommon in the Hg-ore deposits of ASSM, Sb-bearing minerals as stibnite (Sb_2S_3) were found sparse in the MAMD mineralizations (Rimondi et al., 2015) and due to the accumulation at the ASS site of gangue from other mining sites, this could explain the localized spikes in Sb concentration which, in few piezometers, reaches values above the threshold limit for drinking water (5 µg/L, defined by the Italian law D. Lgs. 31/01). In the S6N_May21, the Sb content reached 14.9 ± 1.8 µg/L (DL = 0.1 µg/L), in agreement with previous sampling campaigns (Vaselli et al., 2015). While the KOH and KClO seemed to increase its concentration up to 20 ± 1.3 µg/L, Fe(III) and liquid ferrate were able to lower it under the law limit (3.8 ± 0.9 and 1.9 ± 0.2 µg/L respectively), confirming the efficacy of iron-based reagents for antimony removal and the higher Fe(VI) performances when combined with other Fe sources materials (Fig. 3.17) (Johnson & Lorenz, 2015) .

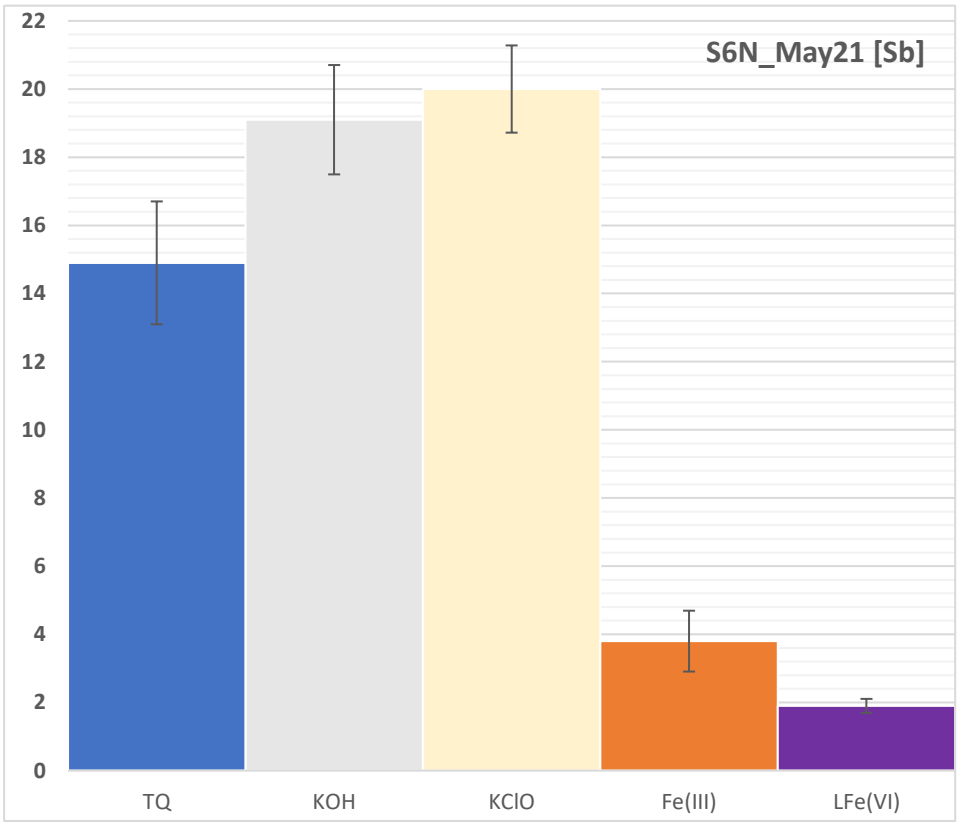

Figure 3.17: Sb content, in µg/L (ppb), in the treated S6N_May21 using different reagents. Results from the ICP-MS analyses conducted in the Department of Earth Sciences of the University of Florence.

3.3.2. Solid by-products investigations

A SEM-EDX investigation was performed on the solid deposits from the 0.45 µm filtering of the post-treatment water. The investigation, realized in the earliest part of the PhD project on the precipitates from the S6N_Oct20 and GITA_Oct20 trials, gave some further insights on the Hg content behavior shown in the previous paragraph.

The Secondary and Back-Scattered Electrons (SE and BSE) examinations of the natural deposit of the GITA water, as well as of all the different deposits, didn't reveal any obvious presence of Hg phases. Under the SEM investigation, the GITA_TQ precipitate showed an abundant clay matrix, very fine-grained, in which it is difficult to observe individual particles of the constituent mineralogical phases, with irregularly shaped Ca-S + O and Fe + O dominant phases (probably gypsum/anhydrite and iron oxydes/hydroxides) diffuse all over it (Fig. 3.18). Si and Al are also omni-present in each analyzed spot, varying from few wt % points up to 15-18 wt % and Na, K and Mg, when measured, didn't exceed 1 wt % (probably kaolinite).

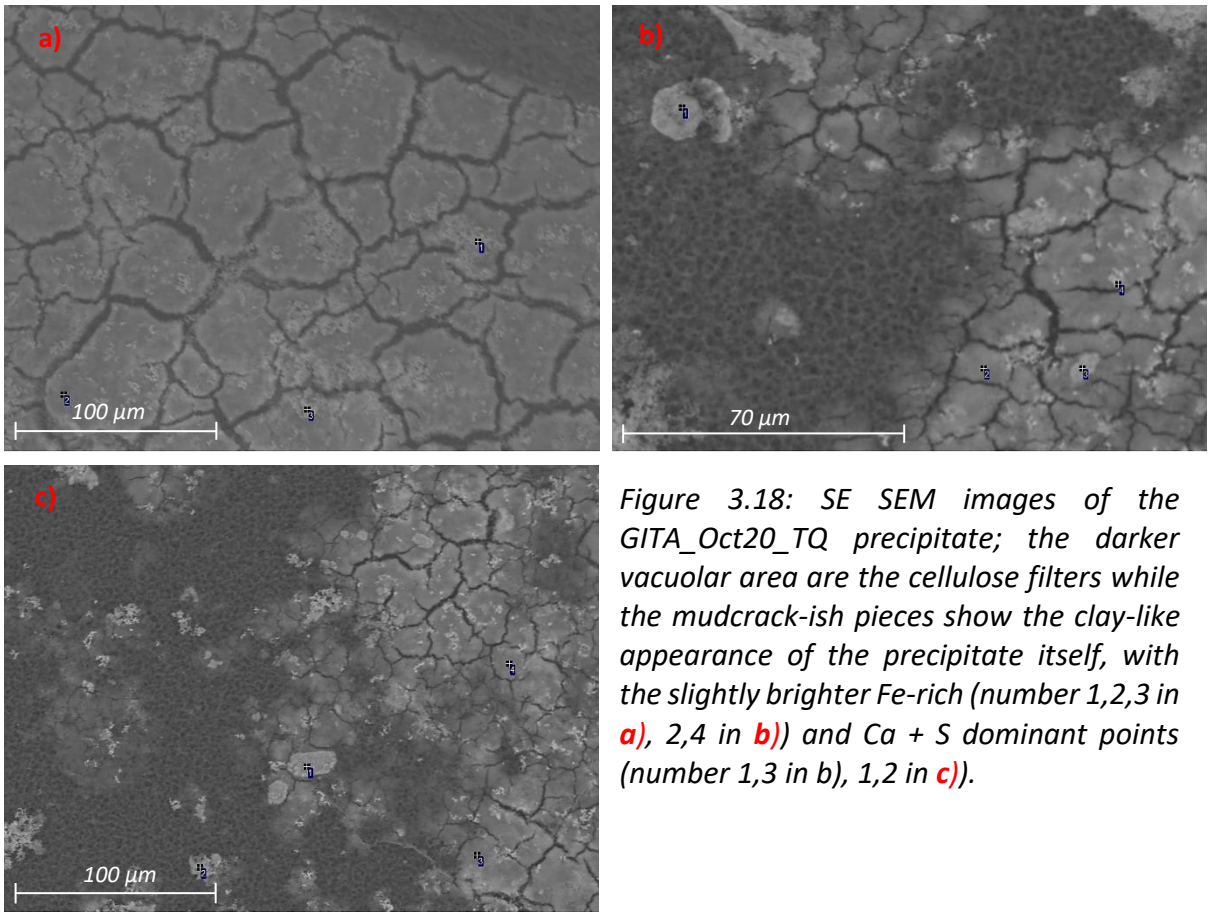

*Figure 3.18: SE SEM images of the GITA_Oct20_TQ precipitate; the darker vacuolar area are the cellulose filters while the mudcrack-ish pieces show the clay-like appearance of the precipitate itself, with the slightly brighter Fe-rich (number 1,2,3 in **a**), 2,4 in **b**)) and Ca + S dominant points (number 1,3 in b), 1,2 in **c**)).*

Different is the case for the precipitate from S6N water, which immediately showed a widespread presence of Hg-dominated phases (Fig. 3.19). The S6N_TQ precipitate appearance was that of a set of crystalline agglomerates with dimension of tens of µm. K-Al (alkaline feldspars) and Al-Mg-Fe-K (probably micas, biotite) silicate phases, together with Si-O (quartz) were widespread together with diffuse Hg-dominant phases, always associated with sulfur in 1:1 ratio and often with oxygen in apparently random proportions, easily recognizable for their brightest color in the BSE observations, which presented isolated particles up to 10-20 µm and µm/sub-µm ones scattered all over the filter (Fig. 3.19d). The associated oxygen signal was probably coming from other adjacent mineral particles due to the relative high sampling volume, typical of EDX analyses, while the Hg was never found in association with oxygen only. Irregular shape Sr-Ca + O crystals (with Sr up to 70 wt%, probably strontianite) up to 50-60 µm long where also found.

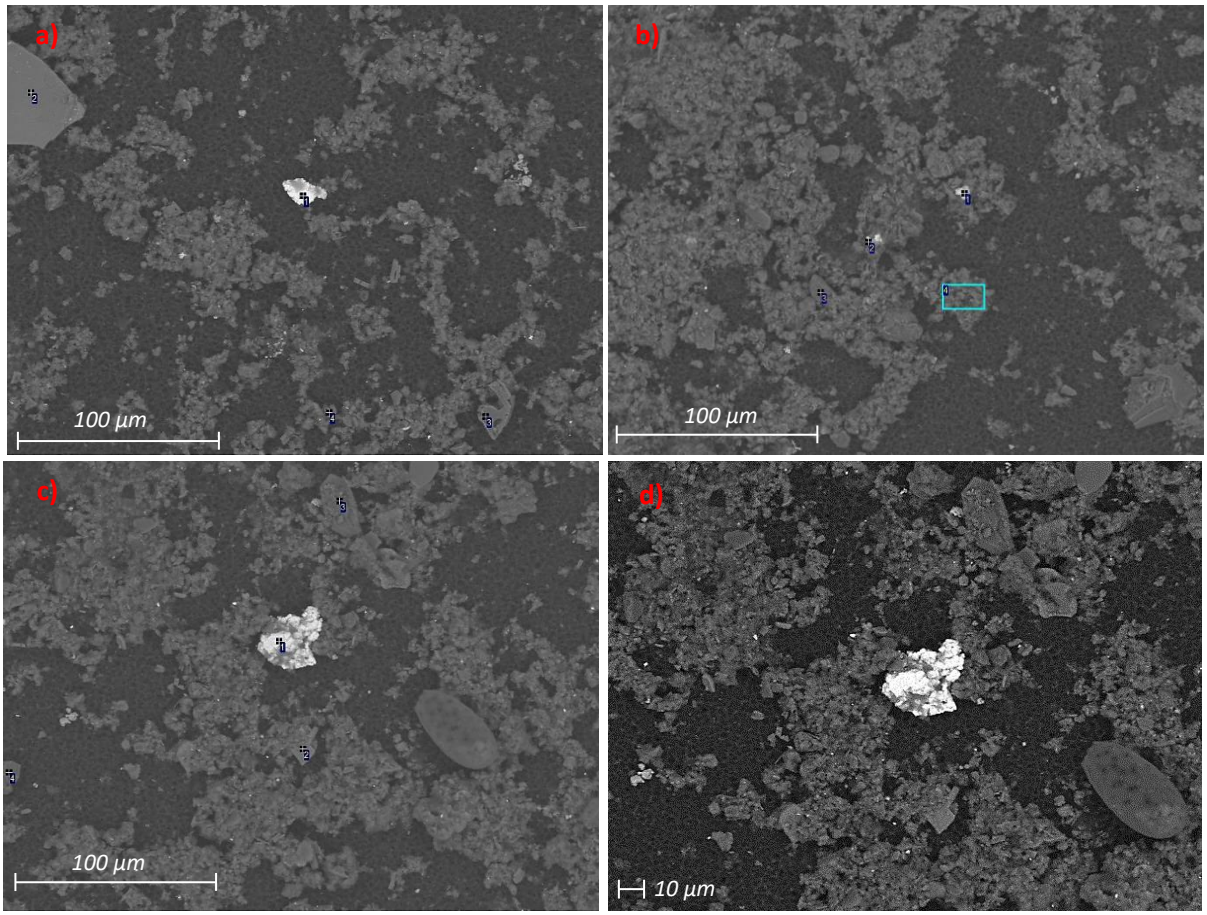

*Figure 3.19: BSE SEM images of the S6N_Oct20_TQ precipitate; the darker vacuolar area are the cellulose filters. K-Al + Si-O phases (3 in **a)**, 4 in **c)**) together with Al-Mg-Fe-K + Si-O ones (2 in **a)**, 2 in **c)**) are widespread into the crystalline agglomerates, together with diffuse Hg-S and Hg-S-O dominated smaller particles (1,4 in **a)**, 1,2 in **b)**, 1 in **c)**. In d), the higher contrast highlights the Hg-S dominated locations which, at this scale, appear as the bright white central particle + bright white small dots scattered around.*

The KOH, KClO, Fe(III) and LFe(VI) treatments altered completely the morphology of the S6N_TQ precipitate, while introducing high K, Fe and/or Cl in every analyses points and completely modifying the original wt % element ratio at the scale achievable with the available SEM. Despite this, some important considerations can be made regarding the distribution of the heavier elements (Fig. 3.20). In the S6N_KOH precipitate (Fig. 3.20a, 3.20b) the presence of Hg-dominant isolate particles up to 10-20 µm and scattered µm/sub- µm ones can be easily noticed thanks to their bright white color in BSE imaging, together with Sr-Ca + O crystals. Unlike the S6N_TQ, some of the investigated Hg particles were associated with sulfur and oxygen, whereas some others presented oxygen only (HgO). Conversely, even after an in-depth search, in the S6N_KClO solid deposit (Fig. 3.20c, 3.20d, 3.20e), no Hg-containing spots were visible. In this sample, the brightest white spots were now diffuse W and scarce Ag and Au small particles, easy to be noticed when the contrast was boosted in order to mask out the signals coming from the lighter phases (Fig. 3.20d). The presence of these elements is not

surprising, given their already known association with TMP deposits ((Morteani et al., 2011) and personal communication). Due to the high quantity of iron introduced with the Fe(III) (Fig. 3.20f) and LFe(VI) (Fig. 3.20g, 3.20h) treatments in comparison to the low amount of TQ solid deposit, it was not possible to say with certainty whether the absence of Hg, W, Au and Ag spots in the relative precipitates is due to an interaction with the reagent or is masked by the abundant by-products.

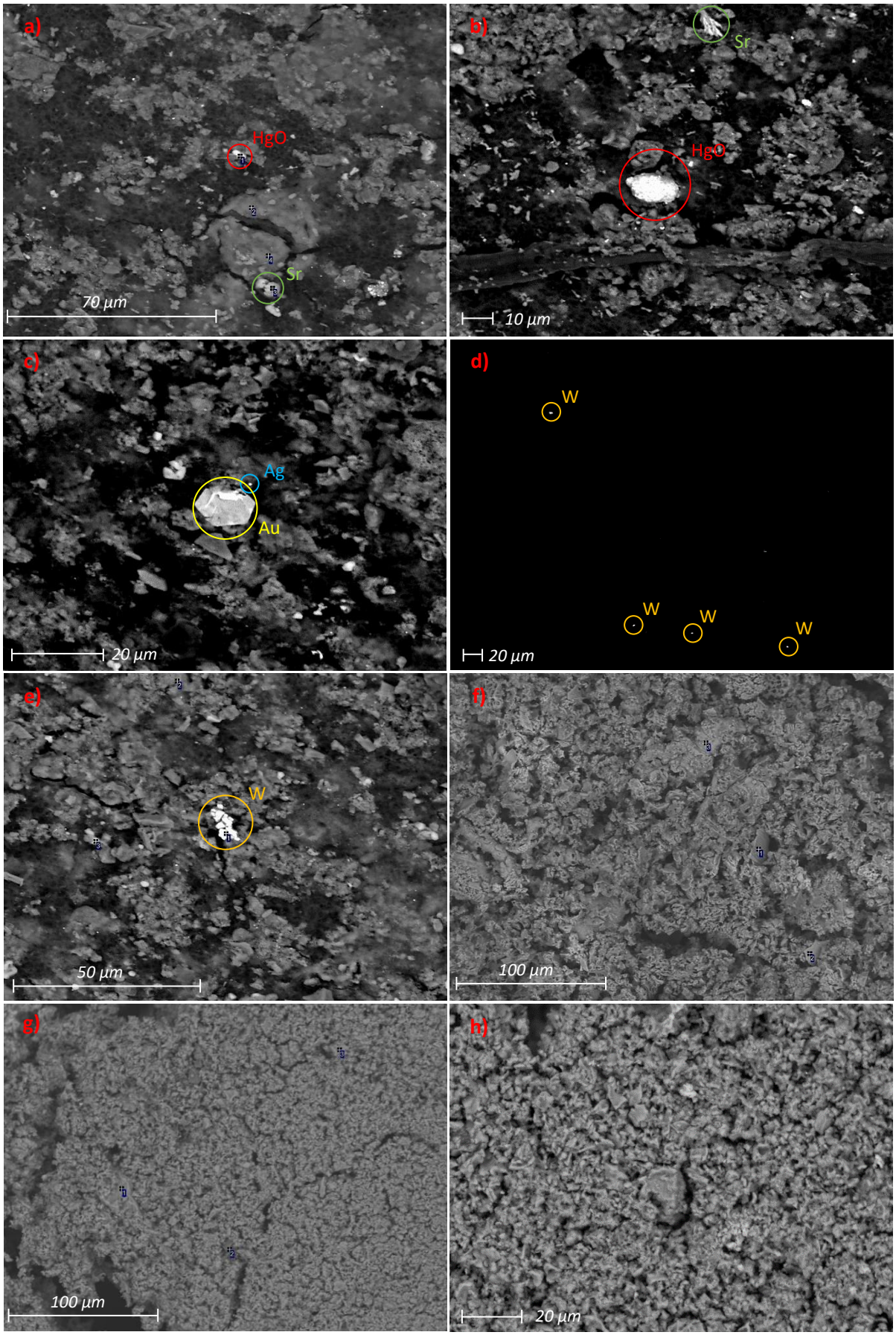

*Figure 3.20: BSE SEM images of **a)**, **b)** S6N_Oct20_KOH, **c)**, **d)**, **e)** S6N_Oct20_KClO, **f)** S6N_Oct20_Fe(III) and **g)**, **h)** S6N_Oct20_LFe(VI).*

3.3.2.1. XAS results

Mercury speciation and its transformation through the different treatments applied to the S6N_May21 and S6N_Apr22 waters were investigated inside the respective solid products by means of XANES and, whenever possible, EXAFS. Although relatively high elemental concentrations are usually required to acquire detailed-enough spectra, usually in the tens of ppm minimum, the intensity and quality of the signals were high enough to extract important information about the relative abundances of the various components inside the precipitates and the different Hg-ligands. Despite working with natural waters with about 200 ppb Hg content and few mg of natural deposit (as discussed in the paragraph below), this result was made possible by a properly crafted experimental design, which is the result of multiple preliminary tests and the "in-depth" knowledge accumulated during the period spent within LISA-BM08 laboratory. One of the main difficulties encountered concerned the simultaneous presence of much higher iron contents in comparison to Hg in the various treated samples. Due to the iron lower X-ray absorption edge energies (Fe K-edge = 7112 eV (Merritt, n.d.)) the Fe atoms were also excited during the Hg probing causing high X-rays scattering up to the saturation of fluorescence detector. Accordingly, the Fe signal was preferentially filtered using Al foils; while reducing the amount of Hg counts too, the overall Hg signal/noise ratio improved, allowing for acquisition of extremely low-concentrated samples up to short EXAFS spectra. However, the still extremely-high Fe:Hg signal almost saturated the florescence detector, requiring long acquisition times (up to 1h45 per spectrum) to obtain enough Hg counts in the respective Region Of Interest (ROI).

3.3.2.1.1. XANES and LCF

A set of pure Hg compounds with known structures were chosen as reference standards on the basis of their plausible presence in the studied samples. The choice emerged from direct findings in the ASSM area and XAS investigations on other Hg mine wastes (Kim et al., 2000; Vaselli et al., 2015). The XANES standard signals were used as primary components in the Linear Combination Fit (LCF) analyses. With the exception of cinnabar (α-HgS), freshly prepared as a pellet directly from a mineralogical sample, the other compounds came from the LISA-BM08 standard stash and, in this case, were primarily provided by Valentina Rimondi, a researcher of the Department of Earth Sciences of the University of Florence. The XANES portion of the acquired standards spectra are shown in Fig. 3.21, normalized and energy-aligned using the software Athena thanks to the α-HgS sample positioned in the reference chamber, whose spectrum was continuously recorded during each acquisition (par. 2.2.2.1.3.).

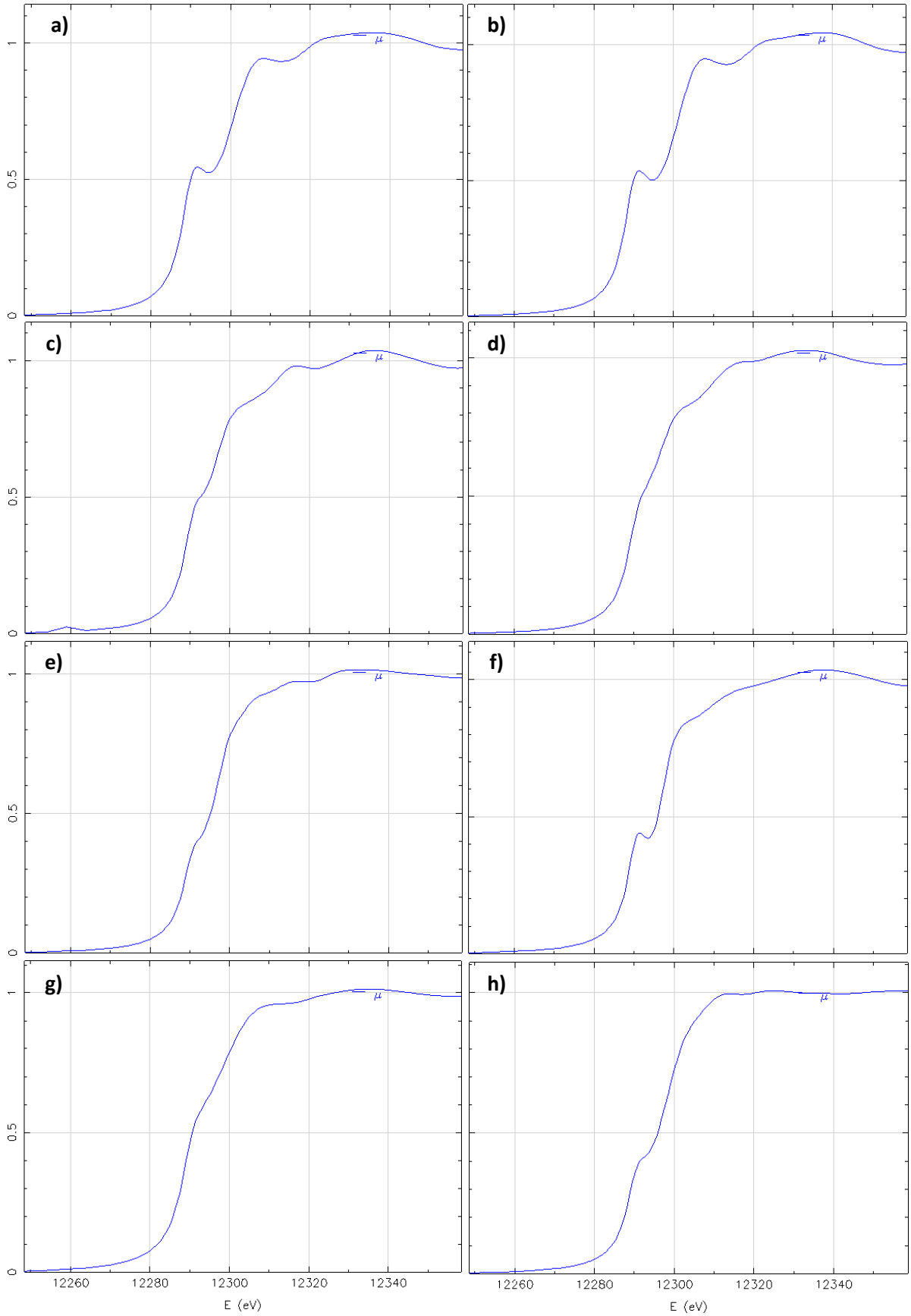

*Figure 3.21: XANES spectra in normalized μ(E) vs E (eV) collected at the L-III edge of **a)** montroydite (Montr), **b)** synthetic HgO (HgO), **c)** cinnabar (α-HgS), **d)** meta-cinnabar (β-HgS), **e)** calomel (HgCl), **f)** mercury(II) chloride ($HgCl_2$), **g)** Hg(0) (Hg(0)) and **h)** mercury(II) sulphate ($HgSO_4$).*

Despite the multiple Hg oxidation states present in the references pool, the overall registered eV difference in terms of edge positions in the standards (defined as the first maximum of first derivative of the spectrum in the energy domain, pre-edge features excluded) was within 1 eV from the ordinary Hg-L_{III} edge value, thus not representing by themselves an appreciable criterion for the components identification inside the samples. This is in agreement with the results found in previous works (Andrews, 2006; Riddle et al., 2002), as well as the 5d nature of the mercury itself (3d and 4d metals are the ones showing high relative ΔeV linked to different valence states, see par. 2.2.2.1.2.). Moreover, the different pre-edge regions didn't present detectable features, probably due to the fact that the lowest-energy non-occupied molecular orbitals in the various mercury oxidation states are mainly 6s which, for a p L_{III}-shell electron, represent a fully allowed transition contributing directly to the XANES signal, as pointed out in Andrews J. C. work (Andrews, 2006). In addition, one should take into account that the energy resolution of the energy florescence detector is not suitable to high-resolution signal resolving, so that some fine details of the spectral features around the edge jump could be lost because of convolution phenomena. A prominent inflection around mid-height of the edge slope was identified as a distinctive feature of the Hg-O and Hg(II)-Cl compounds (Fig. 3.21a, 3.21b, 3.21f) while the different edge shapes and slightly different eV positions were the elements the following LCF analyses relieved on. The LCF analysis routine using the ATHENA software involved the fitting into the energy range -20 to +45 eV (evaluated with reference to the edge position) of the experimental μ(E) spectra of the unknown phases compositions using the 8 standard spectra as primary components, whose weights were forced to vary between 0 and 1 while the total weights sum was let free to vary. All the 154 fit combinations per sample, resulting from using at most 4 standards per combination, were computed and the respective R-factor and χ^2 values recorded. The best fit for each of the analyzed sample was chosen on the basis of the lowest χ^2 value within a ± 10 % margin and, for comparable χ^2 fits, it was prioritized the one with the lowest number of components which was able to better fit the mid-height edge section (red curve in Fig. 3.22). The resulting best fits were double checked by individually running again the fit procedures with progressively lower number of standard components (from the general 8 up to the number indicated by the fit) in order to double check the Athena fitting procedure. No differences emerged from these further LCF trials.

As expected, the normalized signal outputs for montroydite and synthetic HgO standards were equivalent, endorsing the quality of the natural standard pellet and making them undistinguishable in the LCF analyses (also validated by EXAFS analyses, Fig. 3.31, Tab. 3.7); from now on they will be both labelled as "HgO".

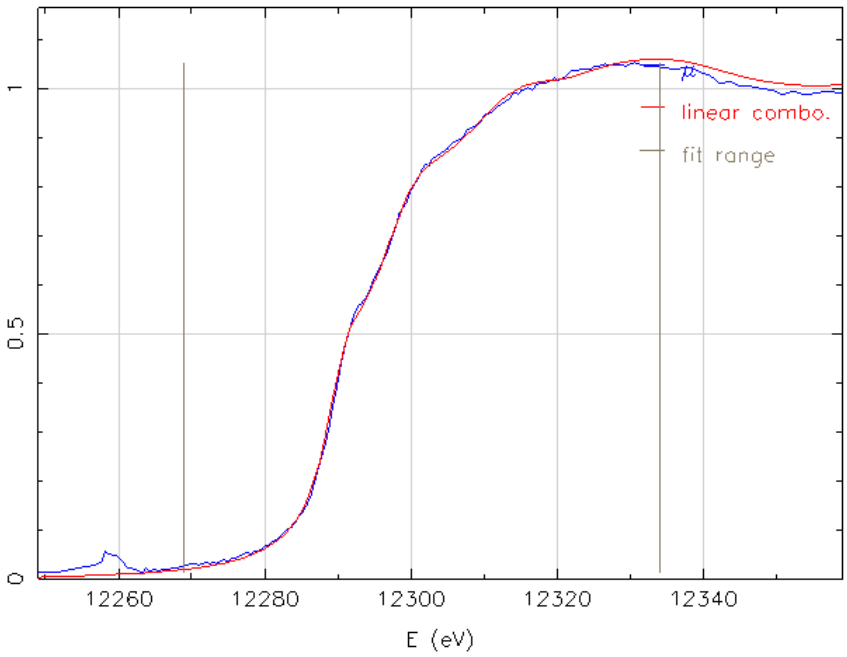

Figure 3.22: experimental XANES spectrum of S6N_Apr22_TQ (blue) vs the best fit from LCF (red) in the energy space.

The XANES spectra, together with the best fit achieved for each of the analyzed samples in the S6N_May21 and S6N_Apr22 trials are shown in Fig. 3.23 and 3.24 respectively. A graphical summary of the components weight abundances from the two LCF procedures are shown in Fig. 3.25 and Fig. 3.26, while the best fits parameters such as R-factor, χ^2 values and components weights are summarized in Tab. 3.5 and 3.6. During the A08-1-1089 experiment, all the prefiltered variant samples were investigated too. However, no complete LCF analysis was performed on them due to the overall sharp decrease of the Hg signal going from the non-prefiltered to the prefiltered samples which, in many cases, affected the quality of the spectra to such an extent that no proper signal processing was possible. This is shown in Fig. 3.27, where the non-normalized Hg L_{III} edge step heights of the non-prefiltered and prefiltered variants, found by the background removal, are shown, being the edge step height of an element proportional to the quantity of the investigated element in the sample. The only samples still presenting good quality signals were the LFe(VI)_Pref and Fe+Ag_Pref_80K which didn't show apparent change in the relative wt % over the respective non-prefiltered variant

in the LCF best fits. In Fig. 3.27g the different edge step heights of S6N_May21_TQ and S6N_Apr22_TQ, found by the background removal, are also compared.

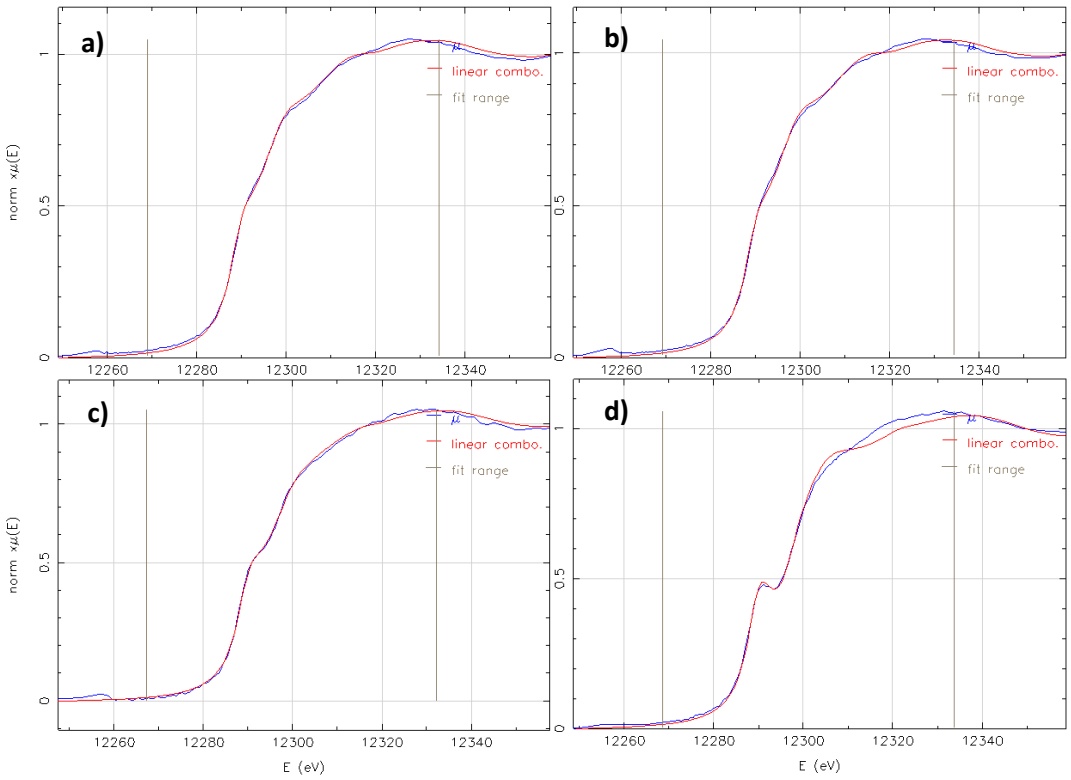

Figure 3.23: experimental XANES spectra of S6N_May21 samples (blue lines) vs the respective best fits from LCF (red lines); ***a)*** *S6N_TQ;* ***b)*** *S6N_KOH;* ***c)*** *S6N_Fe(III);* ***d)*** *S6N_LFe(VI). The fit parameters are summarized in Tab. 3.5.*

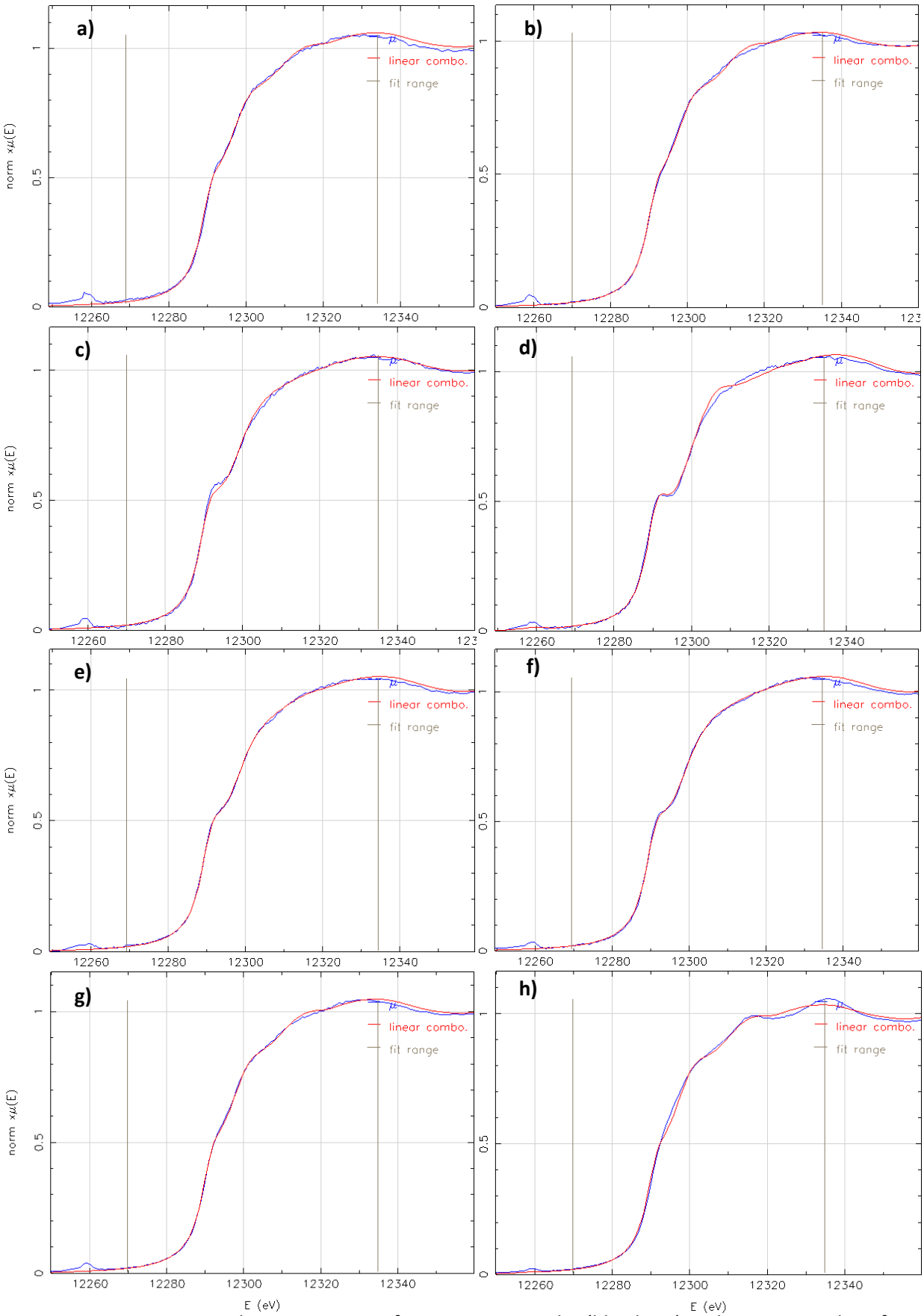

Figure 3.24: experimental XANES spectra of S6N_Apr22 samples (blue lines) vs the respective best fits from LCF (red lines); ***a)*** *S6N_TQ;* ***b)*** *S6N_TQ_80K;* ***c)*** *S6N_Fe(III);* ***d)*** *S6N_LFe(VI);* ***e)*** *S6N_SFe(VI);* ***f)*** *S6N_Mixfer;* ***g)*** *S6N_Fe0_80K;* ***h)*** *S6N_Fe+Ag_80K. The fit parameters are summarized in Tab. 3.6.*

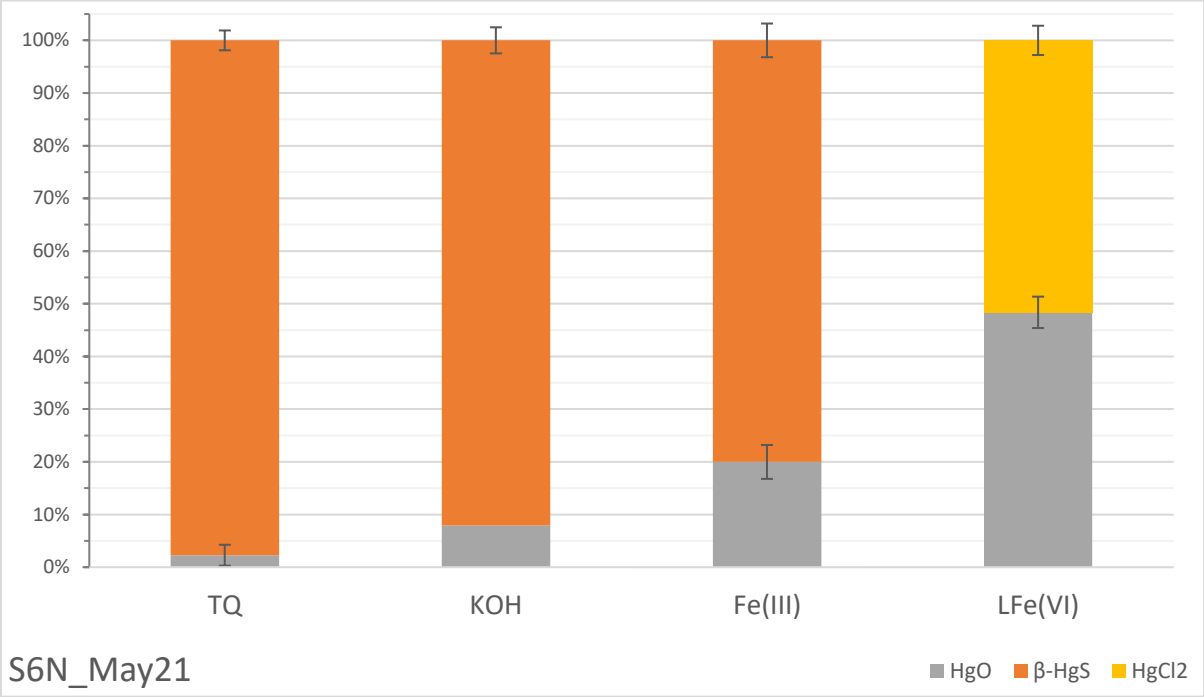

Figure 3.25: graphical representation of the best-fits relative weight abundances in the different S6N_May21 samples, resulting from LCF analyses of the normalized μ(E) signals in the energy space (data from Tab. 3.5).

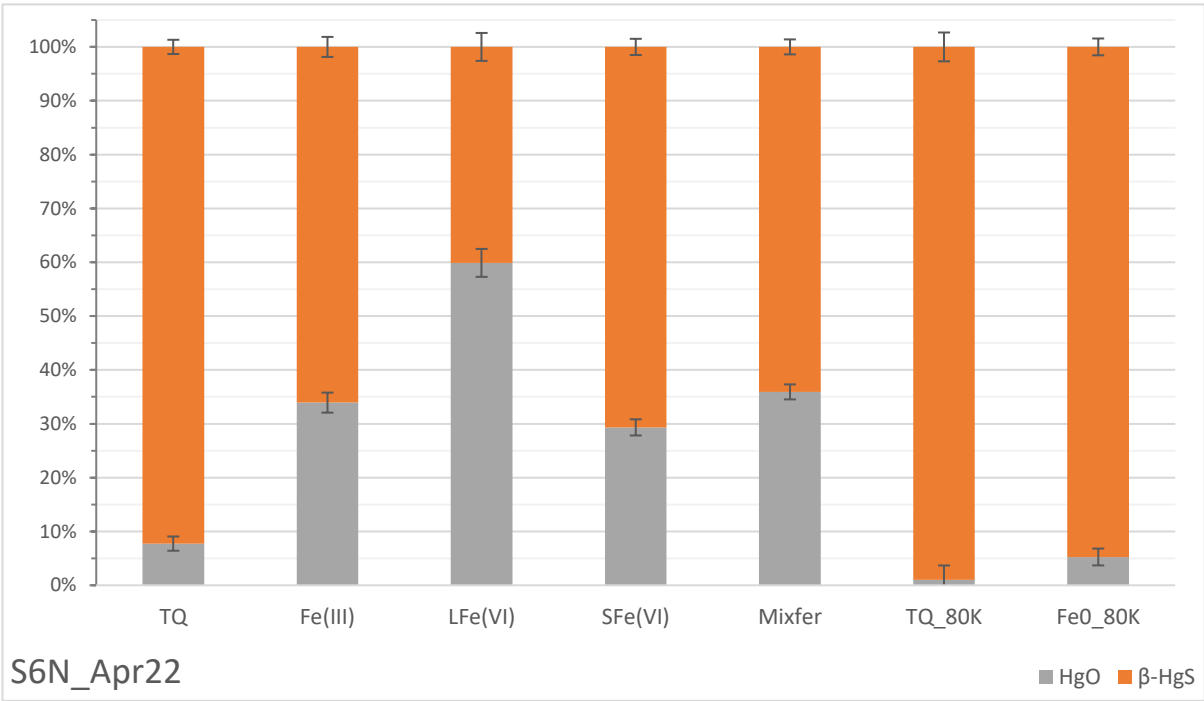

Figure 3.26: graphical representation of the best-fits relative weight abundances in the different S6N_Apr22 samples, resulting from LCF analyses of the normalized μ(E) signals in the energy space (data from Tab. 3.6). "Fe0" = nZVI, "_80K" indicates the spectra acquired at the temperature of 80 K.

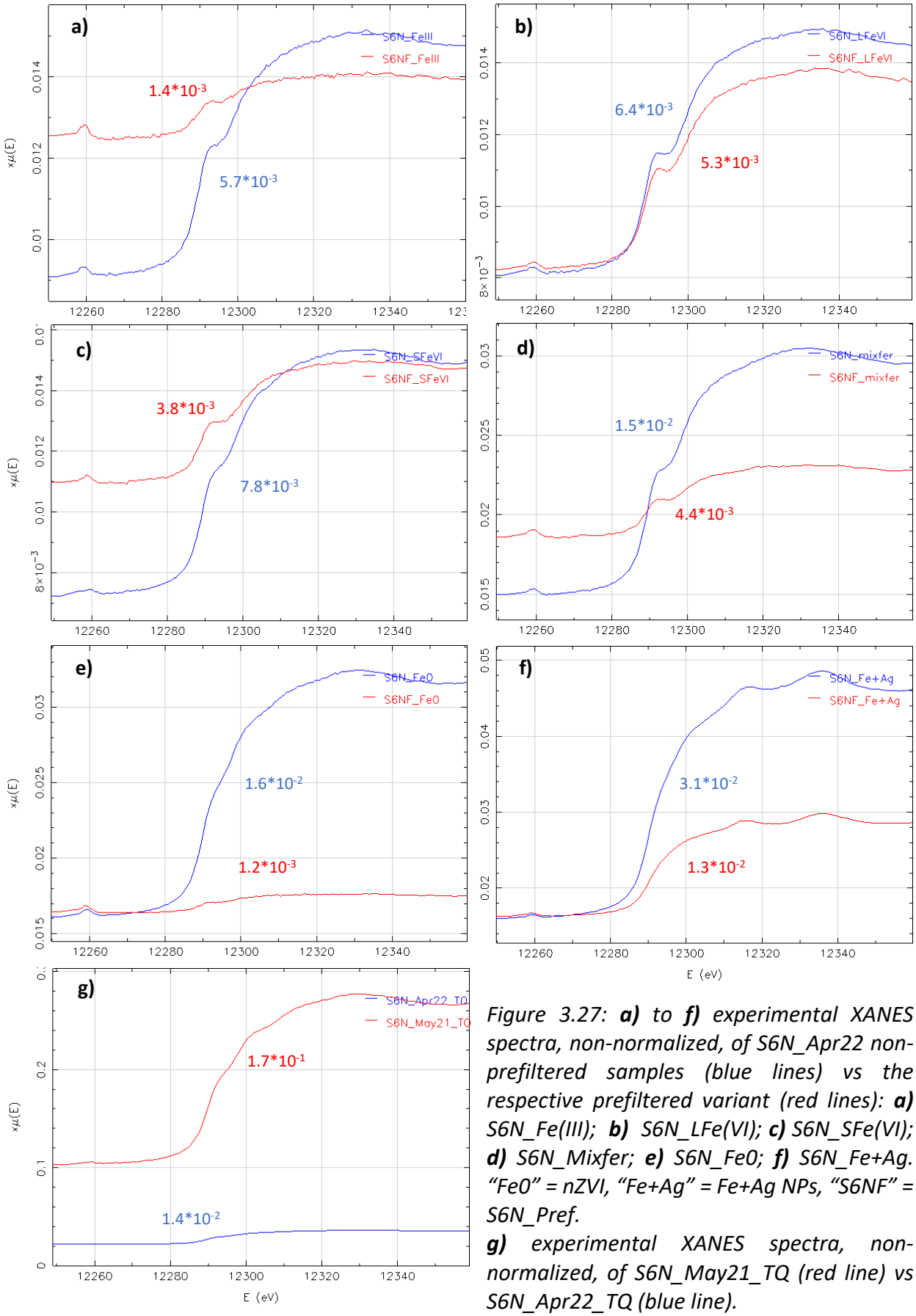

Figure 3.27: ***a)*** *to* ***f)*** *experimental XANES spectra, non-normalized, of S6N_Apr22 non-prefiltered samples (blue lines) vs the respective prefiltered variant (red lines):* ***a)*** *S6N_Fe(III);* ***b)*** *S6N_LFe(VI);* ***c)*** *S6N_SFe(VI);* ***d)*** *S6N_Mixfer;* ***e)*** *S6N_Fe0;* ***f)*** *S6N_Fe+Ag. "Fe0" = nZVI, "Fe+Ag" = Fe+Ag NPs, "S6NF" = S6N_Pref.*

g) *experimental XANES spectra, non-normalized, of S6N_May21_TQ (red line) vs S6N_Apr22_TQ (blue line).*

S6N_May21									
Sample	**R-factor**	**χ^2**	**HgO**		**β-HgS**		**$HgCl_2$**		**Σ**
			wt	Δwt	wt	Δwt	wt	Δwt	
TQ	2.9E-04	1.1E-02	0.02	0.02	0.99	0.02	-	-	1.01
KOH	3.8E-04	1.5E-02	0.08	0.0	0.93	0.03	-	-	1.01
Fe(III)	9.0E-04	3.4E-02	0.20	0.03	0.80	0.03	-	-	1.00
LFe(VI)	5.4E-04	2.4E-02	0.49	0.03	-	-	0.52	0.03	1.01

Table 3.5: summary of the best-fits parameters in terms of R-factor, χ^2 (chi-square) values, and weight abundances (wt) of the components with relative error (Δwt) in the different S6N_May21 samples, resulting from LCF analyses of the normalized μ(E) signals. Σ represents the sums of the component aboundances for each of the sample.

S6N_Apr22									
Sample	**R-factor**	**χ^2**	**HgO**		**β-HgS**		**$HgCl_2$**		**Σ**
			wt	Δwt	wt	Δwt	wt	Δwt	
TQ	1.3E-04	8.4E-03	0.08	0.01	0.94	0.01	-	-	1.02
Fe(III)	2.6E-04	1.6E-02	0.34	0.02	0.67	0.02	-	-	1.01
LFe(VI)	5.1E-04	3.2E-02	0.61	0.03	0.41	0.03	-	-	1.01
SFe(VI)	1.7E-04	1.1E-02	0.30	0.02	0.71	0.02	-	-	1.01
Mixfer	1.4E-04	9.2E-03	0.37	0.01	0.65	0.01	-	-	1.02
TQ_80K	5.3E-04	3.3E-02	0.01	0.03	0.98	0.03	-	-	0.99
Fe0_80K	1.8E-04	1.1E-02	0.05	0.02	0.95	0.02	-	-	1.01

Table 3.6: summary of the best-fits parameters in terms of R-factor, χ^2 (chi-square) values, and weight abundances (wt) of the components with relative error (Δwt) in the different S6N_Apr22 samples, resulting from LCF analyses of the normalized μ(E) signals in the energy space. Σ represents the sums of the component aboundances for each of the sample. "Fe0" = nZVI, "Fe+Ag" = Fe+Ag NPs while "_80K" indicates the spectra acquired at the temperature of 80 K.

As demonstrated by XAS speciation studies on Hg-bearing mine wastes and a comparison between XAS and the Sequential Chemical Extractions technique, limitations about linear least squares fitting procedure for Hg containing samples include: I) the completeness of the Hg reference pool used as source of the primary components; II) a 10 % wt as lowest limit for identification of a Hg-containing phase; III) the concentration threshold of about 100 mg/kg below which measurements of Hg L_{III} edge is difficult (Andrews, 2006; Kim et al., 2000, 2003). While this study demonstrated how the last limitation could be overcome using LCF of the XANES region (the previous studies used LCF on the EXAFS one), the high-intensity ESRF radiation and exploiting long acquisition time with filtration of the Fe signal when needed, all

three conditions still affected these measurements. For example, as will be better explained by the EXAFS results, the absence of any Hg+Ag standard compound invalidated the Fe+Ag NPs speciation results, which ends up to misinterpret the phases distribution and their relative abundance in the samples. Because of that, the resulting S6N_Apr22_Fe+Ag_80K best fit is not reported in Fig. 3.26 and Tab. 3.6.

The removal efficiency of the different reagents, which is correlated to the XAS Hg signal of the respective deposit, showed how KClO was unable to reduce the starting Hg content, even going so far as to double it in S6N_May21_KClO (Fig. 3.11). As a result, the KClO filters from S6N_May21 and S6N_Apr22 treatments were unable to produce any relevant Hg L_{III} signal in the XAS investigations, showing the absence of detectable Hg in those solid samples, in accordance with the SEM observations.

In Figure 3.29 are shown the XANES spectra of S6N_May21 and S6N_Apr22 treated with liquid ferrate, in a comparison with the most representative reference compounds (Fig. 3.29a and 3.29c respectively), plotted with the relative best fits from LCF (Fig. 3.29b and 3.29d respectively). Despite the same treatment, the S6N_May21_LFe(VI) and S6N_Apr22_LFe(VI) XANES spectra presented different edge shapes, in particular different position of the mid-height inflection feature, which were sufficient to result in a different speciation emerging from LCF analyses. The LCF of S6N_May21_LFe(VI) suggested the presence of HgO and $HgCl_2$ in equal parts. Instead, the LCF of S6N_Apr22_LFe(VI) highlighted an about 60/40 wt % split between HgO and β-HgS respectively.

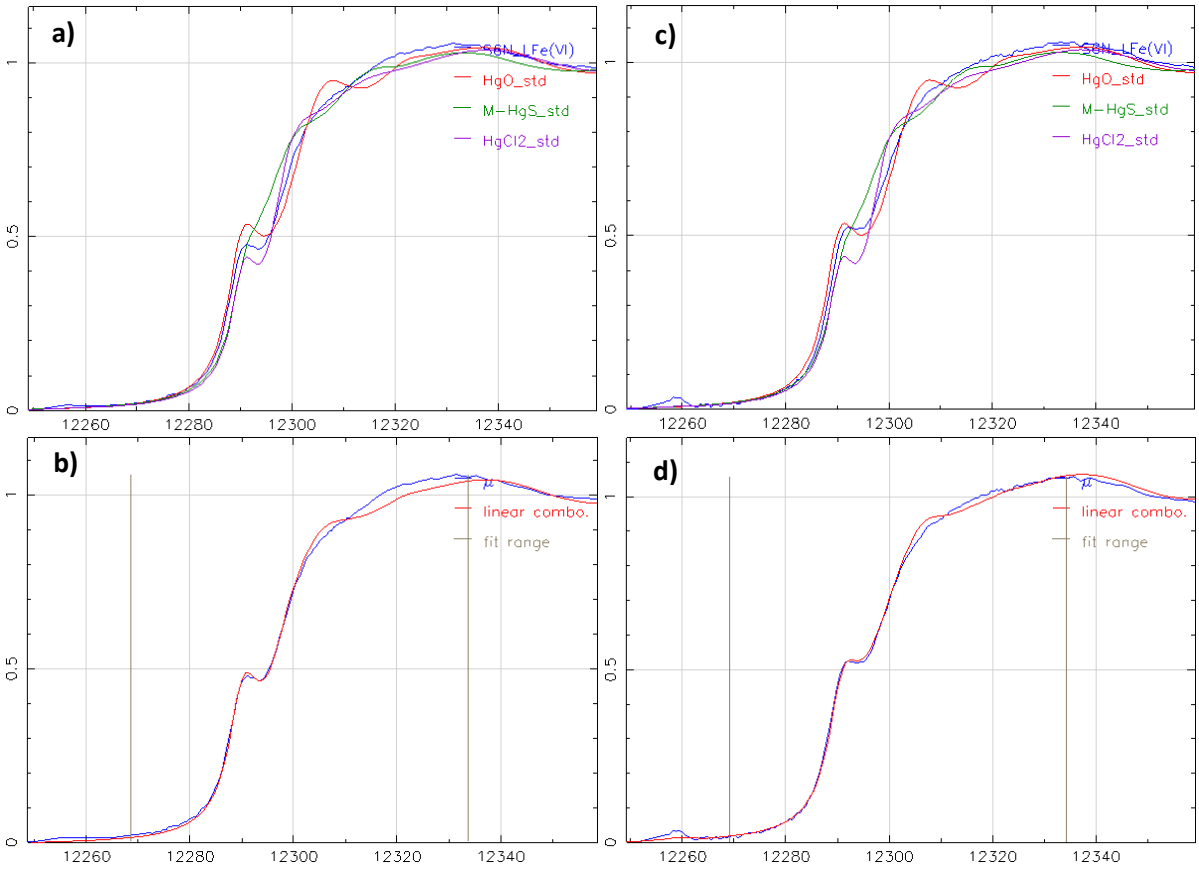

Figure 3.29: XANES norm μ(E) spectrum of the S6N_May21_LFe(VI) sample (blue line) ***a)*** *together with the HgO (red line), β-HgS (M-HgS, green line) and $HgCl_2$ (purple line) standard compounds XANES norm μ(E) spectra and* ***b)*** *together with its best fit from LCF (red line); XANES norm μ(E) spectrum of the S6N_Apr22_LFe(VI) sample (blue line)* ***c)*** *together with the HgO (red line), β-HgS (M-HgS, green line) and $HgCl_2$ (purple line) standard compounds XANES norm μ(E) spectra and* ***d)*** *together with its best fit from LCF (red line).*

In light of the results obtained, the relative uncertainties and the limitations highlighted, the XANES analysis of the various solid reaction by-products provided semi-quantitative information regarding mercury speciation in the various samples, showing an overall dominant presence of mercuric sulfide, in particular in the natural deposit of the two S6N_TQ, measured at ambient temperature and at 80 K. While this is consistent with the fact that cinnabar is the primary ore mineral for the ASSM, the absolute dominance of metacinnabar instead was not expected. A trend common to both the S6N_May21 and S6N_Apr22 waters was also discovered, which saw mercury becoming relatively enriched in the oxide phase at the expense of metacinnabar with each of the different treatments, going from nearly 100 % in the TQ natural deposits and KOH ones to as low as 40 % in the S6N_Apr22_LFe(VI) and 0 % in the S6N_May21_LFe(VI), where the $HgCl_2$ made its appearance. Various intermediates in order of increasing HgO/HgS ratio are solid ferrate, Mixfer and Fe(III). While the Hg speciation

in the Fe+Ag NPs sample cannot be properly addressed, the nZVI seemed to have no effect on the initial mercury phase distribution in the precipitate.

3.3.2.1.2. EXAFS

Structural refinement of the Hg local environments into the different precipitates was performed by least square minimization of the EXAFS signals. The main goal was to achieve a deeper comprehension on the type of chemical element to which mercury binds in the various samples and the relative bonding distances, thereby obtaining information on the solid phases responsible for mercury sequestration. The refinements were performed using different CIF base models (Fig. 3.30), which were downloaded from the American Mineralogist Crystal Structure Database website (Downs & Hall-Wallace, 2003), the choice of which was aided by literature data and observations from the previously analyses. Moschellandsbergite (Ag_2Hg_3) and imiterite (Ag_2HgS_2) were chosen as the model compounds during Fe+Ag NPs EXAFS fitting due to the unavailability of CIF files for the Silver Amalgam group members (e.g. eugenite, paraschachnerite) and the high complexity (e.g. mixed occupancies) and/or high distances between Hg and Ag atoms shown by the perroudite and fettelite structures. The ATOMS routine was used to generate a list of all the atomic coordinates in a cluster of 6 Å size based on the selected CIF, and the FEFF6 macro to calculate all the theoretical photo-electron scattering functions (called "paths") using the ATOMS output, selecting Hg as the atom at the center of the cluster. The resulting photo-electron paths were manually selected within the Artemis software environment in order to evaluate their combined contribution to the experimental signal, obtaining the best possible fits with the lowest R-factor and, consequently, information on the Hg surroundings. Using the basic EXAFS equation as a reference model (eq. (22)), the degeneracy of every single path was fixed to the number of the corresponding atoms of the CIF (otherwise it will be specified in the text). The term describing the amplitude (S_0^2, "amp"), the energy shift (ΔE_0, "delE0"), and the change in the path length (ΔR, "delR") and in the relative mean square displacement due to thermal/structural disorder (σ^2, "ss") relative to the nominal path length from the CIF model (R_effective, "Reff") were let free to vary, in order to be optimized during the fitting procedure. To be considered "good", a fit had to present a small percentage misfit between data and theory ("R-factor", which for EXAFS discriminates more effectively than any χ^2 parameter), a delE0 generally between -10 and +10 eV, a S_0^2 and ss never < 0 and small delR

(in the 10^{-2} Å order of magnitude) ((Bruce Ravel, 2016) and personal knowledge); any deviation from these constrains would inevitably point to a wrong starting model choice. The best fits which had been taken are the ones presenting the lowest R-factors and lowest delR. The fits were carried out in the R-space weighting data with k^2 while double checking their accuracy using the *χ(k)* and *χ(q)* signals. The k window selected for the Fourier transformation into the R-space was variable for the different samples in relation of the noise becoming increasingly higher with increasing k values. The R window was tuned in order to restrain only the signals which were meant to be fitted and it was also responsible for the amount of signal (both experimental and theoretical) transform back into *χ(q)*. Whenever multiple paths were used during the fitting procedure, a common delR factor scaling with the Reff was used, with a shared the Debye-Waller model, fitted through the refinement of the Debye temperature ("dTemp") parameter; the dtemp is not intended to be a determination of the physical Debye temperature but it stands as a way to refine multiple ss using a singular parameter.

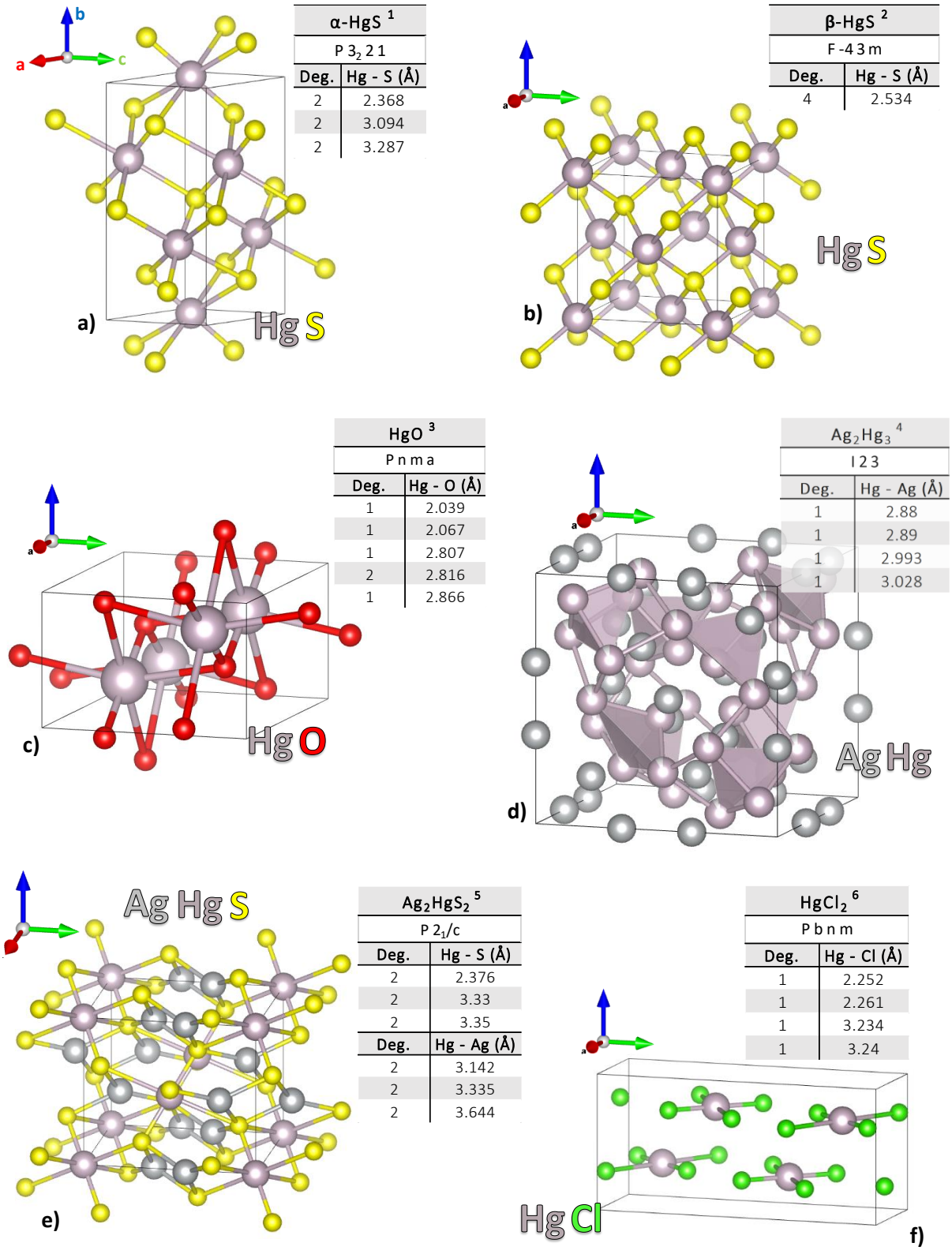

Figure 3.30: crystallographic structural models, realized with VESTA in standard orientations, of: ***a)*** *cinnabar;* ***b)*** *metacinnabar;* ***c)*** *montroydite;* ***d)*** *moschellandsbergite;* ***e)*** *imiterite;* ***f)*** *$HgCl_2$. In the each of the respective table are reported the spatial group to which the phase belongs, as well as distances of the nearest atoms surrounding the Hg ones. Data from [1](Auvray & Genet, 1973), [2, 6] (Wyckoff, 1963), [3](Aurivillius, 1964), [4](Fairhurst & Cohen, 1972), [5] (Guillou et al., 1985).*

The EXAFS spectra acquired for the S6N_May21 set of samples were: S6N_TQ, S6N_KOH, S6N_Fe(III) and S6N_LFe(VI); not enough signal emerged from the S6N_KClO, making it impossible to record a spectrum, as already seen with the XANES processing. Regarding the S6N_Apr22 set of samples, the spectra collected for the EXAFS analysis were: S6N_TQ_80K, S6N_Fe0_80K and S6N_Fe+Ag_80K (collected at T = 80 K). Due to the A08-1-1089 being a XANES-focused experiment, S6N_Apr22 spectra were acquired up to k_{max} = 8 $Å^{-1}$ (about 250 eV over the Hg LIII edge) except for the cases mentioned above, brought to k_{max} = 14 $Å^{-1}$ (about 760 eV over the Hg LIII edge). The investigate short portion of the EXAFS region, together with the low intensity of the Hg signal registered, made the EXAFS processing for the rest of the samples non-significant. The Fe0_Pref_80K and Fe+Ag_Pref_80K were properly investigated in the EXAFS region too; however, regarding the Fe0_Pref_80K, a sharp decrease in the Hg signal invalidated any possible information retrievable. In order to demonstrate the efficacy of the procedure, the montroydite and synthetic HgO standards were both fitted using the montroydite CIF (Fig. 3.30c) as the base model to show the appropriateness and equivalence of the two samples (results in Fig. 3.31 and Tab. 3.7). Afterwards, the cinnabar standard signal was fitted with α-HgS (Fig. 3.30a) and β-HgS (Fig. 3.30b) CIFs to prove the accuracy of the Artemis fitting, capable of discriminating between the two (results in Fig. 3.32 and Tab. 3.8).

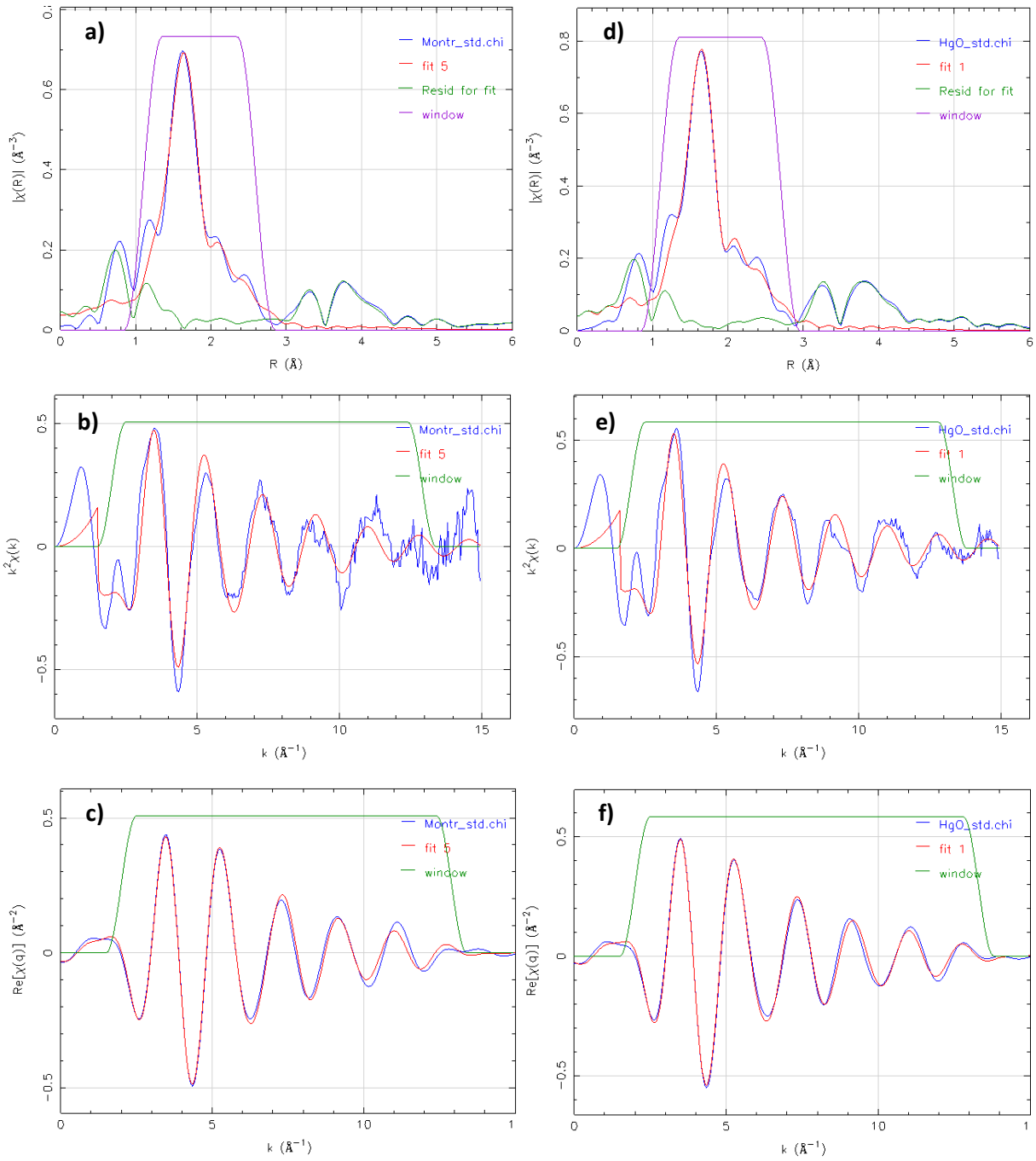

*Figure 3.31: EXAFS fits, using the montroydite CIF model, of montroydite standard sample using **a**) χ(R), **b**) χ(k) and **c**) χ(q) signals, and of synthetic HgO standard sample using **d**) χ(R), **e**) χ(k) and **f**) χ(q) signals. Montroydite model from (Aurivillius, 1964).*

a)

Guess parameters		+/-
R-factor	0.017	
amp	0.78	0.10
delE0	9.15	1.37
delR	-0.006	0.012
ss	0.004	0.002
delR1	-0.018	0.032
dtemp	175.10	34.91
Path 1 (Hg-O1)		
Reff	2.0387	
R	2.0326	0.0117
N	2	
Path 3 (Hg-O3)		
Reff	2.8071	
R	2.7567	0.0315
N	1	
Path 4 (Hg-O4)		
Reff	2.8163	
R	2.7983	0.0315
N	2	

b)

Guess parameters		+/-
R-factor	0.012	
amp	0.79	0.07
delE0	10.37	1.10
delR	0.007	0.009
ss	0.003	0.001
delR1	0.005	0.024
dtemp	192.74	29.74
Path 1 (Hg-O1)		
Reff	2.0387	
R	2.0320	0.0087
N	2	
Path 3 (Hg-O3)		
Reff	2.8071	
R	2.7938	0.0241
N	1	
Path 4 (Hg-O4)		
Reff	2.8163	
R	2.8116	0.0241
N	2	

*Table 3.7: parameter results from the quantitative EXAFS fits of **a**) montroydite standard sample and **b**) synthetic HgO sample, from Fig. 3.31.*

The montroydite and synthetic HgO EXAFS analyses showed an excellent agreement using the montroydite CIF model, as highlighted in Fig. 3.31a and 3.31b. Regarding the portions of χ(R) signal in the $1.1 \leq R \leq 2.6$ range, they were accurately modeled by taking into account the 6 closest oxygen atoms forming a 6-coordinated polyhedral with Hg (Fig. 3.30c) and their own paths of photo-electron retro-diffusion, as shown by the 1.7 and 1.2 % R-factors (Tab. 3.7). Having such quality spectra (high noise coming at around $k = 9$ Å^{-1} for montroydite, Fig. 3.31b), the closest two oxygens were undistinguishable one another due to their proximity and their paths were merged in path 1 (thus presenting degeneracy, "N", = 2, Tab. 3.7). The sixth oxygen didn't have a noticeable contribution. The respective best fits showed excellent consistency between the crystallographic distances of the starting CIF model and the experimental ones, as emphasized by the low delRs between CIF Reffs and experimental Rs, while the energy/k alignment (delE0) and the static and thermal disorder (ss) parameters confirmed their correctness (Tab. 3.7). Since the path degeneracies had been made equal to the coordination numbers, the ideal amplitude reduction factor S_0^2 should be $1 \pm 0.2/0.3$, which is a criterium met by the fits. Evidence of the quality of the fits could be seen by a simple comparison of experimental and theoretical data as χ(k) (Fig. 3.31b, 3.31e) and by the inverse Fourier transformation of the isolated χ(R) signal in χ(q), which show the oscillatory contribution of

the sole isolated experimental and model χ(R) in k space (Fig. 3.31c and 3.31f). The two EXAFS fitting showed how montroydite and synthetic HgO standards shared the same Hg local structural environment, endorsing the quality of the natural standard pellet.

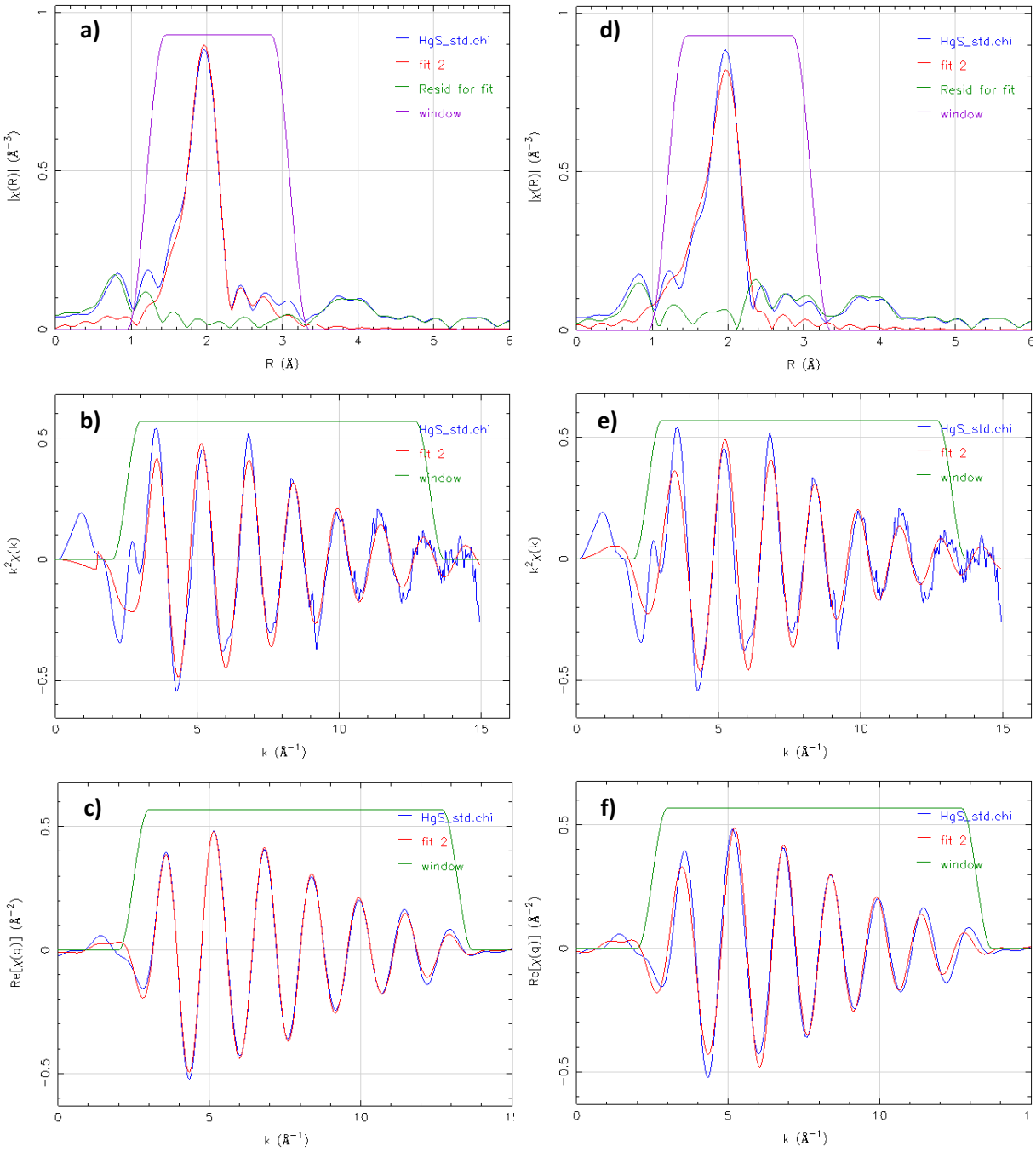

*Figure 3.32: EXAFS fits of cinnabar standard sample using **a**), **b**) and **c**) a α-HgS CIF model, and **d**), **e**) and **f**) a β-HgS one, from (Auvray & Genet, 1973) and (Wyckoff, 1963) respectively.*

a)

Guess parameters		+/-
R-factor	0.010	
amp	0.88	0.06
delE0	8.23	0.81
delR	0.007	0.006
ss	0.004	0.001
delR1	0.088	0.055
ss1	0.03	0.01
Path 1 (Hg-S2)		
Reff	2.3679	
R	2.3748	0.0056
N	2	
Path 3 (Hg-S4)		
Reff	3.0942	
R	3.1818	0.0551
N	2	

b)

Guess parameters		+/-
R-factor	0.04876276	
amp	-0.62	0.09
delE0	-10.95	1.73
delR	-0.045	0.012
ss	0.005	0.001
Path 1 (Hg-S1)		
Reff	2.5339	
R	2.4894	0.0115
N	4	

*Table 3.8: parameter results from the quantitative EXAFS fits of cinnabar using **α**) α-HgS CIF model and **b**) β-HgS CIF model, from Fig. 3.32.*

The EXAFS fitting procedure was further tested using the freshly prepared cinnabar standard sample and two different CIFs (Fig. 3.32). The α-HgS model, which saw the Hg being 6-coordinated with sulfur atoms, showed an excellent agreement with the experimental spectrum within the $1.2 \leq R \leq 3.1$ Å fitting range, as highlighted by the small R-factor and the other EXAFS parameters within the optimal range (Tab. 3.8). As expected, shifting to the β-HgS CIF model produced an inappropriate outcome: the software wasn't unable to fit properly the experimental signal using a perfect tetrahedral coordinated Hg, resulting in a fit which resulted not accurate. While the in-accuracy was noticeable already from a graphical point of view (Fig. 3.32d, 3.32e, 3.32f), as highlighted by the higher R-factor, the main evidence is the output amp parameter which, in this case, is < 0, thus indicating the choice of a wrong starting model to deal with. Trying to vary lower the number of neighbors sulfur down to 2 in order to mimic the α-HgS model, didn't change the outcome, having an effect only on the amp parameter, which stayed < 0 shifting to -1.25 ± 0.19.

Moving on to the natural water samples, the first EXAFS fit shown is the S6N_May21_TQ sample in Fig. 3.33 and Tab. 3.9.

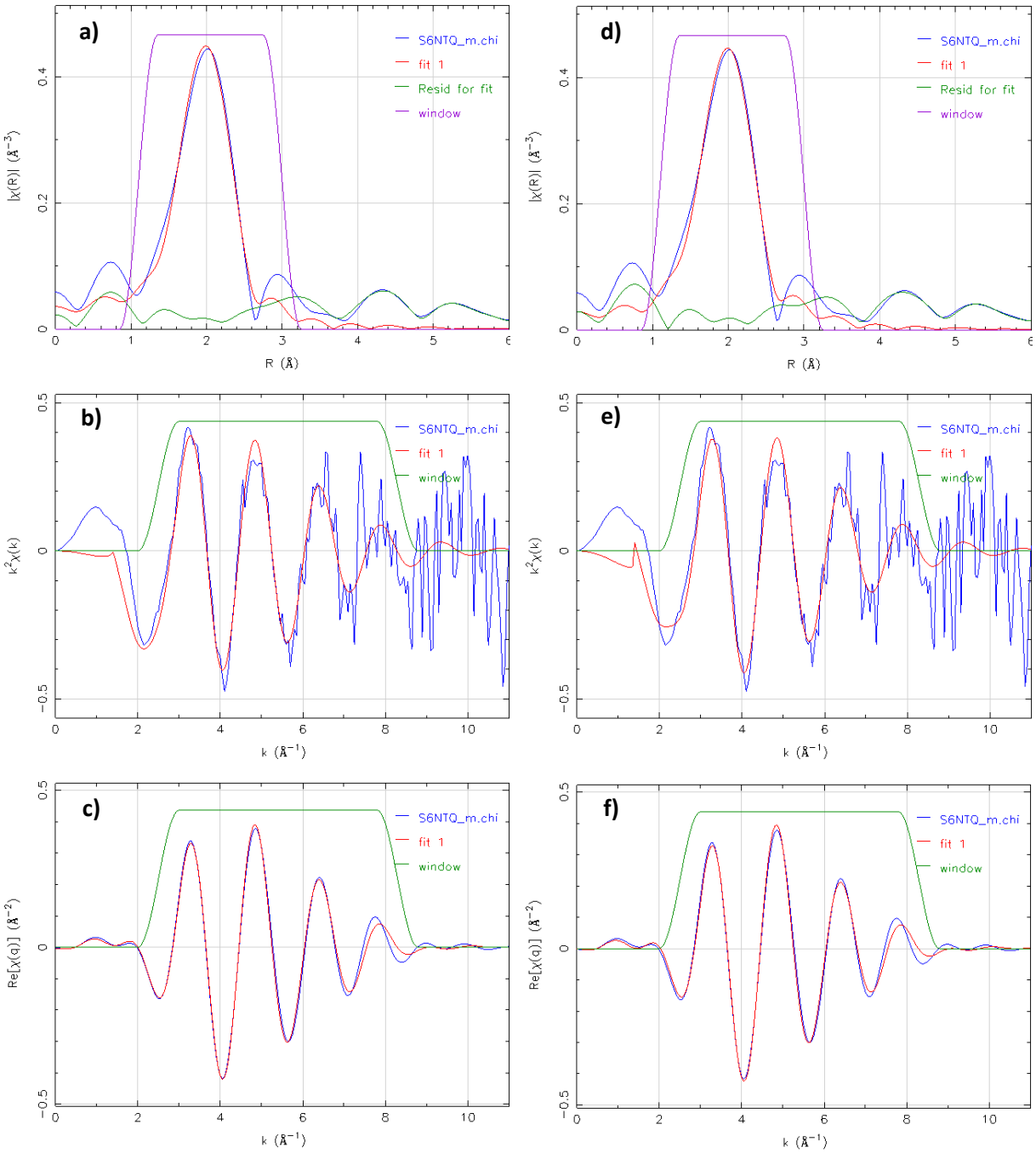

*Figure 3.33: EXAFS fits of S6N_May21_TQ sample using **a**), **b**) and **c**) a α-HgS CIF model, and **d**), **e**) and **f**) a β-HgS one, from (Auvray & Genet, 1973) and (Wyckoff, 1963) respectively.*

a)

Guess parameters		+/-
R-factor	0.010	
amp	1.77	0.26
delE0	7.55	1.22
delR	0.142	0.016
ss	0.020	0.003
Path 1 (Hg-S1)		
Reff	2.3679	
R	2.5100	0.0158
N	2	

b)

Guess parameters		+/-
R-factor	0.010	
amp	0.85	0.13
delE0	7.02	1.22
delR	-0.027	0.016
ss	0.019	0.003
Path 1 (Hg-S1)		
Reff	2.5339	
R	2.5066	0.0160
N	4	

*Table 3.9: parameter results from the quantitative EXAFS fits of S6N_May21_TQ using **a**) α-HgS CIF model and **b**) β-HgS CIF model, from Fig. 3.33.*

Unfortunately, going from standard concentrated samples to highly diluted one severely impacted the Hg LIII signal, even if the natural samples were analyzed in fluorescence mode. The noise/signal ratio dramatically increased around k = 7 $Å^{-1}$ (Fig. 3.33b, 3.33e), limiting the viable χ(k) signal to $2.5 \leq k \leq 8.3$ $Å^{-1}$, which was sufficient to obtain a strong-enough response into the R space (Fig. 3.33a, 3.33d), able to be fitted using the most probable and intense paths from the nearest neighbors atoms. Once confined in a $1.1 \leq R \leq 3.3$ Å range, the fitting procedure didn't show any apparent graphical difference between the two CIFs used as starting models, since both of them presented the same R-factor (Tab. 3.9). The reason for that is that the software identified as the best describing model the one having 4 sulfur atoms located at 2.507 ± 0.016 Å and was able to force the α-HgS CIF to resemble the β-HgS one by simply increasing the distances of the nearest 2 sulfurs in cinnabar to match the ones in metacinnabar (Tab. 3.9). The superiority of the β-HgS model was confirmed also by the amp value, which in the α-HgS dropped to 0.885 ± 0.128 once the N was increased up to 4, as in the metacinnabar case. This result confirmed the previous LCF XANES observation.

Despite the good results achieved with the S6N_TQ sample, the S6N_KOH and S6N_Fe(III) ones were not able to give such clean interpretation, as seen in Fig. 3.34 and Tab. 3.10.

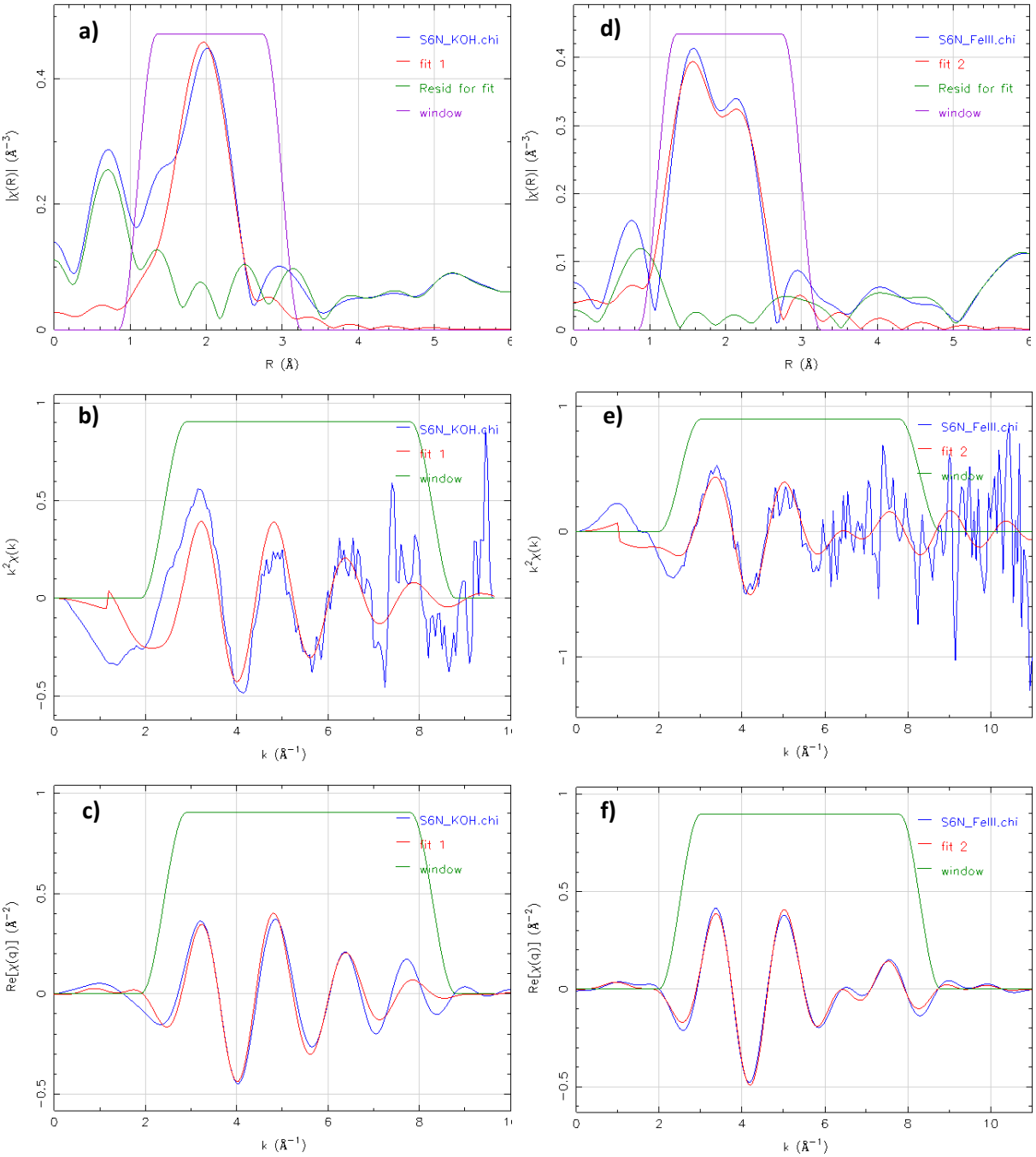

*Figure 3.34: EXAFS fits of **a**), **b**) and **c**) S6N_May21_KOH sample using a β-HgS CIF model, and **d**), **e**) and **f**) of S6N_May21_Fe(III) using the montroydite one, from (Wyckoff, 1963) and (Aurivillius, 1964) respectively.*

a)

Guess parameters		+/-
R-factor	0.084	
amp	0.95	0.42
delE0	5.24	3.62
delR	-0.034	0.048
ss	0.021	0.009
Path 1 (Hg-S)		
Reff	2.5339	
R	2.5002	0.0479
N	4	

b)

Guess parameters		+/-
R-factor	0.015	
amp	0.81	0.29
delE0	4.06	3.31
delR	-0.002	0.041
ss	0.009	0.008
delR1	-0.076	0.047
ss1	0.001	0.01
Path 1 (Hg-O1)		
Reff	2.0387	
R	2.0371	0.0410
N	2	
Path 4 (Hg-O4)		
Reff	2.8163	
R	2.7407	0.0465
N	2	

*Table 3.10: parameter results from the quantitative EXAFS fits of **a)** S6N_May21_KOH using β-HgS CIF model and **b)** S6N_May21_Fe(III) using montroydite CIF model, from Fig. 3.34.*

Accessible signal from S6N_KOH was really limited, with significant noise starting at k = 5 $Å^{-1}$ and apparently "meaningless" χ(k) peak signals at low R values which were not possible to be fitted with any model compound (signals caused by the first low-k oscillation and the one around k = 7.5 $Å^{-1}$, which was scarcely modeled by Artemis due to its high noise/signal ratio) (Fig. 3.34a, 3.34b). While the fitting procedure was not sufficient to properly investigate the whole 1.1 ≤ R ≤ 3.0 Å interval, with a resulting relatively high R-factor value, using a β-HgS CIF model was sufficient to extract the most intense χ(R) peak with significant precision, being recognized by the software as the signal coming from 4-coordinated sulfur atoms about 2.50 ± 0.05 Å far from the central Hg (Tab. 3.10a).

While the signal coming from the S6N_Fe(III) probing was affected by high noise/signal too (Fig. 3.34e), it was possible to fit the 1.1 ≤ R ≤ 3.0 Å χ(R) data using a montroydite CIF model with proper accuracy (Fig. 3.34d, 3.34f). While it was pointless to fit the spectrum using many paths, the two most probable and intense ones were able to achieve a low R-factor and delE0, together with low delR and ss (for the path 1) and delR1 and ss1 (for the path 4) (Tab. 3.10b). Other trials performed with α-HgS only and β-HgS only CIFs were unsuccessful, giving too high delR values (between -0.15 and -0.2 Å) and negative amp respectively. However, contribution from a mercury sulfide phase could be excluded due to the quality of the spectrum.

Better results were achieved by fitting the S6N_May21_LFe(VI) signal, shown in Fig. 3.35 and reported in Tab. 3.11.

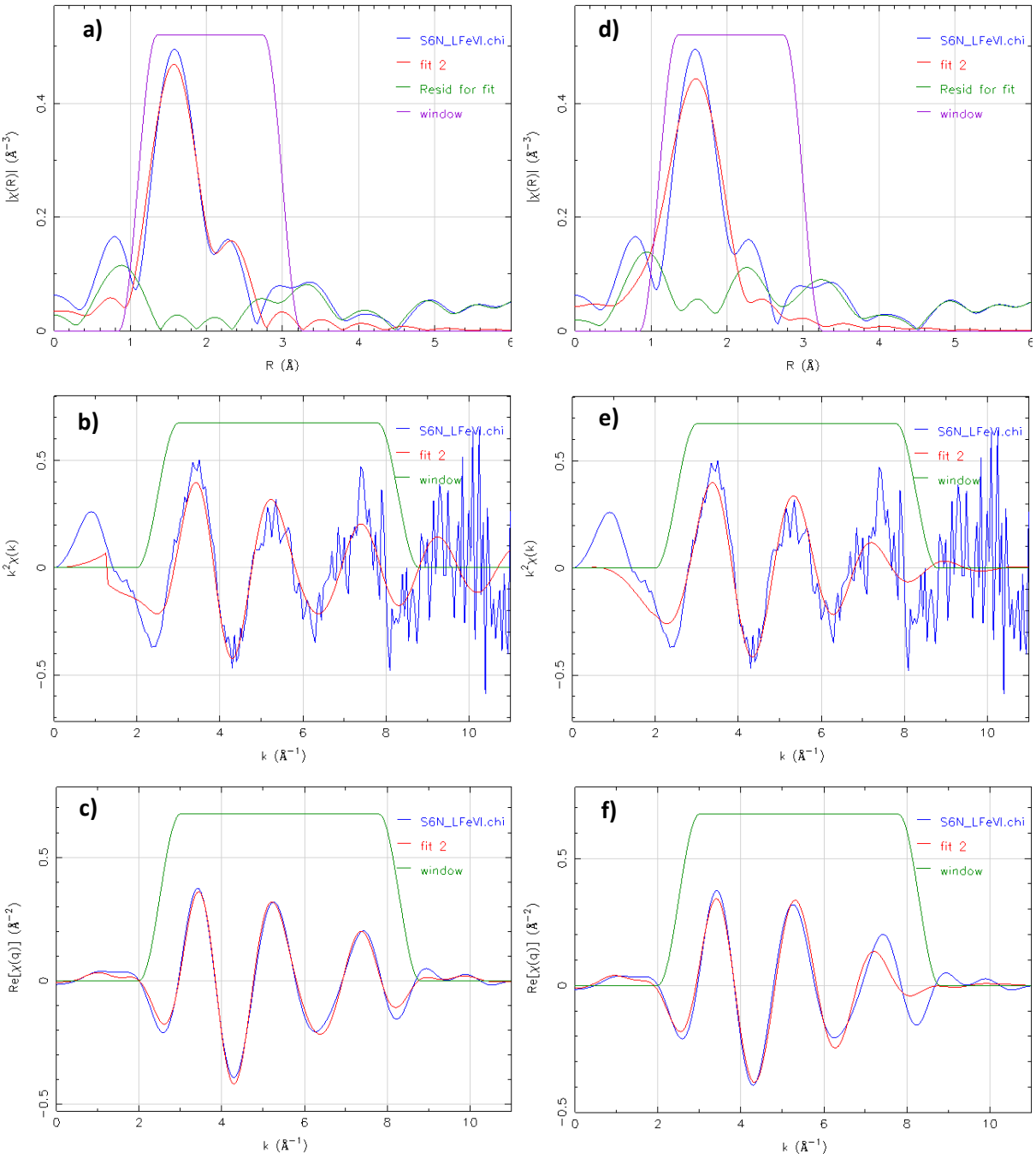

*Figure 3.35: EXAFS fits of S6N_May21_LFe(VI) sample using **a**), **b**) and **c**) a montroydite CIF model, and **d**), **e**) and **f**) a $HgCl_2$ CIF model, from (Aurivillius, 1964) and (Wyckoff, 1963) respectively.*

a)

Guess parameters		+/-
R-factor	0.020	
amp	0.61	0.24
delE0	6.04	3.99
delR	-0.035	0.036
ss	0.002	0.006
delR1	-0.060	0.111
ss1	0.013	0.018
Path 1 (Hg-O1)		
Reff	2.0387	
R	2.0035	0.0358
N	2	
Path 4 (Hg-O4)		
Reff	2.8163	
R	2.7561	0.1112
N	2	

b)

Guess parameters		+/-
R-factor	0.0723	
amp	0.83	0.41
delE0	-6.43	4.79
delR	-0.062	0.047
ss	0.022	0.009
Path 1 (Hg-Cl)		
Reff	2.2516	
R	2.1897	0.0479
N	4	

*Table 3.11: parameter results from the quantitative EXAFS fits of S6N_May21_LFe(VI) using **a)** a montroydite CIF model and **b)** a $HgCl_2$ CIF model, from Fig. 3.35.*

As in most of the cases, the resulting noise/signal ratio was high (Fig 3.35b, 3.35e), but not enough to inevitably alter the oscillatory nature of the χ(k) function in the $2.5 \leq k \leq 8.5$ $Å^{-1}$ range. The resulting best fit showed good agreement with the montroydite CIF model, with low enough values across all the parameters, except for the ± 0.111 Å uncertainty on the delR1 (relative to the path 4), which is still not-compatible with the possible Hg bond lengths of other CIF models (Fig. 3.30). In order to verify the results from LCF XANES (Fig. 3.25) the $HgCl_2$ was also tested with worse outcomes, e.g. higher R-factor (Tab. 3.11b, Fig. 3.35d, 3.35f).

Moving to the S6N_Apr22 trial, the S6N_TQ_80K and S6N_Fe0_80K didn't present any meaningful EXAFS spectra. This time, despite the low T analyses performed to reduce the thermal disorder, the noise/signal ratio was so high to produce limited oscillations in the EXAFS region and, consequently, broad and not properly able-to-be-fitted peaks (Fig. 3.36).

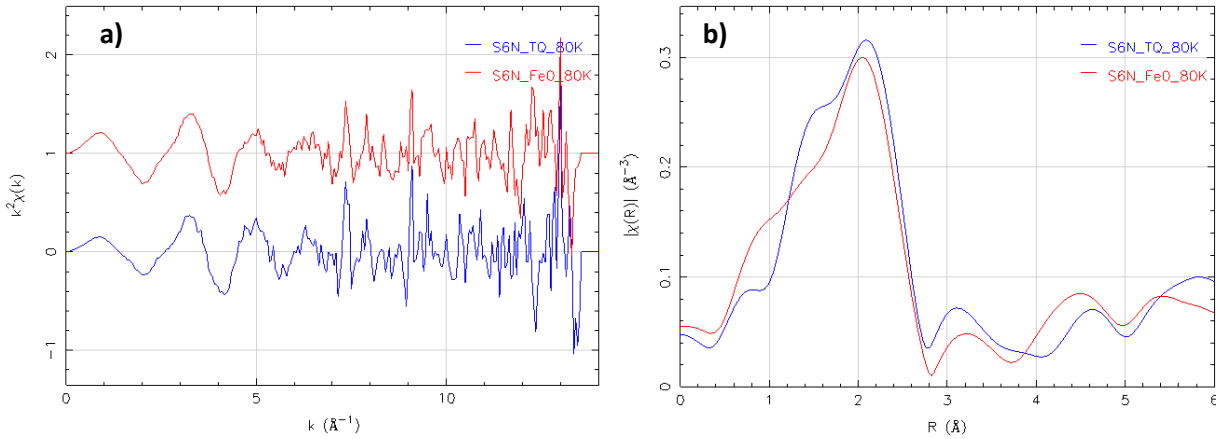

Figure 3.36: ***a)*** *χ(k) and* ***b)*** *χ(R) (from transformation of 2.5 ≤ χ(k) ≤ 8.5 Å^{-1}) signals of S6N_Apr22_TQ_80K (blue line) and S6N_Apr22_Fe0_80K (red line) samples.*

Lastly, the S6N_Fe+Ag_80K data are presented. This sample, resulting from the S6N_Apr22 treatment using Fe+Ag NPs, showed the best signal quality among all the EXAFS samples analyzed. The first results are shown in the Fig. 3.37 and summarized in the Tab. 3.12.

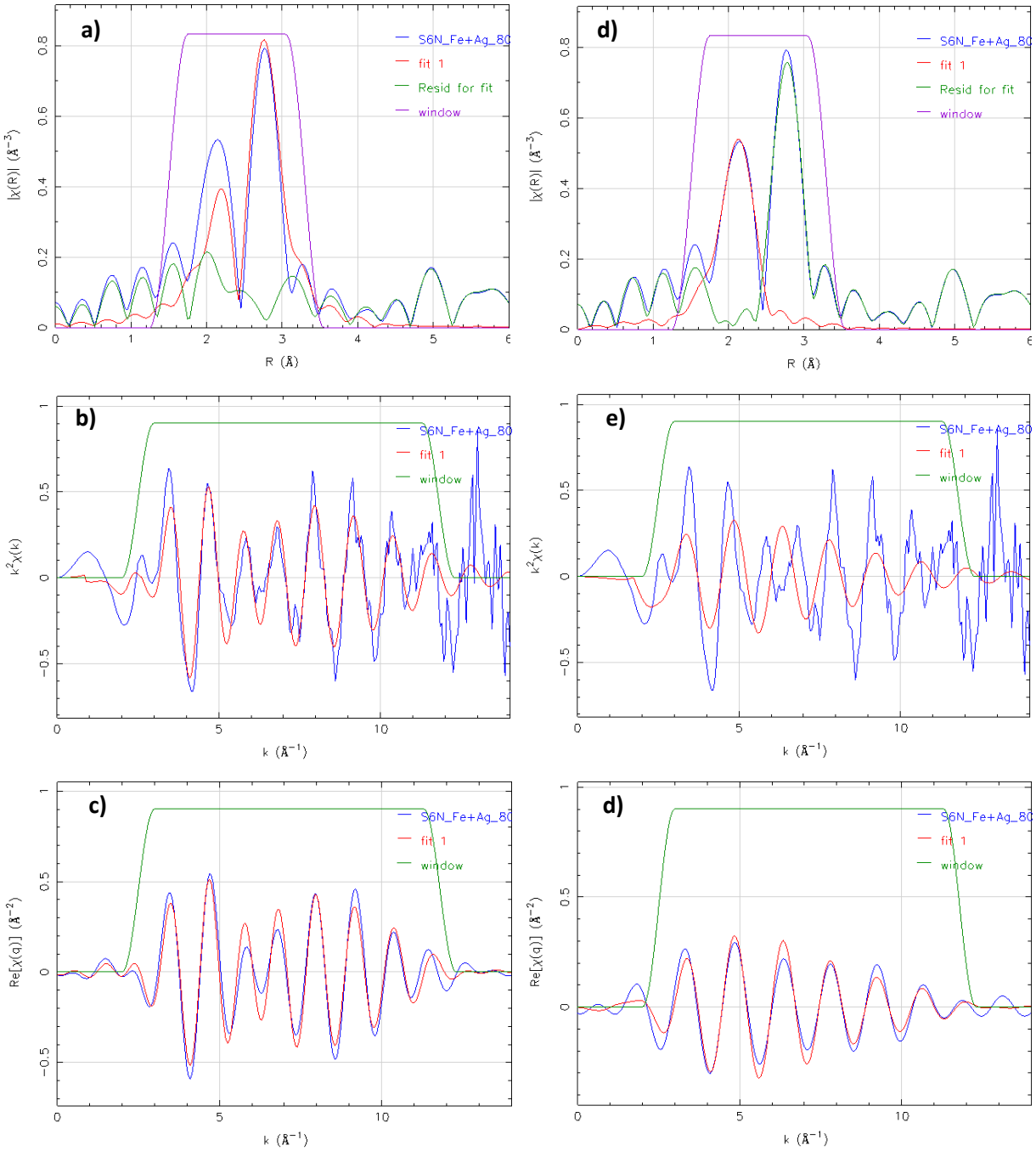

*Figure 3.37: EXAFS fits of S6N_Apr22_Fe+Ag_80K sample using **a**), **b**) and **c**) a moschellandsbergite CIF model, and **d**), **e**) and **f**) a β-HgS CIF model, from (Fairhurst & Cohen, 1972) and (Wyckoff, 1963) respectively.*

a)

Guess parameters		+/-
R-factor	0.0893	
amp	1.09	0.25
delE0	2.85	1.59
delR	0.002	0.015
ss	0.012	0.002
Path 1 (Hg-Ag2_1)		
Reff	2.8798	
R	2.8815	0.0152
N	6	

b)

Guess parameters		+/-
R-factor	0.6331	
amp	0.40	0.39
delE0	11.45	9.47
delR	0.010	0.084
ss	0.006	0.012
Path 1 (Hg-S)		
Reff	2.5339	
R	2.5438	0.0843
N	4	

*Table 3.12: parameter results from the quantitative EXAFS fits of S6N_Apr22_Fe+Ag_80K using **a)** the moschellandsbergite CIF model and **b)** the β-HgS CIF model, from Fig. 3.37.*

The χ(k) signal, this time was transformed into χ(R) from a broader 2.5 ≤ k ≤ 11.8 $Å^{-1}$ which was then fitted in the 1.5 ≤ R ≤ 3.3 Å window (purple line in Fig. 3.37a) using the moschellandsbergite (Ag_2Hg_3) CIF model first. The graphical results showed a good fit of the most intense R peak around R = 2.9 Å while the second most intense, around R = 2.1 Å, wasn't matched in a proper way, resulting in a relatively high R-factor (which could simply be lowered tightening the R fit window, isolating the most intense peak only). Based on fact that the neighbors Ag atoms in the moschellandsbergite cubic structure are quite close (Fig. 3.30d), the best result was achieved employing only the most intense and probable path (path 1, direct retro-diffusion from the closest neighbor) in a 6-coordinated structure where Hg atoms are surrounded by 6 Ag atoms at a distance = 2.882 ± 0.015 Å, in excellent agreement with the moschellandsbergite model and with an optimal amp value (Tab. 3.12a). Afterwards, the same χ(R) portion of the spectrum was fitted using the β-HgS CIF; this produced a really good fit of the second most intense peak only, while the first one was completely ignored, resulting in a really high R-factor joined by good EXAFS parameters. These parameters appeared to unveil the existence of a second Hg phase inside the sample, whose characteristics were really close to sulfur atoms coordination with β-HgS typical Hg-S distances (Tab. 3.12b). The amp value could simply be improved to 0.795 ± 0.788 by decreasing N down to 2, without any resulting change in the other variables. In order to furtherly improved the Fe+Ag NPs fit, a multi-CIF approach was used (moschellandsbergite + β-HgS), thus getting additional evidence of the quality of the single CIF fits through constraining unwanted correlations between parameters, and increasing the ratio between independent points and fit variables by simultaneously considering the contribution of more than one phase (delE0 was refined using the same parameter for both the models) (Fig. 3.38 and Tab. 3.13).

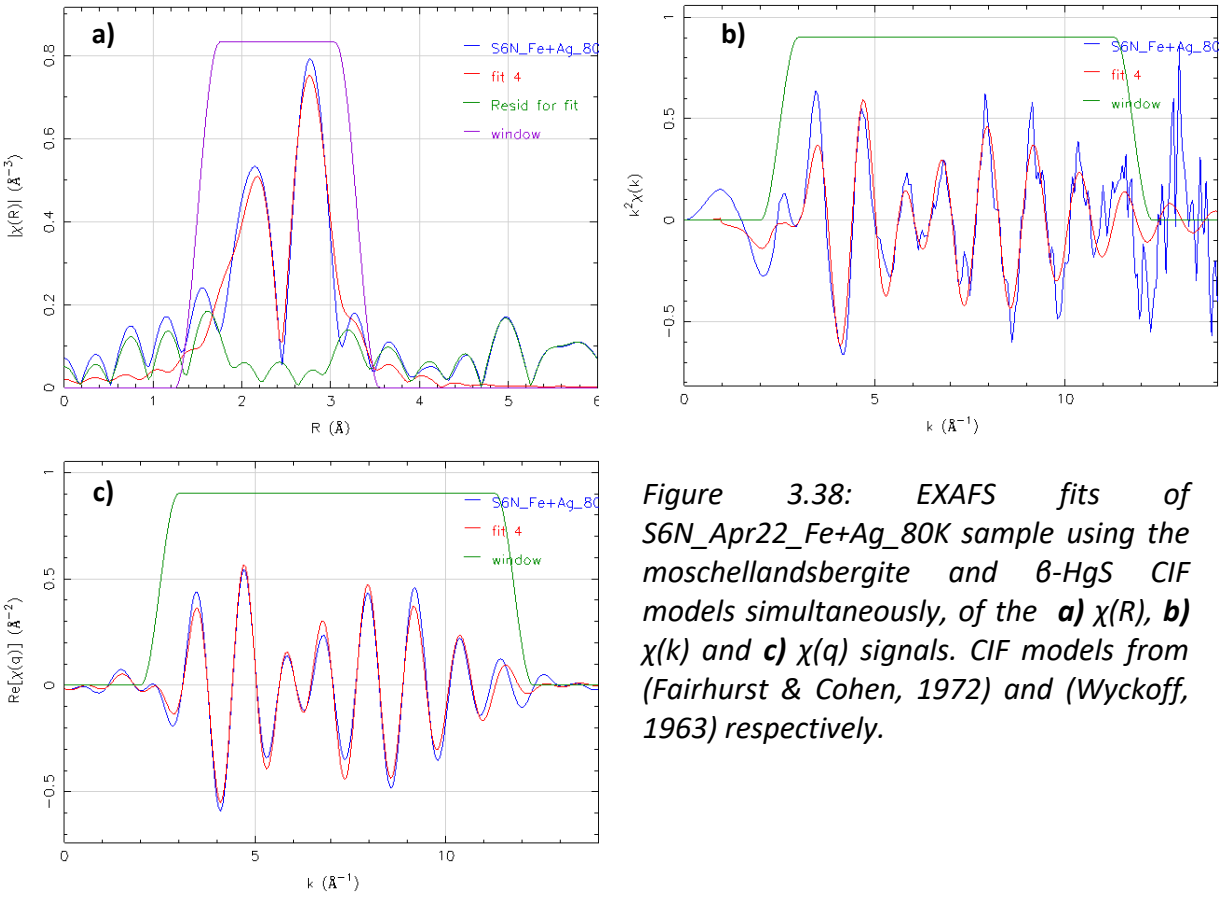

*Figure 3.38: EXAFS fits of S6N_Apr22_Fe+Ag_80K sample using the moschellandsbergite and β-HgS CIF models simultaneously, of the **a)** χ(R), **b)** χ(k) and **c)** χ(q) signals. CIF models from (Fairhurst & Cohen, 1972) and (Wyckoff, 1963) respectively.*

	Guess parameters		+/-
	R-factor	0.0457	
	delE0	3.72	1.69
β-HgS	amp	0.38	0.41
β-HgS	delR	-0.053	0.050
β-HgS	ss	0.009	0.014
Mosch.	amp_1	0.91	0.25
Mosch.	delR_1	0.007	0.016
Mosch.	ss_1	0.011	0.002
	Path 1 (Hg-S)		
	Reff	2.5339	
	R	2.4804	0.0500
	N	2	
	Path 1 (Hg-Ag2_1)		
	Reff	2.8798	
	R	2.8872	0.0156
	N	6	

Table 3.13: parameter results from the quantitative EXAFS fits of S6N_Apr22_Fe+Ag_80K using the moschellandsbergite and the β-HgS CIF models simultaneously, from Fig. 3.38.

The multi-CIF approach resulted in an improvement over the singular CIF options from the graphical point of view, as reflected by the improved R-factor but also the shared delE0, which presented a more moderate value when compared to the previous β-HgS one (Tab. 3.13 vs Tab. 3.12b). The delR values drifted a bit more from the CIF models, especially the β-HgS one, while still be perfectly in agreement with the proposed structural models. The end result saw a sample characterized by a double phase mercury bound to Ag and S, with a moschellandsbergite-compatible structure and a metacinnabar one with Hg coordinated with 6 Ag and 2 S atoms respectively. While the amp_1 for the Hg-Ag multiplicity reached the ideal value of 1 ± 0.2/0.3, the amp relative to the Hg-S phase is appreciably lower, probably because of the prominent role of the moschellandsbergite CIF which took over metacinnabar during the fitting phase (see Fig. 3.37a, which shows how the β-HgS signal is overlapped on one of the component of moschellandsbergite signal). Lastly, the imiterite CIF (Fig. 3.30e) was used in order to furtherly test the Fe+Ag NPs sample, being imiterite a Hg phase containing both S and Ag (Fig. 3.39). Various combinations of the most intense/probable retrodiffusion paths for both the neighbors S and Ag atoms, taken alone or in combination one another, could not reach the overall degree of accuracy of the moschellandsbergite + metacinnabar model. Fit 1, which focused on the path 1 only, which is the main/most probable path involving the 2 closest S atoms (Fig. 3.39a), was the only one capable of fitting the second most intense χ(R) signal, with resulting parameters indicating a compatibility with the Hg-S bonds found in β-HgS more than imiterite (Hg-S bond length = 2.545 ± 0.085 Å). Instead, the fits from 2 to 5 (Fig. 3.39b), results of the combination between sulfur and silver paths with different N, were not able to fit the two most intense χ(R) signals resulting, in the best fits, in delE0 values around -18 to -20 eV, together with negative amp values.

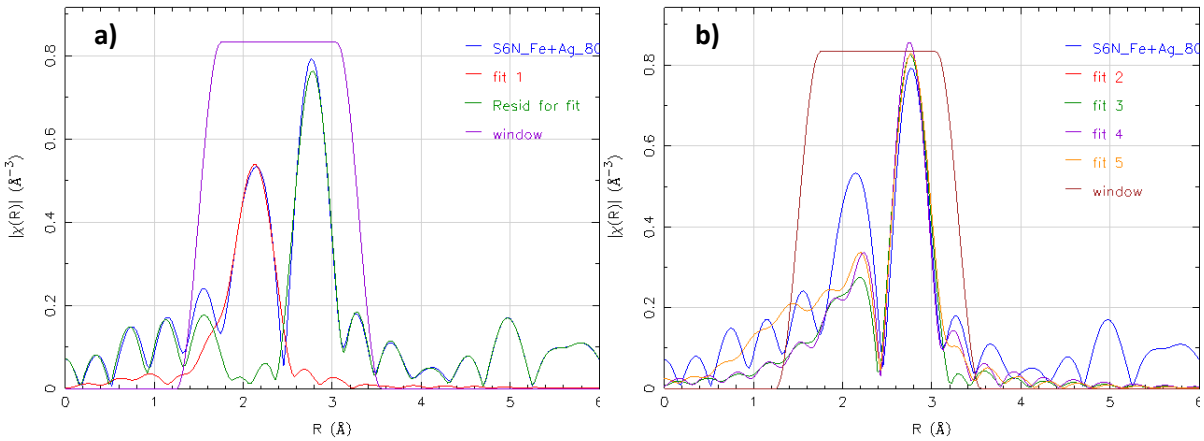

*Figure 3.39: EXAFS fits of S6N_Apr22_Fe+Ag_80K sample using the imiterite CIF model with **a**) only the path 1 (Hg-S) considered and **b**) a combination of path 1 to 4 (Hg-S and Hg-Ag paths). CIF model from (Guillou et al., 1985).*

3.4. Overall discussion

Many different factors help define the viability of a remediation technique applied to instances dictated by real environmental contexts. Among these, for obvious reasons, the target-contaminant removal efficiency is one of the main factors and it can be studied through simple laboratory testing with laboratory-prepared samples. Other very important factors include the speciation of the contaminant in the source material and its post-treatment transformations, for which tests directly involving material from the site to be remediated are necessary. This is because of the usually high complexity of a natural system compared with a laboratory-scale pilot experiment, resulting in outcomes comparable more difficult to be fully understandable in advance. Regarding mercury in aqueous environments, the only two published studies involving ferrates currently concern solutions prepared in the laboratory and both of them present, unfortunately, partial or unclear information (Bartzatt et al., 1992; Murmann & Robinson, 1974). In addition, there is a total lack of studies dealing with issues and matrices from real contaminated environments which, as we will see below, represent a major concern when dealing with any possible judgment on the effectiveness of a remediation method. This study attempted, for the first time, to give preliminary information regarding the removal of mercury from real-environmental aqueous matrices using ferrate(VI) products, as well as testing other more state-of-the-art materials pertaining to the world of nanotechnologies.

3.4.1. HgSS trials

From a mere efficiency perspective, the liquid ferrate synthesized with a new, original procedure during this study, achieved 91 % mercury removal from both the 500 ppb and 1 ppm Hg(II) lab prepared solutions (Fig. 3,9, 3.10, Tab. 3.2), at around 80 ppm Fe(VI) and 400 ppm Fe_{tot} used. This result confirmed both the data from Murmann & Robinson, who observed a > 94 % mercury removal for a 370 ppb Hg(II) solution treated with 50 and 100 ppm FeO_4^{2-}, and the conclusions from Bartzatt et al. who, referring to a series of metal contaminants (including Hg(II)), stated that "in the cases where initial metal cations were dilute (parts per million), potassium ferrate quantitatively removed them from solution (to less than parts per billion)" (Bartzatt et al., 1992; Murmann & Robinson, 1974). The liquid ferrate performance observed is approximately the same achieved by the Fe(III) reagent, employed at the same Fe_{tot} content (around 400 ppm), in HgSS_500ppb and _1ppm (95 and 91 % removal respectively). Such performances are comparable to other modern nano-adsorbent materials, tested at lower Fe/Hg ratios on Hg^{2+} contaminated water ((Chizitere Emenike et al., 2023) and references therein), as well as more traditional ones such as Fe(III) sulphate, tested on $5*10^{-4}$ M Hg(II) solutions over a 4-12 pH range (Inoue & Munemori, 1979). Looking to the results obtained from KOH and KClO treated samples, the extremely high pH values and the simultaneous processes of alkalinization + oxidation appear to not be sufficient to explain the sharp decrease in mercury contents seen with LFe(VI) and Fe(III) treatments, highlighting the key role of the iron aliquot for mercury removal. Regarding the liquid ferrate, FeO_4^{2-} decomposition in water produces a series of Fe(III) oxides/hydroxides/oxyhydroxides (J.-Q. Jiang & Lloyd, 2002; J. Q. Jiang, 2007; Luo et al., 2011; V. K. Sharma, 2007) or, more specifically, core-shell γ-Fe_2O_3/ γ-FeOOH nanoparticles (par. 1.1.1.1.), with strong coagulant behavior and evidences of pollutants being both incorporated in the crystalline sites of the nanoparticles and/or adsorbed onto their surface (Kralchevska et al., 2016; Prucek et al., 2013, 2015). On the other hand, $FeCl_3$, which was added in the Fe(III) tests, is commonly used as a coagulant and flocculant for sewage treatment and potable water production and, together with other iron salts, is capable of removing a broad range of organic and inorganic impurities (Ippolito et al., 2011; X. Lu et al., 2014; Ramli & Aziz, 2015; Tang et al., 2014). $FeCl_3$ has a strong tendency to hydrolyze in water environments, resulting in a list of low molecular-weight complexes in solution, a colloidal system of polynuclear polymers species (which can be isolated as an

amorphous solid phase) and following precipitation of Fe(III) oxides/hydroxides/oxyhydroxides ($Fe(OH)_3$, FeO(OH), Fe_2O_3) (Collins et al., 2016; Cornell et al., 1989; Hellman et al., 2006). The polymerized species are generally acknowledged as the main active ingredients for turbidity and contaminants removal (Tang et al., 2014). The presence of a base (e.g. KOH) immediately leads to precipitation of poorly ordered ferric hydroxide such as ferrihydrite (Cornell et al., 1989), which can also be specifically isolated and used for water treatments thanks to its high adsorption properties (e.g. treatment of groundwaters contaminated with U(VI), (Morrison et al., 1995)). Moreover, similar to amorphous ferrihydrite and goethite, Fe(III) hydroxides/oxyhydroxides contain hydroxyl groups which, in Hg removal trials using $FeCl_3$, were responsible for high mercury absorption ((X. Lu et al., 2014) and references therein). In light of the reported literature evidence, the proposed removal mechanism for the Fe(III) and LFe(VI) containing reagents used in this study is the Hg complexation onto the iron by-products surface active sites + flocculation and precipitation, in accordance with studies performed on Hg(II) absorption on ferrihydrite (Tiffreau et al., 1995) and on goethite (Bonnissel-Gissinger et al., 1999).

When the Mixfer reactant was added to the HgSS, conversely, no significant decrease in the HgSS content was achieved, even with higher Fe_{tot} addition compared to the Fe(III) and LFe(VI) trials (around 530 ppm of Fe_{tot}, of which 99 ppm of Fe(V) and 45 ppm of Fe(VI)). To investigate the possible reason behind this behavior, a further test was operated, looking to the final pH value which would be reached by MilliQ water after a comparable addition of Mixfer. In the test, 152.7 mg of Mixfer were added to 25 cc of MilliQ water. The pH value, measured with the PC 70 Vio multimeter, raised from the initial 6.8 to 12.7 units as a result of the addition. This increase is justified in terms of a KOH content in the Mixfer of about 70 mg, i.e. that the K_2O equivalent content of the Mixfer is around 38 %. On this basis, assuming an analogous behavior during the HgSS_1ppm treatment, one can verify that the change in pH is compatible with the MilliQ test, accounting also for the uncertainty of the pH measurement. In the HgSS case, the excess of hydroxyl anions added concurs to the neutralization of a relevant part of the original acidity but the rise in pH, fully quantitatively justified, wasn't enough to reach a complete neutralization. This induces relevant consequences on the properties of the reacted species, namely the Fe(III) already in the Mixfer and the ones coming from the Fe(>III) decomposition, such as inhibiting the precipitation of solid particulate, responsible for the Hg adsorption and removal from the aqueous environment. This is probably the reason of the

poor performances of the Mixfer in the Hg removal testing and the same mechanism is clearly accountable for the poorly performances of the solid ferrate SFe(VI) too which, despite being added in the same amounts as the Mixfer, presented an even smaller shift in the pH of the treated solution (Tab. 3.3). The lack of characterization on the composition of the SFe(VI) and, in particular, on the active species and the amount of iron within, hindered further speculations.

On the other hand, while low pH values normally boost the performances of ZVI through the acceleration of iron corrosion and dissolution of the passivated oxide layers, very acidic conditions (pH < 3.8) might diminish them. In fact, such conditions could cause a fast loss of ZVI particles due to iron dissolution being highly promoted at extreme pH values, as well as it could lead to an excessive accumulation of H_2 bubbles at the particles surface, decreasing the available reactive surface area (Y. Sun et al., 2016). These mechanisms were probably responsible for the limited effectiveness of the nZVI treatment in HgSS_1ppm when compared to the literature, which recognizes nZVIs and ZVIs in general as optimal Hg removers from lab-prepared solutions ((Chizitere Emenike et al., 2023) and references therein). A 29 % Hg removal using 12.7 mg nZVIs (254 ppm) was obtained in this study, while Gil-Diaz highlighted a 97 % removal using 180 ppm of stabilized nZVIs (NANOFER 25S) in 100 ppm Hg(II) solution at pH = 7 (Gil-Díaz et al., 2021). A more in-depth discussion about the literature data is present in par. 3.4.7.. In contrast, the high removal in Fe+Ag NPs samples suggests that, in this particular reagent, silver plays a more important role than the iron counterpart, even at percentages as low as 7.1 wt%. The 70 % mercury removal observed in the HgSS_1ppm test was achieved at pH = 1.4 using 12.1 mg of Fe+Ag NPs (242 ppm total, of which 17 ppm of Ag(0)), which is lower when compared to the 99 to 98.5 % mercury removal by Wang et al., who used 5 mg (250 ppm total, of which 7 ppm of Ag(0)) of a composite nano-reagent, consisting in Ag NPs supported by tunable porous Covalent Organic Framework (COF), at pH = 1 to 5, tested on a 10 ppm Hg(II) solution (L. Wang et al., 2020). Since bimetallic nanoparticles are very complex and diverse systems, whose main properties such as surface area available, Ag content, selectivity of the element to be removed, stability etc. depend very much on the synthesis process and the support material used (nZVIs, COFs, alumina, graphene etc.), finding a cross-criterion to make comparisons on their removal efficiencies is particularly difficult. One element that may have adversely affected the performance of Fe+Ag NPs is the particularly acidic pH of the HgSS which, although it did not seem to adversely affect the performance of

Ag NPs alone (L. Wang et al., 2020), certainly affected the stability and persistence of the nZVIs used as support, promoting their dissolution. Further discussion over the literature bimetallic Ag NPs can be found in par. 3.4.8..

3.4.2. S6N_TQ

Switching to ASSM groundwaters, the main difference with laboratory-prepared Hg(II) solutions concerns the multi-phase nature of the S6N system, which sees the presence of a natural solid phase containing mercury in turn (Fig. 3.19). After being left to rest at ambient T° for 2 days, filtration of 100 ml of S6N_May21 using a 0.45 µm porosity filter resulted in about 1.6 mg of deposit while, following the same procedure, filtration of 50 ml of S6N_Apr22 gave an amount of deposit under the scale detection limit (a 0.0001 g Sartorius scale was used for the measurements). This information was confirmed by the comparison of the Hg L_{III} edge step heights from S6N_May21_TQ and S6N_Apr22_TQ coming from XAS analyses (Fig. 3.27g), which revealed an approximately 12:1 signal ratio, in agreement with the difference in terms of deposit mass on filters pointed out by weight measurements. The assessment of Hg speciation was done using SEM (par. 3.3.2.), XANES (par. 3.3.2.1.1.) and EXAFS (par. 3.3.2.1.2.) analyses. Although each of these methods present some sort of limitations (SEM-EDX: identification of minor amounts of minerals but qualitative; XANES: 10 % of threshold for mineral abundance, possible lack of a complete pool of reference compounds; EXAFS: relative higher signal/noise necessary for extracting significant information), their combination allowed for significant conclusions to be made. SEM analyses on S6N_Oct20_TQ filtrates showed the occurrence of diffuse mercury sulfide and Hg-S-O particles of micrometer/sub-micrometer sizes up to 10-20 µm in extent (Fig. 3.19). LCF on µ(E) XANES spectra reinforced the SEM observations presenting a Hg speciation in the S6N_May21_TQ precipitate of 99 ± 2 % β-HgS, 2 ± 2 % HgO (Tab. 3.5) and in S6N_Apr22_TQ precipitate of 94 ± 1 % β-HgS, 8 ± 1 % HgO (Tab. 3.6), achieved as best fits over the 154 fits per sample tested, resulting from all the possible combinations of the 8 different Hg standard spectra which make up the XANES pool. The EXAFS analyses on S61_May21_TQ furtherly confirmed the dominant role of metacinnabar over cinnabar (Fig. 3.33, Tab. 3.9). These observations are in agreement with results coming from numerous studies on samples associated with Hg extraction in mining contexts, in particular the waste products (Bernaus et al., 2005; Kim et al., 2000, 2003;

Rimondi et al., 2014). Metacinnabar is commonly found as a conversion product of cinnabar during the roasting procedure at high T°, to which the ore material is subjected for mercury extraction (Bernaus et al., 2005; Kim et al., 2000; Rimondi et al., 2014). More rarely, due to the high T° reached during the formation of the ore deposit, metacinnabar can be found as a raw mineral, as with the Almaden ore deposits, where metacinnabar content ranges from 7 to 19 % (Bernaus et al., 2005). Metacinnabar was found by Rimondi et al. as the sole constituent of one of the soil samples collected inside ASSM area, as well as an important component (37-60 %) in waste calcines resulting from the Hg extraction process retrieved nearby (Rimondi et al., 2014). Moreover, it was found also in "La Gora" lake sediments (24 %) and in the suspended particulate matter of Pagliola Creek (20 %), indicating how the physical weathering and erosion of calcines contributed to β-HgS transport into downstream sediments, a process which is still ongoing (Rimondi et al., 2014). Metacinnabar was also found in slags sampled at the exit of Almaden treatment implant (42-88 %) (Bernaus et al., 2005), in calcines from other various mining sites (39-84 %) (Kim et al., 2000) as well as gold mine tailings (30-64 %) and marine sediments from the Bay of Trieste (62%) (Kim et al., 2003). Regarding the ASSM area, metacinnabar was found during the drilling of the control piezometers, which highlighted the heterogeneous filling material constituting the terrain where part of ASSM structures lie (Vaselli et al., 2015). Accounting for the geochemical heterogeneity presented by the groundwaters in the area, this implies a strong spatial connection between the S6N piezometer waters collected for this study and β-HgS-containing materials, probably calcines resulting from the ore processing.

3.4.3. S6N_KOH and _KClO

The S6N water treatment trials produced results that, in contrast to the HgSS, highlighted one of the focal points of this study: when it comes to mercury-related environmental remediation, laboratory tests are not sufficient to fully predict the final outcomes, making tests using matrices directly from the remediation site necessary. The main example for this is represented by the employment of potassium hypochlorite, which furtherly stressed the multiphasic character of natural waters. While in the HgSS, the KClO solution didn't lowered in an appreciable way the Hg content (Fig. 3,9, 3.10, Tab. 3.2), in the S6N_May21 and _Apr22 trials, instead, the resulting treated waters presented a substantial increase, up to +100 %, in

the starting mercury concentration (Fig. 3.11, 3.12, Tab 3.2). The most significant example involves the S6N_Oct20 water, even though the 5 months elapsed between sampling and testing prevent further quantitative considerations of the system. Despite having a starting Hg content below legal limits ($[Hg]_{S6N\_Oct20\_TQ}$ = 0.7 µg/L), addition of the KClO solution resulted in a 127 µg/L Hg content in the S6N_Oct20_KClO (Fig. 3.13). Due to the controlled experimental setup, thus being able to rule out external contamination, the most plausible hypothesis is that the KClO solution had a leaching effect on the mercury contained in the solid particulate matter of the waters, thus increasing its concentration in the liquid phase. This is straightforward in samples where the water was filtered before the reagent (_Pref) as such particulate matter is removed through filtration prior to the addition of hypochlorite, resulting in a markedly smaller increase in mercury content after treatment, at the limit of the analytical uncertainty range provided by the external laboratory. Further supporting evidence was provided by SEM observations, where no Hg phase was found when observing the post-treatment precipitate (Fig. 3.20c, 3.20d, 3.20e), and by XAS analyses, where _KClO was the only sample that did not exhibit a Hg-L_{III} signal strong enough even to acquire a low-quality XANES spectrum. This last evidence points out the marked decrease in mercury content on those filters compared to all other ones since, with this reagent, no Hg adsorption and precipitation was promoted. As the added KClO solution was prepared from a 19% KClO solution raised to a content of 10 M KOH, the possible concomitant effect of KOH was evaluated. From the experimental data, KOH alone appeared to have no effect on the starting Hg content both in S6N_May21, where no significant increase/decrease was observed (Fig. 3.11), and in S6N_Oct20, where no Hg leaching from the precipitate was observed too (Fig. 3.14) ($[Hg]_{S6N\_Oct20\_KOH}$ < 0.1 ppb). Taking into consideration the Hg speciation into the solid TQ deposit resulting from the different techniques employed, these results were confirmed by multiple literature studies which highlighted how both cinnabar and metacinnabar do not dissolve in strong bases (1 M KOH) but in saturated Na_2S solution or *aqua regia*, while the KOH is normally used for extraction of Hg organo-complexed species (Hg-humics, CH_3HgCl, Hg_2Cl_2) ((Chen et al., 2017; Kim et al., 2003) and references therein). This further supports the validity of TQ and KOH deposits Hg-speciation coming from XAS analyses (par. 3.3.2.1.), thus going so far as to negate a role of the KOH in increasing mercury concentration by solid particulate leaching. The literature regarding hypochlorite-mercury interaction endorses what seen so far. As typical for members of the hypochlorite ion salt class, potassium hypochlorite is a

strong oxidizer, predominantly of organic compounds, often substituted by calcium hypochlorite for the greater stability or by the less expensive sodium hypochlorite (International Agency for Research on Cancer, 1991). Siregar et al. found that different kind of soils treated with 6 % NaOCl removed up to 72 % of Organic Matter (OM) without significantly affecting soil crystalline mineral phases (Siregar et al., 2005). However, as reported in Pedroso et al. study, dilute hypochlorite is able to dissolve mercury sulfide and elemental mercury by converting them in more water soluble mercuric ions ((Pedroso et al., 1994) and references therein). In their work, they achieved up to a 97 % of mercury extraction from a 152 ppm_{Hg} industrial sludge (69.9 % of mercury as "insoluble in strong HCl") using a leaching hypochlorite solution with 0.26 % active chlorine and a solid/liquid ratio of 0.3 (Pedroso et al., 1994). These results were endorsed by Liu et al., who improved the 58 % leaching efficiency of their new iodide-based Hg-recover method up to 96 % using a 0.06 M solution of NaClO (or, alternatively, H_2O_2 or $Fe(NO_3)_3$). The tested material was an acid sludge waste from a lead smelter, mainly composed by metacinnabar, mercury selenide (HgSe), selenium and anglesite ($PbSO_4$), with a Hg mass fraction = 22.06 %, as by XRF analysis (Liu et al., 2019). Moreover, Radepont et al. studied the instability of α-HgS in pigments induced by $ClO_{(g)}$, both from thermodynamic calculations and experiments involving artificial aging of cinnabar pellets, discovering the conversion of cinnabar to calomel and corderoite (α-$Hg_3S_2Cl_2$). Coming back to the results of this PhD study, further experimental evidence comes from tests done on the S63 soil (Fig. 3.13) which, after the KClO addition, showed a marked increase in Hg content in the aqueous phase (308 ppb) compared to sample S63_TQ, where MilliQ water alone was unable to go beyond 1 ppb of leached mercury. However, taking into account the amount of soil used for the experiment and its mercury content, the leaching efficiency demonstrated is significantly low and corresponds to only about 15 %, over the 38 % lowest extraction value reported by Pedroso et al. (Pedroso et al., 1994). The reasons behind these markedly higher values are many, beginning with the continuous stirring level of 1050 rpm maintained throughout the experiment, as opposed to the simple initial agitation for the trials in this study, being the grade of contact between the source material and the leaching solution one of the main controlling factors. Moreover, in Pedroso et al. study, the hypochlorite concentration tested was between 0.026 and 0.26 % (w/w) over the 0.005 % (w/w) in the S63 tests (best value possible, accounting for the non-degradation of the 19 % KClO starting solution). Also, in Pedroso et al. study, an inversely proportional trend was discovered

between Hg leaching and pH (77 % extraction at pH = 7.5 vs 51 % at pH 11, all other conditions being equal) and 50 to 150 g/L NaCl were always added to the leaching solution, boosting the Hg leaching effectiveness. However, taking into consideration the smaller amount of solid particulate matter in S6N waters compared to the amount of S63 soil tested (< 1 mg vs ~ 300 mg respectively), the micrometric/sub-micrometric dimensions of the Hg particles found inside and the other experimental evidences (SEM: no Hg phases remaining, XAS: no sufficient Hg-L_{III} signal detectable), it is possible to conclude that the KClO leaching efficiency in the different S6N trials could be significantly higher than 15 %, reasonably up to complete dissolution of the solid HgS phases.

3.4.4. S6N_Fe(III)

Moving on, Fe(III) addition was able to significantly reduce the initial Hg concentrations, scoring around 68 and 75/80 % mercury removal in S6N_May21_Fe(III) and S6N_Apr22_Fe(III)/S6N_Apr22_Fe(III)_Pref respectively (Fig. 3.11, 3.12, Tab. 3.2). These results confirmed the high effectiveness of Fe-based materials in removing dissolved Hg, albeit failing to repeat the values that emerged from the HgSS test, particularly in the S6N_May21 trial, despite the same amount of the reagents used through the different tests. Although a clear explanation for this decrease in effectiveness is not straightforward, a possible cause is likely to be found in the multiphasic nature of the S6N water, especially taking into account that the greatest lost in removal % compared to the HgSS occurred in the S6N_May21 test, where the water showed higher amount of solid particulate over the S6N_Apr22 one. The EPA 7473 2007 method, used for the analytical quantification of Hg in the treated waters, is for the determination of "total mercury (organic and inorganic) in soils, sediments, bottom deposits, and sludge-type materials as well as in aqueous wastes and ground waters […] by thermal decomposition, amalgamation, and atomic absorption spectrophotometry" (U.S. EPA, n.d.). Taking into consideration the diffuse presence of HgS in the form of µm/sub-µm particles in the TQ deposit (SEM-EDX analyses, Fig. 3.19) and the previously discussed dissolution resistance of mercury sulfides in highly alkaline environments, together with the ability of the EPA method to detect any form of mercury in almost any kind of matrix, it is possible to assume the presence of a suspended solid HgS particulate, less than 0.45 µm in size, which is not attacked by the Fe(III) treatment and it is not removed by post-treatment

filtration using a 0.45 µm filter. This suspended particulate matter could represent a non-negligible reservoir of mercury, not affected by the addition of a simple coagulant agent under the conditions of this experiment, but which contributes to the amount of dissolved mercury detected by the EPA method. Unfortunately, the 2200X magnification reached during the SEM observations was not enough to prove or deny this hypothesis, which would require much higher resolution images to evaluate the presence of such particulate (e.g. an high resolution SEM with a Field Emission Gun source). Meanwhile, XAS analysis provided interesting data regarding Hg speciation within the solid deposit. Notably, the LCF on XANES spectra showed an overall increase in the HgO component over the β-HgS one in comparison to the S6N_TQ, which appears to be the consequence of the Hg adsorbed by the reagent (Fig. 3.25, 3.26). The increase is relatively small in the S6N_May21_Fe(III) (wt_{HgO} = 20 ± 3 %, $wt_{\beta\text{-}HgS}$ 80 ± 3 % in S6N_Fe(III) vs wt_{HgO} = 2 ± 2 %, $wt_{\beta\text{-}HgS}$ 99 ± 2 % in S6N_TQ) while it is more pronounced in the S6N_Apr22_Fe(III) (wt_{HgO} = 34 ± 2 %, $wt_{\beta\text{-}HgS}$ 67 ± 2 % in S6N_Fe(III) vs wt_{HgO} = 8 ± 1 %, $wt_{\beta\text{-}HgS}$ 94 ± 1 % in S6N_TQ) (Tab. 3.5, 3.6). This trend appears to be reflecting once again the difference in the amount of solid material in the two S6N waters. Since the Fe(III) reagent does not dissolve the β-HgS in the deposit, as opposed to the KClO and testified by the S63_Fe(III) and S6N_Oct20 samples (Hg content in S63_Fe(III) = 2.7 ppb, in S6N_Oct20_Fe(III) = 1.2 ppb, Fig. 3.13, 3.14)), the largest amount of solid particulate matter with size greater than 0.45 µm in the S6N_May21 gave proportionate higher Hg-L_{III} output signal coming from metacinnabar than the one coming from the Hg adsorbed by the Fe(III), while in the S6N_Apr22, characterized by smaller amount of starting solid deposit and higher dissolved Hg content, the HgO/β-HgS signal ratio consequently increased. Unfortunately, the EXAFS acquisition over the S6N_Apr21_Fe(III) filter did not retrieve a signal with a good-enough extension in k and proper signal/noise ratio, allowing only the montroydite model to be fit on the experimental data (fig. 3.34, Tab. 3.10b). The parameters of the resulting fit from the montroydite-only model indicate an excellent match with the EXAFS spectrum, meaning that the HgO component is able to be modelized, even if the broad FWHM and the shape of the curve in the R space suggests the possible presence of a further component, even more when compared to the other sample spectra which present clearer contributions from single phases. Unfortunately, the quality of the data makes this hypothesis impossible to be tested because increasing the complexity of the fit procedure through the use of a joint montroydite + metacinnabar model with such a poor-quality signal is meaningless and could lead to unwanted systematic errors.

An attempt of fitting procedure with the cinnabar CIF only was made, considering the contributions from the paths relative to the two closest pairs of sulfur atoms (not reported). The resulting fit yielded a good output at the graphical level, comparable with that of the fit made with the montroydite CIF, but it forced the software to considerably modify the delRs of the starting system, showing how therefore cinnabar is not a phase apparently contained in the sample. On the other hand, a consequent fit attempt made by considering the metacinnabar contribution showed a clearly wrong output result, due to the high R-factor and the negative amp (not reported). On closer inspection, the common factor controlling the quality of the output fits was discovered to be the number of retrodiffusion paths considered. Failure to fit using the metacinnabar model was not due to the absence of the compound from the investigated signal but to the software itself, which attempted to fit an experimental signal likely composed of multiple phases contribution with a CIF that predicts sulfur atoms within a regular tetrahedron, ergo a single Hg-S distance. This is confirmed by the cinnabar fit, which presented good approximation but resulting deeply altered Hg-S distances, and by the more ideal results emerged from the montroydite fit, that indicate its presence on the filter, which are due to the two disjointed Hg-O distances that the system can individually refine. Even without a firm answer by the EXAFS, it is possible to say that the XAS analyses on the S6N_Fe(III) confirm the observation made so far, endorsing the presence of "unreacted" β-HgS coming from the TQ and Hg adsorbed on the surface of the Fe(III) hydrolysis products, maybe with an higher HgO/β-HgS wt % than the one found with LCF XANES analysis.

3.4.5. S6N_LFe(VI)

While Fe(III) had been affected by lowered efficiencies, also the liquid ferrate was unable to repeat the results seen with HgSS. The reason behind its apparent ineffectiveness (no removal/slight [Hg] increase in S6N_May21_LFe(VI), 38 % removal only in S6N_Apr22_LFe(VI), Tab. 3.2) is to be found in the strong oxidizing power of Fe(VI). As well as hypochlorite, the ferrate ion has one of the highest redox potentials in the literature (Tab. 1.2), which caused the metacinnabar solid deposit naturally present in S6N natural water to be attacked and dissolved, as in the case of KClO, bringing more mercury into solution. While there were no direct SEM evidence recorded regarding such behavior, one need only to consider the S63 and S6N_Oct20 trials to notice this phenomenon (Fig. 3.13, 3.14), given the spikes in the post-

treatment Hg concentrations in samples S63_LFe(VI) and S6N_Oct20_LFe(VI) (157 and 65.5 ppb respectively), although starting from TQ solutions with minimal mercury content (1.03 and 0.7 ppb respectively). This mechanism of oxidation and simultaneous removal by adsorption and coagulation is typical of ferrate(VI), which presents the advantage of being a multipurpose material in many studied systems (Tab. 1.5). Unfortunately, in this case, the boundary conditions did not seem to have been favorable for the proper development of this mechanism since, for the same Fe_{total} ppm added, the LFe(VI) performances were lower than those of the Fe(III) reagent. In accordance with what seen so far, filtration of the source water significantly improved the situation, although it was not sufficient to achieve the efficiencies previously seen with the HgSS_LFe(VI) trials or with the S6N_Fe(III) samples (40 % Hg removal for S6N_May21_LFe(VI)_Pref and 51 % Hg removal for S6N_Apr22_LFe(VI)_Pref). Understanding the balance behind the uptake of mercury in solution, given by the oxidizing action of Fe(VI) onto the solid particulate, and its simultaneous adsorption, caused by the hydrolysis of un-oxidized Fe(III) present in liquid ferrate and the decomposition products of Fe(VI) itself, is not straightforward. First of all, the Hg removal efficiency for liquid ferrate should not be calculated based on the initial content of the TQ water but on the post treatment value of S6N_KClO for the S6N_LFe(VI) sample and of S6N_KClO_Pref for the S6N_LFe(VI)_Pref, assuming that the added liquid ferrate had an oxidant capability comparable to the KClO reagent. Another necessary assumption concerns the kinetics of oxidation and adsorption. Given the tendency of Fe(VI) to oxidize in milliseconds to minutes most of the contaminants with which it had been tested and to decompose to Fe(III)-based products (par. 1.1.1.1.), it is safe to assume that the dissolution of β-HgS was largely completed in a small time-frame, helped by the high surface area of the metacinnabar particles, having µm dimensions. That said, the recalculated Hg removal efficiencies correspond to: 49 % for S63_LFe(VI); 48 % for S6N_Oct20_LFe(VI); 59 % for S6N_May21_LFe(VI) and 52 % for S6N_May21_LFe(VI)_Pref; 61 % for both S6N_Apr22_LFe(VI) and S6N_Apr22_LFe(VI)_Pref. These values, although significantly lower than the tests with HgSS, appear relevant considering the conditions of the system, induced by the nature of the liquid ferrate itself, namely the high pH and the direct contribution of the “unreacted reagents”. High pH values are disadvantageous for the ferrate(VI) removal of potentially toxic trace elements such as As and, in particular, Sb and phosphates (Johnson & Lorenz, 2015; Kralchevska et al., 2016; Prucek et al., 2013). Being the pH_{PZC} (point-of-zero charge) of γ-Fe_2O_3 nanoparticles in the 6.6

to 7.8 range and the isoelectric point of γ-FeOOH between 7.2 and 8.4, the surfaces of the Fe(III) decomposition products are largely negative at high alkaline pH, thus hindering the interactions with the negatively charged species of phosphates and antimony (Johnson & Lorenz, 2015; Kralchevska et al., 2016). On the contrary, Co(II), Ni(II), Cu(II) and Cd(II) removal was positively impacted by high pH, with maximum values at pH 7 and 10 (Prucek et al., 2015). Meanwhile, liquid ferrate, in addition to high amounts of OH^-, also brings with it abundant chlorine from the synthesis process, in particular in the form of KCl impurities. The dissolution of HgS in the presence of chlorine ions results in the formation of chlorine complexes, particularly the soluble stable $HgCl_4^{2-}$ complex, whose stability range is extended by the addition of NaCl and, consequently, also KCl (Pedroso et al., 1994). This is evident in Radepont et al. study where a comparison between two Hg-S-Cl-H_2O Eh-pH diagrams from thermodynamic calculations shows the broad $HgCl_2$ stability field engulfing the HgO one when Cl is taken as a predominant specie over Hg (Fig. 3.40) (Radepont et al., 2015). These latter evidence are in agreement with the marked difference in terms of removal efficiency between the Hg(II) solution prepared from $Hg(NO_3)_2*H_2O$ and the S6N natural water, justifying a relatively higher content of mercury in solution for the S6N_LFe(VI). In addition, the role of chlorine may explain also the difference in efficiency with S6N_Fe(III), given the formation of negatively charged chlorine complexes that are more difficult to be adsorbed at high pH.

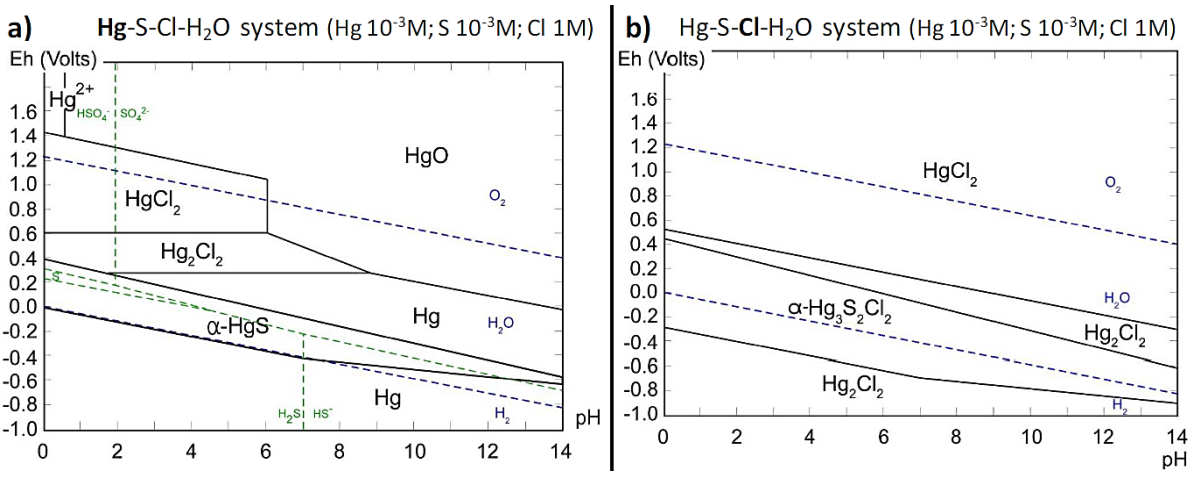

Figure 3.40: Eh-pH diagrams at 25° for the Hg-S-Cl-H_2O system with, in bold predominant species and in brackets activities of corresponding elements. ***a)*** *diagram obtained by superimposing the Hg-S-H_2O and Hg-Cl-H_2O diagrams with Hg as predominant specie and* ***b)*** *with the Cl as the predominant element in the system. From (Radepont et al., 2015).*

Furthermore, such arguments are consistent with the XAS analyses too and offer a deeper key to understand them. The LCF on S6N_May21_LFe(VI) showed a HgO abundance more than doubled in comparison with S6N_May21_Fe(III) (49 ± 3 % vs 20 ± 3 % respectively, Fig. 3.25), which reflects the decrease of β-HgS in the particulate deposit and the related increase of the mercury oxide phase given by Fe(III) adsorption. On the other hand, the other unique component that emerges from the best fit is $HgCl_2$ (52 ± 3 %), which shows that metacinnabar, if still present, represents an undetectable percentage after dissolution by addition of liquid ferrate (< 10 %). From the EXAFS analysis of the precipitate, the best fit was achieved using the montroydite CIF model over the $HgCl_2$ one (Fig. 3.35). This result is recalling of what was seen with the S6N_Fe(III) sample: although the quality of the signal in this case was better, it was still too low to determine whether a fit with two CIFs would give better results. Moreover, in this case, the fit using the $HgCl_2$ CIF revealed an higher R-factor but good amp, delE0 and delR parameters. This could be compatible with the actual existence of the chlorine component. The signal of this phase, however, is hidden by a more intense signal coming from the HgO (and, for the most part, of course, by the low signal-to-noise ratio). It is therefore possible to confirm the clear presence of an HgO phase and the absence/scarcity of β-HgS, but without denying the possible presence of a Hg-Cl phase within the precipitate, perhaps with a higher HgO:$HgCl_2$ ratio than the one seen with the LCF. Moving on to the S6N_Apr22_LFe(VI) sample, the situation that emerged from the LCF seems to be different and partially in disagreement with what seen so far. In this case, the best fit did not reveal the presence of any Hg-Cl component to accompany the abundant HgO (61 ± 3 %) but of metacinnabar (41 ± 3 %) (Fig. 3.26). These data could represent a lower efficacy of the liquid ferrate synthesized just before the Apr22 trial or indicate a possible different mechanism of action in this specific case, but there is one more piece of data that might help clarify them. Comparing the non-normalized XANES spectra between the S6N_Apr22_LFe(VI) sample and the prefiltered variant, a relatively small drop in signal intensity (- 17 %) could be observed (Fig. 3.27b), in contrast to all other samples where the height of the edge step halves in the "best" case scenario (the S6N_SFe(VI), where the drop is the smallest), down to an order of magnitude less in samples such as the S6N_Apr22_Fe0. The important decrease in signal in the prefiltered samples represents the removal of a consistent portion of solid mercury from the investigated material, consistent with the removal of the natural deposit that characterizes the S6N_TQ water, rich in metacinnabar, in the prefiltration phase. In addition, the small drop in signal

intensity with the S6N_Apr22_LFe(VI)_Pref sample allowed LCF to be applied to that sample as well and the resulting best fit saw 64 % HgO and 38 % M-HgS, totally in line with the non-prefiltered result. The fact that prefiltration had no effect on the resulting XANES signal would suggest that almost no metacinnabar had been removed with it, in contrast with all the evidence accumulate so far, from the SEM images (which clearly showed HgS on the _TQ and _KOH filters) to the XAS data (XANES and EXAFS). The most plausible hypothesis that would account for the lack of difference in XANES signal intensity between the S6N_Apr22_LFe(VI) and the "_Pref samples is that metacinnabar in the two deposits was equally consumed and is scarce or absent in both of them. Meanwhile, the identical Hg speciation between the two filters would seem to support the possibility of misattribution of the lesser component. The anomalous best fits coming from the LCF of the S6N_Apr22_LFe(VI) and "_Pref samples may be affected by the limitations of the XANES technique already mentioned. More specifically, they could be affected by the choice of an incomplete pool of standards (e.g., lack of the corderoite spectrum ($Hg_3S_2Cl_2$), a HgS alteration product seen by Radepont et el.) or difficulty in discerning the signals of the various standards components at such concentrations, since the characteristic mid-height edge feature clearly present in the S6N_LFe(VI) samples is common to both HgO and $HgCl_2$ (Fig. 3.21). Despite this possibility, in the S6N_Apr22 trial a percentage increase in the fraction of HgO out of the total components could be observed over the other samples, in agreement with the trend already noticed in the S6N_May21 trial. Concluding the discussion over the liquid ferrate treatment, some other interesting trends could be observed from the ICP analyses of the resulting waters, along with the Fe(III) one. First, it was possible to rule out an increase in the concentration of iron in solution compared to the starting water (Fig. 3.15), testifying how both types of reagents were able to remove themselves from the system by precipitating to the bottom. Secondly, a marked decrease in Sr content (> 94 %) was noticeable following both treatments, probably indicating removal selectivity toward this element and, most likely, also toward calcium (Fig. 3.16). Finally, the content of antimony in the TQ water was reduced below legal limits following the addition of both the Fe(III) (74 % removal) and the LFe(VI) (87 % removal) reagents (Fig. 3.17), in agreement with previous studies highlighting the high performance in terms of Sb removal of Fe reagents, particularly Fe with mixed oxidation states (Johnson & Lorenz, 2015).

3.4.6. S6N_Mixfer and _SFe(VI)

Regarding the solid ferrate-based reagents, Mixfer and SFe(VI), the efficiency results obtained in the S6N trial did not show major differences with the HgSS one, despite the different pH regime (Fig. 3.12). The S6N_SFe(VI) sample showed a slight increase in the post-treatment mercury content (+17 %) while the prefiltration accounted for a slight decrease (-21 %) in comparison with the starting S6N_TQ. Unfortunately, due to the S63_SFe(VI) been lost during transportation, no data on the HgS dissolution effectiveness on soil only are available. Furthermore, because of the lack of chemical characterization of the product, which represents the only successful attempt to separate a solid fraction containing Fe(VI) from liquid ferrate, only few qualitative considerations could be made. First, thanks to UV-visible measurements that showed a Fe(VI) content comparable to that of Mixfer, the supposed ppm of Fe(VI) added to the S6N sample should be around 50. Because of the scattering of solids and rapid degradation to Fe(III)) which hindered the accuracy of the measurement, that value is subjected to an high degree of uncertainty. Taking into account the HgS dissolution effect of the ferrate ion, given its high redox potential and what has been seen before with the LFe(VI) sample, it is expected that SFe(VI) also affected the mercury concentration in solution due to the interaction with the natural precipitate contained in the S6N. Although no direct examples of that interaction could be seen due to the loss of the S63_SFe(VI) sample, it is safe to assume that the solid ferrate used was, at least, partially able to attack metacinnabar because of the significant difference in terms of mercury content between S6N_SFe(VI) and S6N_SFe(VI)_Pref, which demonstrates how the removal of the solid precipitate containing β-HgS greatly reduced the post-treatment mercury content in solution. As a result, the real performances in terms of mercury removal by the SFe(VI) reagent are higher, given that the uptake of mercury from the solid phases brought the real starting values within a range between the value found in S6N_TQ to that in the S6N_KClO and S6N_KClO_Pref samples. Unfortunately, due to the lack of the total iron content in the reagent, it is difficult to speculate on the degree of adsorption given by the Fe component with oxidation state other than (VI). Fe(III), in particular, probably accounted for a significant weight % of the reagent, due to the failure to properly purify the liquid ferrate sample after its filtration. XANES analysis showed a spectrum lacking a clear feature at mid-height and with a consequent Hg speciation from LCF which saw the predominance of the β-HgS signal (71 ± 2 %) with a minority component

from the HgO (30 ± 2 %) (Tab. 3.6). This distribution presents a HgO/HgS ratio even lower than the S6N_Fe(III) sample, which appears to suggest the hypothesis of an overall β-HgS dissolution and/or Hg adsorption, but significantly lower than the liquid ferrate ones. Regarding Mixfer, the mercury content resulting from sample S63_Mixfer immediately showed a dissolution action at the expense of the HgS contained in the soil, as demonstrated by the post-treatment mercury concentration of 119 ppb (Fig. 3.13). In this case, the mg/kg of Fe(VI), calculated using the data provided by the RCPTM, would correspond to about 10, while the total iron added would amount to about 107 ppm. Using instead the value that emerged from UV-Vis analysis, the amount of Fe(VI) added would increase to about 28 ppm. The mismatches in terms of the amount of Fe(VI) and Fe_{tot} added compared to the _Fe(III) and _LFe(VI) samples was a constant flaw that was repeated throughout the overall experiment, particularly in the S6N trial, due to an error in the computation of the amount % of Fe in the total sample. This procedural error, which came to light recently during a review of the various experiments, affected any comparisons with other samples, while still allowing some important observations to be made. First of all, the S63 trial highlighted the high dissolution power on HgS exerted by Mixfer, which manages to reach 76 % of the final mercury concentration achieved by the liquid ferrate in the same trial with significantly lower amounts of Fe(VI) added, although it is necessary to consider the higher amount of Fe_{tot} in the LFe(VI) aliquot, which probably provided a greater adsorption effect. Concerning the natural water, in the S6N_Mixfer sample, the Mixfer addition introduced into the system only around 68 ppm of Fe_{tot}, which correspond to about 6 ppm of Fe(VI), calculated using the RCPTM provided data, or about 18 ppm if the measured UV-Vis concentration value is employed. Regarding the S6N_Mixfer_Pref, the Fe_{tot} added corresponded to around 58 ppm and the Fe(VI) to 5/15 ppm (RCPTM/UV-Vis wt %). Such low concentrations appeared to have not a significant effect on the overall S6N system, but this was not totally the case, as with every Fe(VI) containing reagent. Taking into account the pH variations into the S6N_Mixfer samples, from the starting circumneutral-to-slightly-basic initial conditions only a modest rise in pH value was registered (from 8.0 to 10.4 for the S6N_Mixfer and to 10.1 for the S6N_Mixfer_Pref, Tab. 3.3). From the test performed in MilliQ water, which is discussed at the beginning of this paragraph, those pH increases are not justified by the supposed concentration of additional hydroxyls added to the system, since the calculated final pH values would be higher than any possible instrumental error on the measurements (11.2 non-prefiltered / 11.1 prefiltered). While the

corresponding pH rise in the HgSS_Mixfer sample was appropriately contrasted by the original acidity of the solution, in the S6N another source of acidic generation was present, able to compensate most of the available hydroxyls. From observations of this study, a relevant role could be played by the solid particulate which, through the metacinnabar dissolution such as the observed in the S63 trial, could liberate a relevant amount of protons. In the case of the prefiltered sample, this role could be taken by a possible suspended particulate matter capable of overcoming the barrier posed by the filter used during filtration, the existence of which has been hypothesized in the discussion of the data from Fe(III) treatments. Regarding the XANES analysis, a slightly higher HgO/HgS ratio emerged from the LCF (37/65 wt %), similar to the one already seen in the SFe(VI) sample. As expected from the lower amounts of Fe(VI) and Fe_{tot} added, this is probably the result of a lower-intensity dissolution and/or adsorption processes.

3.4.7. S6N_Fe0

Lastly, the results from the application of the nanoparticles reagents on the S6N water will be discussed, starting from the Zero Valent Iron nanoparticles. During the last 20 years, nZVIs have been deeply tested, gaining widespread acceptance as a powerful environmental remediation agent thanks to their broader reactivity toward many organic and inorganic compounds, with a particular focus on heavy metals (Fu et al., 2014; Mukherjee et al., 2016; Zou et al., 2016). Many papers investigated the efficiencies and the mechanisms behind mercury removal by nZVIs but, for the most part, using artificial samples prepared with stock solutions (Gil-Díaz et al., 2021; Guo et al., 2016; Sahu et al., 2022; Yan et al., 2010). In this study, the addition of about 132 ppm of nZVIs (6.6 mg) to the S6N water led to a mercury removal of about 41 %, decreasing slightly to 33 % when the concentration of the added reagent was reduced to about 40 ppm (2 mg) (Fig. 3.12). From a comparison with the literature, Gil-Diaz et al., tested a similar addition of 0.05 % nZVIs (90 ppm as Fe) but over a 100 ppm Hg^{2+} solution, obtaining an higher removal efficiency of 67.8 % (Gil-Díaz et al., 2021). The nZVIs used by Gil-Diaz et al. exhibited stabilization by an organic surfactant (polyacrylic acid) and therefore showed a lower potential degree of aggregation. Double the amount of nZVIs (0.1 %) increased the Hg removal efficiency up to 97 %, without apparently being influenced by pH variation in a 3-9 range. The same high removal degree was observed by Yan

et al. already after few minutes from the application, using self-prepared nZVIs with an average diameter of ~ 60 nm but a strong tendency to form hundreds-of-nm-long chain-like formations due to absence of stabilizers; the tested nZVIs amount was 500 ppm against a 40 ppm Hg^{2+} solution (Yan et al., 2010). An interesting effect occurred after switching to micrometers ZVIs (mZVIs) with a mean diameter of 4.1 μm: at the same ZVI/Hg of the previous trial, the mZVIs showed no Hg removal at all, which the authors inferred was the effect of a thick surface passivation layer of iron oxide which negatively influenced the Fe(0) reducing capability (Yan et al., 2010). Together with a different Hg speciation in the natural water, such passivation mechanism could be one of the reasons behind the nZVIs low mercury removal efficiency emerged in the S6N_Fe0 sample. In the Markova et al. paper, which discusses the treatment undergone by the nZVIs employed in this study (as well as the synthesis of Fe+Ag NPs), it is shown by XRD and Mossbauer analyses that the initial composition of NANOFER 25N, which is stated by the manufacturer as "≥ 80 % Fe(0), ≤ 20 % Fe_3O_4" changed to 58 % Fe(0), 42 % Fe_3O_4 due to the aging process in water, to which the particles were subjected to increase their stability in air thanks to the formation of an iron oxide shell surrounding the Fe(0) cores (Markova et al., 2013). In the Ribas et al. article, it was shown how thick and compact oxide layers, induced for air stability and storing purposes, significantly impacted the nZVIs performances towards the reduction of Cr(VI), compared to non-stabilized ones. To overcome the problem, they tested an activation procedure which partially dissolved the passivation layer without impacting the metallic core, which resulted in a 3.4 and 4.7 increase factor in the particles reactivity (Ribas et al., 2017). Guo et al. also experienced the inhibiting effect of a dense and compact passivation layer forming over the surface of ZVIs, as highlighted by SEM images (Guo et al., 2016). The addition of common oxidants to the solution (NaClO, $KMnO_4$ or H_2O_2), in concentrations of 1 mM, weakened this layer which became uneven, rugged and fragmented, to the point of promoting the formation of high adsorptive iron hydroxides and accelerating the corrosion of the Fe(0) core, bringing the removal values of Hg(II), Cd(II) and As(V) to above 95 % (from the starting 56-77 %) (Guo et al., 2016). This experimental data takes on a particularly important value once the S6N system is considered, because the combined addition of hypochlorite and nZVIs, in addition to a possible performance boost to the nanoparticles, would affect the solid particulate in the water by leaching its mercury content starting precisely with the finest HgS suspended particulate matter, which represents a possible source of easier methylation (O'Connor et al., 2019).

Further testing will be needed to verify this hypothesis. Guo et al. experienced an additional issue regarding the mechanism of mercury removal by reducing particles. In the above-mentioned works, XPS analyses on the solid products resulting from nZVI treatment showed the almost exclusive presence of signal compatible with Hg(0) alone, resulting from the mechanism of reduction of Hg(II) contained in the tested solutions by Fe(0), a reduction energetically favorable given the high difference in terms of the standard redox potential of iron (E_h^0 = - 0.44 V for the Fe^{2+}/Fe^0) and mercury (E_h^0 = + 0.86 V for the Hg^{2+}/Hg^0) (Gil-Díaz et al., 2021; Guo et al., 2016; Sahu et al., 2022; Yan et al., 2010). Moreover, the oxidation to Fe(II) and, with excess Hg(II), to Fe(III) (E_h^0 = 0.77 V for the Fe^{3+}/Fe^{2+}) on the nZVIs surface increases the sorption effect of Hg(II) onto the iron hydroxide/oxyhydroxide active sites, while the metallic core continues to act as an electron source (Yan et al., 2010). Guo et al. expected the same kind of behavior from their sample, additionally motivated by the high degree of Hg removal observed. Instead, XPS spectrometry found no Hg peak positions, which was explained by the transformation of Hg(II) to Hg(0) and, thanks to Hg(0) high volatility, its subsequent evaporation into air because of the vacuum-freeze drying performed during sample XPS pre-treatment (Guo et al., 2016). Vernon and Bonzongo postulated that, once the Hg(II) have been reduced to Hg(0), it quickly partitions between the aqueous and gaseous phase due to its low solubility, with volatilization accounting for nearly 10 % of the total Hg removal (Vernon & Bonzongo, 2014). So, the S6N_Fe0 LCF analysis, which showed a Hg speciation analogous to the S6N_TQ one (95 ± 2 % β-HgS and 5 ± 2 % HgO, Fig. 3.26, Tab. 3.6) without presenting any evidence of Hg(0), could be influenced by the XAS analysis procedure, which saw a long acquisition time (at least 5 hours) under medium vacuum conditions (10^{-6} mbar) at 80 K, compatible with the loss of Hg(0) from the sample seen by Guo et al. which, by the way, worked with much higher amounts of both Hg(II) and ZVI (Guo et al., 2016). Another alternative hypothesis concerning the absence of the Hg(0) component could be the heterogeneous distribution of the reacted nZVIs on the filter, due to the low amount employed and their high aggregation tendency, which may have led to the sampling of an area of the S6N_Fe(0) filter containing only S6N natural deposit. Lastly, an additional small inconsistency is the slightly decrease of Hg removal efficiency in the prefiltered samples, which appears in contrast to what we have seen so far but reinforce the evidence of nZVIs not reacting with the Hg.

3.4.8. S6N_Fe+Ag

The last reagent which was tested in combination with ASSM water was the second nanoparticle sample from RCPTM, specifically the Fe+Ag NPs. Looking to the published remediation studies involving Ag-based reagents and mercury, nanoscale silver is preferred over bulk silver for its higher reactive power, due to the Ag reduction potential being comparable to that of mercury and size reduction generally inducing a decrease in reduction potential, increasing the difference in terms the standard redox potential between Ag and Hg (besides the increased superficial reactivity) (Sumesh et al., 2011). However, because of the strong aggregation tendency of the metal nanoparticles, Ag NPs are commonly fashioned in hybrid composites with various supporting matrices such as activated alumina (Al_2O_3) and mercaptosuccinic acid (MSA) (Sumesh et al., 2011), graphene (Qu et al., 2017), and Covalent Organic Frameworks (COF) (L. Wang et al., 2020). The Fe+Ag NPs provided by RCPTM meet both of the mentioned conditions (nanometric size and bimetallic nature), offering the indisputable advantage of a simple, low-engineered, tunable synthesis procedure, since the Fe(0):Ag(0) ratio can be easily controlled (the Fe+Ag NPs tested in this study had Ag(0) = 7.1 % but the Ag(0) could increase up to 53 % of the final phase composition) (Markova et al., 2013). Over multiple studies on aqueous Hg(II) solutions, really high removal efficiencies were achieved by Ag NPs-based materials, with higher values registered over acidic to very acidic pHs (Qu et al., 2017; Sumesh et al., 2011; L. Wang et al., 2020). In fact, the presence of OH^- promotes the transformation of Hg^{2+} into $Hg(OH)^+$ and then $Hg(OH)_2$, which were accounted as not beneficial for the Hg absorption by Ag NPs; 1000 ppm of Ag NPs/graphene (no data on the Ag wt%) achieved 93.7 and 98.8 % removal over a 100 ppm Hg(II) solution at pH = 3 and 5, which decreased down to 79 % at pH = 11 (Qu et al., 2017). A similar behavior was observed by Sumesh et al., who achieved a ~ 95 % removal over a 2 ppm Hg(II) solution using 1000 ppm of 1:6 Ag:MSA NPs/alumina (0.5 % Ag(0), equivalent to 50 ppm) and ~ 85 % using the same amount of 1:3 Ag:MSA NPs/alumina (0.3 % Ag(0), equivalent to 30 ppm) at pH = 5, which decreased to ~ 80 % for both at pH = 8 and significantly further for pH > 8 (Sumesh et al., 2011). In this study, Fe+Ag NPs added to the natural matrix S6N scored 82 % Hg removal, the best absolute result over the two S6N trials (Fig. 3.12, Tab. 3.2). This result was achieved with a 6.6 mg addition of Fe+Ag NPs with an Ag content of 7 wt %, corresponding to 132 ppm of which about 9 ppm of Ag(0). This result is comparable with the best results from literature,

while offering an air-stable, relatively easy-to-synthesize product. As with the nZVIs, the mentioned studies were performed on laboratory prepared solution, not considering the possible complexity of a natural matrix. In the final part of their work, Sumesh et al. used "normal tap water" with pH = 8, spiked up to 2 ppm Hg^{2+} with the same $Hg(OOCCH_3)_2$ employed for the other test solutions, in order to verify the effect of "other ions like Ca^{2+}, Mg^{2+}, Cl^-, NO_3^-, SO_4^{2-} etc." on the mercury uptake. Despite the same 1000 ppm of 1:6 Ag:MSA NPs/alumina and 1:3 Ag:MSA NPs/alumina added in the other trials, the Hg removal efficiencies found were 68 and 46 % respectively, showing how critical it is to use an appropriate matrix when drawing conclusions that can be meaningful from an environmental remediation point of view.

In all the literature studies, the removal mechanism found was the complexation/adsorption of Hg(II), followed by reduction to Hg(0) and possible slow diffusion into the interior of the silver particles, with consequent formation of Ag-Hg alloys (amalgamation). For the 1:3 Ag:MSA/alumina, TEM and XRD data pointed to the formation of the paraschachnerite alloy, whose stoichiometry Ag_3Hg_2 was supported by the $Ag_{2.6}Hg_{2.0}$ composition found by EDX analysis (Sumesh et al., 2011). Wang et al., analyzing the XRD, XPS and HR-TEM responses of their Ag/COF samples after the Hg adsorption, found the presence of insoluble AgCl and a $Ag_{1.1}Hg_{0.9}$ nanoalloy, together with signal coming from Hg(II), which were interpreted as the result of a cyclic mechanism of physical adsorption -> Hg reduction -> Hg(0) diffusion and formation of Hg-Ag alloy -> exchange of Ag(I) outside with formation of AgCl -> new surface available for the physical adsorption (L. Wang et al., 2020). The XAS study on the S6N_Fe+Ag and S6N_Fe+Ag_Pref samples (which was possible due to the high quality of the output signal) endorse the mechanisms described above with an excellent degree of similarity. Unfortunately, the LCF results cannot be considered definitely valid due to the absence of Hg-Ag samples from the pool of standards used as primary components. Notwithstanding, the prevalent presence in the post-treatment deposit of metacinnabar can be assumed with certainty, due to the confirmation of EXAFS data. EXAFS fit results show that the two most intense signals emerging from the background noise are identified as metacinnabar and moschellandsbergite (Fig. 3.38, Tab. 3.13), a mercury mineral recognized by the International Mineralogical Association (IMA) first found precisely in association with paraschachnerite in the Sala Silver mine, in Sweden (Hazen et al., 2012). Given the absence of any published paraschachnerite CIF in the literature, it was not possible to attempt a further fit with that

mineral as a model. Another attempt was made by taking imiterite as a model structure for the fit (Fig. 3.39), since it has the advantage factor of containing both sulfur and silver within it, which showed anomalies in the resulting parameters, ruling out imiterite as a representative phase for the sample. Moreover, the fact that the S6N_Fe+Ag experimental signal could be properly fit by taking the metacinnabar and moschellandsbergite signals simultaneously confirmed the presence within the post-treatment solid residue of metacinnabar, naturally present in S6N water, and a Hg-Ag alloy with the structural characteristics of moschellandsbergite, resulting from the process of oxidation of Ag(0) and reduction of Hg(II) in solution, as highlighted by the higher residuals and less accurate parameter values of the fits made by taking only one of the two CIFs at a time. This indicates the non-dissolution of the HgS contained in S6N and a mechanism of Hg removal consistent with the literature. Furthermore, the fit of the S6N_Fe+Ag_Pref sample (not reported in the thesis) showed that its EXAFS signal could be modeled by the CIF of the moschellandsbergite alone and the addition of the metacinnabar into the model did not improve any parameter but instead invalidated amp, which took on strong negative values with meaningless errors (-3.92 ± 28.55). This underscores the inadequacy of the sulfide structure in describing any part of the S6N_Fe+Af_Pref sample signal, meaning that the pre-filtering of the S6N water was sufficient to remove the majority of the β-HgS.

- Conclusions -

Coming to the last section of this PhD research thesis, I want to summarize the experimental evidence so far discussed. The aim of this last section is to show advantages and disadvantages of ferrate(VI) materials and all the other reagents tested when applied for mercury removal to a real case scenario such as the ASSM waters.

First of all one, if not the main, discriminating criteria is the removal efficiency, namely the percentage of Hg that can be removed compared to the starting Hg content. In the absence of a solid literature base regarding the removal efficacy of Hg dissolved in water by Fe(VI)-containing compounds, initial tests focused on laboratory-prepared solutions of Hg(II) (HgSS). The liquid ferrate, synthesized with an original procedure developed at the Department of Earth Sciences of the University of Florence, was able to remove 91 % of the HgSS_500ppb and HgSS_1ppm starting Hg concentration, with a ~ 80 ppm of Fe(VI) dose over a ~ 400 ppm of total Fe. These results confirmed the only two "preliminary" works ever published, where it was observed a ~ 94 % mercury removal for a 370 ppb Hg(II) solution treated with 50 and 100 ppm FeO_4^{2-} (Murmann & Robinson, 1974), and "in the cases where initial metal cations were dilute (parts per million), potassium ferrate quantitatively removed them from solution (to less than parts per billion)" (Bartzatt et al., 1992). In addition to being the best achieved efficiencies, the recorded performances were comparable to the more traditional $FeCl_3$ (tested at the same dose of total Fe) and they were actually comparable to other modern nano-adsorbent materials, tested with more concentrated Hg(II) solutions ((Chizitere Emenike et al., 2023) and references therein). But because of the much more complex nature of a natural system such as the contaminated waters of the ASS mining area, such effectiveness has not been replicated in terms of absolute values in the collected samples, requiring a much more in-depth study of why such behavior occurs.

First, characterization of the S6N water was carried out, which was chosen for its usual high Hg content following extensive geochemical monitoring done over the years (Vaselli et al., 2015). In addition to Hg contents well above the threshold limits provided by National Regulations, an important piece of information was the finding of diffuse HgS and Hg-S-O particles in the water deposit, after filtration with 0.45 µm porosity filters (the O content is probably due to anomalies normally introduced by the traditional SEM used and/or the presence of small HgO particles aggregated to the sulfide). As will later be confirmed by XANES

analyses, the deposit showed a mercury speciation consisting of more than 90 % β-HgS (metacinnabar), a typical product of mercury extraction processes from mineral ores, and a < 10 % of HgO (montroydite). Initial tests showed that a sharp increase in pH, following the addition of a concentrated KOH solution, did not lead to appreciable changes in dissolved mercury content. Next came the testing of KClO, another compound used in the synthesis of liquid ferrate, which showed a marked difference from the tests with HgSS, namely a marked increase in the final concentration of Hg in solution after the treatment. Moreover, an equally clear difference was noticeable between the application of the reagent to an unfiltered S6N water versus filtering the water with a 0.45 µm porosity before the KClO application (_Pref samples), which removed the solid deposit or, at least, most of it. The moderate increase in Hg final concentration detectable in the KClO_Pref samples, as well as the clear discrepancy between the HgSS_ and S6N_Fe(III) test results, gave light to the hypothesis of the presence of a fraction of suspended particulate matter containing Hg, whose small size would allow it to pass through the 0.45 porosity filter and, consequently, to increase the amounts of mercury measured in the final Fe(III) treated solutions, lowering the removal efficiencies.

Figure 4.1 shows a schematization of the KClO - S6N water interaction mechanism proposed in this study, based on the emerged experimental evidence. The figure shows the liquid fraction, the solid deposit at the bottom where the metacinnabar particles are embedded, and the solid particulate suspended in the water, outside and inside the diffusion range of KClO. Interactions with the reagent are exemplified by arrows showing the dissolution of Hg(II) within the liquid fraction. The proposed mechanism sees the dissolution by KClO of the metacinnabar contained in the system (red arrows), leading to an increase in Hg(II) in the liquid fraction, which is not counterbalanced by any uptake action by adsorbents or leakage into the air fraction.

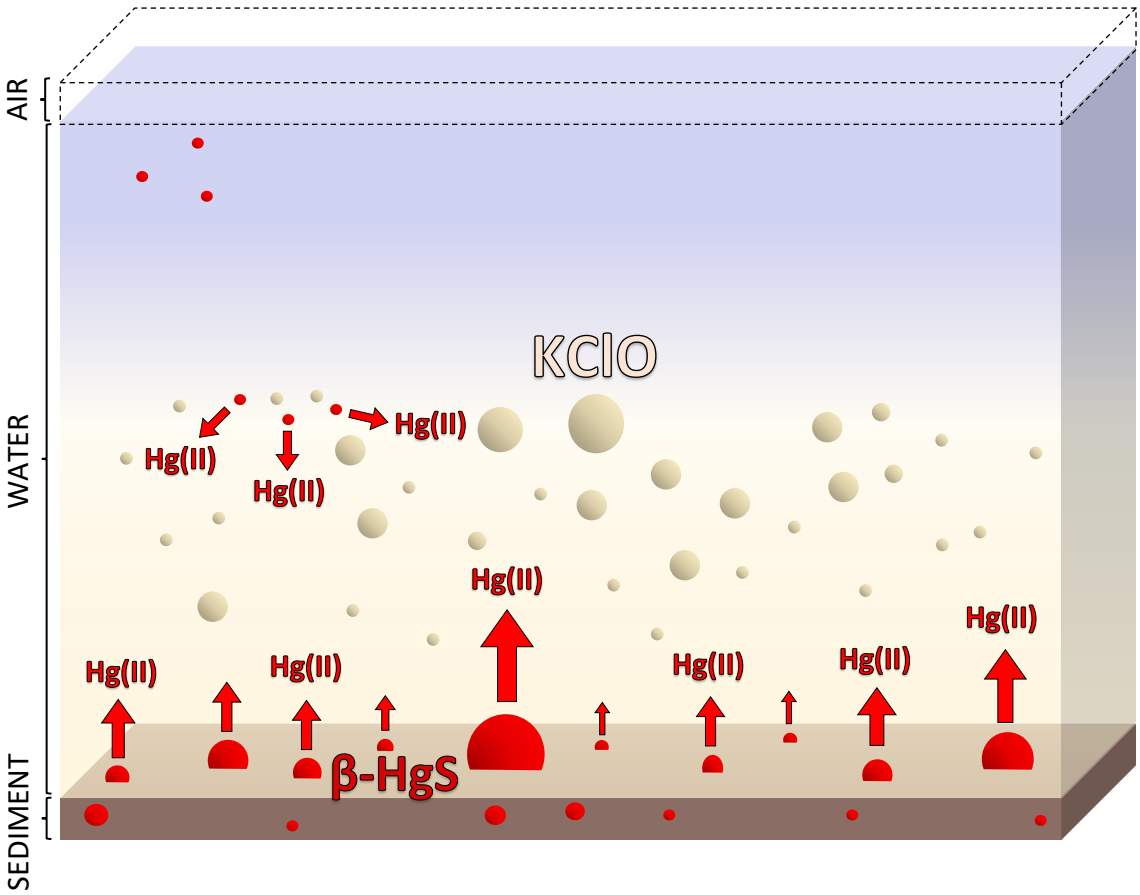

The next treatment considered is with $FeCl_3$ (_Fe(III) samples), the last component used for the synthesis of liquid ferrate and an excellent representative of the Fe(III) fraction contained within it. The Fe(III) treatment was responsible for high mercury absorption thanks to the $FeCl_3$ hydrolyzation into low molecular-weight complexes, a colloidal system of polynuclear polymers species and the following precipitation of Fe(III) oxides/hydroxides/oxyhydroxides (e.g. $Fe(OH)_3$, $FeO(OH)$, Fe_2O_3) (Collins et al., 2016; Cornell et al., 1989; Hellman et al., 2006). In light of the experimental evidence and literature review, a graphical schematic of the proposed removal mechanism for the Fe(III) is depicted in Fig. 4.2. In the figure, the Hg adsorption onto the iron by-products surface active sites of the flocculating material is represented by green arrows. No evidence of β-HgS dissolution was found.

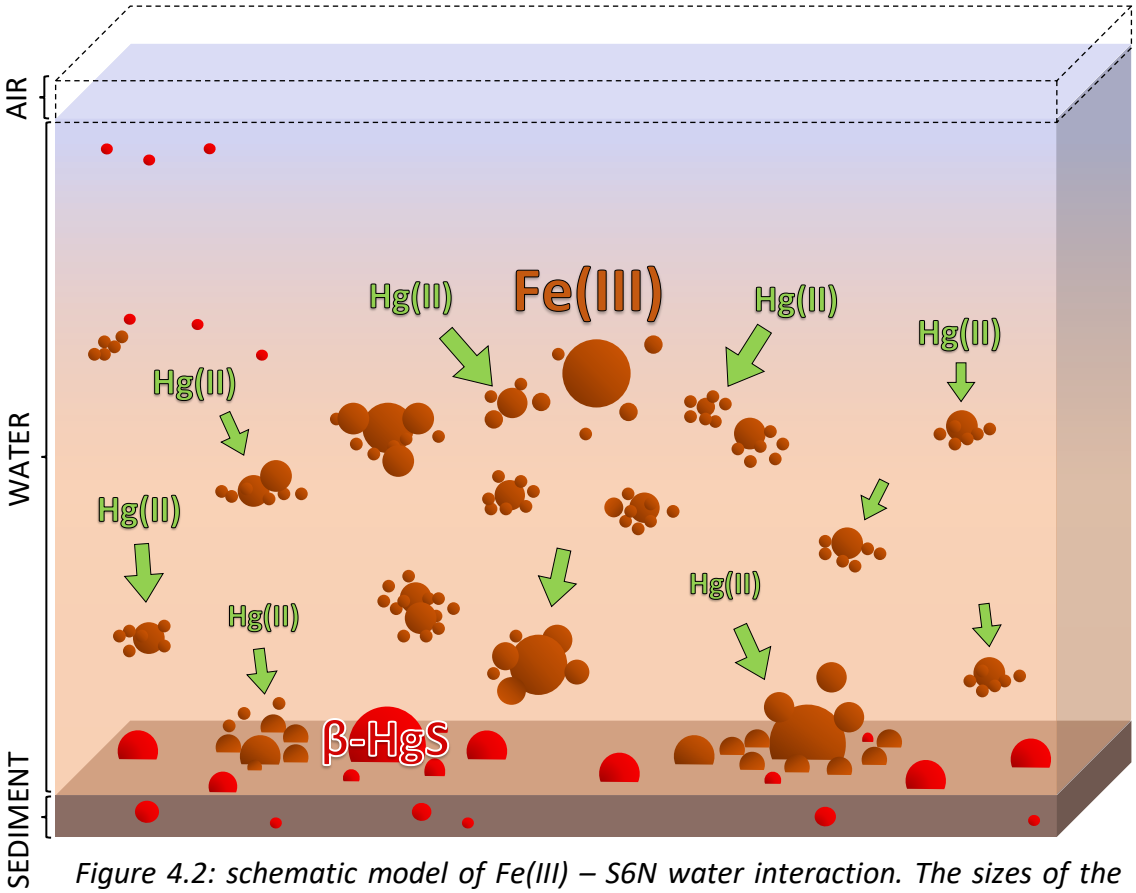

Figure 4.2: schematic model of Fe(III) – S6N water interaction. The sizes of the spheres representing the various components have only qualitative relevance.

We now come to the liquid ferrate and, with it, the mechanism of action of the Fe(VI) it contains. From literature, during multiple trials with many different waters/wastewaters, Fe(VI) proved to be an excellent multi-purpose material, being capable to decompose organic matter and, more important for this study, oxidize in a matter of milliseconds to minutes a wide range of compounds thanks to its really high redox potential. Moreover, the decomposition products of ferrate(VI) consist in γ-Fe_2O_3 and γ-FeOOH nanoparticles with high coagulation properties, making him an apparent good candidate in dealing with complex natural systems. Unfortunately, the characteristic of the system itself combined with the very nature of a product such as liquid ferrate did not allow for the same high efficiencies seen with the HgSS trials, while still being significant. Figure 4.3 schematizes the mechanism of action of Fe(VI) that emerged from this study. Highlighted in the figure is both the dissolution action on the metacinnabar inside the S6N deposit and suspended particulate (red arrows) and the adsorption process of mercury in solution (green arrows) by Fe(III) contained in the liquid ferrate and resulting from the reduction of Fe(VI) (purple to orange arrow).

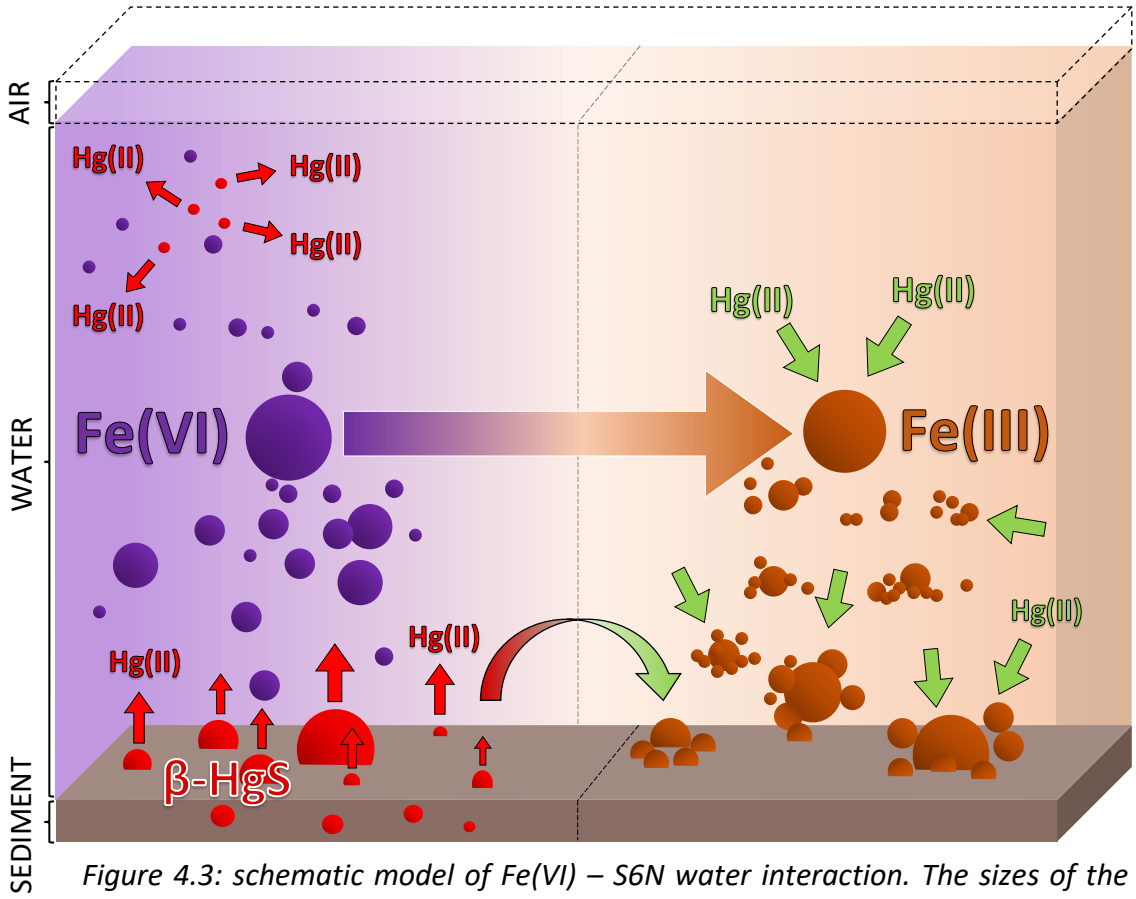

Figure 4.3: schematic model of Fe(VI) – S6N water interaction. The sizes of the spheres representing the various components have only qualitative relevance.

Finally, an additional category of reagents was tested as a comparison, those of reducing nanomaterials, thanks to two materials provided by the RCPTM: ZVI and Fe(0)+Ag(0) nanoparticles. Starting with nZVIs, Hg removal tests did not show the high efficiencies that literature studies showed in synthetic tests on laboratory solutions, evidence of the difference between natural and standard solutions systems probably related to the circumneutral/slightly alkaline pH of the S6N water and the passivation layer present on the nanoparticle surface. Despite this, the collected experimental evidence tend to confirm a removal mechanism compatible with the various published studies with no metacinnabar dissolution, as shown in Fig. 4.4. In the figure, the adsorption mechanisms (green arrows) of Hg(II) on the nanoparticles surface is highlighted in the inset, together with the reduction to Hg(0), typical of ZVI reagents, which can lead to desorption and volatilization of the elemental mercury (white arrows) due to its high volatility and relatively low solubility.

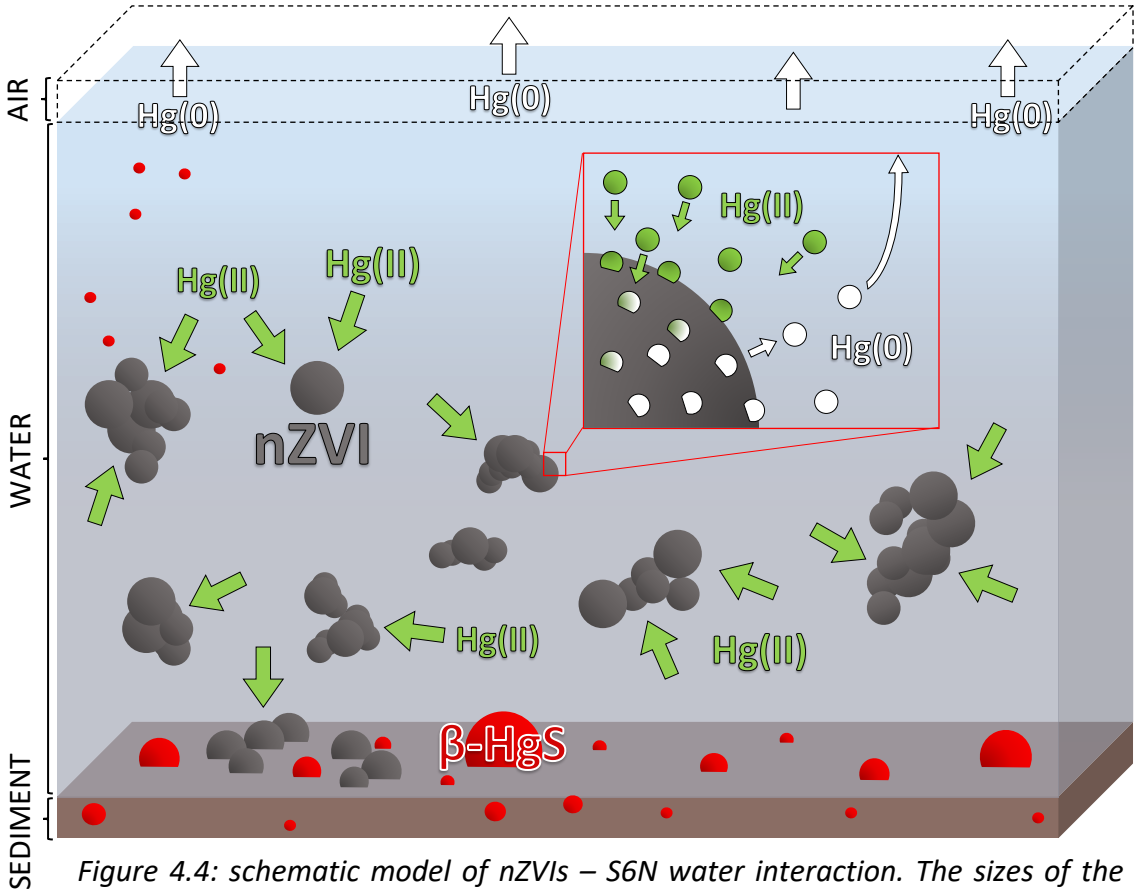

Figure 4.4: schematic model of nZVIs – S6N water interaction. The sizes of the spheres representing the various components have only qualitative relevance.

The Fe+Ag NPs were the last reagent successfully tested, which achieved the best overall result in terms of mercury removal efficiency in the S6N trials. In addition to this result, further noteworthy evidence were the apparent non-interaction with the metacinnabar particles and the formation of an Hg-Ag alloy with a moschellandsbergite-like structure that, unlike nZVIs, ensures effective capture of reduced mercury. In Fig. 4.5 is represented the schematic removal mechanism proposed for the Fe+Ag NPs, where the mechanism of physical adsorption (green arrows), followed by Hg reduction and Hg(0) diffusion inside the Ag NPs (white dotted arrows) are shown in the insets.

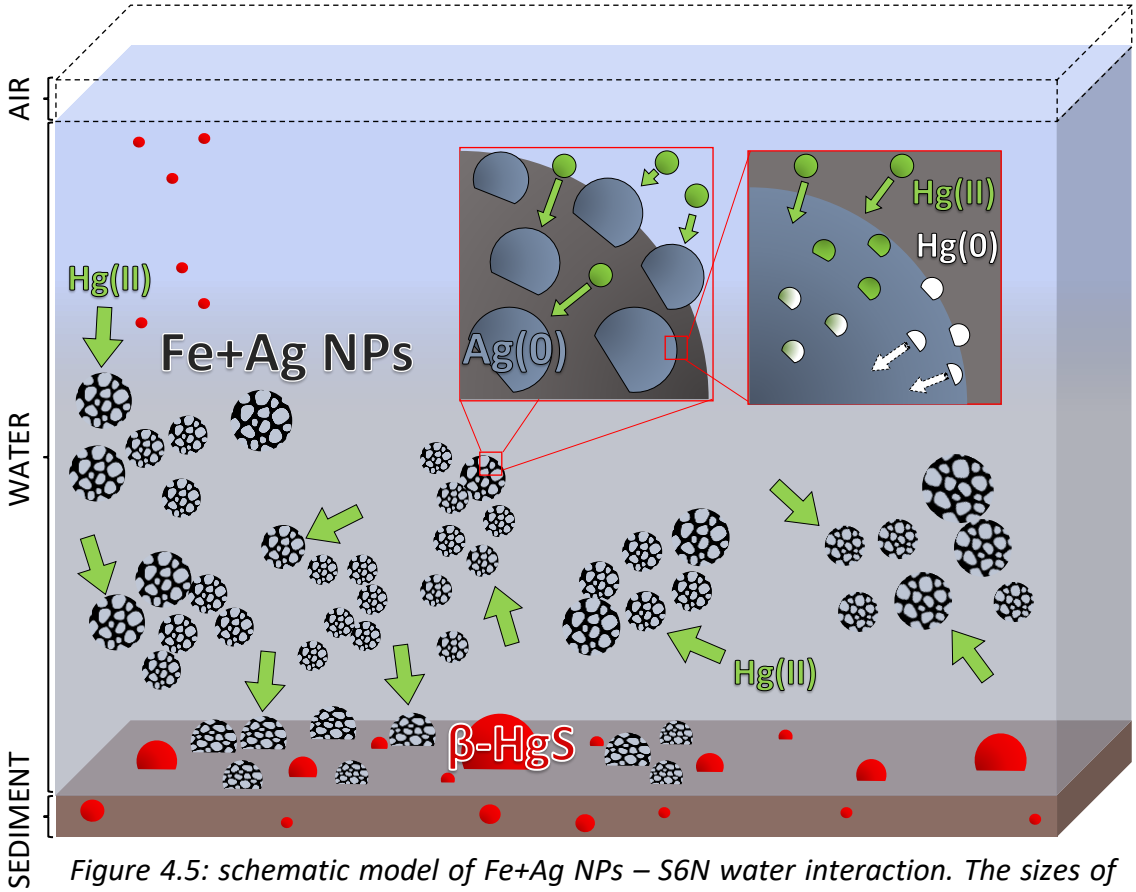

Figure 4.5: schematic model of Fe+Ag NPs – S6N water interaction. The sizes of the spheres representing the various components have only qualitative relevance.

In light of the various mechanisms summarized in these conclusion pages, the supposed interaction mechanisms between the various reagents tested and the HgSS used in preliminary testing are schematically depicted in Fig. 4.6. The main difference with S6N water lies in the absence of a solid phase as a precipitate/suspended particulate that may interact with the reagents tested.

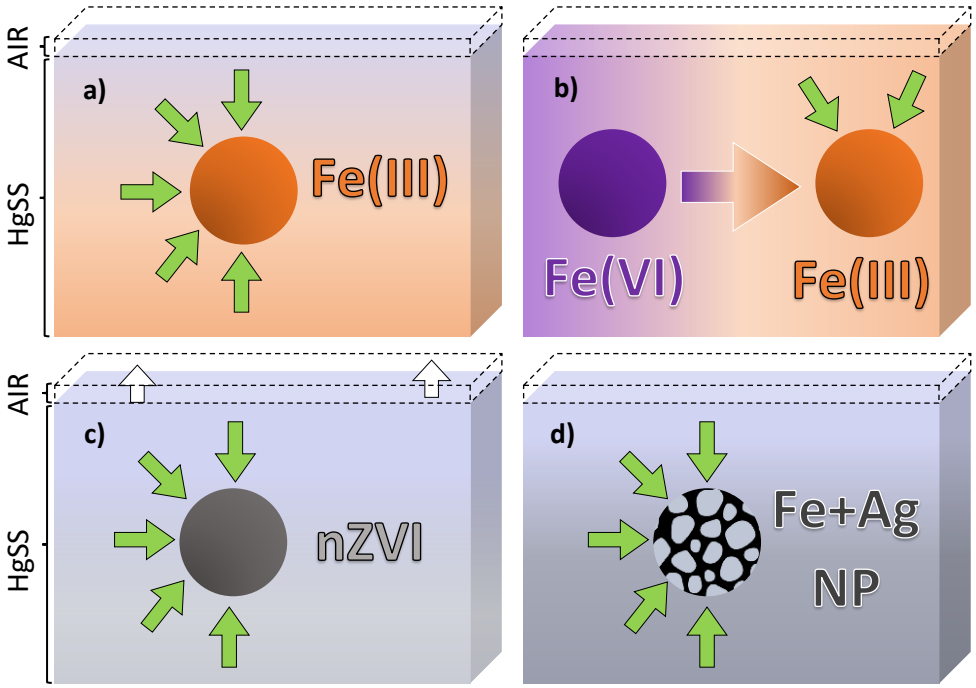

Figure 4.6: schematic model of a) Fe(III), b) Fe(VI), c) nZVIs and d) Fe+Ag NPs interaction with the HgSS. The sizes of the spheres representing the various components have only qualitative relevance.

In conclusion, despite presenting much room for improvement, this study could be defined as an experimental proof of concept for environmental remediation procedures applied to natural matrices. Starting a project in a totally new field both for me and my mentor, less than 4 months before the start of the first lockdown, led to many challenges. First among them was the lack of opportunity for training and acquiring the necessary experience in the use of ferrate products at external laboratories and research centers such as the RCPTM in Olomuc, at which contact had already been made in the starting phase of my PhD course. Joined to my personal inexperience, many attempts that proved unsuccessful/unrealizable were also made. But looking at it from a broader perspective, this study succeeded in creating a solid platform for testing environmental remediation procedures with natural matrices, such as the water from the former mining site of ASS.

One of the first goal achieved resulted from the initial difficulty in getting ferrate products, which gave rise to a long period of testing, culminating in an original liquid ferrate synthesis process with yields comparable to the best published methods. Meanwhile, two internationally recognized and award-winning companies were born in 2019 and 2020 respectively, which use and patented the same type of liquid ferrate syntheses to create

ferrate-based products that are currently being used in real environmental remediation scenarios (Netherlands Enterprise Agency, 2022; Treadway, 2020). More importantly, while many studies have been produced about the acid mining drainage elements and the Hg release still represents an ongoing environmental challenge, this research helps to fill a gap in the literature regarding the use of ferrates for mercury removal, as well as the testing of additional new state-of-the-art reagents with natural matrices. And in doing so, an unconventional technique such as XAS has been learned and successfully employed to obtain important information about the speciation of Hg and the removal mechanisms affecting it, showing how the experience gained in the method has enabled significant results, despite the manifest inherent limitations of the samples investigated.

The starting focus of this project was to study the feasibility in the application of ferrate for the ASS case study, which was only hypothesized at the theoretical level. During the course of its development, it became a broader study for investigating Hg chemical speciation and explore methods that could be used for its remediation. In the end, this work emphasized the importance of taking into account not only the type of treatment, but also the site conditions when considering applying treatments, especially with an *in situ* perspective. Thanks to its oxidation power, Fe(VI) promotes the dissolution of Hg sulfides, which could be identified as a negative factor associated with its use. Instead, this could present the benefit of efficiently removing and collecting mercury from sources that are normally difficult to reach in easily magnetically separable products, as well as impacting on the factors favorable to methyl-mercury formation such as reducing conditions, the presence of organic matter and the availability of HgS nanoparticles (Driscoll et al., 2013; O'Connor et al., 2019). The use of solid products (e.g. Ferr-Tech (Ferr-Tech, n.d.)) would also have the effect of a limited impact on the final pH of the solution and greater stability for transportation and storing. On the other hand, the use of reducing nanoparticles, on which the research has been deeply focusing on for the past 20 years, would likely allow mercury in solution to be retrieved with little impact on the final system from a pH and salinity standpoint. Unfortunately, the nZVIs tested during this study did not show results comparable with the high degrees of removal found in the literature but each reagent based on such technology is profoundly different from the other, and numerous methods to greatly increase the effectiveness of passivation-inhibited particles already exist (Guo et al., 2016; Ribas et al., 2017). However, mitigating risks posed by formation of volatile Hg(0) in natural treated systems has to be considered prior to application

of iron-based nanoparticles; existing technologies that attempt to reduce Hg(II) often require costly capture mechanisms for gaseous Hg(0). A possible alternative is represented by the bimetallic Fe+Ag NPs which, in addition to showing excellent efficiencies under the natural conditions of the system, showed the formation of an Hg-Ag amalgam. Hg amalgams have historically been used widely in dentistry and amalgam formation with other metals provides benefits in respect to mechanical strength and stability, potentially reducing the tendency of Hg(0) to volatilize.

Possible future developments regarding this thesis project involve repeating the removal tests on the natural matrix in light of the experience gained, varying and controlling the boundary conditions such as pH and the amount of reagent used, especially regarding Mixfer, whose data were affected by heavy errors. The use of instruments not available to the Department of Earth Sciences, such as an XPS microscope or a TEM could offer further confirmation and interesting data.

- Bibliography -

Alshahri, A. H., Fortunato, L., Ghaffour, N. E., & Leiknes, T. O. (2019). Advanced coagulation using in-situ generated liquid ferrate, Fe (VI), for enhanced pretreatment in seawater RO desalination during algal blooms. *Science of the Total Environment*, *685*, 1193–1200. https://doi.org/10.1016/j.scitotenv.2019.06.286

Altomare, A., Corriero, N., Cuocci, C., Falcicchio, A., Moliterni, A., & Rizzi, R. (2015). QUALX2.0: a qualitative phase analysis software using the freely available database POW-COD. *Journal of Applied Crystallography*, *48*, 598–603. https://doi.org/10.1107/S1600576715002319

Andrews, J. C. (2006). Mercury speciation in the environment using X-ray absorption spectroscopy. *Structure and Bonding*, *120*, 1–35. https://doi.org/10.1007/430_011

Audette, R. J., & Quail, J. W. (1972). Potassium, Rubidium, Cesium, and Barium Ferrates(VI). Preparations, Infrared Spectra, and Magnetic Susceptibilities. *Inorganic Chemistry*, *11*(8), 1904–1908.

Audette, R. J., Quail, J. W., Black, W. H., & Robertson, B. E. (1973). Crystal Structures of M2FeO4 (M = K , Rb , Cs). *Journal of Solid State Chemistry*, *8*, 43–49.

Aurivillius, K. (1964). Least-Squares Refinement of the Crystal Structures of Orthorhombic HgO and of Hg2O2NaI. *Acta Chemica Scandinavica*, *18*, 1305–1306. https://doi.org/10.3891/acta.chem.scand.18-1305

Auvray, P., & Genet, F. (1973). Affinement de la structure cristalline du cinabre HgS. *Bulletin de La Société Française de Minéralogie et de Cristallographie*, *96*, 218–219.

Babel, S., & Kurniawan, T. A. (2003). Low-cost adsorbents for heavy metals uptake from contaminated water: a review. *Journal of Hazardous Materials*, *B97*, 219–243. https://doi.org/10.1016/s0304-3894(02)00263-7

Bailie, A. G., Bouzek, K., Lukasek, P., Rousar, I., & Wragg, A. A. (1996). Solubility of Potassium Ferrate in 12 M Alkaline Solutions Between 20°C and 60°C. *Journal of Chemical Technology and Biotechnology*, *66*, 35–40. https://doi.org/10.1002/(sici)1097-4660(199605)66:1<35::aid-jctb457>3.0.co;2-m

Ball, J. W., & Nordstrom, D. K. (1991). *User's Manual for WATEQ4F, with Revised Thermodynamic Data Base and Text Cases for Calculating Speciation of Major, Trace, and Redox Elements in Natural Waters*. U.S. Geological Survey.

https://doi.org/https://doi.org/10.3133/ofr91183

Bardelli, F., Giacobbe, C., Ballirano, P., Borelli, V., Di Benedetto, F., Montegrossi, G., Bellis, D., & Pacella, A. (2023). Closing the knowledge gap on the composition of the asbestos bodies. *Environmental Geochemistry and Health*. https://doi.org/10.1007/s10653-023-01557-0

Barişçi, S., Ulu, F., Särkkä, H., Dimoglo, A., & Sillanpää, M. (2014). Electrosynthesis of ferrate (VI) ion using high purity iron electrodes: Optimization of influencing parameters on the process and investigating its stability. *International Journal of Electrochemical Science*, *9*(6), 3099–3117.

Barışçı, S. (2018). Investigation of Different Reactor Configurations for Electrochemical Ferrate (VI) Synthesis. *International Journal of Chemistry and Technology*, *2*(2), 89–94. https://doi.org/10.32571/ijct.452489

Bartzatt, R., Cano, M., Johnson, L., & Nagel, D. (1992). Removal of toxic metals and nonmetals from contaminated water. *Journal of Toxicology and Environmental Health*, *35*(4), 205–210. https://doi.org/10.1080/15287399209531611

Bernaus, A., Gaona, X., & Valiente, M. (2005). Characterisation of Almadén mercury mine environment by XAS techniques. *Journal of Environmental Monitoring*, *7*, 771–777. https://doi.org/10.1039/b502060n

Bielski, B. H. J., & Thomas, M. J. (1987). Studies of Hypervalent Iron in Aqueous Solutions. 1. Radiation-Induced Reduction of Iron(VI) to Iron(V) by C02-. *Journal of the American Chemical Society*, *109*, 7761–7764. https://doi.org/https://doi.org/10.1021/ja00259a026

Bonnissel-Gissinger, P., Alnot, M., Lickes, J. P., Ehrhardt, J. J., & Behra, P. (1999). Modeling the adsorption of mercury(II) on (hydr)oxides II: α-FeOOH (goethite) and amorphous silica. *Journal of Colloid and Interface Science*, *215*, 313–322. https://doi.org/10.1006/jcis.1999.6263

Bouzek, K., & Nejezchleba, M. (1999). In situ Mössbauer study of the passive layer formed on the iron anode in alkaline electrolyte. *Collection of Czechoslovak Chemical Communications*, *64*(12), 2044–2060. https://doi.org/10.1135/cccc19992044

Bouzek, K., & Roušar, I. (1996). Influence of anode material on current yields during ferrate(VI) production by anodic iron dissolution Part I: Current efficiency during anodic dissolution of grey cast iron to ferrate(VI) in concentrated alkali hydroxide solutions.

Journal of Applied Electrochemistry, *26*(9), 919–923. https://doi.org/10.1007/BF00242043

Bouzek, K., & Roušar, I. (1997). Influence of anode material on current yield during ferrate(VI) production by anodic iron dissolution Part III: Current efficiency during anodic dissolution of pure iron to ferrate(VI) in concentrated alkali hydroxide solutions. *Journal of Applied Electrochemistry*, *27*, 679–684. https://doi.org/https://doi.org/10.1023/A:1018483603666

Bouzek, K., Roušar, I., Bergmann, H., & Hertwig, K. (1997). The cyclic voltammetric study of ferrate(VI) production. *Journal of Electroanalytical Chemistry*, *425*, 125–137. https://doi.org/10.1016/S0022-0728(96)04939-X

Bouzek, K., Rousar, I., & Taylor, M. A. (1996). Influence of anode material on current yield during ferrate(VI) production by anodic iron dissolution Part II: Current efficiency during anodic dissolution of white cast iron to ferrate(VI) in concentrated alkali hydroxide solutions. *Journal of Applied Electrochemistry*, *26*, 925–931. https://doi.org/https://doi.org/10.1007/BF00242044

Cadoux, A., & Pinti, D. L. (2009). Hybrid character and pre-eruptive events of Mt Amiata volcano (Italy) inferred from geochronological, petro-geochemical and isotopic data. *Journal of Volcanology and Geothermal Research*, *179*, 169–190. https://doi.org/10.1016/j.jvolgeores.2008.10.018

Cañizares, P., Arcís, M., Sáez, C., & Rodrigo, M. A. (2007). Electrochemical synthesis of ferrate using boron doped diamond anodes. *Electrochemistry Communications*, *9*, 2286–2290. https://doi.org/10.1016/j.elecom.2007.06.034

Casbeer, E., Sharma, V. K., & Li, X. Z. (2012). Synthesis and photocatalytic activity of ferrites under visible light: A review. *Separation and Purification Technology*, *87*, 1–14. https://doi.org/10.1016/j.seppur.2011.11.034

Cashman, S., Gaglione, A., Mosley, J., Weiss, L., Hawkins, T. R., Ashbolt, N. J., Cashdollar, J., Xue, X., Ma, C., & Arden, S. (2014). Environmental and Cost Life Cycle Assessment of Disinfection Options for Municipal Drinking Water Treatment. *U.S. Epa*, *October*, 104.

Cataldo-Hernández, M. A., Bonakdarpour, A., English, J. T., Mohseni, M., & Wilkinson, D. P. (2019). A membrane-based electrochemical flow reactor for generation of ferrates at near neutral pH conditions. *Reaction Chemistry and Engineering*, *4*(6), 1116–1125. https://doi.org/10.1039/c8re00306h

Cataldo-Hernández, M. A., Govindarajan, R., Bonakdarpour, A., Mohseni, M., & Wilkinson, D. P. (2018). Electrosynthesis of Ferrate in a Batch Reactor at Neutral Conditions for Drinking Water Applications. *Canadian Journal of Chemical Engineering*, *96*(8), 1648–1655. https://doi.org/https://doi.org/10.1002/cjce.23142

Cataldo-Hernández, M., Stewart, M., Bonakdarpour, A., Mohseni, M., & Wilkinson, D. P. (2018). Degradation of ferrate species produced electrochemically for use in drinking water treatment applications. *Canadian Journal of Chemical Engineering*, *96*(5), 1045–1052. https://doi.org/10.1002/cjce.23073

Cataldo Hernández, M. A., May, A., Bonakdapour, A., Mohseni, M., & Wilkinson, D. P. (2016). Analytical quantification of electrochemical ferrates for drinking water treatments. In *Canadian Journal of Chemistry* (Vol. 95, Issue 1). https://doi.org/10.1139/cjc-2016-0315

Chen, Y., Yin, Y., Shi, J., Liu, G., Hu, L., Liu, J., Cai, Y., & Jiang, G. (2017). Analytical methods, formation, and dissolution of cinnabar and its impact on environmental cycle of mercury. *Critical Reviews in Environmental Science and Technology*, *47*(24), 2415–2447. https://doi.org/https://doi.org/10.1080/10643389.2018.1429764

Chengchun, J., Chen, L., & Shichao, W. (2008). Preparation of Potassium Ferrate by Wet Oxidation Method Using Waste Alkali: Purification and Reuse of Waste Alkali. *ACS Symposium Series*, *985*, 94–101. https://doi.org/10.1021/bk-2008-0985.ch005

Chizitere Emenike, E., George Adeniyi, A., Iwuozor, K. O., Okorie, C. J., Egbemhenghe, A. U., Omuku, P. E., Chidiebere Okwu, K., & Saliu, O. D. (2023). A critical review on the removal of mercury (Hg2+) from aqueous solution using nanoadsorbents. *Environmental Nanotechnology, Monitoring and Management*, *20*, 100816. https://doi.org/10.1016/j.enmm.2023.100816

Cici, M., & Cuci, Y. (1998). Production of some coagulant materials from galvanizing workshop waste. *Waste Management*, *17*(7), 407–410. https://doi.org/10.1016/S0956-053X(97)10001-0

Collins, R. N., Rosso, K. M., Rose, A. L., Glover, C. J., & Waite, T. D. (2016). An in situ XAS study of ferric iron hydrolysis and precipitation in the presence of perchlorate, nitrate, chloride and sulfate. *Geochimica et Cosmochimica Acta*, *177*, 150–169. https://doi.org/10.1016/j.gca.2016.01.021

Consumer Technology Association. (2022). *FerSol, Ferrate(VI) solution for (waste)watertreatment*. https://www.ces.tech/innovation-

awards/honorees/2022/honorees/f/fersol,-ferrate(vi)-solution-for-(waste)watertreat.aspx

Cornell, R. M., Giovanoli, R., & Schneider, W. (1989). Review of the Hydrolysis of Iron(III) and the Crystallization of Amorphous Iron(III) Hydroxide Hydrate. *Journal of Chemical Technology and Biotechnology*, *46*, 115–134. https://doi.org/10.1002/jctb.280460204

D'Acapito, F., Lepore, G. O., Puri, A., Laloni, A., La Manna, F., Dettona, E., De Luisa, A., & Martin, A. (2019). The LISA beamline at ESRF. *Journal of Synchrotron Radiation*, *26*, 551–558. https://doi.org/10.1107/S160057751801843X

D'Acapito, F., Trapananti, A., Torrengo, S., & Mobilio, S. (2014). X-ray Absorption Spectroscopy: the Italian beamline GILDA of the ESRF. *Notiziario Neutroni e Luce Di Sincrotrone*, *19*(2), 14–23. http://neutronielucedisincrotrone.cnr.it/?page_id=1552

De Koninck, M., Brousse, T., & Bélanger, D. (2003). The electrochemical generation of ferrate at pressed iron powder electrodes: Effect of various operating parameters. *Electrochimica Acta*, *48*(10), 1425–1433. https://doi.org/10.1016/S0013-4686(03)00020-3

Dedushenko, S. K., Perfiliev, Y. D., Goldfeld, M. G., & Tsapin, A. I. (2001). Mössbauer Study of Hexavalent Iron Compounds. *Hyperfine Interactions*, *136*, 373–377. https://doi.org/https://doi.org/10.1023/A:1020541910373

Dedushenko, S K, Perfiliev, Y. D., Golubev, A. M., Melnikov, P., Corbi, P. P., & Saprykin, A. A. (2002). X-Ray and Mössbauer Study of Mixed Potassium-Sodium Ferrate (VI). *Hyperfine Interactions (C)*, *5*, 277–280. https://doi.org/https://doi.org/10.1007/978-94-010-0281-3_69

Dedushenko, Sergey K., Perfiliev, Y. D., Rusakov, V. S., & Gapochka, A. M. (2013). Quadrupole interactions in tetraoxoferrates (VI). *Hyperfine Interact*, *222*, 67–72. https://doi.org/10.1007/s10751-013-0765-1

Dedushenko, Sergey K., Zhizhin, M. G., & Perfiliev, Y. D. (2005). X-ray and Mossbauer study of structural changes in K3Na(FeO4)2. *Hyperfine Interact*, *166*, 367–371. https://doi.org/10.1007/s10751-006-9294-5

Delaude, L., & Laszl, P. (1996). A Novel Oxidizing Reagent Based on Potassium Ferrate(VI). *Journal of Organic Chemistry*, *61*(18), 6360–6370. https://doi.org/10.1021/jo960633p

DeLuca, S. J., Chao, A. C., & Smallwood, C. (1983). Ames test of ferrate treated water. *Journal of Environmental Engineering*, *109*(5), 1159–1167.

https://doi.org/https://doi.org/10.1061/(ASCE)0733-9372(1983)109:5(1159)

Deng, Y., Jung, C., Liang, Y., Goodey, N., & Waite, T. D. (2018). Ferrate(VI) Decomposition in Water in the Absence and Presence of Natural Organic Matter (NOM). In *Chemical Engineering Journal* (Vol. 334). https://doi.org/10.1016/j.cej.2017.12.006

Ding, Z., Yang, C., & Wu, Q. (2004). The electrochemical generation of ferrate at porous magnetite electrode. *Electrochimica Acta*, *49*(19), 3155–3159. https://doi.org/10.1016/j.electacta.2004.01.031

Downs, R. T., & Hall-Wallace, M. (2003). The American Mineralogist crystal structure database. *American Mineralogist*. https://doi.org/10.5860/choice.43sup-0302

Driscoll, C. T., Mason, R. P., Chan, H. M., Jacob, D. J., & Pirrone, N. (2013). Mercury as a Global Pollutant: Sources, Pathways, and Effects. *Environmental Science & Technology*, *47*(10), 4967–4983. https://doi.org/https://doi.org/10.1021/es305071v

Duarte, H. A. (2019). Ferro - um Elemento Quimico Estrategico que Permeia Historia, Economia e Sociedade. *Quim. Nova*, *42*(10), 1146–1153. https://doi.org/10.21577/0100-4042.20170443

Edwards, B. A., Kushner, D. S., Outridge, P. M., & Wang, F. (2021). Fifty years of volcanic mercury emission research: Knowledge gaps and future directions. *Science of the Total Environment*, *757*, 143800. https://doi.org/10.1016/j.scitotenv.2020.143800

Environmental XPRT. (n.d.). *Ferrate Treatment Technologies, LLC*. Retrieved April 24, 2023, from https://www.environmental-expert.com/companies/ferrate-treatment-technologies-llc-19619/

European Synchrotron Radiation Facility. (2023a). *About Us*. https://www.esrf.fr/about

European Synchrotron Radiation Facility. (2023b). *Users & Science*. https://www.esrf.fr/cms/live/live/en/sites/www/home/UsersAndScience.html

Fairhurst, C. W., & Cohen, J. B. (1972). The crystal structures of two compounds found in dental amalgam: Ag2Hg3 and Ag3Sn. *Acta Crystallographica Section B*, *28*, 371–378. https://doi.org/10.1107/s0567740872002432

Ferr-Tech. (n.d.). *Ferr-Tech*. Retrieved April 24, 2023, from https://ferr-tech.com/en/home-en/

Ferrari, L., Conticelli, S., Burlamacchi, L., & Manetti, P. (1996). Volcanological Evolution of the Monte Amiata, Southern Tuscany: New Geological and Petrochemical data. *Acta Vulcanologica*, *8*(1), 41–56. https://hdl.handle.net/2158/205138

Ferrate Solutions® Inc. (n.d.). *Ferrate Technology*. Retrieved April 24, 2023, from http://ferrate-solutions.com/technology/

Ferrate Solutions® Inc. (2019). *First non-U.S. Water Treatability Tests Completed*. http://ferrate-solutions.com/new-info/first-non-us-water-treatability-tests-completed/

Ferrate Solutions® Inc. (2021). *Ferrate is Successfully Removing Tons of Nutrients on the IRL*. http://ferrate-solutions.com/new-info/ferrate-is-successfully-removing-tons-of-nutrients-on-the-irl/

Filip, J., Yngard, R. A., Siskova, K., Marusak, Z., Ettler, V., Sajdl, P., Sharma, V. K., & Zboril, R. (2011). Mechanisms and efficiency of the simultaneous removal of metals and cyanides by using ferrate(VI): Crucial roles of nanocrystalline iron(III) oxyhydroxides and metal carbonates. *Chemistry - A European Journal*, *17*(36), 10097–10105. https://doi.org/10.1002/chem.201100711

Fremy, E. F. (1841). No Title. *Compt. Rend.*, *12*(23).

Fu, F., Dionysiou, D. D., & Liu, H. (2014). The use of zero-valent iron for groundwater remediation and wastewater treatment: A review. *Journal of Hazardous Materials*, *267*, 194–205. https://doi.org/10.1016/j.jhazmat.2013.12.062

Getty, K., Delgado-Jaine, M. U., & Kennepohl, P. (2008). Assignment of Pre-edge Features in the Ru K-edge X-ray Absorption Spectra of Organometallic Ruthenium Complexes. *Inorganica Chimica Acta*, *361*(4), 1059. https://doi.org/doi:10.1016/j.ica.2007.07.029

Gianelli, G., Puxeddu, M., Batini, F., Bertini, G., Dini, I., Pandeli, E., & Nicolich, R. (1988). Geological model of a young volcano-plutonic system: the geothermal region of Monte Amiata (Tuscany, Italy). *Geothermics*, *17*(5/6), 719–734. https://doi.org/https://doi.org/10.1016/0375-6505(88)90033-8

Gil-Díaz, M., Rodríguez-Alonso, J., Maffiotte, C. A., Baragaño, D., Millán, R., & Lobo, M. C. (2021). Iron nanoparticles are efficient at removing mercury from polluted waters. *Journal of Cleaner Production*, *315*, 128272. https://doi.org/10.1016/j.jclepro.2021.128272

Golovko, D. A., Sharma, V. K., Suprunovich, V. I., Pavlova, O. V., Golovko, I. D., Bouzek, K., & Zboril, R. (2011). A simple potentiometric titration method to determine concentration of ferrate(VI) in strong alkaline solutions. *Analytical Letters*, *44*(7), 1333–1340. https://doi.org/10.1080/00032719.2010.511748

Gombos, E., Barkács, K., Felföldi, T., Vértes, C., Makó, M., Palkó, G., & Záray, G. (2013).

Removal of organic matters in wastewater treatment by ferrate (VI)-technology. *Microchemical Journal*, *107*, 115–120. https://doi.org/10.1016/j.microc.2012.05.019

Graham, N., Jiang, C. C., Li, X. Z., Jiang, J. Q., & Ma, J. (2004). The influence of pH on the degradation of phenol and chlorophenols by potassium ferrate. *Chemosphere*, *56*, 949–956. https://doi.org/10.1016/j.chemosphere.2004.04.060

Guillou, J.-J., Monthel, J., Picot, P., Pillard, F., Protas, J., & Samama, J.-C. (1985). L'imitérite, Ag2HgS2, nouvelle espece minérale; propriétés et structure cristalline. *Bullettin de Mineralogie*, *108*, 457–464.

Guo, X., Yang, Z., Dong, H., Guan, X., Ren, Q., Lv, X., & Jin, X. (2016). Simple combination of oxidants with zero-valent-iron (ZVI) achieved very rapid and highly efficient removal of heavy metals from water. *Water Research*, *88*, 671–680. https://doi.org/10.1016/j.watres.2015.10.045

Han, Y., Fan, M., & Russell, A. G. (2015). New insights into synergistic effects and active species toward Hg0 emission control by Fe(VI) absorbent. *Fuel*, *140*, 309–316. https://doi.org/10.1016/j.fuel.2014.09.072

Hazen, R. M., Golden, J., Downs, R. T., Hystad, G., Grew, E. S., Azzolini, D., & Sverjensky, D. A. (2012). Mercury (Hg) mineral evolution: A mineralogical record of supercontinent assembly, changing ocean geochemistry, and the emerging terrestrial biosphere. *American Mineralogist*, *97*, 1013–1042. https://doi.org/10.2138/am.2012.3922

He, T., Zhou, B., Chen, H., & Yuan, R. (2022). Degradation of organic chemicals in aqueous system through ferrate-based processes : A review. *Journal of Environmental Chemical Engineering*, *10*(6), 108706. https://doi.org/10.1016/j.jece.2022.108706

He, W.-C., Wang, J.-M., Zhou, L., Chen, Q.-Q., Shen, B.-C., & Zhang, J.-Q. (2007). Study on the synthesis and physicochemistry properties of tripotassium sodium ferrate(VI). *Acta Chimica Sinica*, *65*(20), 2261–2265. https://doi.org/http://ir.imr.ac.cn/handle/321006/33579

He, W., Wang, J., Shao, H., Zhang, J., & Cao, C. N. (2005). Novel KOH electrolyte for one-step electrochemical synthesis of high purity solid K2FeO4: Comparison with NaOH. *Electrochemistry Communications*, *7*(6), 607–611. https://doi.org/10.1016/j.elecom.2005.04.011

Hellman, H., Laitinen, R. S., Kaila, L., Jalonen, J., Hietapelto, V., Jokela, J., Sarpola, A., & Ramo, J. (2006). Identification of hydrolysis products of FeCl3·6H2O by ESI-MS. *Journal of Mass*

Spectrometry, *41*, 1421–1429. https://doi.org/10.1002/jms.1107

Herber, R. H., & Johnson, D. (1979). Lattice Dynamics and Hyperfine Interactions in M2FeO4 (M = K+, Rb+, Cs+) and M'FeO4 (M' = Sr2+, Ba2+). *Inorganic Chemistry*, *18*(10), 2786–2790. https://doi.org/0020-1669/79/1318-2786S01.00/0

Híveš, J., Benová, M., Bouzek, K., Sitek, J., & Sharma, V. K. (2008). The cyclic voltammetric study of ferrate(VI) formation in a molten Na/K hydroxide mixture. *Electrochimica Acta*, *54*, 203–208. https://doi.org/10.1016/j.electacta.2008.08.009

Hoppe, M. L., Schlemper, E. O., & Murmann, R. K. (1982). Structure of dipotassium ferrate(VI). *Acta Crystallographica Section B Structural Crystallography and Crystal Chemistry*, *38*(8), 2237–2239. https://doi.org/10.1107/s0567740882008395

Hua, K., Xu, X., Luo, Z., Fang, D., Bao, R., & Yi, J. (2019). Effective Removal of Mercury Ions in Aqueous Solutions: A Review. *Current Nanoscience*, *16*(3), 363–375. https://doi.org/10.2174/1573413715666190112110659

Huang, H. H. (2016). The Eh-pH diagram and its advances. *Metals*, *6*(23), 1–30. https://doi.org/10.3390/met6010023

Huang, W., Xing, D. H., Lu, J. B., Long, B., Schwarz, W. H. E., & Li, J. (2016). How Much Can Density Functional Approximations (DFA) Fail? the Extreme Case of the FeO4 Species. *Journal of Chemical Theory and Computation*, *12*(4), 1525–1533. https://doi.org/10.1021/acs.jctc.5b01040

Huggins, F. E., Huffman, G. P., Dunham, G. E., & Senior, C. L. (1999). XAFS Examination of Mercury Sorption on Three Activated Carbons. *Energy and Fuels*, *13*(1), 114–121. https://doi.org/10.1021/ef9801322

Hylander, L. D., & Meili, M. (2003). 500 Years of mercury production: global annual inventory by region until 2000 and associated emissions. *Science of the Total Environment*, *304*, 13–27. https://doi.org/10.1016/S0048-9697(02)00553-3

Inoue, Y., & Munemori, M. (1979). Coprecipitation of Mercury(II) with Iron(lll) Hydroxide. *Environmental Science & Technology*, *13*(4), 443–445. https://doi.org/https://doi.org/10.1021/es60152a001

International Agency for Research on Cancer. (1991). Hypochlorite Salts. In *IARC monographs on the evaluation of carcinogenic risks to humans No. 52* (pp. 159–176).

Ippolito, J. A., Barbarick, K. A., & Elliott, H. A. (2011). Drinking Water Treatment Residuals: A Review of Recent Uses. *Journal of Environmental Quality*, *40*, 1–12.

https://doi.org/10.2134/jeq2010.0242

Jain, A., Sharma, V. K., & Mbuya, O. S. (2009). Removal of arsenite by Fe(VI), Fe(VI)/Fe(III), and Fe(VI)/Al(III) salts: Effect of pH and anions. *Journal of Hazardous Materials*, *169*(1–3), 339–344. https://doi.org/10.1016/j.jhazmat.2009.03.101

Jeannot, C., Malaman, B., Gérardin, R., & Oulladiaf, B. (2002). Synthesis, Crystal, and Magnetic Structures of the Sodium Ferrate (IV) Na4FeO4 Studied by Neutron Diffraction and Mössbauer Techniques. *Journal of Solid State Chemistry*, *165*, 266–277. https://doi.org/10.1006/jssc.2002.9520

Jiang, J.-Q., & Lloyd, B. (2002). Progress in the development and use of ferrate(VI) salt as an oxidant and coagulant for water and wastewater treatment. *Water Research*, *36*, 1397–1408. https://doi.org/10.1016/s0043-1354(01)00358-x

Jiang, J.-Q., Stanford, C., & Petri, M. (2018). Practical application of ferrate(VI) for water and wastewater treatment – Site study's approach. *Water-Energy Nexus*, *1*(1), 42–46. https://doi.org/10.1016/j.wen.2018.05.001

Jiang, J. Q. (2007). Research progress in the use of ferrate(VI) for the environmental remediation. *Journal of Hazardous Materials*, *146*(3), 617–623. https://doi.org/10.1016/j.jhazmat.2007.04.075

Jiang, J., Zhou, Z., Patibandla, S., & Shu, X. (2013). Pharmaceutical removal from wastewater by ferrate (VI) and preliminary effluent toxicity assessments by the zebra fish embryo model. *Microchemical Journal*, *110*, 239–245. https://doi.org/10.1016/j.microc.2013.04.002

Jiang, Jia Qian. (2014). Advances in the development and application of ferrate(VI) for water and wastewater treatment. *Journal of Chemical Technology and Biotechnology*, *89*, 165–177. https://doi.org/10.1002/jctb.4214

Jiang, Y., Goodwill, J. E., Tobiason, J. E., & Reckhow, D. A. (2015). Effect of different solutes, natural organic matter, and particulate Fe(III) on ferrate(VI) decomposition in aqueous solutions. *Environmental Science and Technology*, *49*(5), 2841–2848. https://doi.org/10.1021/es505516w

Johnson, M. D., & Lorenz, B. B. (2015). Antimony Remediation Using Ferrate(VI). *Separation Science and Technology (Philadelphia)*, *50*(11), 1611–1615. https://doi.org/10.1080/01496395.2014.982294

Kanari, N., Ostrosi, E., Diliberto, C., Filippova, I., Shallari, S., Allain, E., Diot, F., Patisson, F., &

Yvon, J. (2019). Green process for industrial waste transformation into super-oxidizing materials named alkali metal ferrates (VI). *Materials*, *12*(12), 1977. https://doi.org/10.3390/ma12121977

Karim, A. V., Krishnan, S., Pisharody, L., & Malhotra, M. (2020). Application of Ferrate for Advanced Water and Wastewater Treatment. *Advanced Oxidation Processes - Applications, Trends, and Prospects*, 1–20. https://doi.org/10.5772/intechopen.90231

Kašlík, J., Kolařík, J., Filip, J., Medřík, I., Tomanec, O., Petr, M., Malina, O., Zbořil, R., & Tratnyek, P. G. (2018). Nanoarchitecture of advanced core-shell zero-valent iron particles with controlled reactivity for contaminant removal. *Chemical Engineering Journal*, *354*, 335–345. https://doi.org/10.1016/j.cej.2018.08.015

Kim, C. S., Bloom, N. S., Rytuba, J. J., & Brown, G. E. (2003). Mercury Speciation by X-ray Absorption Fine Structure Spectroscopy and Sequential Chemical Extractions: A Comparison of Speciation Methods. *Environmental Science and Technology*, *37*(22), 5102–5108. https://doi.org/10.1021/es0341485

Kim, C. S., Brown, G. E., & Rytuba, J. J. (2000). Characterization and speciation of mercury-bearing mine wastes using X-ray absorption spectroscopy. *Science of the Total Environment*, *261*, 157–168. https://doi.org/10.1016/S0048-9697(00)00640-9

Kinniburgh, D. G., & Cooper, D. M. (2011). *PhreePlot: Creating Graphical Output with PHREEQC* (pp. 1–584). https://nora.nerc.ac.uk/id/eprint/19744/1/PhreePlot.pdf

Kiselev, Y. M., Kopelev, N. S., Zavyalova, N. A., Perfiliev, Y. D., & Kazin, P. E. (1989). On the preparation of alkali metal ferrates(VI). *Zhurnal Neorganicheskoj Khimii*, *34*(9), 2199–2202.

Klimkova, S., Cernik, M., Lacinova, L., Filip, J., Jancik, D., & Zboril, R. (2011). Zero-valent iron nanoparticles in treatment of acid mine water from in situ uranium leaching. *Chemosphere*, *82*, 1178–1184. https://doi.org/10.1016/j.chemosphere.2010.11.075

Kooti, M., Jorfi, M., & Javadi, H. (2010). Rapid Chemical Synthesis of Four Ferrate(VI) Compounds. *Journal of the Iranian Chemical Society*, *7*(4), 814–819. https://doi.org/https://doi.org/10.1007/BF03246073

Kopelev, N. S., Perfiliev, Y. D., & Kiselev, Y. M. (1992). Mossbauer Spectroscopy of Iron Oxocompounds. *Journal of Radioanalytical and Nuclear Chemistry*, *157*(2), 401–414. https://doi.org/https://doi.org/10.1007/BF02047456

Kralchevska, R. P., Prucek, R., Kolařík, J., Tuček, J., Machala, L., Filip, J., Sharma, V. K., &

Zbořil, R. (2016). Remarkable efficiency of phosphate removal: Ferrate(VI)-induced in situ sorption on core-shell nanoparticles. *Water Research*, *103*, 83–91. https://doi.org/10.1016/j.watres.2016.07.021

Laurenzi, M. A., Braschi, E., Casalini, M., & Conticelli, S. (2015). New 40Ar-39Ar dating and revision of the geochronology of the Monte Amiata Volcano, Central Italy. *Italian Journal of Geosciences*, *134*(2), 255–265. https://doi.org/10.3301/IJG.2015.11

Lee, D. G., & Gai, H. (1993). Kinetics and mechanism of the oxidation of alcohols by ferrate ion. *Canadian Journal of Chemistry*, *71*, 1394–1400. https://doi.org/doi:10.1139/v93-180

Lee, J., Tryk, D. A., Fujishima, A., & Park, S. M. (2002). Electrochemical generation of ferrate in acidic media at boron-doped diamond electrodes. *Chemical Communications*, *5*, 486–487. https://doi.org/10.1039/b111317h

Lee, P. A., Citrin, P. H., Eisenberger, P., & Kincaid, B. M. (1981). Extended x-ray absorption fine structure - its strengths and limitations as a structural tool. *Reviews of Modern Physics*, *53*(4), 769–806. https://doi.org/10.1103/RevModPhys.53.769

Lee, Y., Um, I., & Yoon, J. (2003). Arsenic(III) Oxidation by Iron(VI) (Ferrate) and Subsequent Removal of Arsenic(V) by Iron(III) Coagulation. *Environmental Science & Technology*, *37*, 5750–5756. https://doi.org/10.1021/es034203+

Lee, Y., Yoon, J., & Gunten, U. Von. (2005). Spectrophotometric determination of ferrate (Fe(VI)) in water by ABTS. *Water Research*, *39*, 1946–1953. https://doi.org/10.1016/j.watres.2005.03.005

Lehnherr, I., St. Louis, V. L., Hintelmann, H., & Kirk, J. L. (2011). Methylation of inorganic mercury in polar marine waters. *Nature Geoscience*, *4*(5), 298–302. https://doi.org/10.1038/ngeo1134

Lepore, G. O., Checchia, S., Baroni, T., Brunelli, M., & D'Acapito, F. (2022). Outstation for x-ray powder diffraction at the Italian beamline at the European synchrotron. *Review of Scientific Instruments*, *93*(11), 113903(1-7). https://doi.org/10.1063/5.0107024

Lescuras-Darrou, V., Lapicque, F., & Valentin, G. (2002). Electrochemical ferrate generation for waste water treatment using cast irons with high silicon contents. *Journal of Applied Electrochemistry*, *32*(1), 57–63. https://doi.org/10.1023/A:1014269523898

Li, C., Li, X. Z., & Graham, N. (2005). A study of the preparation and reactivity of potassium ferrate. *Chemosphere*, *61*(4), 537–543.

https://doi.org/10.1016/j.chemosphere.2005.02.027

Li, S., Wang, W., Liu, Y., & Zhang, W. (2014). Zero-valent iron nanoparticles (nZVI) for the treatment of smelting wastewater: A pilot-scale demonstration. *Chemical Engineering Journal*, *254*, 115–123. https://doi.org/10.1016/j.cej.2014.05.111

Licht, S., Naschitz, V., Ghosh, S., & Lin, L. (2001). SrFeO4 : Synthesis, Fe (VI) characterization and the strontium super-iron battery. *Electrochemistry Communications*, *3*, 340–345. https://doi.org/https://doi.org/10.1016/S1388-2481(01)00167-9

Licht, S., Naschitz, V., Halperin, L., Halperin, N., Lin, L., Chen, J., Ghosh, S., & Liu, B. (2001). Analysis of ferrate(VI) compounds and super-iron Fe(VI) battery cathodes: FTIR, ICP, titrimetric, XRD, UV/VIS, and electrochemical characterization. *Journal of Power Sources*, *101*(2), 167–176. https://doi.org/10.1016/S0378-7753(01)00786-8

Licht, S., Naschitz, V., Rozen, D., & Halperin, N. (2004). Cathodic Charge Transfer and Analysis of Cs2FeO4, K2FeO4, and Mixed Alkali Fe(VI) Ferrate Super-irons. *Journal of The Electrochemical Society*, *151*(8), A1147–A1151. https://doi.org/10.1149/1.1767156

Licht, S., Naschitz, V., & Wang, B. (2002). Rapid chemical synthesis of the barium ferrate super-iron Fe(VI) compound, BaFeO4. *Journal of Power Sources*, *109*, 67–70. https://doi.org/https://doi.org/10.1016/S0378-7753(02)00041-1

Licht, S., Wang, B., & Ghosh, S. (1999). Energetic Iron(VI) Chemistry: The Super-Iron Battery. *Science*, *285*(5430), 1039–1042. https://doi.org/http://www.jstor.org/stable/2898536

Licht, S., Yang, L., & Wang, B. (2005). Synthesis and analysis of Ag2FeO4 Fe(VI) ferrate super-iron cathodes. *Electrochemistry Communications*, *7*, 931–936. https://doi.org/10.1016/j.elecom.2005.06.008

Liu, Z., Wang, D., Yang, S., Liu, H., Liu, C., Xie, X., & Xu, Z. (2019). Selective recovery of mercury from high mercury-containing smelting wastes using an iodide solution system. *Journal of Hazardous Materials*, *363*, 179–186. https://doi.org/10.1016/j.jhazmat.2018.09.001

Lu, J. B., Jian, J., Huang, W., Lin, H., Li, J., & Zhou, M. (2016). Experimental and theoretical identification of the Fe(VII) oxidation state in FeO4-. *Physical Chemistry Chemical Physics*, *18*, 31125–31131. https://doi.org/10.1039/c6cp06753k

Lu, X., Huangfu, X., & Ma, J. (2014). Removal of trace mercury(II) from aqueous solution by in situ formed Mn-Fe (hydr)oxides. *Journal of Hazardous Materials*, *280*, 71–78. https://doi.org/10.1016/j.jhazmat.2014.07.056

Luo, Z., Strouse, M., Jiang, J. Q., & Sharma, V. K. (2011). Methodologies for the analytical determination of ferrate(VI): A Review. *Journal of Environmental Science and Health - Part A Toxic/Hazardous Substances and Environmental Engineering*, *46*(5), 453–460. https://doi.org/10.1080/10934529.2011.551723

Machala, L., Zboril, R., Sharma, V. K., Filip, J., Schneeweiss, O., & Homonnay, Z. (2007). Mossbauer Characterization and in Situ Monitoring of Thermal Decomposition of Potassium Ferrate(VI), K2FeO4 in Static Air Conditions. *Journal of Physical Chemistry B*, *111*, 4280–4286. https://doi.org/https://doi.org/10.1021/jp068272x

Machala, L., Zboril, R., Sharma, V. K., & Homonnay, Z. (2008). Decomposition of Potassium Ferrate(VI) (K2FeO4) and Potassium Ferrate(III) (KFeO2): In-situ Mössbauer Spectroscopy Approach. *AIP Conference Proceedings*, *1070*, 114–121. https://doi.org/https:// doi.org/10.1063/1.3030836

Mácová, Z., Bouzek, K., Híveš, J., Sharma, V. K., Terryn, R. J., & Baum, J. C. (2009). Research progress in the electrochemical synthesis of ferrate(VI). *Electrochimica Acta*, *54*(10), 2673–2683. https://doi.org/10.1016/j.electacta.2008.11.034

Malchus, M., & Jansen, M. (1998). Kombination von Ionenaustausch und Gefriertrocknung als Syntheseweg zu neuen Oxoferraten(VI) M2FeO4 mit M = Li, Na, N(CH3)4, N(CH3)3Bzl, N(CH3)3Ph. *Zeitschrift Fur Anorganische Und Allgemeine Chemie*, *624*, 1846–1854.

Markova, Z., Šiškova, K. M., Filip, J., Čuda, J., Kolár, M., Šafářova, K., Medřík, I., & Zbořil, R. (2013). Air Stable Magnetic Bimetallic Fe−Ag Nanoparticles for Advanced Antimicrobial Treatment and Phosphorus Removal. *Environmental Science & Technology*, *47*, 5258–5293. https://doi.org/dx.doi.org/10.1021/es304693g

Martinez-Tamayo, E., Beltrán-Porter, A., & Beltrán-Porter, D. (1986). Iron compounds in high oxidation states. II*. Reaction between Na2O2 and FeSO4. *Thermochimica Acta*, *97*, 243–255. https://doi.org/10.1016/0040-6031(86)87024-1

Meloni, F., Montegrossi, G., Lazzaroni, M., Rappuoli, D., Nisi, B., & Vaselli, O. (2021). Total and Leached Arsenic, Mercury and Antimony in the Mining Waste Dumping Area of Abbadia San Salvatore (Mt. Amiata, Central Italy). *Applied Sciences*, *11*(17), 7893. https://doi.org/https://doi.org/10.3390/app11177893

Merritt, E. A. (n.d.). *X-ray Absorption Edges*. Retrieved April 30, 2023, from http://skuld.bmsc.washington.edu/scatter/AS_periodic.html

Moeser, L. (1897). Mittheilung aus dem chemischen Laboratorinm des Prof. Alex. Nanmann zu Giessen. *Journal Für Praktische Chemie*, *56*, 425–437.

Monga, Y., Kumar, P., Sharma, R. K., Filip, J., Varma, R. S., Zbořil, R., & Gawande, M. B. (2020). Sustainable Synthesis of Nanoscale Zerovalent Iron Particles for Environmental Remediation. *ChemSusChem*, *13*, 3288–3305. https://doi.org/doi.org/10.1002/cssc.202000290

Morrison, S. J., Spangler, R. R., & Tripathi, V. S. (1995). Adsorption of uranium(VI) on amorphous ferric oxyhydroxide at high concentrations dissolved carbon(IV) and sulfur(VI). *Journal of Contaminant Hydrology*, *17*, 333–346. https://doi.org/https://doi.org/10.1016/0169-7722(94)00039-K

Morteani, G., Ruggieri, G., Möller, P., & Preinfalk, C. (2011). Geothermal mineralized scales in the pipe system of the geothermal Piancastagnaio power plant (Mt. Amiata geothermal area): a key to understand the stibnite, cinnabarite and gold mineralization of Tuscany (central Italy). *Miner Deposita*, *46*, 197–210. https://doi.org/10.1007/s00126-010-0316-5

Mukherjee, R., Kumar, R., Sinha, A., Lama, Y., & Saha, A. K. (2016). A review on synthesis, characterization, and applications of nano zero valent iron (nZVI) for environmental remediation. *Critical Reviews in Environmental Science and Technology*, *46*(5), 443–466. https://doi.org/10.1080/10643389.2015.1103832

Murmann, R. K., & Robinson, P. R. (1974). Experiments Utilizing FeO42- for Purifying Water. *Water Research*, *8*, 543–547. https://doi.org/https://doi.org/10.1016/0043-1354(74)90062-1

Nannoni, A., Meloni, F., Benvenuti, M., Cabassi, J., Ciani, F., Costagliola, P., Fornasaro, S., Lattanzi, P., Lazzaroni, M., Nisi, B., Morelli, G., Rimondi, V., & Vaselli, O. (2022). Environmental impact of past Hg mining activities in the Monte Amiata district, Italy: A summary of recent studies. *AIMS Geosciences*, *8*(4), 525–551. https://doi.org/10.3934/geosci.2022029

Netherlands Enterprise Agency. (2022). *Startup Ferr-Tech goes international with eco-friendly chemical Ferrate*. https://english.rvo.nl/information/startup-and-scale-support/startup-ferr-tech-goes-international-eco-friendly-chemical-ferrate

Ninane, L., Kanari, N., Criado, C., Jeannot, C., Evrard, O., & Neveux, N. (2008). New processes for alkali ferrate synthesis. *ACS Symposium Series*, *985*, 102–111.

https://doi.org/10.1021/bk-2008-0985.ch006

Noorhasan, N. N., Sharma, V. K., & Baum, J. C. (2008). A Fluorescence Technique to Determine Low Concentrations of Ferrate(VI). *ACS Symposium Series*, *985*, 145–155. https://doi.org/10.1021/bk-2008-0985.ch009

O'Connor, D., Hou, D., Ok, Y. S., Mulder, J., Duan, L., Wu, Q., Wang, S., Tack, F. M. G., & Rinklebe, J. (2019). Mercury speciation, transformation, and transportation in soils, atmospheric flux, and implications for risk management: A critical review. *Environment International*, *126*, 747–761. https://doi.org/10.1016/j.envint.2019.03.019

Ogasawara, S., Takano, M., & Bando, Y. (1988). New Hexavalent Iron Compound, K2Sr(FeO4)2. *Bullettin of the Institute for Chemical Research, Kyoto University*, *66*(2), 64–67. https://doi.org/http://hdl.handle.net/2433/77222

Parkhurst, D. A., & Appelo, C. A. J. (2013). Description of Input and Examples for PHREEQC Version 3—A Computer Program for Speciation, Batch-Reaction, One-Dimensional Transport, and Inverse Geochemical Calculations. In *U.S. Geological Survey Techniques and Methods* (Vol. 6, Issue A43, p. 497). https://doi.org/https://doi.org/10.3133/tm6A43

Pattelli, G., Rimondi, V., Benvenuti, M., Chiarantini, L., Colica, A., Costagliola, P., Di Benedetto, F., Lattanzi, P., Paolieri, M., & Rinaldi, M. (2014). Effects of the November 2012 Flood Event on the Mobilization of Hg from the Mount Amiata Mining District to the Sediments of the Paglia River Basin. *Minerals*, *4*, 241–256. https://doi.org/10.3390/min4020241

Peccerillo, A. (2005). The Tuscany Province. In *Plio-Quaternary Volcanism in Italy* (1st ed., pp. 17–50). Springer Berlin, Heidelberg. https://doi.org/https://doi.org/10.1007/3-540-29092-3_2

Pedroso, A. C. S., Gomes, L. E. R., & De Carvalho, J. M. R. (1994). Mercury removal from process sludges via hypochlorite leaching. *Environmental Technology*, *15*, 657–667. https://doi.org/10.1080/09593339409385471

Perfiliev, Y. D., Benko, E. M., Pankratov, D. A., Sharma, V. K., & Dedushenko, S. K. (2007). Formation of iron(VI) in ozonalysis of iron(III) in alkaline solution. *Inorganica Chimica Acta*, *360*, 2789–2791. https://doi.org/10.1016/j.ica.2006.11.019

Perfiliev, Y. D., & Sharma, V. K. (2008). Higher oxidation states of iron in solid state: synthesis and their Mossbauer characterization. *ACS Symposium Series*, *985*, 112–123.

https://doi.org/10.1021/bk-2008-0985.ch007

Prucek, R., Tucek, J., Kolarik, J., Filip, J., Marusak, Z., Sharma, V. K., & Zboril, R. (2013). Ferrate(VI)-Induced Arsenite and Arsenate Removal by In Situ Structural Incorporation into Magnetic Iron(III) Oxide Nanoparticles. *Environmental Science and Technology*, *47*, 3283–3292. https://doi.org/10.1021/es3042719

Prucek, R., Tuček, J., Kolařík, J., Hušková, I., Filip, J., Varma, R. S., Sharma, V. K., & Zbořil, R. (2015). Ferrate(VI)-prompted removal of metals in aqueous media: Mechanistic delineation of enhanced efficiency via metal entrenchment in magnetic oxides. *Environmental Science and Technology*, *49*(4), 2319–2327. https://doi.org/10.1021/es5048683

Puri, A., Lepore, G. O., & Acapito, F. (2019). The New Beamline LISA at ESRF: Performances and Perspectives for Earth and Environmental Sciences. *Condensed Matter*, *4*(12), 1–7. https://doi.org/10.3390/condmat4010012

Qu, Z., Fang, L., Chen, D., Xu, H., & Yan, N. (2017). Effective and regenerable Ag/graphene adsorbent for Hg (II) removal from aqueous solution. *Fuel*, *203*, 128–134. https://doi.org/10.1016/j.fuel.2017.04.105

Radepont, M., Coquinot, Y., Janssens, K., Ezrati, J.-J., De Nolf, W., & Cotte, M. (2015). Thermodynamic and experimental study of the degradation of the red pigment mercury sulfide. *Journal of Analytical Atomic Spectrometry*, *30*, 599–612. https://doi.org/https://doi.org/10.1039/C4JA00372A

Rai, P. K., Lee, J., Kailasa, S. K., Kwon, E. E., Tsang, Y. F., Ok, Y. S., & Kim, K. H. (2018). A critical review of ferrate(VI)-based remediation of soil and groundwater. *Environmental Research*, *160*(October 2017), 420–448. https://doi.org/10.1016/j.envres.2017.10.016

Ramli, S. F., & Aziz, H. A. (2015). Use of Ferric Chloride and Chitosan as Coagulant to Remove Turbidity and Color from Landfill Leachate. *Applied Mechanics and Materials*, *773–774*, 1163–1167. https://doi.org/10.4028/www.scientific.net/AMM.773-774.1163

Ravel, B., & Newville, M. (2005). ATHENA and ARTEMIS: Interactive Graphical Data Analysis using IFEFFIT. *Physica Scripta*, *T115*, 1007–1010. https://doi.org/10.1238/Physica.Topical.115a01007

Ravel, Bruce. (2001). ATOMS: Crystallography for the X-ray absorption spectroscopist. *Journal of Synchrotron Radiation*, *8*(2), 314–316. https://doi.org/10.1107/S090904950001493X

Ravel, Bruce. (2016). *Artemis: EXAFS Data Analysis using Feff with Larch or Ifeffit*. http://bruceravel.github.io/demeter/documents/Artemis/fit/happiness.html

Recovered Earth Technologies. (n.d.). *Ferrate Water Treatment systems*. Retrieved April 24, 2023, from https://www.recoveredearth.com/water-treatment-systems/ferrate-water-treatment/

Rehr, J. J., Albers, R. C., & Zabinsky, S. I. (1992). High-order multiple-scattering calculations of x-ray-absorption fine structure. *Physical Review Letters*, *69*(23), 3397–3400. https://doi.org/https://doi.org/10.1103/PhysRevLett.69.3397

Ribas, D., Cerník, M., Benito, J. A., Filip, J., & Marti, V. (2017). Activation process of air stable nanoscale zero-valent iron particles. *Chemical Engineering Journal*, *320*, 290–299. https://doi.org/10.1016/j.cej.2017.03.056

Riddle, S. G., Tran, H. H., Dewitt, J. G., & Andrews, J. C. (2002). Field, laboratory, and x-ray absorption spectroscopic studies of mercury accumulation by water hyacinths. *Environmental Science and Technology*, *36*, 1965–1970. https://doi.org/10.1021/es010603q

Rimondi, V., Bardelli, F., Benvenuti, M., Costagliola, P., Gray, J. E., & Lattanzi, P. (2014). Mercury speciation in the Mt. Amiata mining district (Italy): Interplay between urban activities and mercury contamination. *Chemical Geology*, *380*, 110–118. https://doi.org/10.1016/j.chemgeo.2014.04.023

Rimondi, V., Chiarantini, L., Lattanzi, P., Benvenuti, M., Beutel, M., Colica, A., Costagliola, P., Di Benedetto, F., Gabbani, G., Gray, J. E., Pandeli, E., Pattelli, G., Paolieri, M., & Ruggieri, G. (2015). Metallogeny, exploitation and environmental impact of the Mt. Amiata mercury ore district (Southern Tuscany, Italy). *Italian Journal of Geosciences*, *134*(2), 323–336. https://doi.org/10.3301/IJG.2015.02

Rimondi, V., Gray, J. E., Costagliola, P., Vaselli, O., & Lattanzi, P. (2012). Concentration, distribution, and translocation of mercury and methylmercury in mine-waste, sediment, soil, water, and fish collected near the Abbadia San Salvatore mercury mine, Monte Amiata district, Italy. *Science of the Total Environment*, *414*, 318–327. https://doi.org/10.1016/j.scitotenv.2011.10.065

Rush, J. D., & Bielski, B. H. J. (1986). Pulse Radiolysis Studies of Alkaline Fe(III) and Fe(VI) Solutions. Observation of Transient Iron Complexes with Intermediate Oxidation States. *Journal of the American Chemical Society*, *108*, 523–525.

https://doi.org/https://doi.org/10.1021/ja00263a037

Rytuba, J. J. (2003). Mercury from mineral deposits and potential environmental impact. *Environmental Geology*, *43*, 326–338. https://doi.org/10.1007/s00254-002-0629-5

Sahu, M. K., Patel, R. K., & Kurwadkar, S. (2022). Mechanistic insight into the adsorption of mercury (II) on the surface of red mud supported nanoscale zero-valent iron composite. *Journal of Contaminant Hydrology*, *246*, 103959. https://doi.org/10.1016/j.jconhyd.2022.103959

Schmidbaur, H. (2018). The History and the Current Revival of the Oxo Chemistry of Iron in its Highest Oxidation States: FeVI – FeVIII. *Zeitschrift Fur Anorganische Und Allgemeine Chemie*, *644*(12), 536–559. https://doi.org/10.1002/zaac.201800036

Schreyer, J. M., & Ockerman, L. T. (1951). Stability of Ferrate(VI) Ion in Aqueous Solution. *Analytical Chemistry*, *23*(9), 1312–1314. https://doi.org/10.1021/ac60057a028

Schreyer, J. M., Thompson, G. W., & Ockerman, L. T. (1950a). Ferrate Oxidimetry. Oxidation of Arsenite with Potassium Ferrate(VI). *Analytical Chemistry*, *22*(5), 691–692. https://doi.org/https://pubs.acs.org/doi/pdf/10.1021/ac60041a022

Schreyer, J. M., Thompson, G. W., & Ockerman, L. T. (1950b). Oxidation of Chromium(lll) with Potassium Ferrate(VI). *Analytical Chemistry*, *22*(11), 1426–1427. https://doi.org/https://doi.org/10.1021/ac60047a022

Sharma, V. K. (2007). Disinfection performance of Fe(VI) in water and wastewater: A review. *Water Science and Technology*, *55*(1–2), 225–232. https://doi.org/10.2166/wst.2007.019

Sharma, Virender K. (2010). Oxidation of nitrogen-containing pollutants by novel ferrate(VI) technology: A review. *Journal of Environmental Science and Health - Part A Toxic/Hazardous Substances and Environmental Engineering*, *45*(6), 645–667. https://doi.org/10.1080/10934521003648784

Sharma, Virender K. (2011). Oxidation of inorganic contaminants by ferrates (VI, V, and IV)-kinetics and mechanisms: A review. *Journal of Environmental Management*, *92*(4), 1051–1073. https://doi.org/10.1016/j.jenvman.2010.11.026

Sharma, Virender K., Smith, J. O., & Millero, F. J. (1997). Ferrate(VI) oxidation of hydrogen sulfide. *Environmental Science and Technology*, *31*(9), 2486–2491. https://doi.org/10.1021/es960755z

Shinjo, T., Ichida, T., & Takada, T. (1970). Fe57 Mossbauer Effect and Magnetic Susceptibility

of Hexavalent Iron Compounds; K2FeO4, SrFeO4 and BaFeO4. *Journal of the Physical Society of Japan*, *29*(1), 111–116. https://doi.org/https://doi.org/10.1143/JPSJ.29.111

Singh, R., Behera, M., & Kumar, S. (2020). Nano-bioremediation: An Innovative Remediation Technology for Treatment and Management of Contaminated Sites. In *Bioremediation of Industrial Waste for Environmental Safety* (pp. 165–182). https://doi.org/https://doi.org/10.1007/978-981-13-3426-9_7 165

Siregar, A., Kleber, M., Mikutta, R., & Jahn, R. (2005). Sodium hypochlorite oxidation reduces soil organic matter concentrations without affecting inorganic soil constituents. *European Journal of Soil Science*, *56*, 481–490. https://doi.org/10.1111/j.1365-2389.2004.00680.x

Song, Y. R., & Ma, J. W. (2013). Oxidation of inorganic contaminants by ferrates (VI)-a review. *Applied Mechanics and Materials*, *361–363*, 662–665. https://doi.org/10.4028/www.scientific.net/AMM.361-363.662

Su, C., & Puls, R. W. (2001). Arsenate and arsenite removal by zerovalent iron: Effects of phosphate, silicate, carbonate, borate, sulfate, chromate, molybdate, and nitrate, relative to chloride. *Environmental Science and Technology*, *35*(22), 4562–4568. https://doi.org/10.1021/es010768z

Sumesh, E., Bootharaju, M. S., & Pradeep, T. (2011). A practical silver nanoparticle-based adsorbent for the removal of Hg2+ from water. *Journal of Hazardous Materials*, *189*, 450–457. https://doi.org/10.1016/j.jhazmat.2011.02.061

Sun, X. H., Wang, L., Li, W. C., & Tuo, W. Q. (2013). Preparation of liquid ferrate and the optimization of process parameters. *Advanced Materials Research*, *772*, 884–887. https://doi.org/10.4028/www.scientific.net/AMR.772.884

Sun, Y., Li, J., Huang, T., & Guan, X. (2016). The influences of iron characteristics, operating conditions and solution chemistry on contaminants removal by zero-valent iron: A review. *Water Research*, *100*, 277–295. https://doi.org/10.1016/j.watres.2016.05.031

Tang, X., Zheng, H., Teng, H., Sun, Y., Guo, J., Xie, W., Yang, Q., & Chen, W. (2014). Chemical coagulation process for the removal of heavy metals from water : a review. *Desalination and Water Treatment*, *57*, 1733–1748. https://doi.org/https://doi.org/10.1080/19443994.2014.977959

Tchounwou, P. B., Yedjou, C. G., Patlolla, A. K., & Sutton, D. J. (2012). Heavy Metal Toxicity and the Environment. *Experientia Supplementum*, *101*, 133–164.

https://doi.org/https://doi.org/10.1007/978-3-7643-8340-4_6

Thompson, G. W., Ockerman, L. T., & Schreyer, J. M. (1951). Preparation and Purification of Potassium Ferrate. VI. *Journal of the American Chemical Society*, *73*(3), 1379–1381. https://doi.org/https://doi.org/10.1021/ja01147a536

Thompson, J. A. (1983). *Process for producing alkali metal ferrates* (Patent No. 4385045).

Tiffreau, C., Lützenkirchen, J., & Behra, P. (1995). Modeling the Adsorption of Mercury(II) on (Hydr)oxides. In *Journal of Colloid and Interface Science* (Vol. 172, pp. 82–93). https://doi.org/10.1006/jcis.1995.1228

Tiwari, D., Kim, H. U., Choi, B. J., Lee, S. M., Kwon, O. H., Choi, K. M., & Yang, J. K. (2007). Ferrate(VI): A green chemical for the oxidation of cyanide in aqueous/waste solutions. *Journal of Environmental Science and Health - Part A Toxic/Hazardous Substances and Environmental Engineering*, *42*, 803–810. https://doi.org/10.1080/10934520701304674

Tratnyek, P. G., & Johnson, R. L. (2006). Nanotechnologies for environmental cleanup. *Nanotoday*, *1*(2), 44–48. https://doi.org/https://doi.org/10.1016/S1748-0132(06)70048-2

Treadway, T. (2020). *Lake Okeechobee algae blooms net $5 million in state grants to help monitor, prevent them*. Treasure Coast Newspapers. https://eu.tcpalm.com/story/news/local/indian-river-lagoon/health/2020/07/29/lake-okeechobee-algae-blooms-state-grants-monitor-prevent/5530646002/

U.S. EPA. (n.d.). *EPA Method 7473 (SW-846): Mercury in Solids and Solutions by Thermal Decomposition, Amalgamation, and Atomic Absorption Spectrophotometry*. Retrieved April 30, 2023, from https://www.epa.gov/esam/epa-method-7473-sw-846-mercury-solids-and-solutions-thermal-decomposition-amalgamation-and

United Nation Environmental Programme. (2013). *Minamata Convention on Mercury - Text and Annexes*. https://mercuryconvention.org/en/resources/minamata-convention-mercury-text-and-annexes

United States Environmental Protection Agency. (2023). *Health Effects of Exposures to Mercury*. https://www.epa.gov/mercury/health-effects-exposures-mercury

Vaselli, O., Lazzaroni, M., Nisi, B., Cabassi, J., Tassi, F., Rappuoli, D., & Meloni, F. (2021). Discontinuous Geochemical Monitoring of the Galleria Italia Circumneutral Waters (Former Hg-Mining Area of Abbadia San Salvatore, Tuscany, Central Italy) Feeding the Fosso Della Chiusa Creek. *Environments*, *8*(15), 1–16.

https://doi.org/10.3390/environments8020015

Vaselli, O., Nisi, B., Rappuoli, D., Bianchi, F., Cabassi, J., Venturi, S., Tassi, F., & Raco, B. (2015). Geochemical characterization of the ground waters from the former Hg-mining area of Abbadia San Salvatore (Mt . Amiata, central Italy): criticalities and perspectives for the reclamation process. *Italian Journal of Geosciences*, *134*(2), 304–322. https://doi.org/10.3301/IJG.2015.03

Vaselli, O., Rappuoli, D., Bianchi, F., Nisi, B., Niccolini, M., Esposito, A., Cabassi, J., Giannini, L., & Tassi, F. (2019). One hundred years of mercury exploitation at the mining area of Abbadia San Salvatore (Mt. Amiata, central Italy): a methodological approach for a complex reclamation activity before the establishment of a new mining park. In *El patrimonio geológico y minero. Identidad y motor dedesarrollo* (pp. 1109–1126). Instituto Geológico y Minero de España, Madrid.

Venkatadri, A. S., Wagner, W. F., & Bauer, H. H. (1971). Ferrate(VI) Analysis by Cyclic Voltammetry. *Analytical Chemistry*, *43*(8), 1115–1119. https://doi.org/https://doi.org/10.1021/ac60303a036

Vernon, J. D., & Bonzongo, J. C. J. (2014). Volatilization and sorption of dissolved mercury by metallic iron of different particle sizes: Implications for treatment of mercury contaminated water effluents. *Journal of Hazardous Materials*, *276*, 408–414. https://doi.org/10.1016/j.jhazmat.2014.05.054

Wagner, W. F., Gump, J. R., & Hart, E. N. (1952). Factors Affecting the Stability of Aqueous Potassium Ferrate(VI) Solutions. *Analytical Chemistry*, *24*(9), 1497–1498. https://doi.org/https://doi.org/10.1021/ac60069a037

Wang, K. M., Shu, J., Wang, S. J., Hong, T. Y., Xu, X. P., & Wang, H. Y. (2020). Efficient electrochemical generation of ferrate(VI) by iron coil anode imposed with square alternating current and treatment of antibiotics. *Journal of Hazardous Materials*, *384*(October 2019). https://doi.org/10.1016/j.jhazmat.2019.121458

Wang, L., Xu, H., Qiu, Y., Liu, X., Huang, W., Yan, N., & Qu, Z. (2020). Utilization of Ag nanoparticles anchored in covalent organic frameworks for mercury removal from acidic waste water. *Journal of Hazardous Materials*, *389*, 121824. https://doi.org/10.1016/j.jhazmat.2019.121824

Water and Energy Exchange Global. (2023). *Innovation Forum Awards 2023*. https://wex-global.com/innovation-forum/

Wei, Y., Wang, Y., & Liu, C. (2015). Preparation of Potassium Ferrate from Spent Steel Pickling Liquid. *Metals*, *5*, 1770–1787. https://doi.org/10.3390/met5041770

Williams, D. H., & Riley, J. T. (1974). Preparatlon and Alcohol Oxidation Studies of the Ferrate(VI) Ion, FeO42-. *Inorganica Chimica Acta*, *8*, 177–183. https://doi.org/https://doi.org/10.1016/S0020-1693(00)92612-4

Wood, R. H. (1958). The Heat, Free Energy and Entropy of the Ferrate(VI) Ion. *Journal of the American Chemical Society*, *80*, 2038–2041. https://doi.org/https://doi.org/10.1021/ja01542a002

World Health Organization. (2017). *Mercury and health*. https://www.who.int/news-room/fact-sheets/detail/mercury-and-health

Wyckoff, R. W. G. (1963). *Crystal structure*. Interscience Publishers.

Xu, Z., Wang, J., Shao, H., Tang, Z., & Zhang, J. (2007). Preliminary investigation on the physicochemical properties of calcium ferrate(VI). *Electrochemistry Communications*, *9*, 371–377. https://doi.org/10.1016/j.elecom.2006.09.015

Yan, W., Herzing, A. A., Kiely, C. J., & Zhang, W. X. (2010). Nanoscale zero-valent iron (nZVI): Aspects of the core-shell structure and reactions with inorganic species in water. *Journal of Contaminant Hydrology*, *118*, 96–104. https://doi.org/10.1016/j.jconhyd.2010.09.003

Yang, W., Wang, J., Pan, T., Xu, J., Zhang, J., & Cao, C. (2002). Studies on the electrochemical characteristics of K2Sr(FeO4)2 electrode. *Electrochemistry Communications*, *4*, 710–715. https://doi.org/https://doi.org/10.1016/S1388-2481(02)00429-0

Yates, B. J., Darlington, R., Zboril, R., & Sharma, V. K. (2014). High-valent iron-based oxidants to treat perfluorooctanesulfonate and perfluorooctanoic acid in water. *Environmental Chemistry Letters*, *12*, 413–417. https://doi.org/10.1007/s10311-014-0463-5

Yates, B. J., Zboril, R., & Sharma, V. K. (2014). Engineering aspects of ferrate in water and wastewater treatment-a review. *Journal of Environmental Science and Health - Part A Toxic/Hazardous Substances and Environmental Engineering*, *49*(14), 1603–1614. https://doi.org/10.1080/10934529.2014.950924

Yngard, R. A., Sharma, V. K., Filip, J., & Zboril, R. (2008). Ferrate (VI) Oxidation of Weak-Acid Dissociable Cyanides. *Environmental Science and Technology*, *42*(8), 3005–3010.

Yu, J. G., Yue, B. Y., Wu, X. W., Liu, Q., Jiao, F. P., Jiang, X. Y., & Chen, X. Q. (2016). Removal of mercury by adsorption: a review. *Environmental Science and Pollution Research*, *23*,

5056–5076. https://doi.org/10.1007/s11356-015-5880-x

Yu, J., Sumita, Zhang, K., Zhu, Q., Wu, C., Huang, S., Zhang, Y., Yao, S., & Pang, W. (2023). A Review of Research Progress in the Preparation and Application of Ferrate(VI). *Water (Switzerland)*, *15*, 699. https://doi.org/10.3390/w15040699

Zboril, R., Andrle, M., Oplustil, F., Machala, L., Tucek, J., Filip, J., Marusak, Z., & Sharma, V. K. (2012). Treatment of chemical warfare agents by zero-valent iron nanoparticles and ferrate (VI)/(III) composite. *Journal of Hazardous Materials*, *211–212*, 126–130. https://doi.org/10.1016/j.jhazmat.2011.10.094

Zeng, F., Chen, C., & Huang, X. (2020). Enhanced electro-generated ferrate using Fe(0)-plated carbon sheet as an anode and its online utilization for removal of cyanide. *Chemosphere*, *241*, 125124. https://doi.org/10.1016/j.chemosphere.2019.125124

Zhang, C. Z., Liu, Z., Wu, F., Lin, L. J., & Qi, F. (2004). Electrochemical generation of ferrate on SnO2-Sb2O3/Ti electrodes in strong concentration basic condition. *Electrochemistry Communications*, *6*, 1104–1109. https://doi.org/10.1016/j.elecom.2004.08.011

Zhao, Y., Han, Y., Guo, T., & Ma, T. (2014). Simultaneous removal of SO2, NO and Hg0 from flue gas by ferrate (VI) solution. *Energy*, *67*, 652–658. https://doi.org/10.1016/j.energy.2014.01.081

Zhou, J., Liu, Y., & Pan, J. (2017). Removal of elemental Mercury from flue gas using wheat straw chars modified by K2FeO4 reagent. *Environmental Technology (United Kingdom)*, *38*(23), 3047–3054. https://doi.org/10.1080/09593330.2017.1287222

Zou, Y., Wang, X., Khan, A., Wang, P., Liu, Y.-H., Alsaedi, A., Hayat, T., & Wang, X. (2016). Environmental Remediation and Application of Nanoscale Zero-Valent Iron and Its Composites for the Removal of Heavy Metal Ions: A Review. *Environmental Science & Technology*, *50*(14), 7290–7304. https://doi.org/https://doi.org/10.1021/acs.est.6b01897

- Acknowledgements –

At the end of this long journey, I would like to thank all the people who have accompanied me, helping me to grow both as a student and as a person.

Francesco Di Benedetto, my supervisor, a wonderful person who had the patience to stand by me over the years. I want to thank him from the bottom of my heart for all the support he showed me, for all the opportunities for growth he offered me, for being more than just a supervisor. I think there are few PhD students as fortunate as I have been. And together with Francesco I want to thank **Giordano Montegrossi**, for the valuable advice and equally valuable laughter.

Thanks also to **Orlando Vaselli** and **Francesco Capecchiacci**, for allowing me to soil the geochemistry labs with my concoctions. Thanks for the valuable advice, jokes and technical support. You are the best!

Thanks to **Francesco D'Acapito**, who passed on unparalleled knowledge about XAS, giving me enormous job satisfaction and the confidence to get where I am now. Special thanks also to **Fabrizio La Manna**, without whom the stay in Grenoble would not have been the same, to **Michela Brunelli**, **Alessio D'Acapito** and all the staff of **LISA**. Working with you has been one of the best experiences of these years.

Thank you to **Jan Filip** for his helpfulness, kindness shown to me and the professionalism he puts into his work, not at all taken for granted, and thank you to the RCPTM staff with whom I came in contact.

Thanks to my families, the one I chose myself and who chose me in turn and my birth family. Thank you to my lifelong friends, the ones from Mugello, life companions with whom I grew up, and those who came into my life and had the patience to stay. Special thanks to **Maso**, **Vale** and their parents, who taught me so much, to **Marta**, **Becchi**, **Francy**, companions of so many of my memories.

Thanks to **my friends from the university**, those who have been with me for years now and those I met the day before yesterday but it already seems like a lifetime. You are more than I could have ever hoped for, and if with many of you our paths have already parted or are about to part, I jealously preserve within me the images of the spritzes, the tears, the sweat we shed together.

Thank you **Aula Studio**, more than a second home, more than an office, in which I felt protected all these years. I hope to continue to feel so at home wherever my life takes me. Thank you to the **Georock** group that on par with a school of life allows me to become more than I am. "If you want to become a better person, play with those who are better than you".

Special thanks to **Giacomone** and his family, populated by people as peculiar as they are fantastic. You will reign in heaven, I am sure. Thank you to **Nick**, a great little brother I never knew I had and with whom I hope to continue to make countless memories. A special thanks to **Nadia**; without you all this, this whole thesis, would never have seen the light of day. You gave me strength when moving forward seemed impossible, you gave me more than I could ever deserve. We have experienced wonderful days and faced insidious moments this past year, and I want with all my heart to continue building experiences with you, good and bad. I will never stop thanking you (and apologizing).

Thanks to **Maria C. P.**; she, more than any other person, knows why.

And thanks to my **parents** and all **my little family**. Like every "corresponding author" it fell to you to send me out into the world and see me come back at every "major revision." You tried to patch me up as best you could and sent me back to the ruthless reviewer that is life. I hope one day to be able to feel as fully realized as if I were an article published in Nature. For now, I am also content with an MDPI. Thank you for all the support you have given me and for always looking out for me.

So long and thanks for all the fish.

- Ringraziamenti –

Alla fine di questo lungo percorso, vorrei ringraziare tutte le persone che mi hanno accompagnato, aiutandomi a crescere sia come studente che come persona.

Voglio iniziare ringraziando **Francesco Di Benedetto**, il mio supervisor, persona stupenda che ha avuto la pazienza di starmi accanto in questi anni. Voglio ringraziarlo dal profondo del cuore per tutto il supporto dimostratomi, per tutte le occasioni di crescita che mi ha offerto, per essere stato più di un semplice supervisor. Credo siano pochi gli studenti di dottorato fortunati come lo sono stato io. Ed assieme a Francesco voglio ringraziare **Giordano Montegrossi**, per i preziosi consigli e le altrettanto preziose risate. Grazie Gio!

Grazie anche ad **Orlando Vaselli** e **Francesco Capecchiacci**, per avermi permesso di sporcare i laboratori di geochimica con i miei intrugli. Grazie per i preziosi consigli, per le battute e per il supporto tecnico. Siete grandi!

Grazie a **Francesco D'Acapito**, che mi ha trasmesso una conoscenza senza pari sulla XAS, regalandomi enormi soddisfazioni lavorative e dandomi la fiducia necessaria ad arrivare dove sono adesso. Un grazie particolare anche a **Fabrizio La Manna**, senza cui il soggiorno a Grenoble non sarebbe stato lo stesso, a **Michela Brunelli**, **Alessio D'Acapito** ed a tutto lo staff di **LISA**. Lavorare con voi è stata una delle esperienze più belle di questi anni.

Grazie a **Jan Filip** per la disponibilità, la gentilezza dimostratami e la professionalità che mette nel suo lavoro, per niente scontata, e grazie allo staff dell'RCPTM con cui sono entrato in contatto.

Grazie alle mie **famiglie**, quella che mi sono scelto e che mi ha scelto a sua volta e la mia famiglia naturale. Grazie agli amici di sempre, quelli del Mugello, compagni di vita con cui sono cresciuto, ed altrettanto a quelli che sono entrati nella mia vita ed hanno avuto la pazienza di rimanerci. Un grazie particolare a **Maso**, **Vale** ed ai loro genitori, che mi hanno insegnato tanto, a **Marta, Becchi**, **Francy**, compagni di tanti miei ricordi.

Grazie agli amici dell'**università**, a coloro che ormai mi accompagnano da anni ed a quelli che ho conosciuto l'altro ieri ma sembra già una vita. Siete più di quanto avessi mai potuto sperare e se con molti di voi le nostre strade si sono già divise o si stanno per dividere, conservo gelosamente dentro di me le immagini degli spritz, delle lacrime, del sudore che abbiamo versato assieme.

Grazie **Aula Studio**, più di una seconda casa, più di un ufficio, in cui mi sono sentito protetto per tutti questi anni. Spero di continuare a sentirmi così a casa in ogni luogo in cui la mia vita mi porterà. Grazie al gruppo **Georock** che al pari di una scuola di vita mi permette di diventare più di quanto sia. "Se vuoi diventare una persona migliore suona con chi è più bravo di te".

Un grazie speciale a **Giacomone** ed alla sua famiglia, popolata da persone tanto peculiari quanto fantastiche. Regnerai in paradiso, ne sono certo. Grazie a **Nick**, un piccolo grande fratello che non sapevo di avere e con cui spero di continuare a vivere innumerevoli ricordi. Un grazie speciale a **Nadia**; senza di te tutto questo, tutta questa tesi, non avrebbe mai visto la luce. Mi hai dato forza quando andare avanti sembrava impossibile, mi hai dato più di quanto potessi mai meritare. Abbiamo vissuto giorni meravigliosi ed affrontato momenti tremendi in quest'ultimo anno, e voglio con tutto me stesso continuare a costruire esperienze con te, belle e brutte che siano. Non smetterò mai di ringraziarti (e chiederti scusa).

Grazie a **Maria C. P.**; lei, più di ogni altra persona, sa perchè.

E grazie ai miei **genitori** ed a tutta la mia piccola famiglia. Come ogni "corresponding author" vi è toccato il compito di inviarmi nel mondo e vedermi tornare indietro ad ogni "major revision". Avete cercato di rattopparmi al vostro meglio e mi avete inviato di nuovo a quel reviewer spietato che è la vita. Spero un giorno di riuscire a sentirmi pienamente realizzato come se fossi un articolo pubblicato su Nature. Per adesso mi accontento anche di un MDPI. Grazie di tutto il supporto che mi avete dato e per guardarmi sempre le spalle.

Addio e grazie per tutto il pesce.